

# STM Investigation of Molecular Architectures of Porphyrinoids on a Ag(111) Surface

## Supramolecular Ordering, Electronic Properties and Reactivity

---

STM Untersuchung von Porphyrinoidarchitekturen  
auf einer Ag(111) Oberfläche

Supramolekulare Ordnung, elektronische Eigenschaften und Reaktivität

Der Naturwissenschaftlichen Fakultät der  
Friedrich-Alexander-Universität Erlangen-Nürnberg

zur Erlangung des Doktorgrades Dr. rer. nat.

vorgelegt von

**Florian Buchner**

aus Burghausen

Als Dissertation genehmigt

durch die Naturwissenschaftliche Fakultät

der Friedrich-Alexander-Universität Erlangen-Nürnberg

Tag der mündlichen Prüfung: \_\_\_\_\_

Vorsitzende/r der Promotionskommission: Prof. Dr. Bänsch

Erstberichtersteller/in: Prof. Dr. Hans-Peter Steinrück

Zweitberichtersteller/in: Prof. Dr. Andreas Görling

# Table of Contents

<b>1</b>	<b>Introduction</b>	<b>1</b>
<b>2</b>	<b>Fundamentals</b>	<b>5</b>
2.1	Principle of the STM	5
2.2	Origin of the Tunneling Current	7
2.3	Scanning Tunnelling Spectroscopy	10
2.4	Contrast Mechanism of Molecular Adsorbates	13
2.5	Temperature Programmed Desorption	16
2.6	Low Energy Electron Diffraction	18
<b>3</b>	<b>Experimental Setup</b>	<b>21</b>
3.1	UHV System	21
3.2	Scanning Tunneling Microscope	23
3.3	Control Electronics and Vibration Isolation	26
3.4	Ag(111)	28
3.5	Porphyrinoids	30
3.6	Preparation of thin Porphyrinoid Layers	33
3.7	Vapor-deposition of Cobalt and Iron	34
<b>4</b>	<b>Results</b>	<b>37</b>
<b>4.1</b>	<b>Self-Assembly and Individual Appearance of Tetraphenylporphyrins on Ag(111)</b>	<b>38</b>
4.1.1	Epitaxial growth	40
4.1.2	Appearance and Intramolecular Conformation	45
4.1.3	Ordering Aspects	47
<b>4.2</b>	<b>Self-Assembly and Individual Appearance of Cobalt(II)-Tetrakis-diterbutylphenylporphyrins on Ag(111)</b>	<b>57</b>
4.2.1	Polymorphism of CoTTBPP	58
4.2.2	Polarity-Dependent Appearance	74

<b>4.3 Coordination of Iron and Cobalt Atoms by Tetraphenylporphyrin Monolayers on Ag(111) and Formation of Metal(II)-Tetraphenylporphyrin .....</b>	<b>77</b>
4.3.1 Coordination of Post-deposited Iron Atoms by Tetraphenylporphyrin Monolayers .....	79
4.3.2 Coordination of Pre-deposited Iron Atoms by Tetraphenylporphyrin Monolayers .....	84
4.3.3 Coordination of Post-deposited Cobalt Atoms by Tetraphenylporphyrin Monolayers .....	88
4.3.4 Discussion of the Metalation Reaction .....	93
<b>4.4 Different Aspects of 2H-Tetrakisdi-tert-butylphenylporphyrin on Ag(111)....</b>	<b>97</b>
4.4.1 Monolayer Preparation.....	98
4.4.2 Arrangement of 2HTTBPP .....	101
4.4.3 Voltage-Dependent Appearance .....	106
4.4.4 Direct Metalation of 2HTTBPP with Co-adsorbed Iron.....	109
<b>4.5 Direct Metalation of a Phthalocyanine Monolayer on Ag(111) with co-adsorbed Iron Atoms .....</b>	<b>111</b>
<b>4.6 Multicomponent Adlayers of Tetraphenylporphyrins on Ag(111).....</b>	<b>121</b>
4.6.1 Understanding the Contrast Mechanism in STM images of Cobalt Tetraphenylporphyrin on Ag(111).....	121
4.6.2 Fingerprints of different Porphyrins .....	131
4.6.3 Addressing Molecular Orbitals of Cobalt- and Iron-Tetraphenylporphyrins by Continuous Imaging Tunneling Spectroscopy .....	149
<b>4.7 Modification of the Growth of Iron on Ag(111) by Predeposited Organic Monolayers.....</b>	<b>159</b>
4.7.1 Growth of Fe on Ag(111) .....	161
4.7.2 Growth of Fe on Ag(111) precovered with different tetrapyrrolic monolayers ..	164
<b>4.8 Geometric and Electronic Aspects of CoTPP upon Dosage of NO .....</b>	<b>175</b>
4.8.1 In-situ Observation of the Rearrangement of CoTPP on Ag(111) .....	177
4.8.2 Modification of the Appearance of CoTPP upon Formation of NO-CoTPP ..	184

---

<b>4.9 Self-Assembly and Voltage-dependent Appearance of Octaethylporphyrins</b>	<b>189</b>
.....	
<b>5 Summary and Outlook</b>	<b>197</b>
<b>6 Zusammenfassung und Ausblick</b>	<b>201</b>
<b>List of Abbreviations</b>	<b>207</b>
<b>Figure Caption</b>	<b>209</b>
<b>References</b>	<b>219</b>
<b>List of Publications</b>	<b>227</b>
<b>Appendix</b>	<b>229</b>



# 1 Introduction

---

The technological capabilities towards the generation of smaller minimum feature sizes, e.g., in microelectronics, are fundamentally limited in the top-down approach. An alternative route to generate nanometer sized functional structures is the self-assembly of atoms or molecules on well defined surfaces [1]. In respect of such a bottom-up strategy, the investigation of large organic molecules on single crystalline surfaces with scanning tunneling microscopy (STM) has become a fast growing field in surface science. One main motivation lies in the exploration of nanodevice concepts and accordingly the perspective to engineer applications with outstanding properties. Additionally it opens up the possibility to gain deeper insight into fundamental properties of the utilized molecular building blocks in real space. In this respect porphyrinoids appear as ideal candidates due to their versatile functionalities basically determined by the corresponding central metal. Prominent examples, where porphyrinoids act as main functional building blocks can be found in biological systems, e.g., magnesium porphyrins in chlorophyll [2], cobalt corrin in cobalamin (vitamin B12) [3], or iron porphyrin in heme, which is essential for oxygen transport in the blood stream of mammals [4].

The combination of their rigid structure, which often triggers long-range order, and an active site, usually the coordinated metal center makes porphyrinoids potential candidates for the nanoscale functionalization of surfaces. Furthermore, the low vapor pressure at room temperature (RT) enables the sublimation of these molecules under ultra-high vacuum (UHV) conditions and allows depositing them on a substrate in a controlled manner. In the work at hand STM has been utilized to study the topography and electronic structure of porphyrinoids on a Ag(111) surface. The corresponding experiments were conducted under UHV conditions and with the sample mostly held at RT. Note that this type of experiments are often performed at low temperatures (4 K - 200 K), which is obviously a problem if one wants to develop applications based on the corresponding results.

The conducted work is embedded in the project A9 “*Adsorption and Reactivity of Redoxactive Metalloporphyrins*” of the SFB 583 “*Redox-Active Metal Complexes: Control of Reactivity via Molecular Architecture*” (funded by the Deutsche Forschungsgemeinschaft), which among others aims towards a detailed understanding of geometric aspects, electronic properties as well as the reactivity of the corresponding molecular networks.

The thesis at hand is organized such, that the introduction (chapter 1) is followed by the fundamentals of the applied surface science techniques (chapter 2) and the experimental setup (chapter 3). Chapter 4.1 and 4.2 particularly address the self-assembly of different porphyrinoids (with and/or without a central metal) and the driving forces, which determine the respective arrangement. In that course it was a prerequisite to acquire STM images of these thin layers with sub-molecular resolution allowing the determination of the internal conformation of the individual porphyrinoids. The latter is expected to play an important role with respect to the reactivity of the organic layers. A novel route to generate metalloporphyrins *in-situ* in UHV was investigated in detail and is reported in chapter 4.3 – 4.5. Once having generated these clean two-dimensional layers of metalloporphyrinoids, it was a major task to study the interaction with small molecules, e.g., nitric oxide (NO), as described in chapter 4.8. The latter experiment could be an important step towards the engineering of functional devices based on, e.g., reversible adsorption, and also with respect to the understanding of the aforementioned biological processes. A detailed investigation of the electronic properties of the adsorbed tetrapyrroles can be found in chapter 4.6 and 4.8. In the spectroscopy mode the STM allows to measure current-voltage (I-V) characteristics, which enabled both to calculate spectra of the local density of states (LDOS) and also to create maps of the electronic structure of a surface. In combination with theoretical calculations the interaction of cobalt-tetraphenylporphyrin (CoTPP) with the Ag(111) substrate was explained.

In summary, a detailed microscopic understanding of the ordering aspects and the electronic structure of different porphyrinoids, in particular of tetraphenylporphyrins on Ag(111), was established. Several novel effects or insights are reported and discussed

like the *in-situ* metalation of different free base porphyrinoids, the role of 2D-chirality in respect to long-range ordering, the complex rearrangement of ordered porphyrin layers upon dosage of small molecules (NO, CO), the preparation of an extremely stable and highly ordered interwoven cobalt-tetrakisdi-*tert*-butylphenylporphyrin (CoTTBPP) phase and the understanding of how the substrate-molecule interaction can influence the molecular orbitals of the corresponding adsorbate system and thus the appearance in STM. These findings constitute potential approaches to engineer functional devices from porphyrinoids on surfaces.



## 2 **Fundamentals**

---

The basic principle of the STM experiment is described in chapter 2.1. A theoretical basis for the treatment of electron tunneling in STM is given by Bardeen's theory [5], which is the preeminent quantitative theory of the tunnelling current in STM [6]. It was published in 1961 and applied to the STM in 1983 by Tersoff and Hamann [7] (chapter 2.2). The latter method is incorporated into nearly every state of the art density functional theory (DFT) code. A simpler model was proposed by Selloni et al. and Lang [8, 9], making use of the Wentzel-Kramers-Brillouin (WKB) approximation. This will be discussed with respect to Scanning Tunneling Spectroscopy (STS) (chapter 2.3). A discussion about the contrast mechanism of organic adsorbates on solid surfaces in STM images is presented in chapter 2.4. Other experimental methods, which were used in the work at hand are Temperature Programmed Desorption (TPD) (chapter 2.5) and Low Energy Electron Diffraction (LEED) (chapter 2.6).

### 2.1 **Principle of the STM**

---

With the invention of the STM in 1982 by Binnig and Rohrer et al. [10] it became possible to investigate not only the topography of a conducting sample with atomic resolution in real space, but also the local electronic properties. The principle of the STM is based on the quantum-mechanical effect of electron tunnelling. This allows an electron to tunnel through a potential barrier even though its classical kinetic energy is lower than the barrier height. This specific process can occur between two materials which are separated by a gap, forming a potential barrier for the electrons. Commonly conductors and/or semiconductors are used as substrates; however, it is noteworthy to mention that ultrathin layers of an isolating material can also be imaged by STM [11, 12].

A metallic tip (e.g., platinum iridium (90:10), or tungsten) is used as the probe and approached towards the surface until a tunneling current flows, when a voltage is applied between the tip and the sample. This occurs when the gap between the tip and the surface is in the order of roughly 1 nm. After the tunnelling contact is established, the tip scans over the surface, actuated by a piezoelectric scanning unit, whose extension can be controlled in three dimensions  $x$ ,  $y$  and  $z$ . This can be realized by applying a specific voltage to the piezoelectric elements of the scanner. Such a microscope is typically capable of recording micrographs of an area of a few nm up to several  $\mu\text{m}$ .

The distance-dependent nature of the tunnelling current is essential for the discrimination of very small surface corrugations (i.e., atomic corrugation of a single crystalline metal surface), since even small changes generate a large change in the tunneling current. The quantum mechanical treatment predicts an exponential decay for the wave function of the electron in the barrier. For a rectangular barrier, the probability of the tunnelling process decreases exponentially with the distance  $d$  between the tip and the sample and with increasing barrier height. The tunnelling current  $I_T$  can be estimated by equation 2.1 (at low voltage and temperature; the tunnelling direction is specified by the polarity of the applied bias voltage) [13]:

$$I_T \propto U \exp(-2d\kappa); \quad (2.1)$$

$$\kappa = \sqrt{\frac{2m_e\phi}{\hbar^2}}.$$

$\phi$  is the average barrier height  $\frac{1}{2}(\phi_{\text{sample}} + \phi_{\text{tip}})$  between the two electrodes,  $m_e$  is the electron mass and  $\kappa$  is the inverse decay length. Due to the exponential dependency of the tunnelling current a vertical resolution of up to 0.01 Å can be achieved. The lateral resolution is lower by a factor of roughly 10; it is determined by the radius of the tip, which ideally exhibits the dimension of only one tip atom.

A three-dimensional STM data set of a surface can be recorded with two different operation modes [13]. Firstly, in both modes, the scanning tip is navigated close to the surface, so that at a certain bias voltages (typically  $U_{\text{Bias}} \sim 5 \text{ mV}$  to 2 V) a tunnelling

current (typically 5 pA to 2 nA) is detectable. In the constant current mode, the tip is scanned over the surface, while the tunnelling current  $I_T$ , between the tip and the surface, is sensed. A feedback loop controls the height of the tip  $z(x, y)$  (realized with the z-piezo actuator), in such a way that the current remains constant. Thus, an image consists of a map  $z(x,y)$  of tip height versus lateral position  $x, y$ .

Alternatively, in the constant height mode the tip is scanned across the surface at constant height and constant bias voltage. In this case, the tunnelling current  $I(x,y)$ , measured at discrete scan positions  $x,y$  constitutes the data set. This mode is advantageous as it allows high scan speeds (low record time per image) and thus avoids large thermal drifts. However, it is limited to very flat surfaces or/and very small scanning areas, as massive surface defects or extended contaminations can cause a crash of the tip.

## **2.2 Origin of the Tunneling Current**

---

Since electron tunnelling occurs from or into electronic states near the Fermi level, which can exhibit a complex structure, it is obvious that the electronic structures of the surface and the tip play a major role determining the tunnelling current. Note that the energy range of this process is given by the applied bias voltage.

In early analyses, the one-dimensional tunnelling problem has been treated extensively [14]; however, few considerations were made in three dimensions. Yet these were desirable in order to interpret STM micrographs. With this respect, in 1983 a theory was developed by Tersoff and Hamann, which is still the standard today. It is based on Bardeen's Transfer Hamiltonian Theory and was introduced to explain Giaver's observations of tunnelling in systems of superconducting electrodes separated by thin oxide barriers [5]. This specific approach had the advantage of describing the many-particle nature of the tunnel junction. In the model, a weak overlap of the wave functions of the surface states of the two electrodes allowed a first-order perturbation

calculation. By summation over all states within a given energy interval  $eV$  from the Fermi level, the tunnelling current  $I_T$  in Bardeen's formalism is given by [5]:

$$I_T = \frac{2\pi/e}{\hbar} \sum_{\mu,\nu} [1 - f(E_\nu + eV)] \times |M_{\mu\nu}|^2 \delta(E_\nu - E_\mu) \quad (2.2)$$

$M_{\nu\nu}$ : Tunnelling matrix element between the eigenstates  $\psi_\mu$  and  $\chi_\nu$

$f(E)$ : Fermi function

$V$ : Voltage across the barrier

$E_\mu$ : Energy of the state  $\mu$

$E_\nu$ : Energy of the state  $\nu$

The indices run over all the states of the surface  $\mu$  and the tip  $\nu$ . Exclusively elastic tunnelling transition is allowed by means of the  $\delta$ -function, i.e., electrons can only tunnel, if there is an unoccupied state with the same energy in the other electrode. When assuming low bias voltages ( $\sim 10$  meV for metal-metal tunnelling, which is much smaller than the average work function, the expression simplifies to [15]

$$I_T = \frac{2\pi}{\hbar} e^2 V \sum_{\mu,\nu} |M_{\mu\nu}|^2 \delta(E_\mu - E_F) \delta(E_\nu - E_F). \quad (2.3)$$

Bardeen [5] showed, that the tunnelling matrix element  $M_{\mu\nu}$  can be written in a form, which only requires knowledge of the wave functions of the two electrodes separately. The matrix element  $M_{\mu\nu}$  in equation 2.3 can be expressed as

$$M_{\mu\nu} = \langle \psi_\mu | H_T | \chi_\nu \rangle = -\frac{\hbar^2}{2m_e} \int (\psi_\mu^* \nabla \chi_\nu - \chi_\nu \nabla \psi_\mu^*) dS \quad (2.4)$$

$M_{\nu\nu}$  is the tunnelling matrix element between the eigenstates  $\psi_\mu$  and  $\chi_\nu$  of the two electrodes, containing the transition probability between the two systems. The integral covers any surface lying in the barrier region between the tip and the sample.

Tersoff and Hamann applied Bardeen's formula to the STM, assuming that the tip wave function is of s-type. Thus the following expression for the tunneling current  $I_T$  in the limit of zero temperature and very low bias was found [15]:

$$I_T = 32\pi^3 \hbar^{-1} e^2 V \Phi^2 \rho_t(E_F) R^2 \kappa^{-4} e^{2\kappa R} \times \sum_{\nu} |\psi_{\nu}(\vec{r}_0)|^2 \delta(E_{\nu} - E_F) \quad (2.5)$$

$$\rho_s(r_0, E_F) \equiv \sum_{\mu} |\psi_{\nu}(r_0)|^2 \delta(E_{\nu} - E_F).$$

- $R$ : Tip radius  
 $\rho_t$ : Density of states per volume of the probe tip  
 $\rho_s$ : Density of states per volume of the sample

In this equation, the tunnelling current depends e.g., on the average work function  $\Phi$  and on the density of states  $\rho_t$  of the tip at the Fermi level. The sample properties are given by the value of the sample wave function  $\psi_{\nu}$  with an energy  $E_{\nu}$  at the center of curvature  $r_0$  of the tip, constituting the LDOS [16]. Thus the LDOS represents the charge density per unit energy at  $E_F$  at a certain point above the surface [15]. Tersoff and Hamann showed that equation (2.5) remains valid, regardless of tip size, as long as the tunnelling matrix elements can be adequately approximated by an s-orbital tip wave function.

It is noteworthy to mention that in this approach it was not intended to accurately describe a real tip, but to find a way to parametrize the effect of a finite tip size [17]. However, experimentally in particular tungsten or platinum iridium tips were used as probes to achieve high-resolution STM images of well defined metal surfaces. In terms of actual tip states, these tip materials exhibit a localized  $d_z^2$  character near the Fermi energy and were proposed by Chen et al. [17] to be favorable to achieve atomic resolution. Furthermore, with respect to imaging semiconductor surfaces i.e., Si(111)7 x 7, it was assumed that the tip may pick up a silicon cluster to form a  $p_z$  dangling bond state at the tip which might then play a role in achieving atomically resolved STM images. Later on, extensions of the Tersoff-Hamann model were developed, making use of the Modified Bardeen Approach (MBA), e.g., different tip states were included.

Obviously, it is challenging to interpret STM images, taking into account the factors that contribute to the tunnelling current. The apparent height  $z(x,y)$  in the micrographs can either be understood in terms of topography and/or electronic effects

of the substrate and the adsorbate on the latter. Several examples, which highlight this discrepancy have been reported in literature, e.g., the STM images of highly oriented pyrolytic graphite (HOPG), where every second carbon atom of the uppermost layer, which has no direct neighbour in the layer below, exhibits an increased apparent height [18]. The observation is attributed to a lower LDOS of those atoms that interact with carbon neighbours directly underneath. Oxygen atoms on Pd(111) appear concave in the micrographs, even though they are topographically convex. This was traced back to the high electronegativity of oxygen. It was shown by Tilinin et al. that as the electronegativity decreases (from the element fluorine to carbon), the depressions gradually switch into a shallow dimple in the case of nitrogen and into a protrusion for carbon [19]. Thus, it is noteworthy to mention that theoretical modelling of STM images (e.g., Hückel theory, density field theory, electron scattering quantum chemistry) in combination with the experiment can be helpful.

## 2.3 Scanning Tunnelling Spectroscopy

---

As demonstrated in chapter 2.2, an STM image presents a convolution of both topography and electronic structure of a surface. With the STM operating in the spectroscopy mode, the electronic information can be separately recorded by scanning tunnelling spectroscopy (STS) [13]. By doing so, scanning is interrupted and the tip is positioned over a region of interest in a distance adjusted by the feedback circuit accordingly to the applied tunneling resistance. It is conducted by opening the feedback loop, followed by ramping the bias voltage  $V$  to measure the tunnelling current  $I$  as a function of applied bias  $I(V)$ . The extraction of the electronic information is carried out by calculating the derivative  $\partial I / \partial V$ , i.e., the differential conductivity, which is proportional to the local density of states (LDOS) [16].

For a discussion of the recorded  $I(V)$  curves, it has to be taken into account that the theory of Tersoff and Hamann is restricted to very low bias voltages, as typically applied for imaging inorganic samples. However, many organics on solid supports

exhibit a gap between the highest occupied molecular orbital (HOMO) and the lowest unoccupied molecular orbital (LUMO) (i.e., HOMO-LUMO gap) in the order of 1 eV, which means that the assumption  $V \approx 0$  is inappropriate. For that purpose and thereupon for applying a simpler model, the theory of three-dimensional tunneling based on the transfer-Hamiltonian formalism has been reconsidered by Selloni et al. [8] and Lang et al. [9].

The theory proposed by Lang et al. [9] makes use of the model of a one-dimensional tunnel junction in the Wenzels-Kramer-Brillouin (WKB) approximation, which was found to be in good agreement with the transfer Hamiltonian calculation, regarding qualitative features [9, 16]. It was recently demonstrated by Wagner et al. [16] and Koslowski et al. [20] that using the WKB approach, the DOS can be recovered in an energy range of roughly  $\pm 2\text{eV}$ . The tunnelling current can be expressed by the integral over the density of states (DOS) of both sample  $\rho_s$  and tip  $\rho_t$  and the transmission function  $T$ .

$$I(d,V) \cong \frac{2\pi e}{\hbar} \left( \frac{\hbar^2}{2m} \right)^{eV} \int_0^{eV} T(d,V;E) [f(E-eV) - f(E)] \rho_s(E) \rho_t(E-eV) dE. \quad (2.7)$$

Note that the one dimensional WKB approach does not consider the wave functions of the electrodes, just as in the Tersoff-Hamann model. Here the density of electronic states is taken into account and combined in a transmission function  $T(d,V;E)$ , depending on the energy of the electrons, the applied voltage and the distance. For a trapezoidal barrier in one dimension the transmission probability can be approximated by:

$$T(d, \Phi_{s,t}, V; E) \cong \exp \left[ -2(d+R) \frac{2}{3} \sqrt{\frac{2m}{\hbar^2} \times \left( \frac{(\Phi_t - E + eV)^{3/2} - (\Phi_s - E)^{3/2}}{\Phi_t - \Phi_s + eV} \right)} \right] \quad (2.8)$$

$R$  is the radius of a local spherical tip, with the center of the curvature at a distance  $d$ .

Tersoff and Hamann [7] demonstrated that the LDOS represents the charge density per unit energy at  $E_F$  at a certain point above the surface. Equation 2.5 also implies that the differential conductivity  $\partial I/\partial V$  is proportional to the sample  $LDOS(E_F)$  near the Fermi energy (i.e., for very small bias voltages). For higher bias voltages, with respect to the one-dimensional WKB approach, the energy- and bias-dependent electron transition probability is implied in the transmission function  $T(r_0, V, E)$  and thus can also be seen as a measure of the charge density of each state that reaches  $r_0$ . Thus the quantity

$$\frac{\partial I}{\partial V} \propto T(r_0, V; E) \rho_s(E) \stackrel{1D-WKB}{\equiv} LDOS. \quad (2.9)$$

is a generalized LDOS at  $r_0$  in terms of the Tersoff-Hamann model [16]. Note that the WKB approach is an approximation due to the voltage-dependence of the transmission. By applying small bias voltages, a constant transmission function and a constant sample density of states can be assumed. Thus it can be concluded:

$$\frac{\partial I}{\partial V} \propto DOS \propto LDOS. \quad (2.10)$$

In particular with respect to inorganic surfaces, Stroscio and Feenstra et al. [21] considered a normalization of the differential conductivity in order to divide out large part of the transmission probability  $T$ .

$$\frac{\partial I}{\partial V} \bigg/ \frac{I}{V} = \frac{d \ln I}{d \ln V} \quad (2.11)$$

However, nowadays this method is not routinely applied to organic adsorbate layers, as it was originally used to determine the DOS for inorganic surfaces. Furthermore, it potentially induces singularities in the energy gap around  $E_F$  and undesired peak shifts. Thus it can be seen more or less as a mathematical method for peak detection, which has to be applied carefully. Alternative methods for DOS recovery were supposed e.g., by Ukraintsev et al. [22], Wagner et al. [16] and Koslowski et al. [20].

## 2.4 Contrast Mechanism of Molecular Adsorbates

---

In the past, STM measurements have mostly been performed to acquire micrographs of flat metal and semiconductor surfaces with atomic resolution. Meanwhile, STM has become a well-established tool for imaging a variety of organic molecular adsorbates. The contrast mechanism of the latter was both interpreted in terms of an adsorbate induced change of the local work function [23] and by molecule-mediated electron transport through orbital channels [24, 25].

It has been shown by Spong et al. [23] that different functional groups attached to the same aromatic core can be distinguished with STM. The observation has been related to the modulation of the local work function of the substrate, induced by adsorbate molecules or fragments. In particular for 5-nonyl-2-n-nonyl-phenylpyrimidine, 4-cyano-4-n-butoxyl-biphenyl and 4-(4-n-propyl-cyclohexyl)-cyano-cyclohexane, it was proposed that the contrast can not be interpreted by resonant tunneling, since the molecular levels are too far from the Fermi level (assuming weak adsorption) to be accessible by STM.

The magnitude of the tunneling current is sensitive both to changes in the local work function and the distance; consequently changes of material and topography can be detected. A polarizable molecule or part of it, exposed to the electric field inside the tunneling barrier modifies the work function and in turn changes the barrier height  $\Phi$ . Thereby the local barrier height of a clean surface,  $\phi$  is altered,

$$\Phi = \phi - e\mu / \epsilon_0 \quad (2.12)$$

with  $\mu$  being the dipole moment density of the adsorbed species,  $e$  the electronic charge and  $\epsilon_0$  the permittivity of free space. The dipole moment of the adsorbed species can both be permanent,  $\mu_p$  or induced ( $\mu_i$ ) by an electric field  $E$  through its polarizability  $\alpha$ :

$$\mu = \mu_p - \mu_i(\alpha, E) \quad (2.13)$$

It was shown, that the alkyl tails of the above mentioned molecules adsorbed on highly oriented pyrolytic graphite appear dimmer in constant current images than the aromatic center. The observation was proposed to be due to lower polarizability and consequently less modification of the local work function of the aromatic entity [23]. Thus, regarding adsorbate molecules for which the frontier molecular energy levels are located well above or below the Fermi level, the observed constant current images can be interpreted in terms of the local variation of the work function  $\Phi$ , modified by the permanent and/or the induced dipole moment of physisorbed molecules.

The individual molecular appearance can also be interpreted in terms of the distribution of the electron density in the frontier molecular orbitals of the adsorbate. An additional tunnelling contribution, e.g., observable as peak in STS data, contributes when the energy of the tunnelling electron equals the energy of a molecular orbital of the adsorbed molecule. Thereby an electron channel through the respective orbital is opened up, resulting in an increase of the tunnelling current. The process is referred to as resonant or orbital mediated tunnelling (OMT) [16, 24, 25].

Taking into account an adsorbate molecule, the tunnelling barrier can be described as one-dimensional and rectangular including an inserted potential well (figure 2.4.1 (a)) [25]. It is proposed that the molecule exhibits discrete energy levels inside the well (indicated by the HOMO and the LUMO). The first barrier exists between STM tip and molecule  $w_1$ , the second one between adsorbate and substrate  $w_3$ . The Fermi energy of the sample  $E_{FS}$  and the tip  $E_{FT}$  exhibit no potential difference in the case of tunnelling contact and zero bias voltage condition.

The energy schemes (figure 2.4.1 (b)-(c)) highlight the principle of orbital mediated tunnelling with respect to positive bias voltages applied to the sample. This means that electrons tunnel from occupied states of the tip into unoccupied states of the sample. If an energy  $eU = E_{LUMO}$  is applied to the tunnelling junction, a potential difference between the Fermi energies of the two electrodes is induced (figure 2.4.1 (b)).

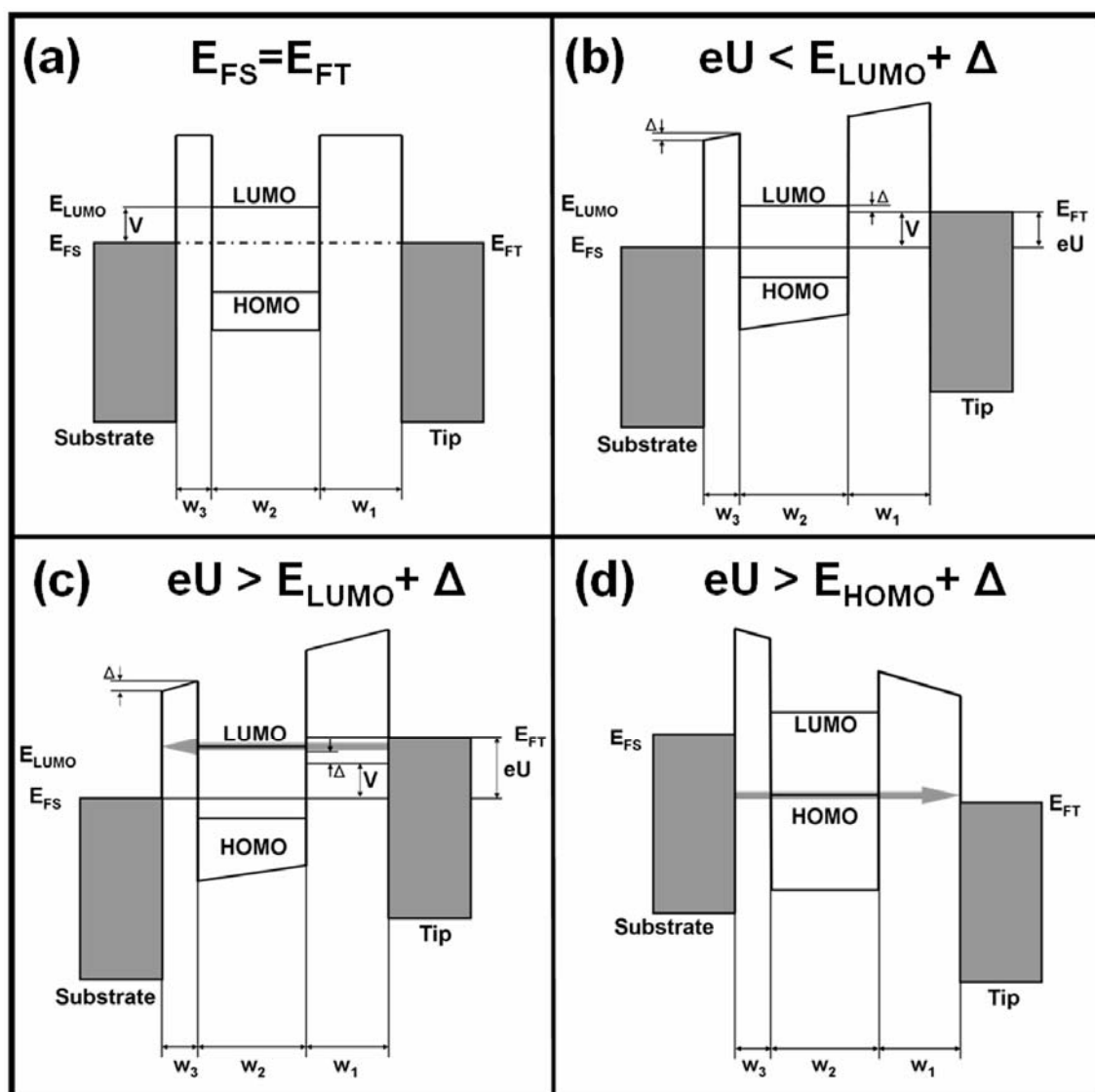


**Fig 2.4.1.** (a) Tunnelling junction at zero bias conditions. The adsorbed molecule is represented by an inserted potential well inside the barrier. (b) An energy of  $eU < V + \Delta$  is applied to the tunnelling junction. (c) At an energy,  $eU > V + \Delta$ , mediated tunnelling through the LUMO is observable (indicated by the arrow). (d) Mediated tunneling through the HOMO is observable by applying appropriate negative bias voltages (depicted by the arrow).

$V$  indicates the LUMO's energy level measured from the Fermi energy under zero-bias conditions. It is obvious that the applied energy  $eU$  is smaller than the amount  $V + \Delta$ , i.e., no resonant amplification of the tunnelling current occurs. The electric field gradient

through the tunnelling junction is taken into account by the amount  $\Delta$ , depending on the position of the molecule inside the barrier, e.g.,  $w_3 = 0; \Rightarrow \Delta = 0$ , assuming a symmetric position inside the barrier  $w_3 = w_1; \Rightarrow \Delta = a$ . In this respect,  $\Delta$  represents bias voltage induced shift of the orbital of interest. The amount of the shift and therefore the peak position in STS can be expressed by

$$V_{Peak} = V + \frac{\frac{1}{2}w_2 + w_3}{w_1 + \frac{1}{2}w_2} V \quad (2.14)$$

The energy of at least  $V+\Delta$  has to be applied (figure 2.4.1 (c)) to observe a significant increase in the tunnelling current. Thereby, the transmission probability increases, induced by mediated tunneling through the LUMO (indicated by the arrow).

By applying a negative bias voltage electron tunnelling occurs from occupied states of the sample into unoccupied states of the tip. At an appropriate bias voltage OMT takes place through the HOMO (indicated by the grey arrow in figure 2.4.1 (d)) and is observable as an increase of the tunnelling current as well.

## 2.5 **Temperature Programmed Desorption**

---

TPD spectroscopy was a prerequisite for the preparation of well defined monolayers, as it was essential to determine the temperature, which is adequate to desorb multilayer porphyrinoids, but too low to desorb the monolayer molecules. Thus basic considerations of TPD will be given in this chapter. In the experiment a certain molecular coverage is generated on the sample, followed by subsequent annealing with a constant temperature ramp to desorb the molecules. The detection of desorbing particles is achieved by a quadrupole mass spectrometer, which allows the plotting of the intensity against the temperature. Thermal desorption is often described by an Arrhenius expression, which is also referred to as Polanyi-Wigner equation [26].

$$r_{des} = \frac{\partial \theta}{\partial T} = \nu(\theta) \cdot \theta^n \cdot \exp\left(-\frac{E_D(\theta)}{k_B T}\right) \quad (2.15)$$

- $\theta$ : coverage  
 $T$ : temperature  
 $\nu$ : preexponential factor  
 $E_D$ : desorption energy  
 $k_b$ : Boltzmann constant  
 $n$ : order of desorption  
 $r_{des}$ : desorption rate

Both the position and the shape of the peaks in TPD spectra can be analyzed, with the shape determining the order of desorption. 0<sup>th</sup> order is typically observable for multilayer desorption. In this case, the desorption rate  $r_{des}$  is independent of the coverage  $\theta$ . 1<sup>st</sup> order desorption is found in the case of a monolayer, where the participating particles exhibit no lateral interactions. The desorption rate is directly proportional to the coverage. 2<sup>nd</sup> order desorption can be observed in the case of reactions in the monolayer, followed by subsequent desorption.

Numerous ways to analyze TPD spectra have been proposed in literature. One route to evaluate the activation energy of desorption is given by the Redhead equation [27], utilizing solely the temperature of the desorption maximum  $T_m$ . This assumes that  $\nu$  and  $E_D$  are independent of the coverage  $\theta$ . The derivative of the Polanyi-Wigner equation against the temperature  $T$  (assuming  $n = 1$ ) results in

$$E = RT_m \left[ \ln\left(\frac{\nu T_m}{\beta}\right) - 3,46 \right] \quad (2.16)$$

To evaluate desorption energies typically preexponential factors  $\nu$  of  $10^{13}$  are taken into account.

Another way to determine desorption energies is the Habenschaden-Küppers or leading-edge analysis [28], assuming that the preexponential factor  $\nu$  is independent of

the coverage. In that course, a small interval of the TPD spectrum in the region of the low temperature and high coverage side is taken into the analysis, to ensure insignificantly ( $< 5\%$ ) variations of  $\theta$ . Thus, this method is appropriate to calculate desorption energies in the case when the coverage does not change significantly. For this purpose, the logarithm of the Polanyi-Wigner equation is applied:

$$\ln r_{des} = \ln \nu + \ln \theta^n - \frac{E_{des}}{RT} \quad (2.17)$$

By plotting a spectrum as  $\ln r_{des}/\theta^n$  against  $1/T$ , a straight line can be obtained with the slope of  $m = E_{des}(\theta)/R$ , from which the desorption energy can be calculated. For 0<sup>th</sup> order this equation holds over the complete desorption spectrum.

## 2.3 Low Energy Electron Diffraction

---

Low energy electron diffraction (LEED) is a well-established tool to determine the geometric structure of both single crystalline surfaces and adsorbed phases under UHV conditions. In LEED, electrons are accelerated to kinetic energies in the range of 20 to 500 eV and hit the sample perpendicular. In contrast to X-rays, which can be used for bulk structure analysis, these electron exhibit a low mean free path in a solid, thus giving information of the uppermost layers. The electrons wavelength is given by de Broglies equation:

$$\begin{aligned} \lambda &= \frac{\hbar}{mv}; E_{kin} = \frac{1}{2}mv^2 = eU; \\ \Rightarrow \lambda &= \frac{\hbar}{\sqrt{2m_e eU}} \end{aligned} \quad (2.18)$$

The corresponding de Broglie wave length of 0.3 nm to 0.05 nm is in the range of inter-atomistic and/or inter-molecular dimensions. Therefore, surface atom or adsorbate induced diffraction of electrons occurs. In the LEED experiments, the diffraction spots are observed on a fluorescence screen; they represent a projection of the reciprocal

space. This allows the drawing of conclusions on the size and shape of the real space unit cell of a surface or molecular layer.



## 3 Experimental Setup

---

All experiments and the sample preparation were performed in a two chamber UHV-system with a base pressure in the low  $10^{-10}$  mbar regime (chapter 3.1). The STM, located in one of the chambers, is a *RHK UHV VT STM 300* (chapter 3.2) with *RHK SPM 100 electronics* (chapter 3.3). In the STM experiments, the bias voltage refers to the sample and the STM images were recorded in constant current mode. The STM raw data was processed with WSxM©, (<http://www.nanotec.es>); typically moderate low pass filtering was applied to reduce noise in the images. Cut Pt/Ir tips were used as STM probes; the raw material was purchased from *MaTeck GmbH*. The substrate was a Ag(111) surface, which is described in chapter 3.4. LEED was applied to check the quality of a freshly prepared Ag(111) surface (chapter 3.4). An overview of the porphyrinoids used in the STM experiments is presented in chapter 3.5. The porphyrinoid layer preparation is described in chapter 3.6. Furthermore the deposition of metals was carried out with an electron beam evaporator (chapter 3.7).

### 3.1 UHV System

---

The UHV-System consists of the preparation and the STM chamber, which are separated by a gate valve. A schematic drawing of the vacuum system with the relevant pumps to maintain UHV and the respective valves is shown in figure 3.1.1. The preparation chamber is equipped with a sputter gun to clean the sample. Annealing is conducted via electron bombardment or radiative heating with a filament located behind the sample. Additionally the chamber houses a LEED optics (see chapter 3.5), a QMS (chapter 3.6) and a thickness/ rate monitor (chapter 3.7). Sample transport into the STM chamber is conducted with a linear transfer.

The STM chamber is also connected to a load-lock, which allows a fast transfer from ambient to UHV, of e.g., freshly cut Pt/Ir tips, samples, etc. Furthermore, a gas

dosing system is attached to the STM chamber, which allows the dosage of gases e.g., NO via a leak dosing valve. The gas dosing system is directly attached to the STM chamber to avoid mechanical coupling from the environment, which might disturb the STM experiment. During STM measurements, the vacuum in the chambers is solely maintained by getter pumps, again to avoid mechanical coupling from the turbo pumps. Both chambers are equipped with titan sublimation pumps. The UHV pressure measurement is realized by ionization gauges, while the rough vacuum is controlled via Pirani gauges. The turbo molecular pump TCP 121 (figure 3.1.1) is switched on to adjust a constant argon flux needed for sputtering the sample. Further turbo molecular pumps are connected to the porphyrin evaporator, to the load-lock and to the STM chamber. All turbo pumps are used in the course of the evacuation of the vented UHV system, starting from ambient conditions. After the initial pumping phase the apparatus is covered with a home-made aluminum housing and baked out at roughly 135 °C for 3 days to efficiently remove residual gases, in particular water, from the UHV system.

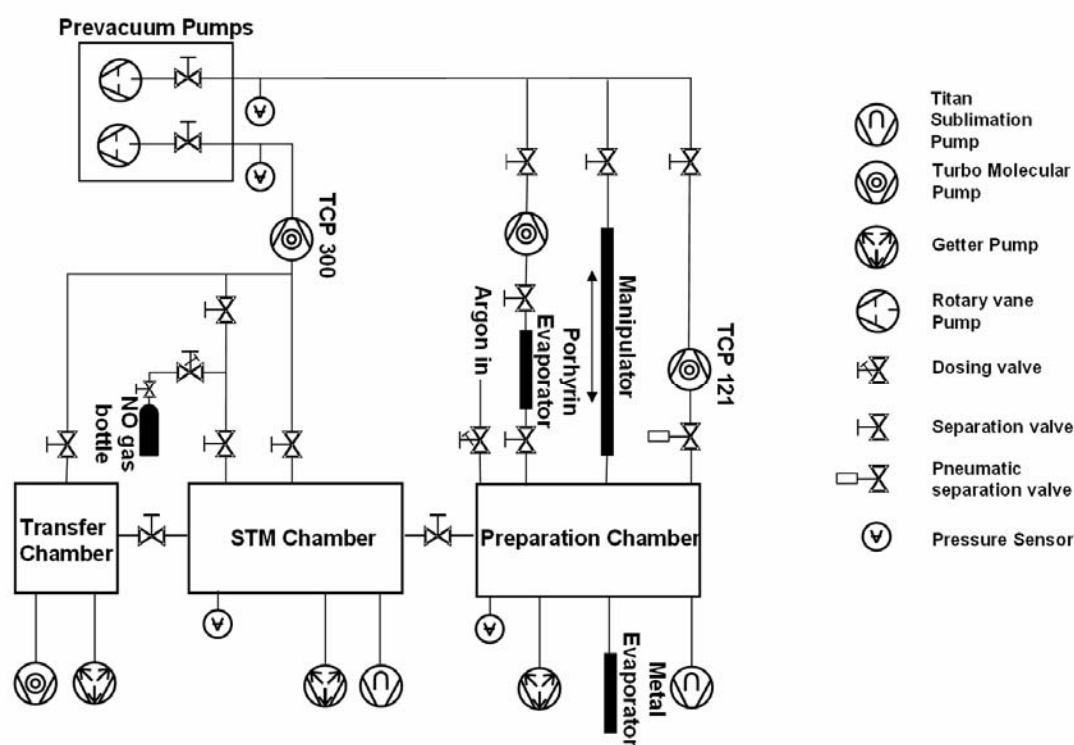


*Figure 3.1.1. Scheme of the UHV system*

## 3.2 Scanning Tunneling Microscope

---

The STM scan head is based on the “Walker type” design. The description of the STM was adopted in parts from the *RHK UHV VT STM 300* User’s Guide [29]. Figure 3.2.1 (a) and (b) are schematic drawings of the scan head at different viewing angles. Figure 3.2.1 (c) shows the sample holder.

The scan head consists of four identical piezoelectric tubes and a “Mexican hat”-shaped body. The three outer piezoelectric tubes are mounted 120 degrees apart on a circle to form the “legs” of the scan head which are used for the tip coarse approach and lateral movement. The fourth tube located in the center of the head is the scanning tube (figure 3.2.1 (b)), which holds the tip. Sapphire balls are attached to the end of each of the legs with an intermediate ceramic adapter. In the case of the scan tube the ceramic adaptor holds a tip socket. The tip socket assembly is light weight and has four springs inside, which firmly hold the stainless steel tube part of the tip holder.

The sample holder (figure 3.2.1 (c)) is based on the *Physical Electronics’ (PHI)* sample holder, consisting of a double grooved copper body and a helical molybdenum top ramp. The double grooves in the sample holder body provide for fixing the sample into the sample stage and for transferring the sample holder between the various stages in the STM apparatus by means of a wobble stick and linear transfer rods. Note that the sample is sandwiched between two sapphire washers so it can be heated to elevated temperatures by electron bombardment without excessive heating of the sample holder. The holder has a built-in K-type thermocouple to measure the sample temperature accurately. The two leads of the thermocouple stick out on one side of the sample holder.

Each of the three legs of the scan head rests on one of the three segments of the helical ramp of the sample holder, when the head is connected to the holder as shown in figure 3.2.2. Each ramp segment of the sample holder has a height of 0.75 mm and covers an angle of 120 degrees. By applying appropriate voltage pulses to the four segments of the piezoelements on each leg, the STM head can be either translated

laterally or rotated with respect to the ramp. By rotating the head, the tip either approaches towards or retracts away from the sample surface. This motion is generated by sawtooth type voltage pulses that cause a stick-slip movement of the legs. The thermocouples of the sample contact with a pair of spring thermocouple contacts on the sample stage when the holder is placed on the stage (figure 3.2.2).

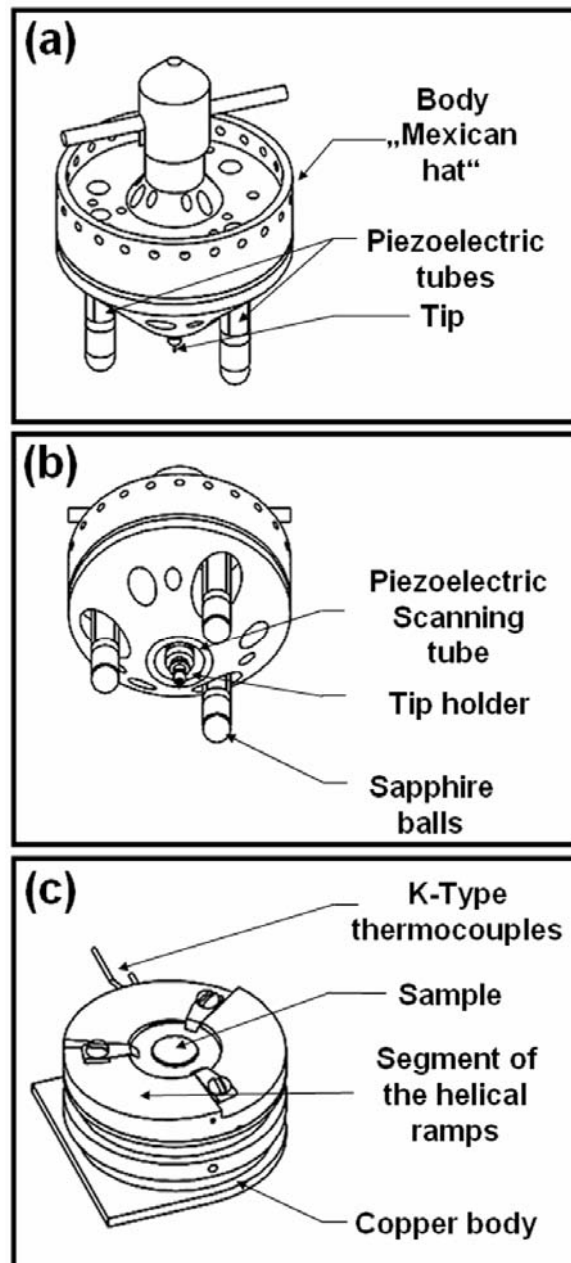


**Figure 3.2.1.** (a) and (b) STM scan head. (c) Sample holder. The drawings are reprinted from RHK's User Guide [29].

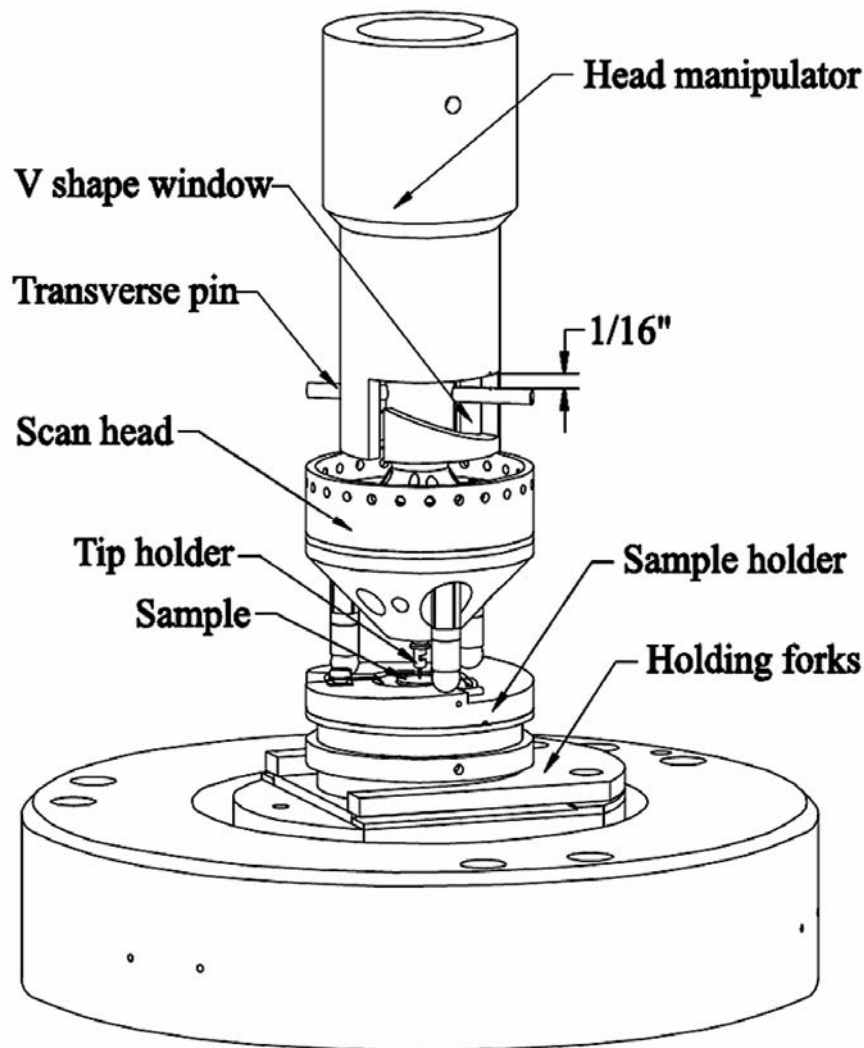


*Figure 3.2.2. Scan head touched down on the sample holder. The drawing is reprinted from RHK's User Guide [29].*

The sample holder body has a U-shaped bottom (figure 3.2.2), that fits in the holding fork on the sample stage in only one direction. In this way the sample holder will always be in the same position and correctly oriented. A transverse pin is mounted on the top of the scan head body, which hook into two asymmetric “V”-shaped windows on the head manipulator (figure 3.2.2). The pin is used to pick up the scan head by the head manipulator, when it is not sitting on the sample holder. The top of the scan head is conically shaped and mates with a stationary tube inside three holes is

attached to the lower part of the STM scan head. The three holes mate with three rods on the tip transfer holder to find alignment of the tip exchange mechanism.

The scan head (Figure 3.2.1 (a) and (b)) is connected to the *SPM 1000 electronics* from *RHK Technologies* (chapter 3.3) by seventeen Kapton insulated 0.075 mm copper wires. All of the connections to the piezo tubes are the wires that protrude through the side of the scan head. The tip current wire comes out of the top of the scan head. The high rim of the scan head body is used to guide the connecting wires, coming out of the scan head body.

### **3.3 Control Electronics and Vibration Isolation**

---

The microscope is controlled by *SPM 1000 electronics* from *RHK Technologies*. The control electronics are card interfaced to a data-acquisition computer, which runs the data processing software *SPM-32* from *RHK*. The electronic allows for various user controls over the waveforms applied to the piezo tube; the shape, period and amplitude of the waveform. Approaches are typically achieved by applying sawtooth waveforms of  $\pm 130$  V to the piezo tube. Current preamplification is provided by a *RHK IVC-200* preamplifier providing a gain of  $10^8$  through current-to-voltage conversion. In addition an improved *Femto DLPCA-200* preamplifier was applied, which provides a gain of  $10^9$  and allows to measure with tunnelling currents down to  $\sim 10$  pA. The preamplifier is located in close proximity to the chamber, to avoid capacitive coupling, which reduces the signal to noise ratio. The tunnelling current is adjusted with a control loop via a Proportional Integral Differential (PID) controller. The signal of the control variable is compared to the setpoint using a comparator stage, which utilizes a differencing amplifier to generate a signal proportional to the difference between the setpoint and the actual current. This error signal is then sent through a different amplifier with variable gain (from 0-10, determined by the setting of the “Gain” potentiometer control on the controller front panel). Afterwards, the signal is integrated for a certain period of time. This time is fixed by the setting of the “Time Constant” potentiometer on the controller

front panel (0-10 ms.). The analogue voltage is then amplified and feed back to the tip piezo.

By adjusting the control loop, three controller response regimes can be observed [30]: Overdamping occurs, when the electronics cannot quickly respond to the changing surface, either because of time delays in the electronics (high time-constant settings), high scan speeds or a combination of both. STM images, which are overdamped, often appear unsharp and flattened. Underdamping can be experienced by oscillations in current: the controller continually overcompensates for the difference between the current setpoint and the actual current, generally as a result of a high gain setting on the amplifier stage, but also possibly due to a too short integration time of the integrator. Underdamped images will show a difference in features between the forward and backward scans (surface features will appear streaked in the direction of scanning). The desirable scanning regime is critical damping. Thereby the gain is sufficient to adequately reposition the tip and the time constant and scan speed allow for the tip to respond quickly to changing surface conditions without oscillating.

Noise in the STM is mainly induced vibrationally and/or electrically. Vibrational noise results when the tip is either not stable in respect to the sample or too long which can lead to oscillations. The strongly distance-dependent nature of the tunnelling current translates these vibrations into anomalous surface features in the STM image. Therefore the tip-sample distance has to be very stable. In this respect, the resonance frequency is an important parameter in the design of the STM, because it determines the stability with respect to vibrations. Generally, low frequency resonances go along with large amplitudes, which would obviously disturb the measurement. Thus a good STM design means a high resonance frequency. The specified resonance frequency of the *RHK UHV VT STM 300* is 5 kHz, i.e., frequencies much lower, do not effect the measurement. This means that relative movements of tip and sample are almost identical and their gap remains very stable. Furthermore a rigid design is desirable to avoid that low frequency vibrations affect the relative motion in the STM. Both a high resonance frequency of the scanner and a rigid mechanical construction is necessary for high quality imaging. Typically viton elements below the sample holder eliminate vibrations

in the range of  $f > 50$  Hz, whereas environmental and building vibrations are in the range of 0-10 Hz and are isolated by air springs.

### 3.4 Ag(111)

Ag(111) was chosen, as it is generally a weak interacting substrate. Thus, no co-adsorption of residual gases in the UHV chamber is expected at RT [32, 33]. Silver crystallizes in a face centered cubic (fcc) lattice, which is typical for many noble metals (figure 3.4.1 (a)); the lattice parameter was determined to  $a = 4.085 \text{ \AA}$  [34]. Thus, the next neighbour distance in the close-packed (111)-plane is 0.289 nm (drawn in figure 3.4.1 (b)). The substrate used in this work was an Ag single crystal (purity  $> 99.999\%$ ) purchased from *Surface Preparation Laboratory* with a polished (111) surface, which was aligned to  $< 0.1^\circ$  with respect to the nominal orientation. The sample was cleaned by repeated cycles of  $\text{Ar}^+$ -ion sputtering (500 eV) at an Ar background pressure of  $5 \times 10^{-5}$  mbar and annealing up to 825 K after pumping out the Ar. More precisely, the crystal was heated with a temperature rate of 1 K/s, held at 825 K for 20 minutes and then slowly cooled down with a rate of 0.5 K/s. An overview towards the preparation of

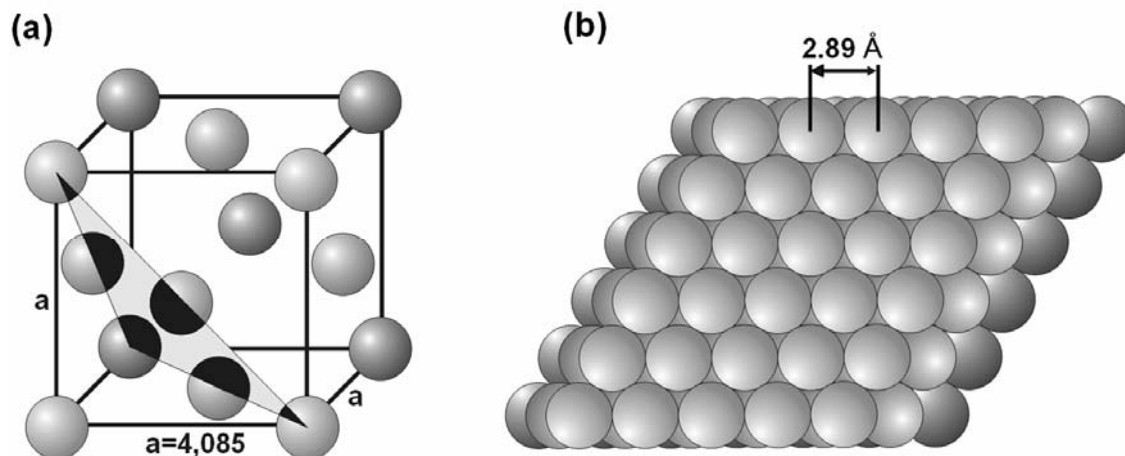


**Figure 3.4.1.** (a) Face centered cubic (fcc) lattice of the silver crystal with the drawn in (111) plane. (b) Top view on the (111) plane [31].

atomically clean surfaces of selected elements was given by Musket et al. [35].

Although it is challenging to image the small corrugation of the Ag(111) surface with STM, micrographs with atomic resolution could be acquired (figure 3.4.2 (a)). This difficulty also arises from the mobility of the silver atoms at RT. It was demonstrated by Quaas et al. by STM that mass transport on Ag(111) occurs mainly by step edge diffusion [36]. Furthermore, the reshaping of two-dimensional vacancy islands during coalescence has been monitored by Eßer et al. at RT using fast STM [37]. The quality of the freshly prepared Ag(111) was also checked with a *SPECS ErLeed*. The LEED pattern shows six sharp diffraction spots (figure 3.4.2 (b)), which evidence the long-range hexagonal close-packing of the surface.

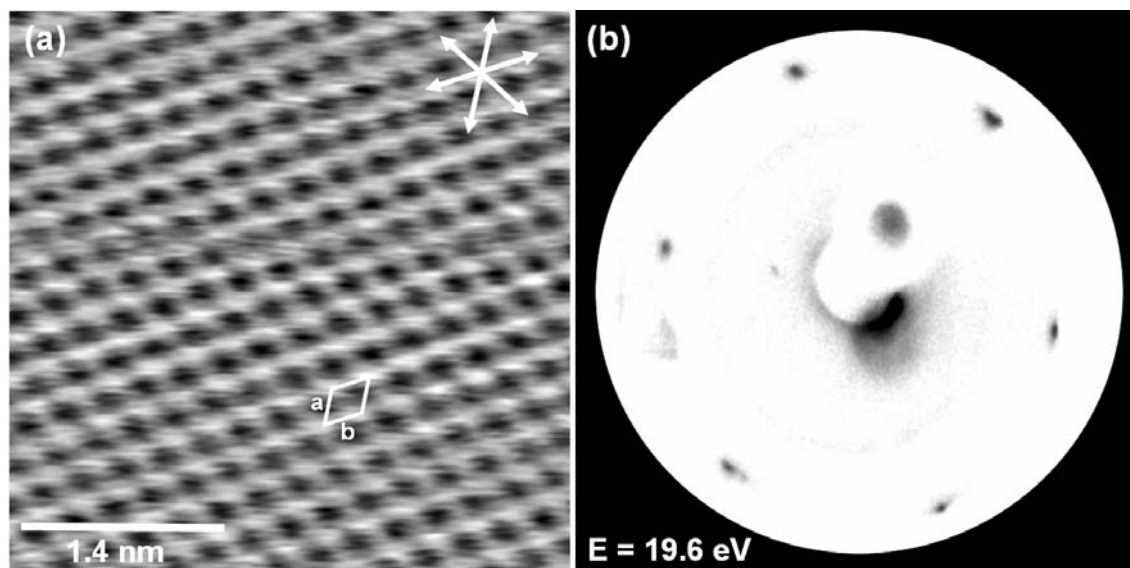


**Figure 3.4.2.** (a) STM image of the pure Ag(111) surface with atomic resolution ( $U = -38$  mV,  $I = 1.22$  nA). The unit cell and the preferential directions are drawn in. (b) Corresponding LEED pattern of the clean Ag(111) surface.

## 3.5 Porphyrinoids

The porphyrinoids applied in the experiments are listed in table 3.5.1.

Porhyrinoids	Supplier	Specified Purity
2H-5,10,15,20-tetraphenylporphyrins (2HTPP)	Porphyrin Systems	>98 %
Cobalt(II)-5,10,15,20-tetraphenylporphyrins (CoTPP)	Porphyrin Systems	>98 %
2H-5,10,15,20-Tetrakis-(3,5-di-tert-butyl)-phenylporphyrin (2HTTBPP)	N. Jux, Friedrich-Alexander-Universität Erlangen-Nürnberg	n.a.
Cobalt(II)-5,10,15,20-Tetrakis-(3,5-di-tert-butyl)-phenylporphyrin (CoTTBPP)		n.a.
2H-phthalocyanine (2HPc)	Sigma-Aldrich	>99 %
Iron(II)-phthalocyanine (FePc)	Sigma-Aldrich	>90 %
2H-Octaethylporphyrin (2HOEP)	Porphyrin Systems	>98 %
Cobalt(II)-Octaethylporphyrin (CoOEP)	Porphyrin Systems	>98 %

**Table 3.5.1.** Overview of the applied porphyrinoids

The molecular weights and the applied sublimation temperatures are shown in table 3.5.2. Note that each substance was outgassed in vacuo by heating to 410 K for 24 hours, before vapor-deposition (chapter 3.6) was performed.

Name	Formula	Molecular weight [g/mol]	Sublimation temperature [K]
2HTPP	$C_{44}H_{30}N_4$	614.74	610
CoTPP	$C_{44}H_{28}CoN_4$	671.65	610
2HTTBPP	$C_{76}H_{94}N_4$	1063.75	610
CoTTBPP	$C_{76}H_{92}CoN_4$	1119.66	610
2HPc	$C_{32}H_{18}N_8$	514.54	670
FePc	$C_{32}H_{16}FeN_8$	568.37	670
2HOEP	$C_{36}H_{46}N_4$	534.79	520
CoOEP	$C_{36}H_{44}CoN_4$	591.70	520

**Table 3.5.2.** Molecular weight and applied sublimation temperature of the porphyrinoids.

The main feature of all the applied porphyrins is the tetrapyrrolic macrocycle, which is capable to bind different metal atoms, e.g., Fe or Co. In addition, the macrocycle can be terminated with different side groups. Top and side view on space filling models (with or without an inserted metal) of such modified porphyrinoids, are shown in figure 3.5.1. Note that the space filling models show the configuration of the porphyrinoids as intuitively expected in the gas phase and not the internal conformation upon adsorption on a flat surface, i.e., the phenyl rings of the models in figure 3.5.1 (a), (b) and (e), (f), respectively, are oriented nearly perpendicular to the tetrapyrrolic macrocycle.

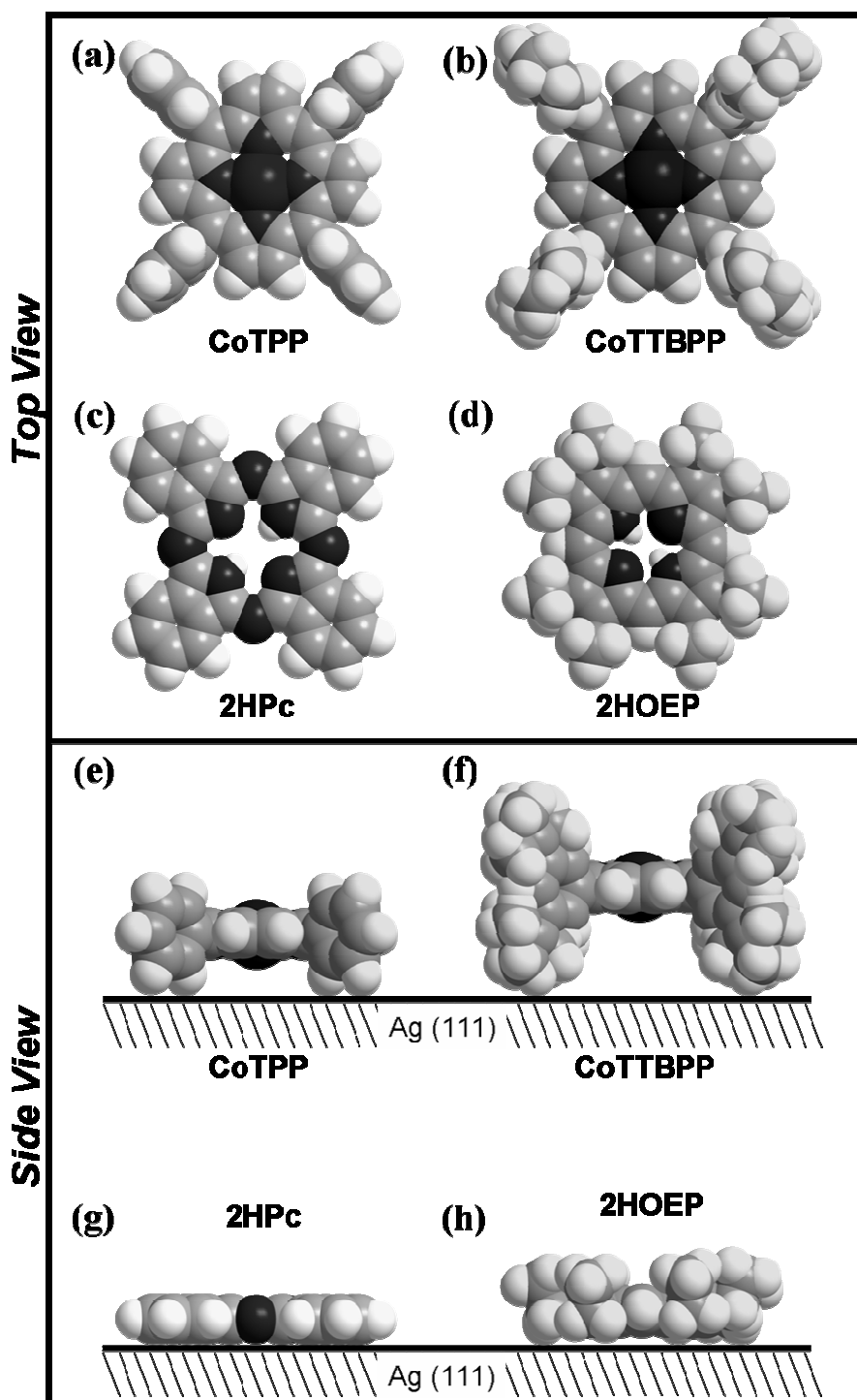


*Figure 3.5.1. (a-d) Top view on space filling models of the applied porphyrinoids, as expected in the gas phase. (e-f) Side view, illustrating how the individual substituents could determine the distance of the porphyrin macrocycle to the Ag(111) surface in this naive model. (g) and (h) anticipate the conformation on a flat surface.*

## 3.6 Preparation of thin Porphyrinoid Layers

---

Porphyrinoids are UHV compatible, large organic molecules that have a sufficiently low vapor pressure at RT. This allows the preparation of molecular layers by means of sublimation under UHV conditions.

One possible route for the preparation of monolayers is the vapor-deposition of multilayers from a home-built Knudsen cell onto the Ag(111) surface held at RT. The absolute coverage of one monolayer is defined as the amount of deposited porphyrinoids that entirely cover the substrate surface ( $\theta_{abs} = 1$ ). During deposition, the temperature of the Knudsen cell was held at a specific temperature between 520 K and 670 K (table 3.5.2), depending on the porphyrinoid material. By heating the substrate to the multilayer desorption temperature for roughly 30 s, the preparation of the monolayer can be achieved. This temperature is sufficient to desorb excess multilayer molecules, but too low to desorb or thermally decompose the porphyrinoids in the monolayer [38]. The corresponding multilayer desorption temperatures were determined with thermal programmed desorption (TPD) (see chapter 4.1, 4.4, 4.5, 4.9).

Alternatively, monolayers were prepared by vapor-deposition of the corresponding amount of molecules needed to completely cover the substrate. This approach is difficult to realize due to fluctuations of the porphyrin flux from the evaporator. The problem can mainly be traced back both to the change in the filling level of the evaporator and the thermal inertia of the latter. Thus to achieve a constant flux, the power output of the *Gossen Konstanter (44 T 20 R 10)* had to be changed gradually, which is not practicable. Therefore, this method possibly results in deviations from the desired coverage. Thus the multilayer desorption approach was the preferred one. However it was a prerequisite for the realization of some of the experiments (chapter 4.1, 4.3.2, 4.8) to deposit the amount of molecules needed for less than a monolayer coverage ( $\theta_{abs} = 1$ ). For this purpose reproducible deposition rates are necessary. Therefore prior to deposition, the peak intensity in the mass spectrum of the respective porphyrinoid was monitored with a quadrupole mass spectrometer (*Pfeiffer QMS 422*).

The sublimation temperature was increased, until a predetermined peak intensity (e.g. ~1000 counts per second) was reached. Such a QMS spectrum for 2HTPP is shown in figure 3.6.1. The position of the peak with the highest intensity correlates quite well with the actual molecular weight of 614.74 g/mol. The remaining peaks can be ascribed to isotope effects. Assuming a stable molecular flux, determined by the peak intensity in the mass spectrum, a deposition time of roughly 120 s was determined by STM to achieve a monolayer coverage ( $\theta_{abs} = 1$ ). Thereupon the evaporation rate is about 0.5 ML/min. With respect to the preparation of multilayers deposition times of roughly 10 minutes were applied.

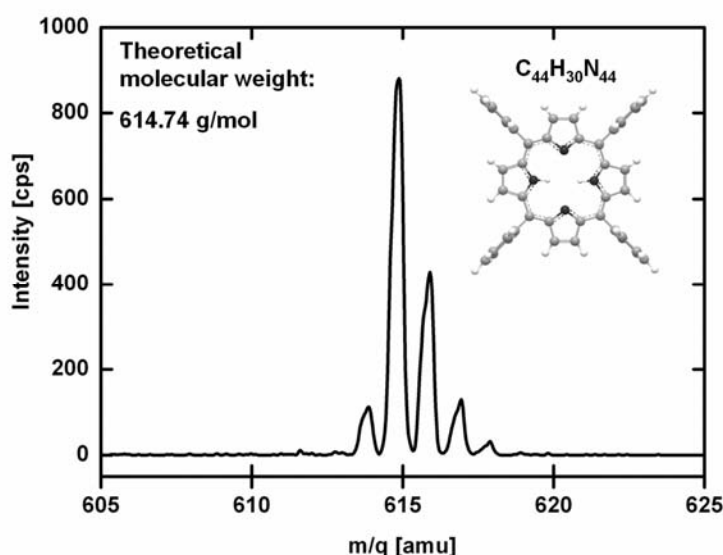


Figure 3.6.1. QMS spectrum of 2HTPP

## 3.7 Vapor-deposition of Cobalt and Iron

---

The vapor-deposition of iron and cobalt atoms was carried out with an *Omicron EFM 3* electron beam evaporator. Evaporant materials were iron and cobalt rods with diameters of 2 mm and purities of 99.99 % purchased from *Mateck*. The deposition of the metal was conducted in the experiments described in chapter 4.1, 4.3 - 4.7. In this respect the relative coverage  $\theta_{rel}$  was implemented. Thereby one monolayer on the

Ag(111) substrate is defined as the number of adsorbed molecules per surface atom. The relative coverage of 2H-tetraphenylporphyrin (2HTPP) and 2H-phthalocyanine (2HPc) was determined based on acquired STM images, by dividing the measured unit cell area of Ag(111) ( $0.072 \text{ nm}^2$ ) by that of the respective porphyrinoid ( $1.96 \text{ nm}^2$ ) resulting in a coverage of  $\theta_{\text{rel}} = 0.037 \text{ ML}$ . The relative coverage of 2H-tetrakisdi-tert-butylphenylporphyrin (2TTBPP) was calculated to  $\theta_{\text{rel}} = 0.024$ . For the vapor-deposition of metal atoms, these numbers equal the coverage of vapor-deposited metal atoms necessary to provide one metal atom for each molecule in the monolayer. Thereupon, it was desired to reliably deposit the metal in coverage ranges smaller than the latter, i.e., to successively deposit sub-stoichiometric portions onto monolayers of free base porphyrinoids. For that purpose the integrated flux monitor of the *Omicron EFM 3* was calibrated with a thickness monitor.

At a given electron emission of the electron-beam evaporator ( $I_{\text{fil}} = 2.1 \text{ A}$ ,  $I_{\text{Em}} = 14 \text{ mA}$ ) and the electron beam voltage ( $U = 810 \text{ V}$ ), the ion flux was measured with an ion collector at the beam exit column, which is directly proportional to the flux of evaporated atoms ( $I_{\text{flux}} = 5 \text{ nA}$ ). The flux was calibrated with a *Sycon Instruments STM-100/ MF Thickness/ Rate* monitor. By adjusting  $I_{\text{flux}}$  to  $5 \text{ nA}$ , a very stable deposition rate of  $\Delta d/\Delta t = 0.025 \text{ nm/min}$  was achieved both for iron and cobalt as shown in figure 3.7.1. Thus, a deposition time of  $22 \text{ s}$  should be suitable to achieve a coverage of  $\theta_{\text{rel}} = 0.037 \text{ ML}$ . However, the experiments in chapter 4.1 and 4.3 - 4.7 show, that a correction factor of roughly  $0.5$  has to be included. This factor can be traced back to different positions of the sample and the quartz thickness monitor with respect to the electron beam evaporator.

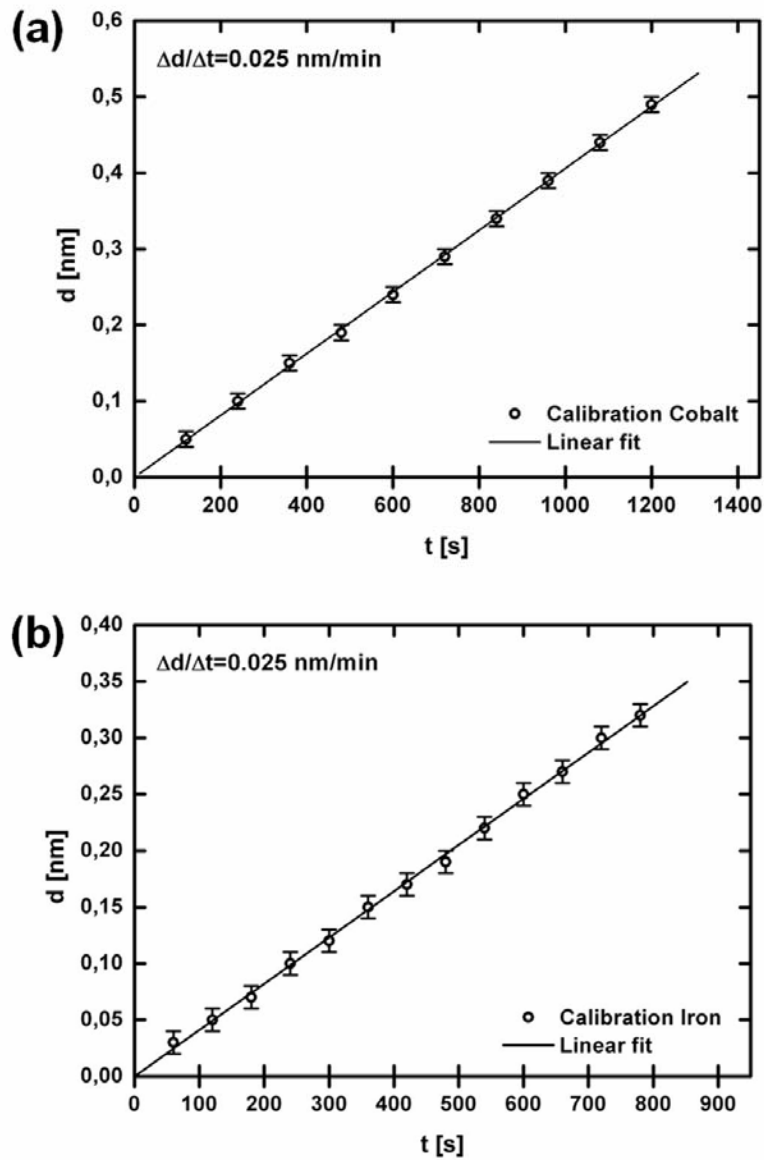


**Figure 3.7.1.** Calibration of the metal flux of (a) cobalt and (b) iron. The flux monitor of the evaporator was adjusted to  $I_{flux} = 5nA$ . To calibrate the metal flux, the thickness was measured as a function of time by a microbalance.

## 4 Results

---

Thin films of porphyrinoids on Ag(111) have been characterized with STM at RT. The following aspects will be discussed in this section: the internal conformation and supramolecular ordering, surface-confined synthesis of metalloporphyrinoids, electronic properties as well as the interaction with small molecules, i.e., NO. It is noteworthy to mention that the work at hand is organised such to enable the readership the understanding of the chapters independently. Aspects concerning the self-assembly of porphyrins (TPP, TTBPP) are mainly addressed in chapter 4.1 and 4.2. Besides the long-range order, micrographs with sub-molecular resolution allowed to draw conclusions on the internal conformation of the respective porphyrinoids. Both the supramolecular arrangement and the internal conformation play a role concerning the reactivity and were therefore fundamental with respect to further investigations. In the subsequent experiments, layers of free base porphyrinoids (2HTPP, 2HTTBPP, 2HPc) were prepared to explore a novel type of surface reaction, i.e., the direct metalation of different free base porphyrinoids upon vapor-deposition of metals, i.e., iron or cobalt (chapter 4.3 – 4.5). The latter method opened up the potential to engineer multicomponent, i.e., binary and tertiary adlayers containing ultra-clean metalloporphyrins and in that course tailoring the active sites (chapter 4.6). The different porphyrinoids (2HTPP/FeTPP/CoTPP) were identified in high-resolution STM images, in particular exploiting the voltage-dependent appearance of the individual molecules in the constant current images. Thus adsorbate-substrate coupling of CoTPP with Ag(111) was verified in a combined experimental and theoretical work. Spectromicroscopic measurements also enabled the identification of the different species emphasizing the individual electronic fingerprints (chapter 4.6). Such well defined and extensively characterised monolayers (i.e., long-range order, internal conformation, electronic properties) constituted the basis of studying the interaction with small molecules. i.e, the system CoTPP/Ag(111) upon dosage of NO, as discussed in chapter 4.8.

## 4.1 Self-Assembly and Individual Appearance of Tetraphenylporphyrins on Ag(111)

---

The self-assembly of different tetraphenylporphyrins (x-TPP) with and/or without a central metal atom ( $x = 2\text{H}, \text{Fe}, \text{Co}$ ) on Ag(111) was studied with STM at RT. The epitaxial growth of TPP from sub-monolayer coverage to the multilayer regime reveals that TPP molecules easily diffuse and self-assemble into highly ordered domains exhibiting surface chirality within. The three-fold rotation symmetry of the domains at sub-monolayer coverage indicates a registration to the substrate. It was found that independent of the composition of the monolayer (2HTPP, MTPP or mixed MTPP/2HTPP,  $M = \text{Fe}, \text{Co}$ ) the same square arrangement of the molecules was observed. The orientation of the domains is determined by adsorbate-substrate interactions while the origin of the square packing is triggered by intermolecular “T-type” interactions. The square order occurs in two types of chiral domains. The multilayer consists of domains with a short-range square ordering and a decreased size of the unit cell, indicating non-flat adsorption geometry.

### **INTRODUCTION**

STM has been utilized to determine both the long-range order of large organic molecules on flat surfaces and the corresponding intramolecular conformation of the participating molecular building blocks. Numerous studies report that layers of porphyrinoids assemble in well defined long-range ordered supramolecular architectures on flat substrates [39-48]. Beyond the long-range order, the epitaxial growth of porphyrins and their structural analogue phthalocyanines was investigated intensely, often under UHV conditions and at low temperatures, e.g., carboxyphenyl-substituted porphyrins on Au(111) [49], copper octaethylporphyrin on Ag(100) [12], cobalt phthalocyanines on Au(111) [50], cobalt and vanadyl phthalocyanine on Au(111) [51], iron phthalocyanines on Au(111) [52, 53], hexadecafluorophthalocyanine on Ag(111) [54] and iron phthalocyanines on Au(111) [52]. Generally, the self-assembly of these

structures underlies a subtle balance of intermolecular and molecule-substrate interactions. In this respect, it was shown that the ordering is e.g., triggered by the side groups of the porphyrins [55]. Furthermore, the central metal ion (Fe/Co) was found to play an essential role for the adsorption in the multilayer, i.e., adsorption of the multilayer molecules either on top or hollow sites of the underlying molecular layer [50, 52].

STM has also emerged as a tool to identify individual molecular species and to give insight in the internal conformation of different porphyrin derivatives [42, 47, 56, 57]. The discrimination of porphyrin entities in multicomponent adlayers, with and without metal ions, was previously demonstrated [47, 56-59]. E.g., in an intermixed layer of CoTPP and 2HTPP, the latter exhibit a central cavity in STM images and individual CoTPPs show a protrusion due to orbital mediated tunneling through the Co(II)  $3d^6$ -orbital system of the central Co ion [42, 60] and simple topographical considerations. These intermixed layers can either be prepared by vapor-deposition of an ex-situ prepared mixture, or alternatively by in-situ vapor-deposition of the corresponding metals on the free base porphyrin (M = Fe [56, 61], Co [42, 60], Zn [42, 62]). Note that this novel preparation route is reported in detail in the work at hand in chapter 4.3– 4.5.

Concerning the engineering of molecularly functionalized surfaces it is desirable to control the formation of the corresponding building blocks on the surface. Thus it is fundamental to gain a deeper understanding of the relevant processes, i.e., to identify the driving forces, which determine the self-assembly of the participating entities. Studying the corresponding coverage-dependent molecular ordering can contribute to gain insight into the self-assembly process. In this respect the epitaxial growth of different x-TPP (x=Fe, Co, 2H) with and without iron or cobalt ions on Ag(111) is systematically addressed in this chapter. Furthermore, from STM images with sub-molecular resolution, conclusions are drawn on both the intramolecular conformation and the long-range order.

## 4.1.1 Epitaxial growth

---

In the following the epitaxial growth of TPP on Ag(111) upon successive increasing coverage is discussed. Starting with a CoTPP coverage of  $\theta_{abs} \sim 0.05$  (note that  $\theta_{abs} = 1$  is defined as the amount of deposited TPP that entirely covers the substrate surface), it was found that the previously featureless silver steps were decorated with CoTPP, which appear as single dots in the medium resolution STM image and exhibit an intermolecular distance of  $1.4 \pm 0.05$  nm (figure 4.1.1 (a)). Since basically all observed molecules are located at the steps they must have a diffusion length that is at least as long as the width of the individual terrace at RT [57, 63, 64]. It was shown in a previous publication that at very low coverage no iron phthalocyanines (FePc) are observable on the reconstructed terraces of the Au(111) surface, while on the step edges FePc molecules can be observed in the STM images at 5 K, indicating the high mobility of the porphyrinoids in this system [52]. Furthermore, the Ehrlich-Schwoebel barrier and/or energetically favorable adsorption sites are proposed to hinder the diffusion at the steps [65, 66]. Note that the agglomeration of deposited material at the steps can also be found for several heteroepitaxial systems of metals [57, 63-65, 67-69].

Upon incremental increase of the CoTPP coverage ( $\theta_{abs} \sim 0.4$ ), one observes two dimensional porphyrin islands on the terraces (figure 4.1.1 (b)), whereas the decoration of the silver steps as already found for the lower coverage, persists. The molecules within the islands are lying flat on the surface, forming a square unit cell with a lattice constant of  $1.4 \pm 0.05$  nm [47, 56, 57, 60]. The individual domains are rotated by  $120^\circ$  to each other on the substrate, which exhibits a three-fold symmetry. This indicates that the orientation of the islands is mediated by adsorbate-substrate interactions. Stripy features in regions between the islands in the horizontal scan direction were recorded and are attributed to laterally mobile molecules at RT, probably displaced by the scanning tip [44, 70, 71]. In a STM time series (not shown here) it was observed that individual molecules might leave or attach to the agglomerated islands.

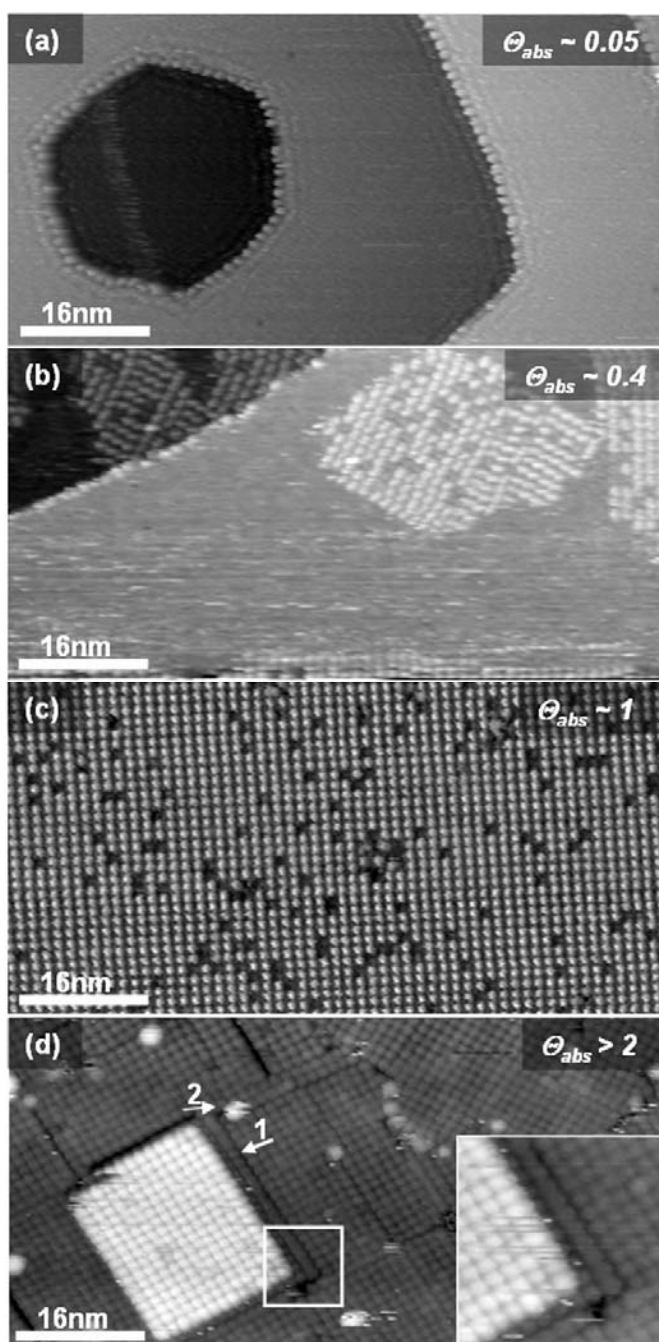


**Figure 4.1.1.** Sequence of STM images of CoTPP on Ag(111) acquired upon incremental increase of the coverage  $\theta_{abs}$ . (a) The Ag(111) steps are decorated with CoTPP at a low coverage ( $U = -1.25$  V,  $I = 15$  pA). (b) Two-dimensional islands evolve at medium coverage ( $U = -1.20$  V,  $I = 255$  pA). (c) Monolayer of CoTPP ( $U = -1.21$  V,  $I = 41$  pA). (d) STM image of the multilayer regime ( $U = 5.13$  V,  $I = 25$  pA).

This observation is in line with the treatment of the diffusing molecules in the framework of a 2D-gas, in which the islands would correspond to the respective condensation [72]. In addition, the assumption that single molecules can easily diffuse on Ag(111) is strengthened by the fact that no single CoTPP can be imaged on Ag(111) at RT. Thus the mutual lateral stabilization between two or more molecules obviously account for the formation of the 2D-islands. It is noteworthy to mention that within the islands some of the molecules appear with a decreased apparent height compared to the majority of the molecules. It was demonstrated by Comanici et al. [60] that in monolayers of CoTPP on Ag(111) roughly 10% of the molecules also appear with decreased apparent height and are identified to be 2HTPP (see chapter 4.6.1).

Increasing the CoTPP coverage further to one monolayer results in a long-range ordered square assembly of the porphyrins (figure 4.1.1 (c)), with lattice constants of  $1.4 \pm 0.05$  nm in agreement with the molecular ordering within the islands as described above for sub-monolayer coverage. As aforementioned, roughly 10 % of molecules appear with reduced apparent height at the given tunneling conditions and are identified as 2HTPP [60]. The layer shown in figure 4.1.1 (c) was prepared by multilayer desorption [57, 73] (see chapter 3.6), whereat the desorption temperature was determined with TPD. Note that the desorption spectrum shown in figure 4.1.2 was recorded with respect to 2HTPP, however the evaluated temperature could also be successfully applied for the preparation of a monolayer of CoTPP. Two desorption peaks can be identified. The peak at 490 K can be attributed to multilayer desorption, the one at 630 K to monolayer desorption. The relatively broad peak at 544 K is most probably due to desorbing molecules from the sample holder. This is plausible as the temperature gradient on the latter is very uneven, typically inducing such broad peaks. From the spectrum it can be deduced that an annealing step up to  $550 \pm 10$  K, i.e., the temperature range between the multilayer and the monolayer peak, should be a good choice for desorbing excess multilayer molecules.

Following the deposition of more than one monolayer CoTPP ( $\theta_{abs} > 2$ ) the STM image in figure 4.1.1 (d) was acquired. In this coverage regime, it was only possible to record micrographs by applying a very low tunnelling current at large bias voltage (e.g.,

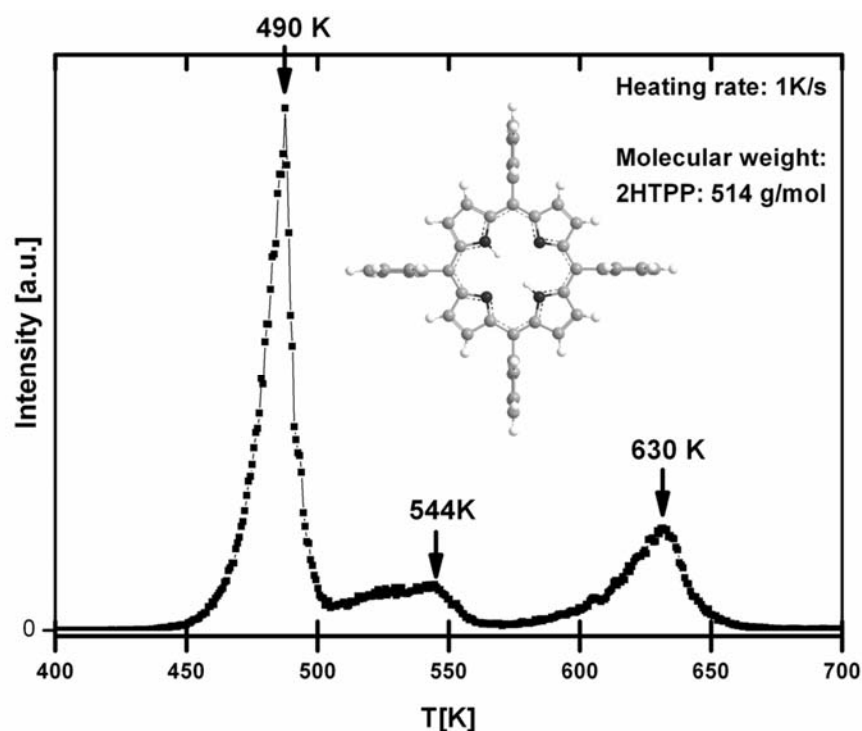


**Figure 4.1.2.** TPD spectrum of 2HTPP on Ag(111).

$I = 15 \text{ pA}$ ,  $U = 5.1 \text{ V}$ ), which is indicative for an enhanced resistance of the multilayers. In the constant current image different domains, which are separated by gaps or troughs, are observable (as indicated by arrow **1** in fig 4.1.1 (d)). The inserted zoom image highlights the situation. The unit cell is square with a lattice constant of  $1.25 \pm 0.05 \text{ nm}$ , i.e., the unit cell area is roughly 20 % smaller than in the submono- and monolayer regime. The compression of the unit cell could be explained by a tilting of the molecule plane in respect to the surface, i.e. the porphyrin plane is not parallel to the surface anymore. Note that on top of the layer (marked by arrow **2**) bright dots were observed which could be attributed to initial aggregates of CoTPP on the multilayer.

Cheng et al. [52] showed that iron phthalocyanines (FePc) adsorb nonplanar within multilayers with one of the four benzene rings trapped in a four-fold hollow position of the layer below. Thus there exist four equivalent directions in which the elevated sub-unit of the molecule can point. They also observed gaps in the multilayer and interpreted them to as boundaries between two domains with diametrically opposing tiltangle. Takada et al. [50] reported that cobalt phthalocyanines (CoPc) adsorb directly

on top of the central cobalt ion within the multilayers with a small tilt angle of  $\sim 3^\circ$  (i.e.,  $0^\circ$  is defined to be parallel to the surface). In the work at hand it is assumed that the gaps in CoTPP multilayers are indeed due to molecules which are tilted in opposing direction in the respective domains. The reduced dimension of the unit cell (compared with the monolayer) could be interpreted with a gradual change of the tilt angle of the porphyrins within one domain. Following the idea that e.g., the first layer serves as a kind of template for the next molecular layers it is clear that the different unit cell areas will induce stress and consequently the size of the multilayer domains is restricted. Neighbouring domains possibly exhibit the reverse gradual change of the tilt angle  $\pm \delta_n$  of the molecules (figure 4.1.3). However, the latter interpretations are quite speculative, as no systematic investigation of the molecular growth mechanism in the multilayer range was conducted in the work at hand.

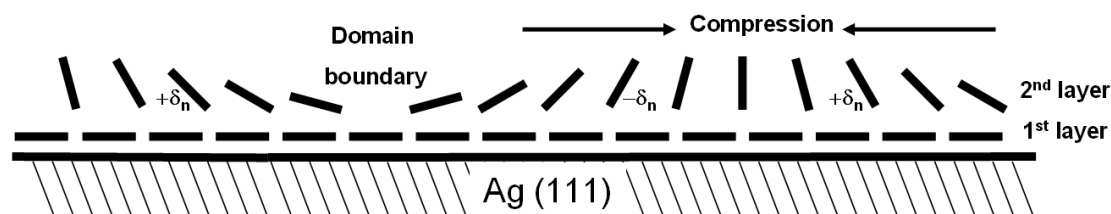


**Figure 4.1.3.** Side view on the potential adsorption of CoTPP in the multilayer regime. The molecules in the 1<sup>st</sup> layer are lying with the porphyrin macrocycle parallel to the surface  $\delta_n = 0$ . The compression of the multilayer is explained by a gradual change of the tilt angle  $0^\circ < \delta_n < 90^\circ$  within one domain, limiting the size of the domains. The observed domain boundaries can be traced back to a reverse gradual change of the tilt angle  $\pm \delta_n$ .

## 4.1.2 Appearance and Intramolecular Conformation

The high-resolution STM images of individual  $x$ -TPP ( $x = \text{Fe}, \text{Co}, 2\text{H}$ ), which are shown in figure 4.1.4, highlight the specific molecular sub-units of the porphyrins. It is clearly visible that the symmetry of the molecules, which in the gas phase belongs to  $D_{4h}$  point groups (the respective model is shown in chapter 3.5), is reduced.

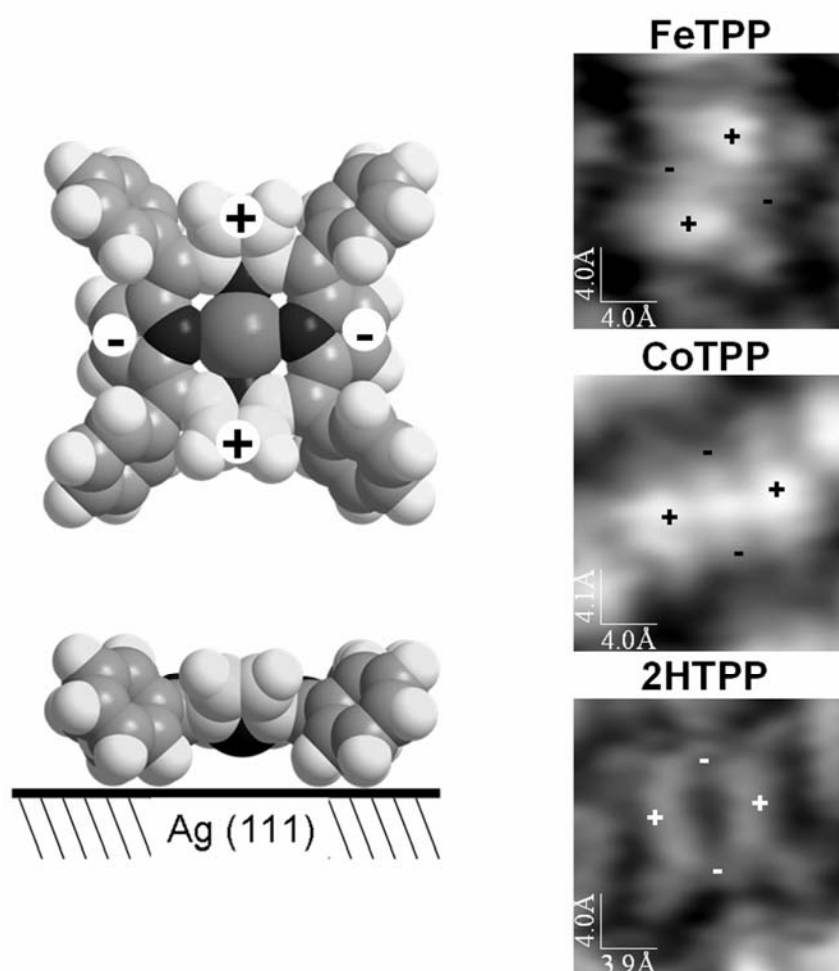


**Figure 4.1.4.** Space-filling models showing top and side view on TPP adsorbed on Ag(111). The incorporated sign “+” addresses elevated positions on the model, “-” depressed. STM images nearby highlight the anisotropic appearance of individual  $x$ -TPP ( $x = \text{Fe}, \text{Co}, 2\text{H}$ ). The latter observation is less pronounced for 2HTPP ( $U_{\text{FeTPP}} = -1.25 \text{ V}$ ,  $I_{\text{FeTPP}} = 15 \text{ pA}$ ) ( $U_{\text{CoTPP}} = -1.18 \text{ V}$ ,  $I_{\text{CoTPP}} = 58 \text{ pA}$ ), ( $U_{2\text{HTPP}} = -7 \text{ mV}$ ,  $I_{2\text{HTPP}} = 54 \text{ pA}$ ).

This is obvious for FeTPP and CoTPP in figure 4.1.4, which appear anisotropic with two dots, located diametrically opposing with respect to the molecular center. FeTPP shows no significant central intensity, against what CoTPP exhibits a central protrusion mostly interpreted as orbital mediated tunneling through the half filled  $d_{z^2}$  orbital of the central ion [42, 60]. In addition, four peripheral protrusions per molecule are visible, which appear dimmer and can be attributed to the terminal phenyl rings. In previous STM studies of FeTPP and iron(II)-tetrapyrrolic porphyrin (FeTPyP) on Ag(111), Auwärter et al. [47] observed an anisotropy of the molecules appearing with a rod-like shape. With respect to FeTPP adsorbed on Ag(111), this was assumed to be due to a saddle-like deformation of the tetrapyrrolic macrocycle [47]. The adsorbed porphyrin interacts with the surface in a way that the terminal phenyl rings are rotated to roughly  $60^\circ$  in respect to the porphyrin plane, whereupon a steric repulsion between the outermost hydrogen atoms of the phenyl rings and the pyrrol rings induces the pronounced deformation, i.e., two opposing pyrrol rings, which are lifted and two, which are lowered [39, 44, 57, 74]. Note that the twist angle of roughly  $60^\circ$  was reported in several publications [74-76]. Therefore, the two protrusions located diametrically opposing to the molecular center can be attributed to two opposing pyrrol rings lifted upwards [57]. The inserted sign “+” in the STM images in figure 4.1.4 indicates positions of the elevated pyrrol rings, “-“, the lowered pyrrol rings. The space filling models (top and side view) in figure 4.1.4 illustrate the described deformation. (Note that superimposed and scaled space-filling models in the STM image in figure 4.1.6 (b) confirm that two bright spots per molecule match the positions of two opposing pyrrol rings of the porphyrin ring). The STM image of a single 2HTPP (figure 4.1.4) shows the tetrapyrrolic macrocycle with a central cavity and four dim peripheral spots, which can be attributed to the phenyl substituents. The mentioned rod-like shape for 2HTPP is less pronounced than for FeTPP and CoTPP. However two opposing positions on the tetrapyrrol, which appear elevated and two which are lowered are identified (see also figure 4.1.6 (d) and figure 4.1.7 (c)). Thus it is assumed that 2HTPP is also deformed in a saddle-like shape [77].

### 4.1.3 Ordering Aspects

---

As mentioned before, no single isolated porphyrins were observed with STM on Ag(111), possibly due to a weak molecule-substrate interaction. Thus it is highly probable that the self-assembly is mainly governed by intermolecular interaction. Comparing the lattice constant of  $\sim 1.4$  nm and the overall dimensions of the TPP molecules with the largest extension along the diagonal of 1.9 nm it is obvious that the proposed intermolecular forces must originate from the periphery of the molecules, i.e., the phenyl rings. Immediately two types of alignments, with the corresponding interactions of the phenyl legs of adjacent TPPs, appear to be likely, i.e.,  $\pi$ - $\pi$  stacking or T-stacking. The  $\pi$ - $\pi$  interactions have often been investigated on a benzene dimer model system. In particular, one of the proposed lowest energy structures in this system is T-shaped [78]. Meyer and Diederich [79] reported that T-shaped structures involving aromatic rings play a key role in both chemical and biological recognition. Burley and Petsko [80] demonstrated that the aromatic side chains of proteins are involved in  $\pi$ - $\pi$  interactions, whereby the predominant arrangement was a T-shaped edge-to-face structure emphasizing the importance of this type of structure. The T-shaped motif also appears as the preferred one for both liquid [81] and for crystalline benzene [78]. In this respect, TPP space filling models (a twist angle of the phenyl ring of  $90^\circ$  to the tetrapyrrol was assumed) were applied for the construction of two potential unit cells of TPP on Ag(111). The two arrangements are also easily distinguishable by the azimuthal angles of the individual porphyrins in respect to the lattice vector of the supramolecular order. Thus an azimuthal angle of  $15^\circ$  out of the unit is characteristic for the  $\pi$ - $\pi$  stacking as indicated in figure 4.1.5 (a). However, this goes along with a steric repulsion of the phenyl rings with the pyrrol rings of the neighbouring tetrapyrrol and should therefore be unfavourable. In figure 4.1.5 (b) an azimuthal angle of the molecular axis by  $30^\circ$  out of the unit cell can be estimated for the perpendicular alignment of the phenyl legs of adjacent porphyrins. In figure 4.1.5 (c) and (d) the applied models exhibit the internal conformation of TPP on Ag(111) as discussed in chapter 4.1.2. It is obvious, that the arrangement in figure 4.1.5 (c) is not preferable because of steric reasons. Thus the

pronounced T-stacking, which goes along with an azimuthal orientation of  $30^\circ$  out of the unit cell, should be favourable.

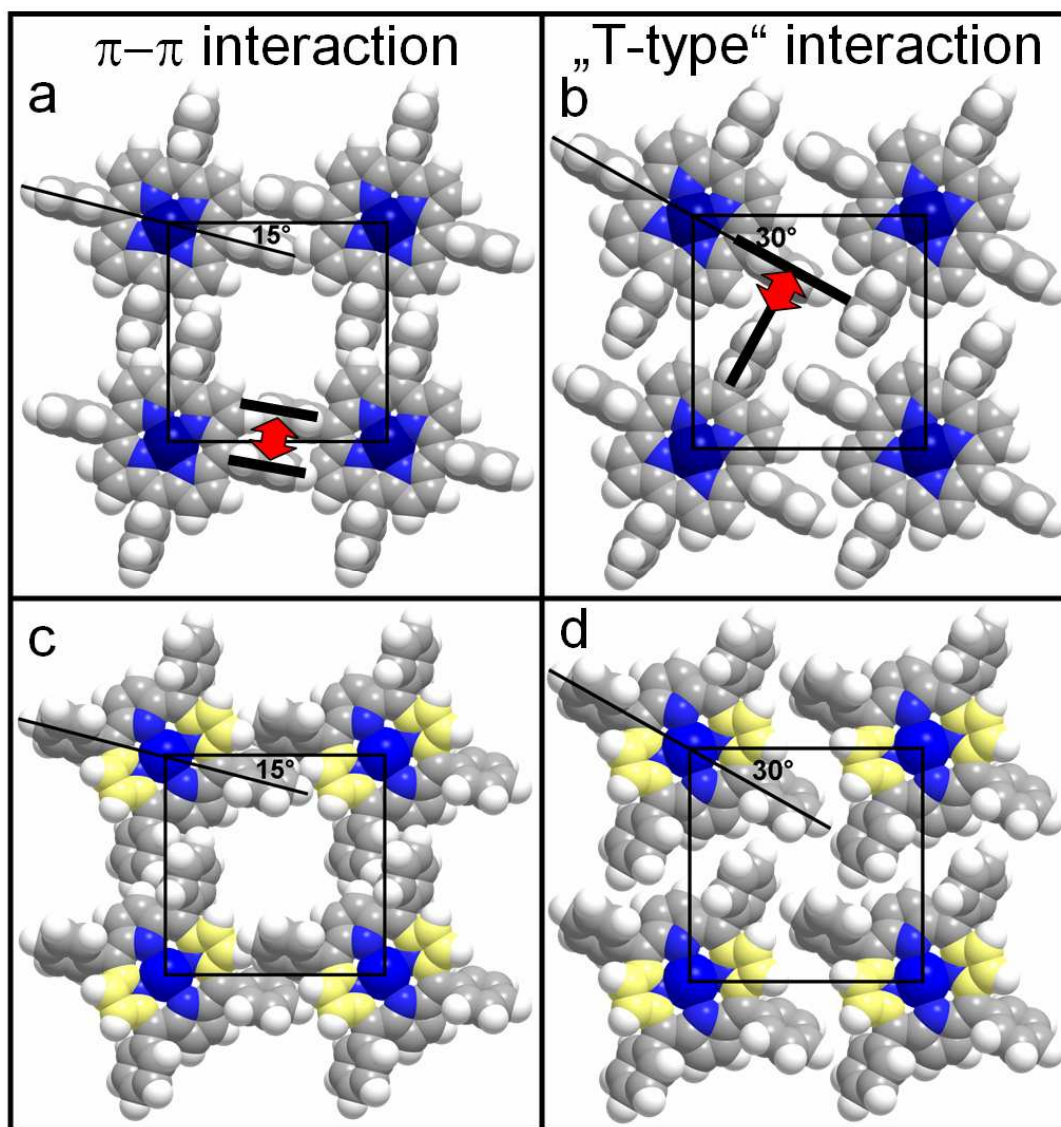


**Figure 4.1.5.** Potential arrangements of TPP on Ag(111). (a) A rotation of the molecular axis out of the unit cell by  $15^\circ$  results in a parallel alignment of adjacent phenyl legs, i.e.,  $\pi$ - $\pi$  stacking. (b) A rotation by  $30^\circ$  results in a perpendicular motif of neighbouring phenyl rings, i.e., T-stacking. The space-filling models applied in (c) and (d) exhibit the internal conformation of TPP on Ag(111) as determined by STM (see figure 4.1.3) and show the corresponding arrangements with respect to (a) and (b). Obviously the arrangement of the aggregate in (c) is highly unfavourable because of a large steric hindrance.

Measurements of the effective azimuthal orientation of TPP on Ag(111) were now conducted in high-resolution STM images. In the micrograph in figure 4.1.6 the square arrangement of a mixed monolayer of 2HTPP and FeTPP is emphasized, whereupon sub-molecular units are clearly visible. Individual FeTPP molecules appear with a reduced symmetry and are apparently elevated compared to 2HTPP. As demonstrated before the latter molecules exhibit a characteristic central cavity (chapter 4.1.2). Note that FeTPP was prepared by direct metalation of 2HTPP with iron by dosing the corresponding amount of the metal (see chapter 4.3-4.5) [47, 56, 57]). An enlarged image is shown in figure 4.1.6 (b), wherein superimposed and scaled space-filling models are inserted. The square unit cell is drawn in and the molecular axes (connections between diagonal opposing phenyl rings) of the individual porphyrins are depicted by crosses. One of the two axes of each molecule is rotated counter-clockwise out of the unit cell by an azimuthal angle of  $\sim 30^\circ$ . Indeed, as proposed in figure 4.1.5 (b), the phenyl rings of neighbouring x-TPP in close proximity to each other are ordered perpendicular. Thus specific intermolecular interactions of T-type stabilize the square packing and dominate over site specific adsorption. The STM images in figure 4.1.6 document that x-TPP on Ag(111) either with or without a central metal ion strictly arrange in a square arrangement with equal lattice constants. Figure 4.1.6 (c) and (d) show high-resolution STM images of both a mixed layer of CoTPP/2HTPP and 2HTPP, in which the individual species can clearly be identified. The molecular axes are marked in the images, confirming the observed orientation of the molecules and the proposed “T- type” interaction. Interestingly the molecular arrangements marked in figure 4.1.6 (a) and (c) are different such that they can not be transformed into each other by a simple rotation or translation in the plane, but by a mirror operation. This corresponds to assemblies with different 2-D chirality.

Generally, chiral objects can be found in two distinguishable mirror, or so-called enantiomeric forms. The property of chirality is of particular interest as it is known to have effects in physics, chemistry and biology, e.g., exclusively one mirror form of amino acids is used by all life forms on earth [82]. It has been shown that the adsorption of non-chiral molecules at non-chiral metal surfaces can lead to chirality at a metal surface and is basically referred to as surface chirality or 2D-chirality [82-84]. Chirality

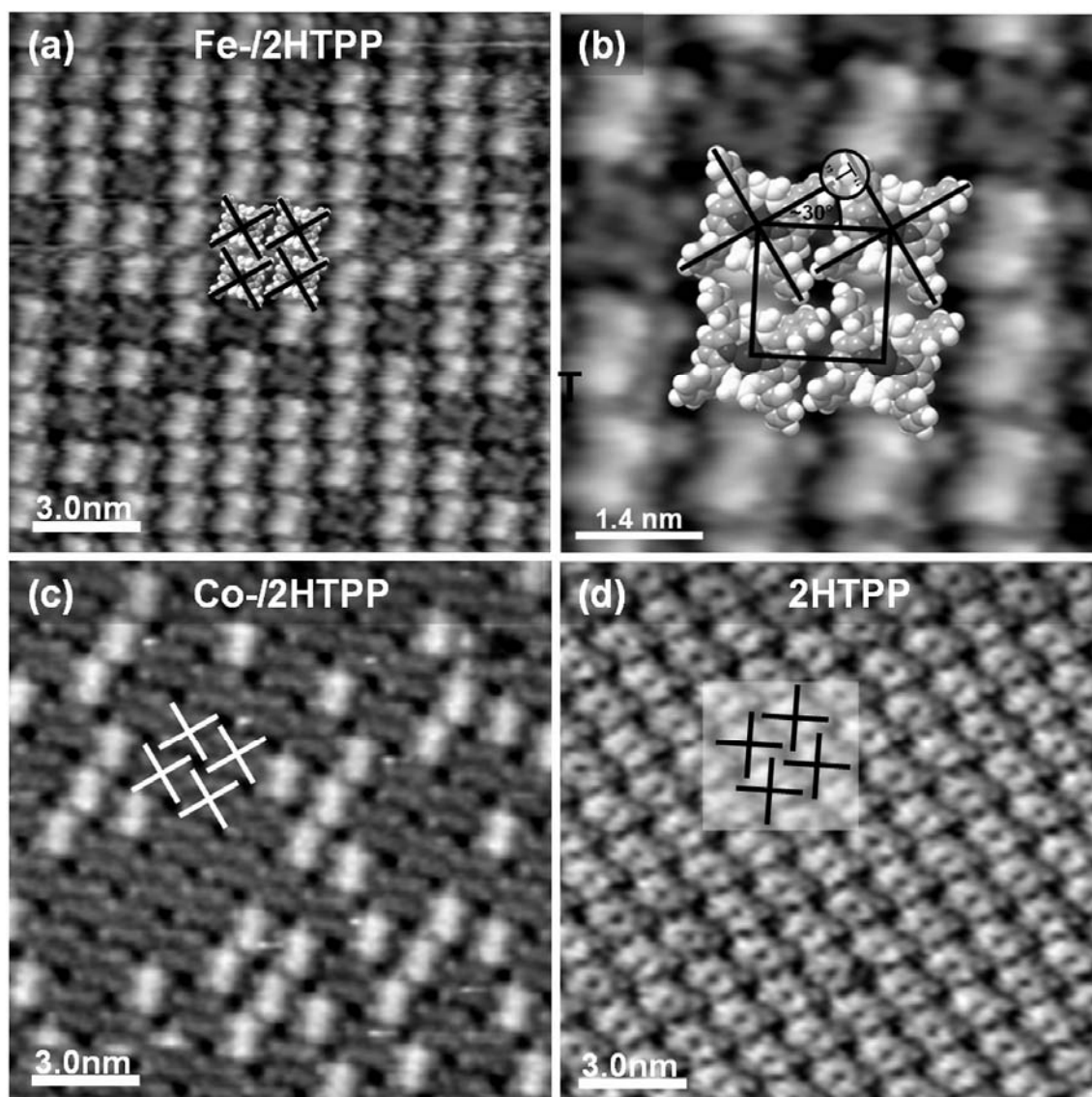


**Figure 4.1.6.** (a) STM image of a mixed monolayer of FeTPP/2HTPP ( $U = -100$  mV,  $I = 46$  pA). (b) Enlarged image of (a), which is superimposed with corresponding space-filling models. The proximate substituents show a “T”-shaped arrangement. (c) Mixed layer of CoTPP/2HTPP exhibiting the same arrangement as the layer in (a) ( $U = -1.35$  V,  $I = 35$  pA). The T-shaped motif is again apparent and illustrated by the included molecular axis. (d) 2HTPP monolayer showing the analogue arrangement as the layers in (a) and (c) ( $U = +454$  mV,  $I = 25$  pA).

is broken down in several classes, whereby the observation in figure 4.1.6 can be ascribed to *local organisational chirality*, e.g., for the non-chiral TPP, there exists a

probability of nucleating into chiral mirror domains on non-chiral Ag(111). Organisational chirality was recently reported for the system mesotetramesitylporphyrin on Cu(100) [85]. Such systems always consist of coexisting chiral mirror domains, leading to an overall non-chiral, racemic surface. This is reasonable as chirality is only locally observable and declines at the global level.

Remarkably, it was found that all domains boundaries investigated in the work at hand separate two enantiomeric domains. Figure 4.1.7 (a) shows such a domain boundary of an intermixed layer of FeTPP/2HTPP (the domain boundary is depicted by the dash-dotted line) wherein the corresponding domains exhibit different 2D-chirality. The sub-molecular units of FeTPP are clearly visible in both domains (figure 4.1.7 (a)). The unit cells are marked to emphasize that they exhibit the same size and orientation and are shifted by half of a lattice vector, which is apparent at the boundary. In particular, the azimuthal orientation of the molecules in both domains is different, which is illustrated by the superimposed and scaled space-filling models. In the course of a systematic illustration now the anisotropy axis of FeTPP (connection between the two elevated pyrrol rings) was conducted as marker for the molecules orientation (see drawn in dumb-bells). The inserted models are shown enlarged in figure 4.1.7 (b). In domain **I** the dumb-bells are rotated counter-clockwise out of the unit cell by  $\sim 15^\circ$ , in contrary to these of domain **II**, which are oriented clockwise. Thus the domains exhibit surface chirality formed by achiral single entities on the also achiral Ag(111) surface. This observation was confirmed for x-TPP ( $x = 2\text{H}, \text{Co}$ ) in figure 4.1.7 (c) and (d) and was always found for neighbouring domains in high-resolution STM images. Note that the micrograph in figure 4.1.7 (d) was acquired at a positive bias voltage. Obviously, the individual molecular appearance drastically changes and it turns out that now the substituents are visible in the STM images. Four domains with alternating chirality could be recorded, emphasizing that it is likely that adjacent domains generally exhibit different chirality. Thus, in particular the observed domain boundaries can be traced back to *local organisational chirality*.

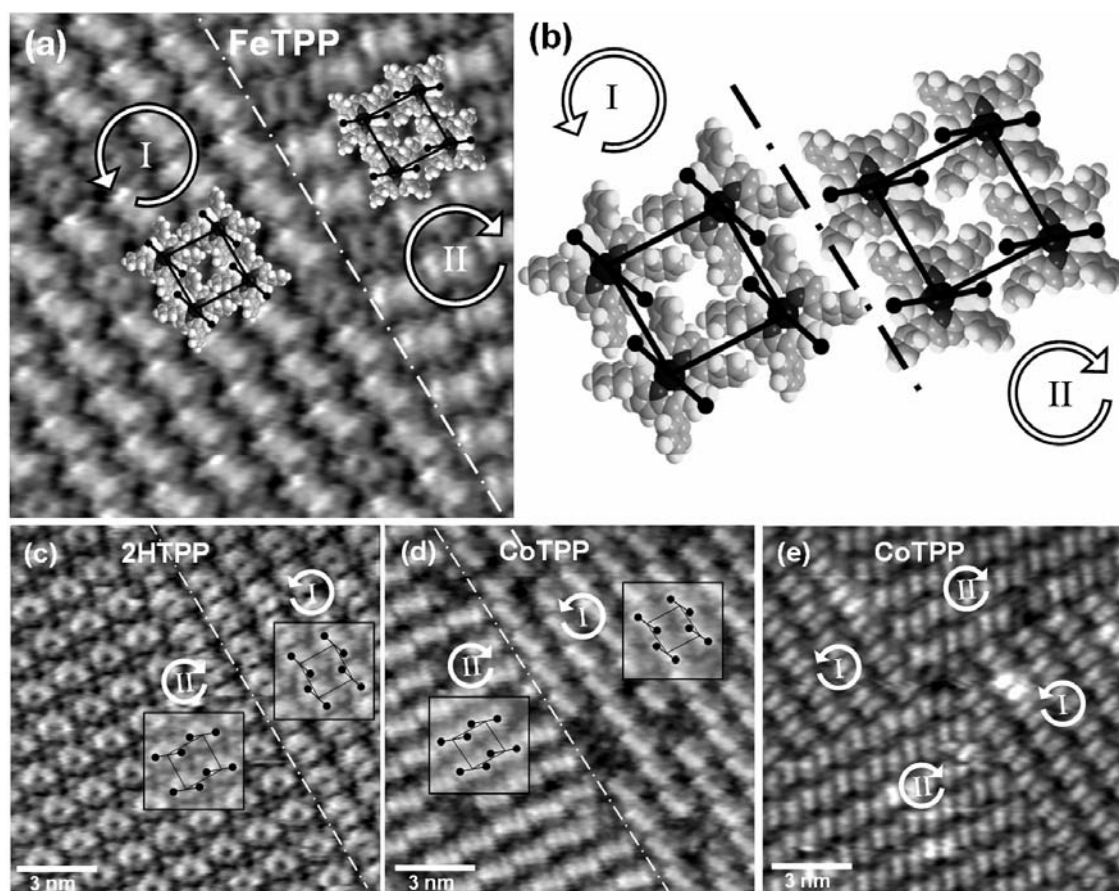


**Figure 4.1.7.** (a) Constant current image of a monolayer of FeTPP/2HTPP emphasizing the chiral domain I and II ( $U = -7$  mV,  $I = 11$  pA). The domains differ by the sense of rotation. (b) Enlarged image of the superimposed and scaled space-filling models, which underline the surface chirality. Note that at the domain boundary the unit cells are shifted by half of the length of a lattice vector. (c)-(e) STM image of layers of 2HTPP and CoTPP confirming 2D-chirality ( $U_{2HTPP} = 461$  mV,  $I_{FeTPP} = 24$  pA) ( $U_{CoTPP} = -1,18$  V,  $I_{CoTPP} = 58$  pA), ( $U_{CoTPP} = 1.82$  V,  $I_{CoTPP} = 23$  pA).

An STM image of a sub-monolayer of FeTPP ( $\theta_{abs} \sim 0.7$  ML) is shown in figure 4.1.8 (a). Beside the decoration of the silver steps, different FeTPP domains are visible, which are rotated in respect to each other by multiples of  $60^\circ$ . The specific orientation of the domains can be traced back to adsorbate-substrate interactions. Note that this type of orientation could also be monitored for a corresponding coverage of CoTPP. Within the domains the arrangement of the molecules establishes surface chirality (as discussed

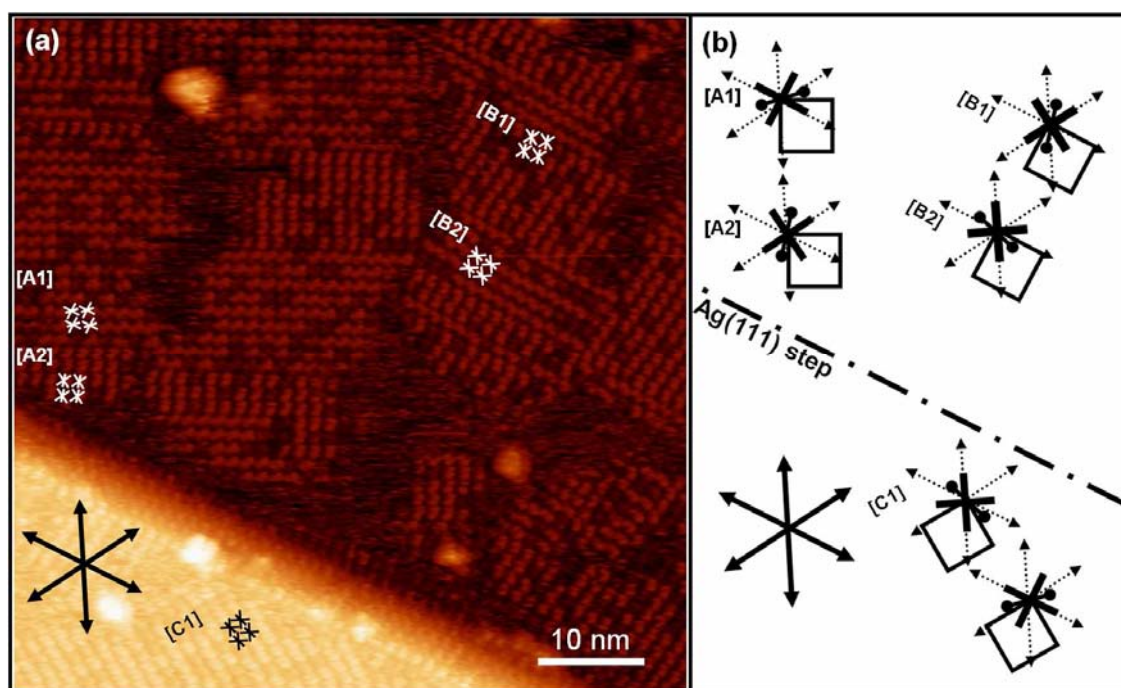


**Figure 4.1.8.** (a) Constant current image of a sub-monolayer of FeTPP/2HTPP. The domains are rotated by multiples of  $60^\circ$ . Internally, each of the domains exhibits 2D-chirality ( $U = -213$  mV,  $I = 37$  pA). (b) The individual unit cells of the domains are shown enlarged and the corresponding molecular axes of FeTPP are depicted. The drawn in dumb-bells highlight the anisotropy axis per molecule. The high-symmetry directions of the Ag(111) surface are marked by arrows. In each of the drawn in unit cells strictly one of the two molecular axis points towards one high-symmetry direction of Ag(111).

above), with the molecular axes either rotated clockwise or counter-clockwise out of the unit cell. (Note that both the molecular axes (connection between opposing phenyl rings) and the anisotropy axes (connection between elevated pyrrol rings) are drawn in the image as marker). The high-symmetry directions of the Ag(111) surface were deduced from the orientation of the Ag(111) step in figure 4.1.8 (a). The simplified models were placed over the STM images and are shown in figure 4.1.8 (b). Six different domains, i.e., three domains with different orientations induced by the substrate, exist in two chiralities. The domains are labeled with  $[XN]$  with the orientation index  $X$  (A,B,C) and the chirality index  $N$  (1,2). Note that the domain [C2] is not present in the STM image,

however it was included in figure 4.1.8 (b). Obviously, one of the molecular axes is always aligned along one of the high-symmetry directions of Ag(111) inside the individual domains. Thus a substrate-induced specific orientation of the individual molecules can be assumed, whereupon the square ordering is proposed to be governed by lateral T-type interactions. Auwärter et al. followed a similar approach, assuming that the packing of tetrapyrrolyl porphyrins on Ag(111) is determined by lateral interactions, while the orientation is substrate-induced [76]. A specific orientation of the molecules due to adsorbate-substrate interactions was also proposed for iron phthalocyanine [52] and cobalt phthalocyanine on Au(111) [50].

Based on the findings discussed before, the observation of 2D-chirality of TPP on Ag(111) at RT is highlighted with the scaled space-filling models placed on the substrate (figure 4.1.9). The axes of the molecules in figure 4.1.9 (a) (domain [A1]) are strictly aligned along the preferential direction  $a_3$  of the Ag(111) surface, that in figure 4.1.9 (b) (domain [A2]) to  $a_2$ . The finding emphasizes the origin of the domains' orientation, i.e., adsorbate-substrate coupling. The interaction of the phenyl groups of neighbouring TPPs is of T-type, two per phenyl-ring (eight per porphyrin), as indicated by the "Ts" in figure 4.1.9 (a) and (b). The specific arrangement both stabilizes the square order and allows surface chirality.

## **CONCLUSION**

The self-assembly of x-TPP (x=Fe, Co, 2H) was studied in detail ranging from the sub-monolayer to the multilayer regime. Exactly the same square arrangement was observed independently of the molecular sub-unit in the center of x-TPP (x = Fe, Co, 2H), indicating that the central moiety of the molecules does not determine the ordering. In the sub-monolayer range, three domains with different orientation could be observed exhibiting a three-fold rotational symmetry. The orientation of the individual domains can be attributed to a coupling between adsorbate and substrate. The square ordering of the molecules as well as the observed surface chirality is mediated by intermolecular interactions of T-type between the terminal phenyl rings. In the multilayer range the size of the unit cell decreases and the long-range order is limited. This was interpreted to as

a gradually changing tilt angle of the whole molecule in the multilayer with respect to the underlying layer. Probably, the tilt angle is limited because of energetic reasons, thus a domain boundary emerges, proceeding with the molecular arrangement in reverse order. However the latter interpretation with respect to the arrangement of multilayer molecules remains speculative.

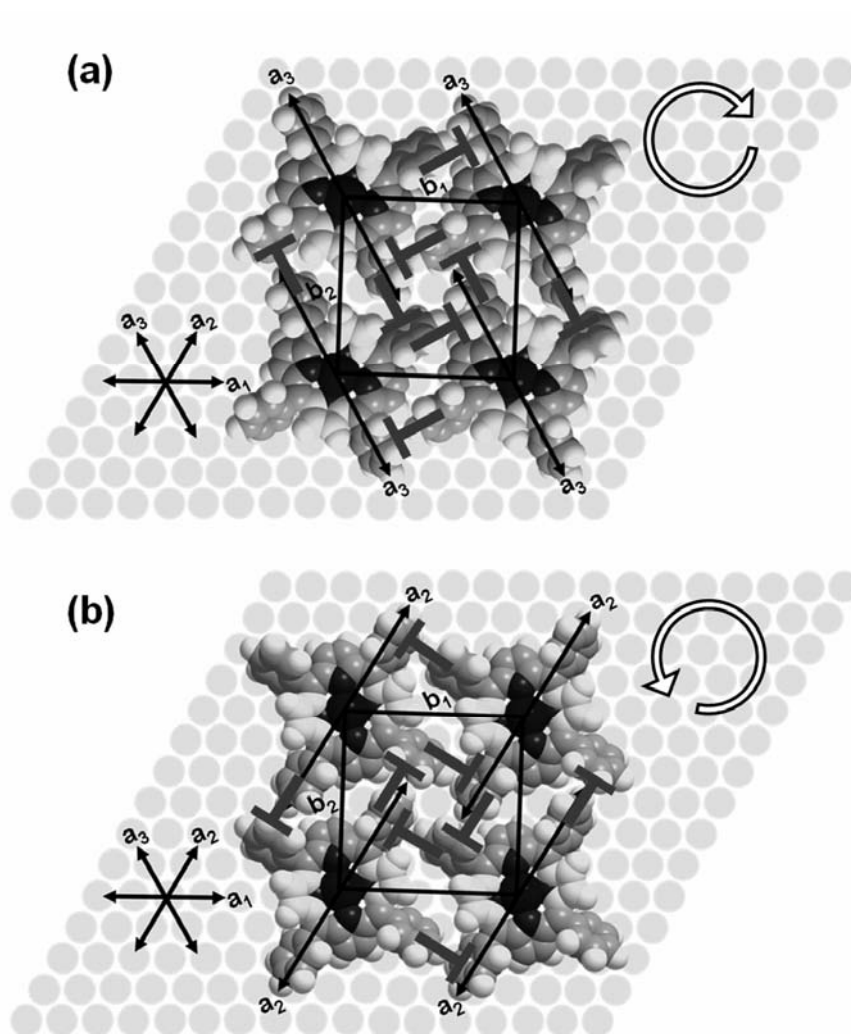


**Figure 4.1.9.** (a) and (b) Space-filling models placed on a Ag(111) model surface. The changing registration of respectively one of the two molecular axes per molecule in chiral domains towards one of the main axes of Ag(111) is highlighted. The lateral stabilization of the square arrangement is driven by two T-type structures at each phenyl ring.



## 4.2 Self-Assembly and Individual Appearance of Cobalt(II)-Tetrakisdi-tert-butylphenylporphyrins on Ag(111)

---

In chapter 4.2.1 the molecular arrangement and the internal conformation of CoTTBPP on Ag(111) is demonstrated. Interestingly, four different molecular arrangements were found, using different routes to prepare the porphyrin films. After the preparation of a film with coverage slightly below one monolayer by thermal sublimation, three clearly distinguishable molecular arrangements were observed. Alternatively, a monolayer was prepared by deposition of a multilayer followed by subsequent annealing to desorb the excess multilayer molecules. Thereby, an additional, very rigid herringbone structure formed, covering most of the surface. The four ordered phases go along with different conformations of the individual molecules. Based on STM images with sub-molecular resolution, models for the lateral arrangements of the different polymorphs including the internal conformation of the individual molecules, are proposed. Thereby, as an extension to previous works, the rotation of the upper tert-butyl groups of CoTTBPP was taken into account. The derived molecular arrangements in combination with the intramolecular conformations give insight into the intermolecular interactions within and the nature of the different molecular phases.

Furthermore, it is demonstrated (chapter 4.2.2) that different sub-units of CoTTBPP are addressed depending on the polarity of the bias voltage. The origin of the observed sub-molecular features could be deduced.

## 4.2.1 Polymorphism of CoTTBPP

---

CoTTBPP consists of the porphyrin macrocycle, which is terminated by four phenyl rings attached to the 5, 10, 15 and 20 positions of the central porphyrin ring; each phenyl group additionally has two tert-butyl ligands at the 3 and 5 positions. A corresponding molecular model for CoTTBPP is shown in figure 4.2.1 (a) and (b). The TPP molecule is a smaller version of the TTBPP without the tert-butyl groups investigated in chapter 4.1. STM studies for various TPPs on different surfaces reveal square molecular arrangements with a lattice constant of  $\sim 1.4$  nm [56, 70, 86]. In contrast, TTBPP molecules exhibit different molecular arrangements, ranging from no long-range order (ZnTTBPP on Ag(100) [87]), square arrangements (PtTTBPP on Cu(100) [72], CuTTBPP on Au(110) and Cu(100) [39]) and closed packed hexagonal phases (2HTTBPP on Au(111) [88, 89]) to a herringbone structure (CuTTBPP on Cu(111) [90]). In most cases a certain conformation of the single molecule is associated with a particular long range order. To describe the conformation, the dihedral or twist angle  $\Theta$  around the  $\sigma$ -bonds between the phenyl rings and the porphyrin macrocycle [39] and the tilt angle  $\Phi$  [91] of the phenyl groups relative to the porphyrin plane are used, as illustrated in figure 4.2.1 (c) and (d). In a constant current STM image the topography of a single molecule is then expected to be dominated by the uppermost TB groups (marked yellow in Figure 4.2.1), which should appear as four protrusions. For  $\Theta$  values close to  $0^\circ$ , all eight TB groups can be visible in the STM image, resulting in eight protrusions or bright spots [90, 92].

The overall conformation of the individual molecule on a surface is generally regarded as the result of the interplay of different factors like the steric repulsion between the ortho-substituents and attractive interactions with the surface or surface features [39, 89]. Calculations for the undisturbed molecule result in  $\Theta = 90^\circ$  [89], i.e., with the phenyl group perpendicular to the porphyrin core, as shown in figure 4.2.1 (a) and (b). For CuTTBPP, Jung et al. report dihedral angles of  $90^\circ$ ,  $45^\circ$  and  $30^\circ$  for adsorption on Cu(100), Au(110) and Ag(110), respectively [39]. Furthermore, Moresco et al. [92] and Loppacher et al. [93] showed that it is possible to switch the dihedral

angle via STM manipulation from a roughly perpendicular to a flat confirmation of the phenyl group.

By applying two different preparation methods, the ordering behaviour of CoTTBPP on Ag(111), including the internal molecular conformation, has now been investigated in this work. Based on STM images with sub-molecular resolution it was possible to identify four differently ordered phases and to determine the intramolecular conformation, i.e., twist angle,  $\Theta$  and tilt angle,  $\Phi$ , in all cases. In the course of the analysis it turned out, that both tilting and twisting of the phenyl rings is required to

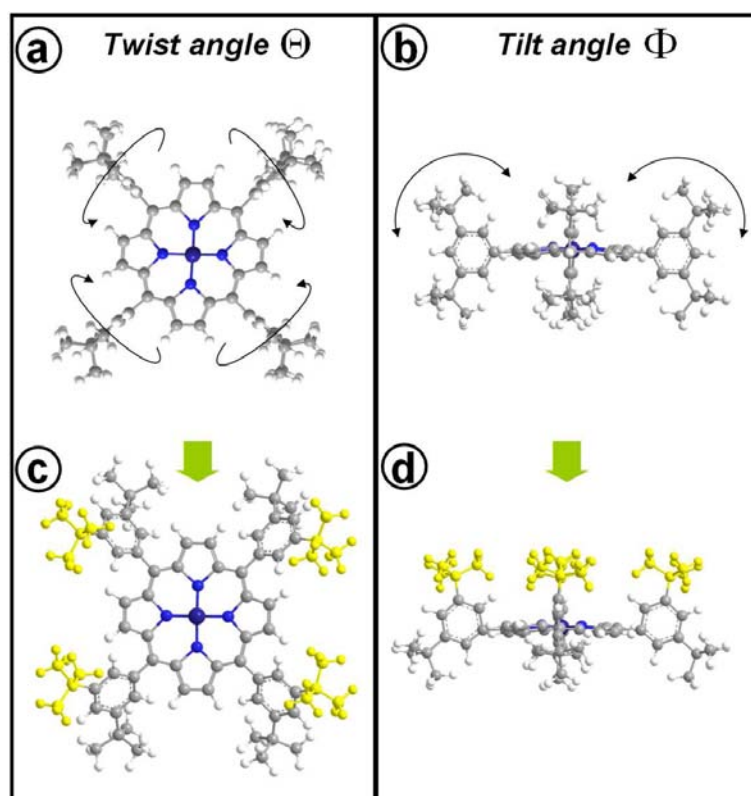


**Figure 4.2.1.** Top view (a) and side view (b) of CoTTBPP, with the phenyl group oriented perpendicular to the plane of the porphyrin macrocycle (twist angle  $\Theta = 90^\circ$ ). In (c) a possible molecular deformation is shown, with the TB-phenyl substituent rotated out of the porphyrin macrocycle plane ( $\Theta < 90^\circ$ ). Thereby, the quadratic arrangement of the upper TB groups (indicated in yellow) changes to a rectangle. In (d) the TB-phenyl ligands are tilted towards the porphyrin macrocycle (tilt angle  $\Phi$ ). Thereby the distance between the upper TB groups (yellow) is reduced.

obtain a good correlation between the proposed model structures and the STM images. The observed polymorphism of CoTTBPP on Ag(111) with four clearly distinguishable phases represents the largest variety of ordered phases of large molecules under UHV conditions observed for a single adsorbate system.

STM images of the porphyrin layers in the sub-monolayer regime, prepared by evaporation at RT, are shown in figure 4.2.2. Individual molecules can be identified by four bright lobes corresponding to the four upper tert-butyl groups. Surprisingly, the STM images in figure 4.2.2 exhibit three clearly distinguishable ordered phases, namely two hexagonal (*hex A* and *hex B*) and one *square*. For all phases domains with different azimuthal orientations are observed. In figure 4.2.2 (a), the two coexisting hexagonal phases *hex A* and *hex B* are clearly visible, as indicated by the capital letters A and B, respectively. Two domains with *square* order, indicated with C and one *hex A* domain are found in figure 4.2.2 (b). Furthermore, in figure 4.2.2 (b) noisy regions in between the ordered porphyrin domains are observed. For these regions it is proposed that the silver surface is only partially covered with CoTTBPP molecules, which are very mobile [71]. This explanation is also likely, because time sequences of STM images show that molecules at grain boundaries can exchange between the domains.

A fourth molecular arrangement was solely observed for a CoTTBPP monolayer, which was prepared using a different route, namely the deposition of a multilayer at RT, followed by subsequent heating (~45 s at 550 K) and thereby desorbing the multilayer molecules. The multilayer after deposition at RT was identified by typical stripy features in the scanning direction of the tunnelling tip as shown in figure 4.2.3 (a). With the tip moving alternately in both horizontal directions, these features can be ascribed to the relatively easily moveable molecules within the multilayer. After the thermal treatment the surface exhibited mainly two situations. In few surface regions, the STM images showed the coexistence of domains with *square* and *hex B* order, as shown in figure 4.2.3 (b). However, for most of the surface, STM images as shown in figure 4.2.3 (c) and on an enlarged scale in figure 4.2.3 (d) were found. Here, a well ordered and stable phase was observed over large areas. Within this phase, the CoTTBPP molecules are arranged in a *herringbone* structure.

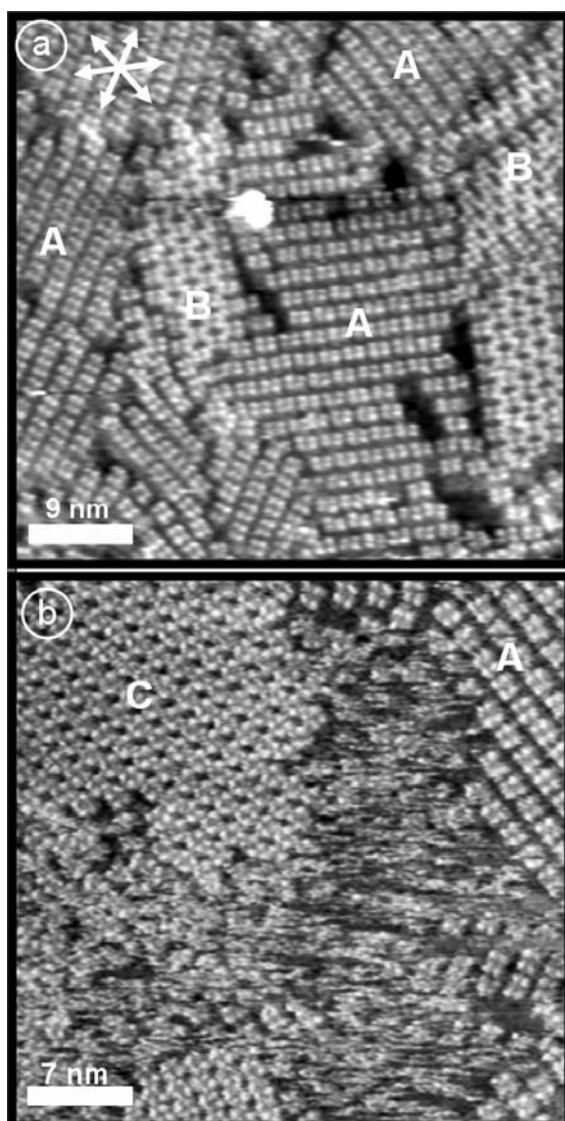


**Figure 4.2.2.** STM constant current images of a self-assembled CoTTBPP film on Ag(111), with a coverage slightly below one monolayer. Three phases with different long range order and different molecular conformations are clearly distinguishable, as indicated by the capital letters A, B, and C. For each phase several domains are observed; (a) and (b) show different regions of the same sample. According to their structure, the different molecular phases are indicated as hex A (A), hex B (B), and square (C). The arrows in the upper left corner of (a) indicate the three azimuthal orientations of different domains of phase hex A (A), which are rotated to each other by  $120^\circ$ .

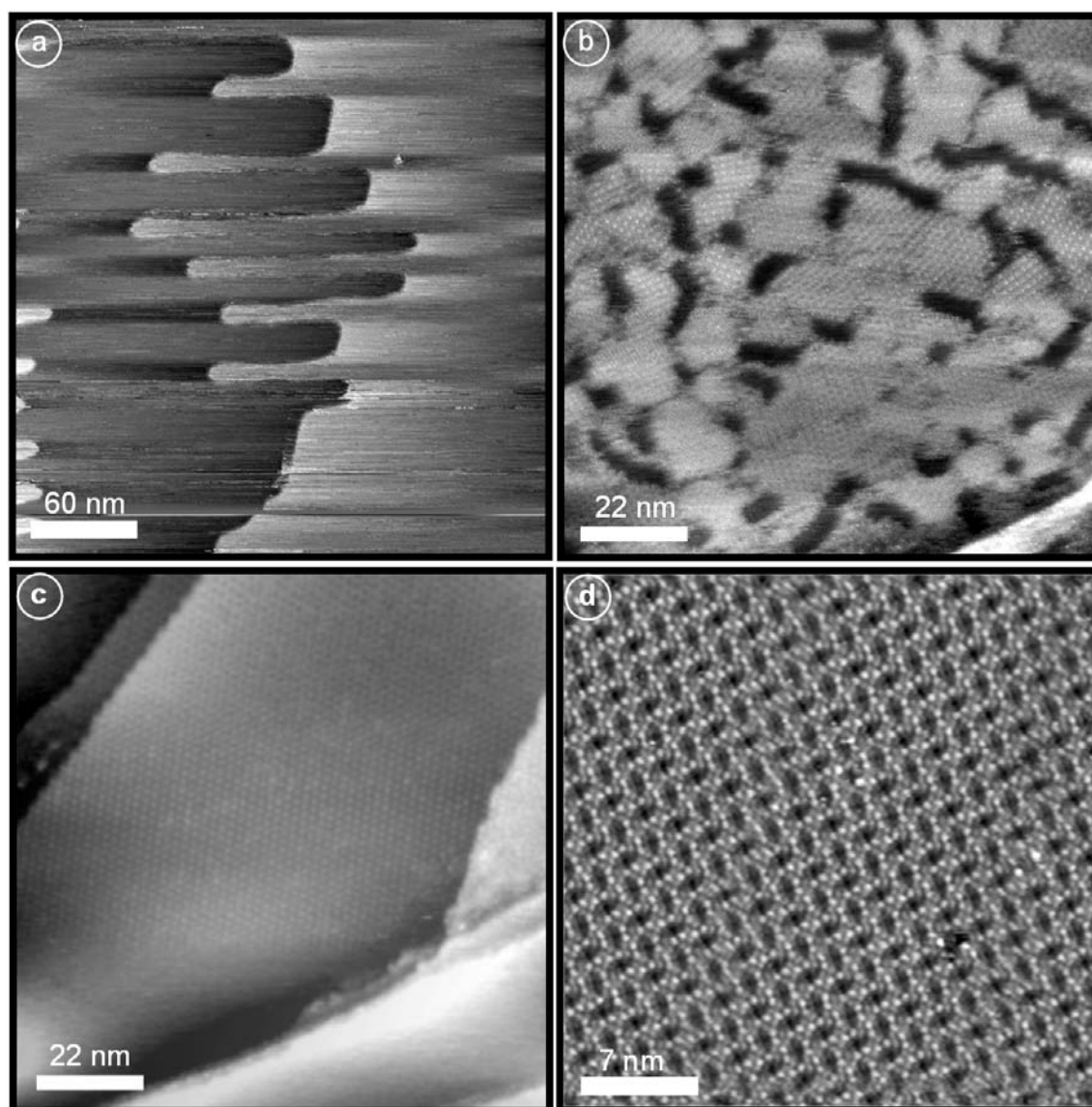


**Figure 4.2.3.** (a) Typical STM image of CoTTBPP in the multilayer regime. The stripy features are tip induced. (b)-(d) STM images of a monolayer of CoTTBPP, acquired after a thermal treatment (45 s at 550 K) of the multilayer. Mainly two situations are found: The minority observation is a mixture of the square and the hex B phase, shown in (b). Most of the investigated areas exhibited the herringbone phase, shown in (c) as large area image and (d) as a high-resolution image.

In contrast to the other three phases (*hex A*, *hex B* and *square*) which appear with four bright spots per molecule in the STM image, the individual molecules now exhibit

eight bright spots, four brighter and four slightly dimmer ones. Each of the spots is assigned to one TB group. The visibility of all TB groups indicates a conformation of CoTTBPP, where the phenyl rings are almost parallel to the porphyrin plane. This is a clear hint that different molecular arrangements go along with altered internal conformations.

In the following, the properties of the four observed molecular arrangements will be described and elucidated in detail. For that purpose, the lattice parameters were extracted from the STM images by averaging measurements from different data sets; the given errors are the standard deviations. The values for the lattice constants,  $a$  and  $b$ , the enclosed angle,  $\alpha$ , and the resulting molecular 2D-density,  $\rho$ , are given in table 4.2.1, column A-D. The side lengths,  $s$  (short side) and  $l$  (long side) of the rectangles formed by the protrusions, which are identified as the upper TB groups of a single molecule, were measured to estimate the internal molecular conformation (see also last columns of figure 4.2.5). However, this interpretation is limited in accuracy because the TB groups are larger than the actual protrusions. Since all measurements presented in this work were performed at RT it is to be expected that a rotational motion of the TB groups is excited (e.g., see Gribble et al. [94]), i.e., that the TB groups are more or less freely rotating. This should be considered if one interprets the protrusions inside the STM images. Figure 4.2.4 shows the rotation of one TB group, with the three outer carbon atoms moving along the circular trajectory indicated by the green circle. Thus, the protrusions in the STM images should correspond to the highest point of this trajectory.

In figure 4.2.4, this situation is illustrated by aligning the TB group such that one CH<sub>3</sub> subgroup (marked in red) is in the most upward position. The position of the corresponding carbon atom is then interpreted as the maximum of the protrusion in the STM image. Including the rotation of the TB group is an extension to previous works and proved to be crucial to establish an optimized modelling of the internal molecular confirmation. The colour code in figure 4.2.4 was similarly applied in figure. 4.2.5 (upper TB: red for highest CH<sub>3</sub> group and yellow for remaining CH<sub>3</sub>-groups; lower TB: orange).

	A	B	C	D	E	F	G	H	I	J	K	L
Phase	a	b	$\alpha$	$\rho$	$l_{\text{exp}}$	$s_{\text{exp}}$	$l/s$	$l_{\text{mod}}$	$s_{\text{mod}}$	$l/s$	$\Theta$	$\Phi$
$\downarrow$	[nm]	[nm]	[ $^\circ$ ]	[mol/nm $^2$ ]	[nm]	[nm]	exp	[nm]	[nm]	mod	[ $^\circ$ ]	[ $^\circ$ ]
<i>Square</i>	1.60 $\pm 0.06$	1.60 $\pm 0.06$	90	0.39	0.76 $\pm 0.07$	0.76 $\pm 0.07$	1.00	0.74	0.74	1.00	90	25
<i>Hex A</i>	2.30 $\pm 0.05$	2.07 $\pm 0.10$	65	0.24	0.92 $\pm 0.05$	0.72 $\pm 0.07$	1.28	1.04	0.75	1.39	60	20
<i>Hex B</i>	1.89 $\pm 0.10$	1.89 $\pm 0.10$	60	0.31	1.11 $\pm 0.07$	0.70 $\pm 0.03$	1.59	1.23	0.73	1.68	45	15
<i>Herring-bone</i>	1.89 $\pm 0.05$	1.89 $\pm 0.05$	60	0.31	1.31 $\pm 0.04$	0.65 $\pm 0.04$	2.02	1.49	0.74	2.01	20	5

**Table 4.2.1.** Overview of the values extracted from the STM data (columns A-G) and the corresponding model values (columns H-L).

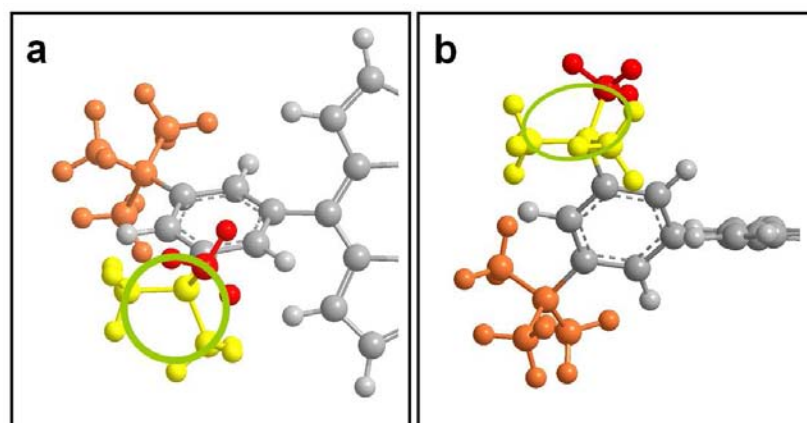


**Figure 4.2.4.** (a) Top view and (b) side view of a schematic drawing, indicating the thermal induced rotation of the tert-butyl groups (circle). The upper TB group (yellow) is shown in the geometry, where one CH $_3$  group (red) is in the most upward position. The lower TB groups are colored orange.

The estimation of the internal molecular conformation is based on the comparison of the values  $l_{exp}$  and  $s_{exp}$  (short and long side of rectangle, respectively, in figure 4.2.5 (d)) as extracted from the experimental data and  $l_{mod}$  and  $s_{mod}$ , as measured in the corresponding models; the corresponding values are given in columns E-J in table 4.2.1. The rotation of the side groups (phenyl ring with two TB groups) by the dihedral angle  $\Theta$  leads to an asymmetric twist of two opposite TB groups [39], yielding a rectangular shape of the molecule in the STM image. This type of deformation results in increasing values for the aspect ratio  $l/s$  but the perimeter of the resulting rectangle ( $2l + 2s$ ) remains unchanged. The values for the aspect ratio,  $l/s$ , and the resulting values for  $\Theta$  as given by Jung et al. [39] were considered as an informative basis for the estimation of  $\Theta$  in the present paper. Decreasing perimeters of the rectangle coincide with an increasing tilt angle,  $\Phi$ . Based on the aspect ratio described above, preliminary values for  $\Theta$  and  $\Phi$  were estimated. The optimization was performed by varying these values by increments of  $5^\circ$  and comparing the resulting dimensions of the model with the experimental data.

The *square* phase as shown in figure 4.2.5 (a) exhibits an average length of the lattice vectors of  $1.60 \pm 0.06$  nm and an angle between them of  $90^\circ \pm 3^\circ$ . The azimuthal angle between the molecular axis and the lattice vector is  $30 \pm 5^\circ$ . This arrangement exhibits the highest molecular density ( $\rho = 0.39$  molecules/nm<sup>2</sup>) of all observed phases. The internal shape of each molecule established by four bright lobes (protrusions) per molecule is a square with a side length of  $0.76 \pm 0.07$  nm and consequently a perimeter of 3.04 nm. As the four upper TB groups form a square (aspect ratio  $l/s = 1$ ) it is assumed that the CoTTBPP molecules are in a conformation, where all phenyl rings are oriented perpendicular to the porphyrin macrocycle [39].

However, the measured distance of the lobes  $s = l = 0.76 \pm 0.07$  nm compared to roughly  $\sim 1$  nm for the undisturbed conformation ( $\Theta = 90^\circ$ ,  $\Phi = 0^\circ$ ) differs, if one assumes the uppermost CH<sub>3</sub> group as a measuring point. The smaller distance of the four lobes can be explained as discussed above by an inward tilting of the phenyl rings [95]. The square symmetry of the upper TB groups is maintained, if all phenyl rings are tilted inwards by the same angle  $\Phi$ . In the absence of a twist rotation, i.e.,  $\Theta = 90^\circ$ , and for a tilt angle  $\Phi = 25^\circ$  one obtains a side length of 0.74 nm, in good agreement with the

experimental value. Figure 4.2.5 (b) and 4.2.5 (d) shows the molecular model based on these considerations, scaled to fit and superimposed on the STM image by hand.

A blow up of the *hex A* phase is shown in figure 4.2.5 (e). It consists of parallel straight rows of molecules (again appearing as four bright lobes) with an intrarow distance from molecule center to molecule center of  $2.07 \pm 0.10$  nm. These rows have a normal distance of  $1.95 \pm 0.04$  nm and are shifted against each other by roughly half an interrow molecular distance. This results in a slightly distorted hexagonal structure, as

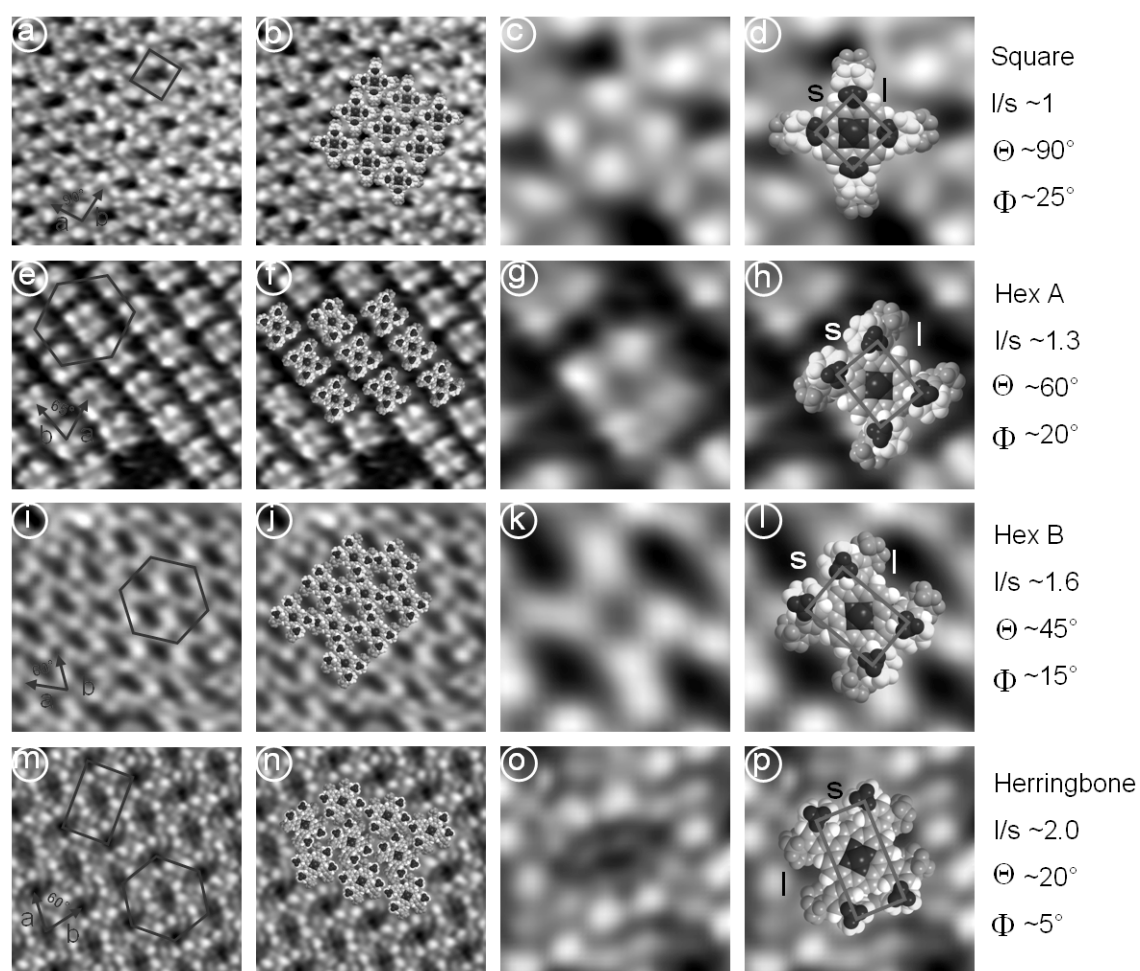


**Figure 4.2.5.** Overview of STM images of the four phases with and without the corresponding molecular models superimposed: (a-d) square phase, (e-h) hex A phase, (i-l) hex B phase and (m-p) herringbone phase. The size of the STM images is  $(10 \times 10)$  nm<sup>2</sup> for the first two columns and  $(3 \times 3)$  nm<sup>2</sup> for the remaining. The molecular models are scaled to fit and placed by hand in the STM images.

indicated in figure 4.2.5 (e), and is thus labeled *hex A*. The corresponding unit cell can be characterized by the two lattice constants  $a = 2.30 \pm 0.05$  nm and  $b = 2.07 \pm 0.10$  nm, with an enclosed angle of  $\alpha = 65^\circ$ , resulting in a molecular density of  $\rho = 0.24$  molecules/nm<sup>2</sup>. The detailed inspection of figure 4.5.2 (a) reveals that the directions of the rows in the different *hex A* domains are rotated by multiples of  $120^\circ$  (indicated by the arrows in figure 4.2.2 (a)). Considering the three-fold symmetry of the substrate surface, it is likely that the molecular arrangement underlies a certain registry to the surface corrugation. This is in line with the fact that the *hex A* structure has the lowest molecular density and consequently the stabilization due to intermolecular forces should be smaller than for a more densely packed structure. The internal shape of the single molecules as given by the four protrusions is rectangular with side lengths  $l = 0.92 \pm 0.05$  nm and  $s = 0.72 \pm 0.07$  nm, yielding  $l/s = 1.28$ . The resulting perimeter of 3.28 nm is larger than for the *square* phase. As pointed out above, upon a rotation of the phenyl rings alone, the perimeter does not change, but the shape of the upper TB shifts towards a rectangle. Consequently, a combined deformation, with a twist angle of  $\Theta = 60^\circ$  and a tilt angle  $\Phi = 20^\circ$ , had to be applied to achieve a good agreement between model and STM image.

The phase denoted as *hex B* is a clear-cut closed packed hexagonal structure (as indicated in figure 4.2.5 (i)), with the unit cell parameters  $a = b = 1.89 \pm 0.05$  nm,  $\alpha = 60^\circ$  and  $\rho = 0.31$  molecules/nm<sup>2</sup>. The measured parameters for the internal molecular configuration are  $l = 1.11 \pm 0.07$  nm and  $s = 0.70 \pm 0.03$  nm. Compared to the *hex A* phase, the internal molecular conformation within the *hex B* phase exhibits an increased ratio  $l/s = 1.59$  and an increased perimeter of the rectangle formed by the four protrusions. This indicates an increased twist angle  $\Theta$  and a decreased tilt angle  $\Phi$ . A good fit with the model was achieved with the parameters  $\Theta = 45^\circ$  and  $\Phi = 15^\circ$ .

The unit cell of the *herringbone* structure can be ascribed as a rectangle ( $a' = 3.27 \pm 0.09$  nm,  $b' = 1.89 \pm 0.05$  nm) with a molecule at every corner and a central molecule with a different azimuthal orientation (figure 4.2.5 (m)). If one neglects the azimuthal orientation of the molecules, a hexagonal arrangement can be found as indicated in figure 4.2.5 (m). For the sake of comparability, the values for a hexagonal unit cell are

chosen to describe the *herringbone* phase. The parameters are:  $a = b = 1.89 \pm 0.05$  nm,  $\alpha = 60^\circ$  and  $\rho = 0.31$  molecules/nm<sup>2</sup>, i.e., identical to the *hex B* phase. A perimeter of the four bright lobes per molecule (figure 4.2.5 (p)) of  $\sim 4$  nm ( $l = 1.31 \pm 0.04$  nm,  $s = 0.65 \pm 0.04$  nm) was measured, which indicates a small value of the tilt angle  $\Phi$ . The high aspect ratio of  $l/s = 2.02$ , which is significantly larger than observed for the other conformations, must be due to a low value of  $\Theta$ . Indeed, the appearance of the individual molecule can be reproduced by a twist angle of the phenyl rings of  $\Theta = 20^\circ$  and a tilt angle of  $\Phi = 5^\circ$  (figure 4.2.5 (p)). As mentioned before, the molecules inside the *herringbone* structure exhibit in addition to the four bright lobes four additional slightly dimmer protrusions, as clearly visible in figure 4.2.5 (m) and (o). These additional lobes are identified as the lower TB groups. This becomes evident, since the positions of the orange marked lower TB groups in figure 4.2.5 (p) coincide with the four dimmer spots in figure 4.2.5 (o), exhibiting a smaller apparent height [89, 96]. Consequently, they are closer to the surface, considering the STM image as a result of the pure topography. The visibility of all eight TB groups of an individual molecule in the STM image also is in line with the low value of  $20^\circ$  for  $\Theta$ , i.e., an orientation of the phenyl rings nearly parallel to the porphyrin macrocycle. For the observed low  $\Theta$  value of  $20^\circ$  in the *herringbone* structure, it is assumed that the rotational barrier due to steric repulsion of the H atoms of the porphyrin macrocycle and the phenylring [97] is overcome by the thermal energy applied during multilayer desorption. For a rotation of the phenyl rings by such large angles, a deformation of the porphyrin ring has been proposed [98]. Conclusions on the deformation of the porphyrin macrocycle can however not be derived from our study.

From the detailed analysis of the STM images, a consistent picture and description of the four observed phases could be established. With the proposed models one can also roughly estimate the distance,  $d$ , of the central porphyrin plane to the surface, yielding the following values:  $d(\text{square}) = 0.42$  nm,  $d(\text{hex A}) = 0.39$  nm,  $d(\text{hex B}) = 0.39$  nm and  $d(\text{herringbone}) = 0.36$  nm. Since the substrate is the same, differences in the molecule-molecule interactions in the various phases should be responsible for the different heights. This is especially remarkable, since up to now changes in the internal molecular conformation were solely regarded as due to substrate-adsorbate interactions

(e.g., high substrate-adsorbate interaction yield low values of  $\Theta$ ) or induced by manipulation. In order to obtain a good fit of the measured values  $s$  and  $l$ , in the present study it was absolutely necessary to vary the tilt angle  $\Phi$ . In this context, it is noteworthy to mention that with two exceptions [91, 92] the tilt angle  $\Phi$  was not taken into account in the literature, which would lead to a wrong estimation of the distance between the central porphyrin plane and the substrate surface. Furthermore, we also want to note, that from our measurement no conclusions can be derived on whether the Co atom is located exactly in the plane of the macrocycle or if some dislocation out of this plane is induced by the interaction with the substrate.

The information obtained for both the molecular arrangements and the corresponding internal conformations of the CoTTBPP molecules on Ag(111) can now be exploited to deduce general conclusions on the intermolecular interactions within these phases. This was done by analyzing the corresponding 3D-models, derived from the values for  $a$ ,  $b$ ,  $\alpha$ ,  $\Theta$ , and  $\Phi$ , given in table 4.2.1. In figure 4.2.6 (a), (b) and (c) top views on the *square*, the *hex B* and the *herringbone* phase, respectively, are shown. In each model, the blue rectangle indicates the internal conformation of the individual molecule, as shown in the right hand column of figure 4.2.5. As height information, the uppermost CH<sub>3</sub> groups (which are made responsible for the protrusions observed in the STM images), are indicated in red. To illustrate the 3D-character of the molecular interactions in figure 4.2.6 (b) and (c), the position of the lower TB groups is marked with an orange circle. The key issue to understand the formation of the different phases are the intermolecular interactions within each of the four phases. Van der Waals interactions between different molecules are considered to contribute, when parts of the involved molecules are in close proximity.

As the first example the *square* phase as shown in figure 4.2.6 (a) will be discussed. As evident from figure 4.2.5 (d), due to the tilting of  $\Phi = 25$ , the lower TB groups extend further out. Therefore, four lower TB groups from four different molecules form a junction, while due to their smaller lateral extensions the upper TB groups (marked with red circle) do not contribute. Within one junction one lower TB group is in direct proximity to two lower TB groups from two different other molecules.

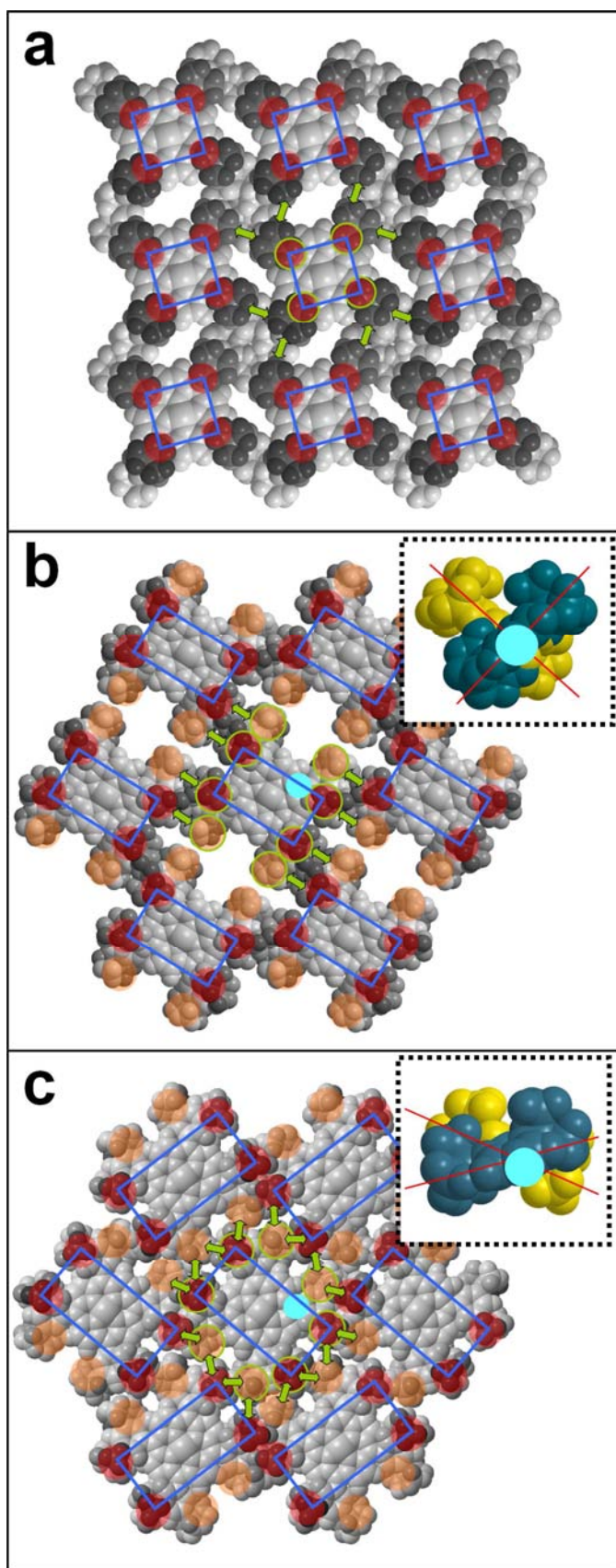


**Figure 4.2.6.** Models of the phases: (a) square, (b) hex B and (c) herringbone. The internal conformation of the molecules is indicated by the blue rectangles formed by the uppermost  $\text{CH}_3$  groups marked with the red transparent circles. Green arrows illustrate the intermolecular interactions of the central molecule with the neighbouring molecules (details see text). The orange circles in (b) and (c) indicate the lower TB groups. The inserts in (b) and (c) demonstrate the cross linked character of the side group interactions. They represent a view obtained, when looking (in plane of the porphyrin macrocycle) along the sigma bond to the phenyl ring (marked with the blue circle) towards the corresponding sigma bond (ligand) of the neighboring molecule.

This is indicated for the central molecule in figure 4.2.6 by the green arrows. Considering all four lower TB groups of an individual molecule yields eight “contact points” to neighbouring TB groups (arrows). As the *square* phase is the densest of all observed phases, attractive interactions between the molecules are assumed as the driving force for its formation.

The detailed model of the *hex A* phase is not shown, since the main features can be seen from figure 4.2.5 (f). Due to the low density of  $\rho = 0.24$  molecules/nm<sup>2</sup> the distance of the side-groups of the neighbouring molecules is increased, and consequently the attractive intermolecular interactions are reduced (four “contact points”), compared to the *square* phase. Indeed, during STM imaging, the *square* phase seemed to be more stable than the *hex A* arrangement, as is concluded from the observation that the size of *square* domains increased with time at the expense of *hex A* domains, which also indicates weaker intermolecular interactions in the latter.

The molecular arrangement of the *hex B* structure is shown in figure 4.2.6 (b). Due to the higher twist angle of the phenyl groups, side groups of neighbouring molecules interact in a way that the upper TB group of one molecules is positioned above the lower TB group of the other (and vice versa), thus partly covering it (figure 4.2.6 (b)). Thereby, a “vertical” interaction between molecules is realized. For the central molecule in figure 4.2.6 (b), these interaction sites (“contact points”) are indicated by eight green arrows pointing to neighboring molecules. In the contact region a sort of crosslink is formed, with four TB groups of two side groups being involved; this is schematically shown in the inset, where the side view of the crosslinked substituents of CoTTBPP is shown; note that for better visibility, the molecule is cut at the sigma bond between the macrocycle and the phenyl group (indicated by the blue full circle) and only the phenyl groups are shown. The clearly visible cross shaped linkage should also enhance the overall stability of the *hex B* structure. Indeed, the *hex B* phase seemed to be very stable in STM, since in contrast to the *hex A* and less pronounced for the *square* phase, no diffusion of molecules from a *hex B* phase was observed.

The *hex B* phase is assumed to be the precursor to the *herringbone* structure, because some STM images of the *herringbone* phase exhibit a small number of

molecules in *hex B* order within the *herringbone* phase (not shown here). Since the density of both phases is equal, i.e.,  $\rho = 0.31$  molecules/nm<sup>2</sup>, a transition from *hex B* to the *herringbone* structure could be realized by an intramolecular transformation accompanied by a change of the azimuthal angle, but without a change of the position of the molecule. Considering the fact that the *herringbone* structure was solely observed after a thermal treatment corroborates the conclusion that the transformation from *hex B* to the *herringbone* phase is an activated process. Thereby the thermal energy is required for the conformational change of the internal structure and for the azimuthal rotation.

The *herringbone* structure seems to be extremely rigid, not only in terms of the intermolecular arrangement but also with respect to its internal conformation that appears to be very regular; this is reflected in the lowest statistical errors of the experimental values of all four phases listed in table 4.2.1. The extraordinary stability is also evident from the model of the *herringbone* structure, as shown in figure 4.2.6 (c). Due to the smaller twist angle and the resulting close to parallel orientation of the phenyl rings, the number of interactions of the TB groups of the central molecule with the respective groups of neighbouring molecules is doubled (16 green arrows) compared to the *hex B* phase. The interactions again have partly vertical character and two of the interacting side groups per molecule exhibit the crosslink junction similar to the *hex B* phase (see inset in figure 4.2.6 (c)). The red and orange circles in figure 4.2.6 (c) indicate systematics of the contribution of certain regions within the molecules to the intermolecular interactions. At the short side of the blue rectangle, the upper TB groups (red circle) contribute to the interaction with neighbouring molecules, whereas at the long side the lower TB groups (orange circles) are in close proximity to the neighbouring molecules. In a simplified picture one might think of two opposing sides of the molecule bent downwards (orange circles) and the other two are upwards (red circles). In this way, the molecules represent ideal building blocks for the observed interwoven structure.

The *herringbone* structure seems as an extraordinary rigid molecular arrangement, which might be interesting as stable template for hierarchical structures. At this point it should be noted that the observation of this particular structure is not limited to the

Ag(111) surface. Terui et al. presented a STM image of a 2HTTBPP derivative on Cu(111) [99], which appears similar to the structure which was denoted as *herringbone* in the present work. Unfortunately, the authors do not provide details on preparation or structure. Grill et al. report a similar structure for CuTTBPP on Cu(111) after the deposition of the porphyrin using a pulse injection technique and subsequent annealing at 493 K for 5 minutes [90]. They suggest an internal conformation of the molecules, with an orientation of the phenyl plane parallel to the surface. The same molecule deposited by thermal sublimation exhibits basically the same internal conformation for submonolayer coverage, but does not exhibit the *herringbone*-like long range order. While these studies did not focus on the structural aspects of the *herringbone* type structures, they indicate that the formation of this particular structure might be a process of general nature, which possibly can be found in a variety of systems.

## CONCLUSION

A wealth of four clearly distinguishable ordered monolayer phases of CoTTBPP was found on Ag(111), using two different preparation routes. From high-resolution STM images, the orientation and internal conformation of the individual molecules within the different phases was determined and corresponding models were deduced. In the analysis, two types of intramolecular deformations had to be introduced to develop consistent models, namely the twist angle  $\Theta$  of the TBP groups and their tilt angle  $\Phi$  out of the molecular plane of the porphyrin macrocycle. In addition the rotational motion of the upper TB groups was taken into account. Altogether, a very good consistency between experimental STM images and the modeled data could be achieved. Modeling of the different molecular arrangements considering the internal conformation as well as the long range order helped to understand the intermolecular interactions and the different stabilities of the observed phases. A particular focus was put on the *herringbone* phase, which was solely observed after a thermal treatment of the sample; accordingly its formation is interpreted as an activated process. This phase proved to be especially rigid, which is attributed to its strongly interwoven structure. The observations in the STM images in combination with the deduced models allows to preliminary rank the four phases in terms of increasing stability from *hex A*, *square* and

*hex B* (with comparable stability) to *herringbone*. Due to the particular high stability of the *herringbone* phase and since there are indications that this type of molecular arrangement is observed on several surfaces, we propose these structure as a template for functional devices based on organic monolayers.

## 4.2.2 Polarity-Dependent Appearance

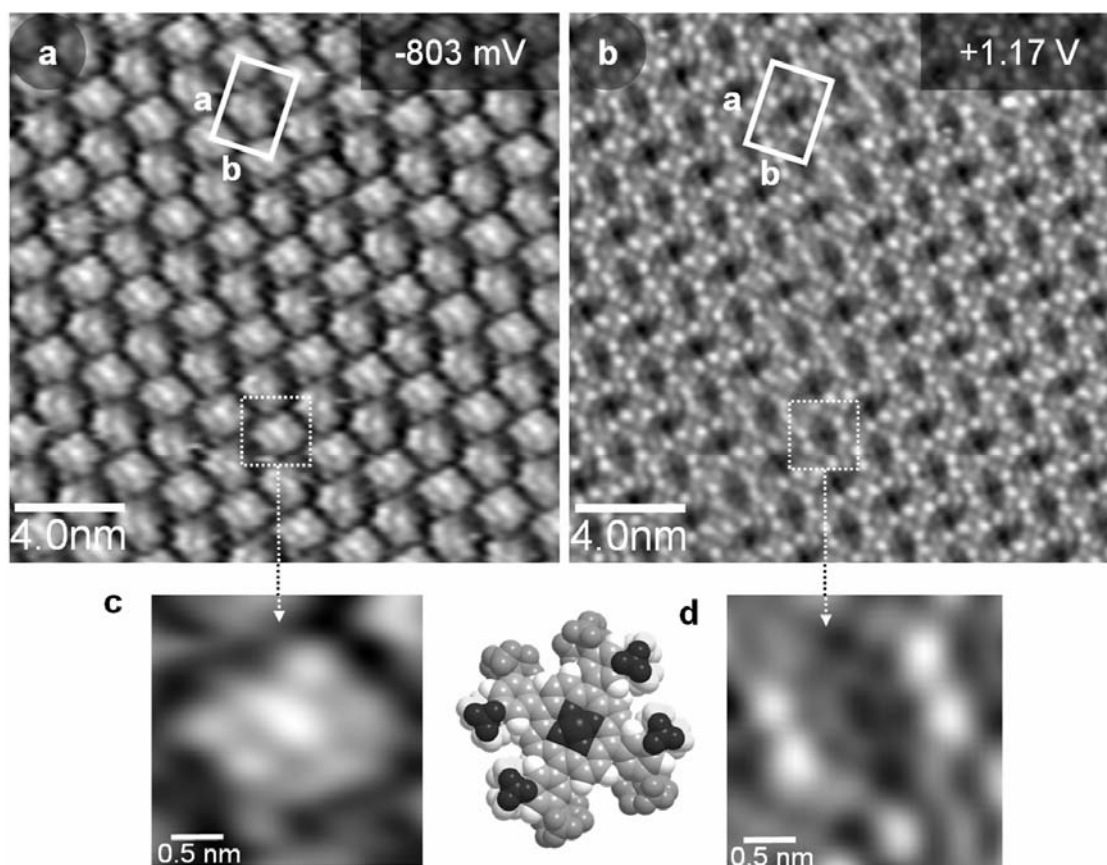
---

Figure 4.2.7 (a) and (b) show sub-molecularly resolved STM images of CoTTBPP, which were recorded at a different polarity of the bias voltage ( $U = -803$  mV,  $U = +1.17$  V). Note that both STM images were acquired at the same silver terrace and in the same domain (slightly shifted due to thermal drift). The rectangle unit cell of the herringbone arrangement of CoTTBPP is drawn in the constant current images, pointing out that both unit cells exhibit the same orientation. Obviously, the individual molecular appearance changes, depending on the polarity of the bias voltage. The extracted zoom images on single molecules (figure 4.2.7 (c) and (d)) highlight the different appearance.

At a positive bias voltage ( $U = +1.17$  V) (figure 4.2.7 (b)) four lobes per molecule appear elevated and can be attributed to the upper tert-butyl groups of CoTTBPP as also discussed in chapter 4.2.1. The four lower tert-butyl groups can be identified as four weaker protrusions. The molecule exhibits a cavity at the position of the cobalt ion. The cavity is surrounded by a ring, which can be ascribed to the porphyrin macrocycle.

At negative bias voltages ( $U = -803$  mV) (figure 4.2.7 (a)), the center of each molecule shows an oval-shaped protrusion and four surrounding lobes, which form a rectangle. For different TTPs adsorbed on single crystalline surfaces, a saddle-shape of the tetrapyrrolic macrocycle was confirmed, consisting of two opposing pyrrol rings, which are lifted up and two which are lowered [59, 61, 100] (see chapter 4.1). This deformation was reported to be induced by a tilting of the phenyl rings ( $\Theta \sim 60^\circ$ ), which causes a steric repulsion between the outermost hydrogen atoms of the phenyl rings and the porphyrin ring [39]. Taking into account the estimated twist angle of the phenyl rings of CoTTBPP ( $\Theta = 20^\circ$ ) (chapter 4.2.1), a saddle-shaped macrocycle would be

reasonable. Thus, the observed oval shaped protrusion (figure 4.2.7 (c)) is probably due to electronic and/or topographic contributions both from the central cobalt ion and two lifted pyrrol rings of the porphyrin ring.



**Figure 4.2.7.** (a) Constant current image of a monolayer of CoTTBPP, recorded at a negative bias voltage ( $U = -803$  mV,  $I = 44$  pA). (b) CoTTBPP layer, acquired at a positive bias voltage ( $U = +1.17$  mV,  $I = 36$  pA). (c) Zoom on a single molecule extracted from figure (a), whereupon a centered oval-shaped protrusion, probably due to both the central cobalt ion and two opposing pyrrol rings, is visible. (d) Enlarged image of a single molecule acquired at positive polarity, extracted from (b). The peripheral upper tert-butyl-groups appear elevated; the central cobalt ion is not visible.

The four lobes, observable at a bias voltage of -803 mV, can not be assigned to the terminal tert-butyl groups as demonstrated at a bias voltage of +1.17 V. Comparing the dimensions of the four rectangular arranged lobes (long side  $l$  and short side  $s$  in table

4.2.2) observed at negative polarity with that one at a positive, a significant difference of the geometry is found.

U [mV]	l [nm]	s [nm]
+ <b>1170</b>	$1.31 \pm 0.04$	$0.65 \pm 0.04$
- <b>803</b>	$0.98 \pm 0.04$	$0.52 \pm 0.04$

**Table 4.2.2.** Comparison of the long side *l* and the short side *s* of CoTTBPP in dependence of the polarity of the bias voltage.

Thus, taking into account the established molecular deformation (chapter 4.2.1), conclusions from the measured side length can be drawn on the accountable molecular sub-unit. A scaled space filling model is inserted in figure 4.2.7, illustrating the discussed situation. The tert-butyl groups, observable in the micrograph at +1.17 V, are coloured black in the model. In the limits of accuracy, the four lobes, which are apparent at negative polarity, correspond with the position of the phenyl rings.

## **CONCLUSION**

From the polarity-dependent STM images it is evident that different sub-units of CoTTBPP are addressed. At a positive bias voltage (electron tunnelling occurs from tip to sample), both the upper and lower tert-butyl groups and the porphyrin macrocycle are visualized. In contrast, at a negative bias voltage, the interpretation is somehow speculative, but probably both the central cobalt ion and two lifted pyrrol rings of the porphyrin macrocycle and the phenyl rings are monitored.

## 4.3 Coordination of Iron and Cobalt Atoms by Tetraphenylporphyrin Monolayers on Ag(111) and Formation of Metal(II)-Tetraphenylporphyrin

---

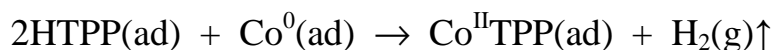
The in-situ metalation of monolayers of 2HTPP with Fe atoms on Ag(111) was studied with STM. This surface-confined coordination reaction results in the formation of adsorbed FeTPP. It is demonstrated that metalation of 2HTPP is achieved either by depositing iron atoms onto a monolayer of 2HTPP at RT, or, alternatively, by depositing 2HTPP onto a Ag(111) surface with pre-deposited iron. The latter route requires elevated temperatures, indicating that this reaction includes at least one step with an activation barrier.

### **INTRODUCTION**

One particularly interesting property of porphyrins is their capability to bind various metal ions to its center [101]. The most prominent candidates of these so-called metalloporphyrins are the iron porphyrins, with a Fe(II) ion complexed to the four nitrogen atoms in the center of the conjugated ring system. They play a key role in a number of oxidative catalytic processes, including biological systems. Iron porphyrins can undergo reversible redox reactions and are very sensitive towards oxidation [86]. Hence, they are very difficult to handle at ambient conditions and to sublime as a pure compound. Nevertheless, the investigation of clean iron porphyrins under ultra clean conditions in UHV is of fundamental interest among others due to their key role as functional building blocks in important biological molecules such as cytochrome P-450 and haemoglobin [102, 103].

Recently, Gottfried et al. [104] demonstrated in a XPS study that CoTPP can be produced under clean UHV conditions by in-situ metalation of free base 2HTPP monolayers with cobalt atoms, which are deposited using an electron beam evaporator.

Thus the following reaction was formulated:



This approach appears to be of particular importance, as it is very difficult to deposit clean FeTPP via direct sublimation, due to the above mentioned high reactivity. Thus, up to now, no clean iron porphyrin layers could be prepared and consequently the interaction with small molecules could not be studied under UVH conditions, i.e., in the absence of any solvents. Encouraged by the successful complexation with cobalt it was chosen to follow the same procedure to evaluate the possibility of generating iron porphyrins (chapter 4.3.1, 4.3.2). Furthermore, it was desirable to provide microscopic evidence for the the metalation reaction with cobalt (chapter 4.3.3).

Another central aspect is related to the order in which the porphyrin molecules and the metal atoms are deposited on the surface. For the metalation of 2HTPP with Zn, it was shown that the order is irrelevant for the result: The Zn atoms can be deposited onto the 2HTPP monolayer or, alternatively, 2HTPP can be deposited on a Ag surface pre-covered with submonolayer coverages of Zn atoms. In both cases, zinc(II)-tetraphenylporphyrin (ZnTPP) is formed upon heating to 550 K. This observation implies that the Zn atoms are "picked up" by the 2HTPP molecules, coordinated, and oxidized to the Zn(II) ions. This reaction is one of the very few examples of an oxidative dissolution of a metal by a large organic ligand. In chapter 4.3.2 it will be demonstrated that this "pick-up" reaction is not limited to Zn, but is also observed for vapor-deposited Fe atoms. Microscopic evidence for this reaction will be provided and it will be show that it results in the consumption of Fe islands formed at the steps on the Ag surface.

The pronounced metalation reaction, which is highlighted in chapter 4.3.1- 4.3.3, was also reported in a joint theoretical and experimental study by Shubina et al. [42]. (Note that the STM results presented in chapter 4.3.3 contributed to this work). The fundamental results found out by theory will be discussed in chapter 4.3.4.

### 4.3.1 Coordination of Post-deposited Iron Atoms by Tetraphenylporphyrin Monolayers

---

Figure 4.3.1 (a) shows a constant current image of a monolayer of the free base 2HTPP on Ag(111), as reported in chapter 4.1. The macrocycle of the molecules is aligned parallel to the surface; the molecules are ordered in a square arrangement with a lattice constant of 1.4 nm (see chapter 4.1). Sub-molecular resolution images were reproduced, which allow identifying four weak protrusions per molecule, due to the phenyl groups and a small cavity at the center of each molecule. The overall conformation of the single molecules is predominantly the result of a steric repulsion between the ortho-substituents [97]. The dihedral angle between the central porphyrin ring and the phenyl groups is assumed to be between 60 to 90 degrees [39]. This results in a spacing of about 0.3 nm between the porphyrin ring and the surface. The relative coverage  $\theta_{\text{rel}}$  of 2HTPP in the saturated monolayer corresponds to 0.037 ML (with 1ML defined as one molecule per surface atom (see chapter 3.7)).

Figure 4.3.1 (b) shows an STM image of a 2HTPP monolayer after the deposition of  $0.03 \pm 0.006$  ML of iron, i.e.,  $\sim 70\%$  of the amount needed to complex all 2HTPP molecules (0.037 ML). After the Fe deposition 59% of the molecules appear as protrusions. The other molecules (41%) still exhibit the central cavity as seen for the 2HTPP monolayer. Figure 4.3.1 (c) shows a profile through three protrusions and two molecules with a central cavity as indicated by the line in figure 4.3.1 (b). The observation of a protrusion at the center of each molecule is to be expected due to the changed topography of a metalloporphyrin compared with the free base has been reported for STM images of various metalloporphyrins [70, 105, 106]. For the closely related FePc a significant tunnelling contribution was reported at the center of the molecule, which was attributed to the Fe(II)  $d^6$  system with significant d-orbital character near the Fermi Energy [106]. Thus after a metalation with iron a change in the central height of the TPP porphyrin molecule in STM is expected. Based on these considerations the protrusions in figure 4.3.1 (b) and 4.3.1 (c) are interpreted as

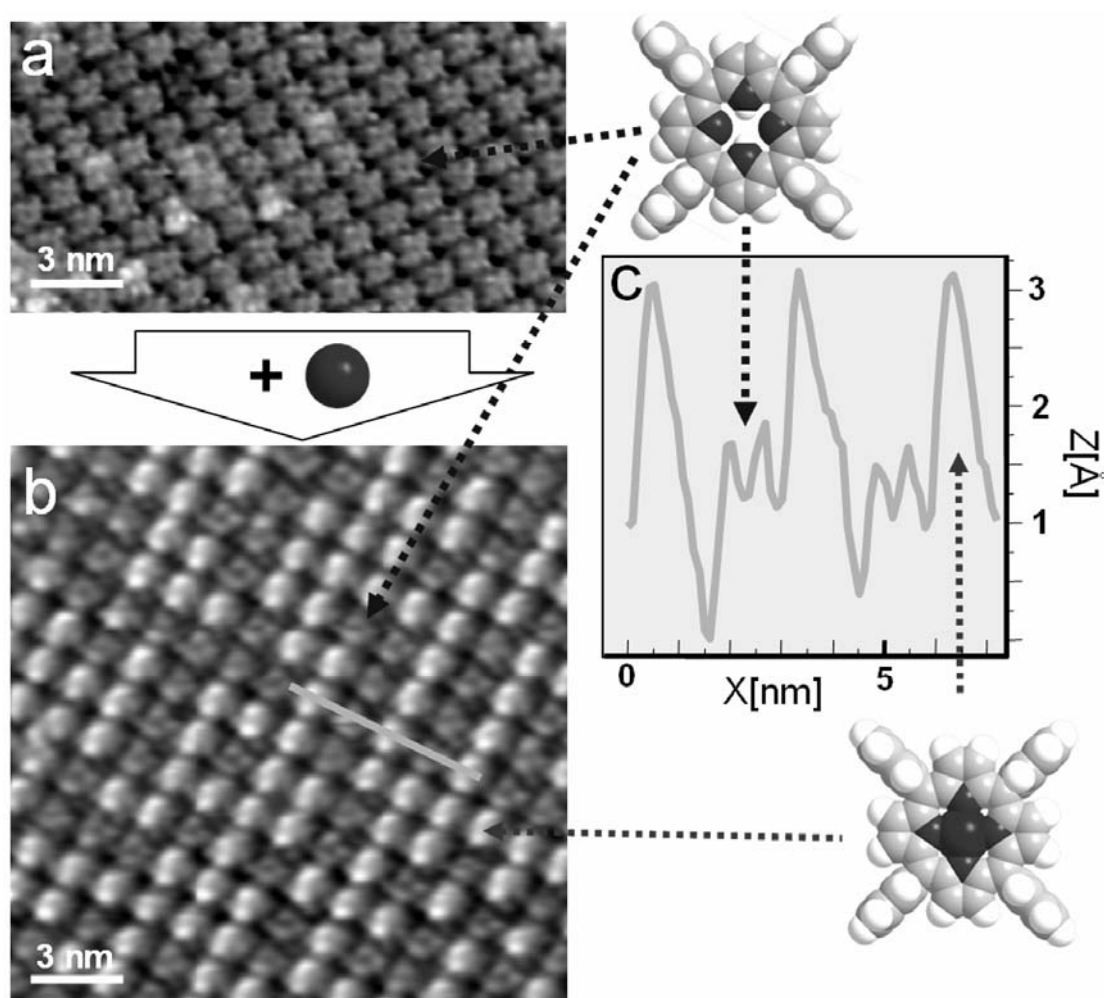


**Figure 4.3.1.** (a) STM image of a monolayer of 2HTPP on Ag(111). b) STM image of a monolayer of 2HTPP on Ag(111) after evaporation of 0.03 ML Fe. c) Height profile extracted along the line in figure 4.3.1 (b). Above the profile a filled space model of 2HTPP and below a model of FeTPP is shown. The arrows indicate the positions of the molecules in the images and the profile.

Fe(II)TPP formed by metalation. The remaining molecules with the central cavity are identified as 2HTPP.

Figure 4.3.2 (a)-(d) shows STM images acquired after the incremental deposition of portions of 0.012 ML Fe (as calibrated by a quartz microbalance) onto a monolayer of 2HTPP as shown in figure 4.3.1 (a). Evidently, the fraction of protrusions increases with the amount of deposited Fe.

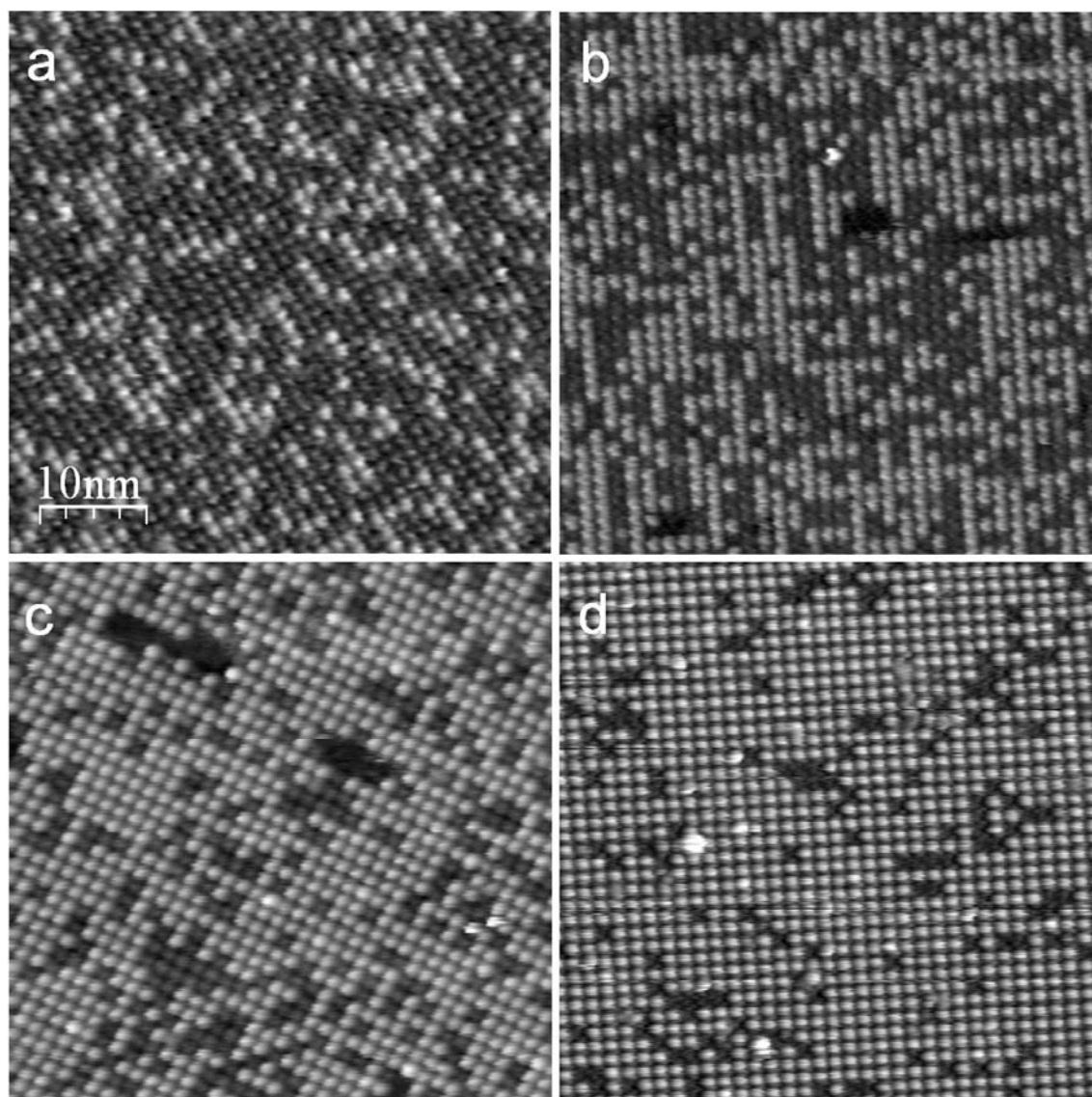


**Figure 4.3.2.** (a)-(d) Series of STM images after the successive evaporation deposition of equal amounts of Fe.

Note that the fraction of protrusions, i.e., the quantitative ratio of the two species, is very similar for different regions of the surface, as has been verified by corresponding STM measurements taken after each deposition (not shown). The fraction of protrusions (i.e., FeTPP molecules) increases with the nominal amount of deposited Fe; the corresponding numbers for figure 4.3.2 are: (a) 29% / 0.012 ML, (b) 60% / 0.024 ML, (c) 73% / 0.036 ML and (d) 89% / 0.048. It is evident that at least for the first two deposition steps the efficiency of the metalation is close to 100%. The apparent slightly

lower yield in the last two steps could be due to a lower efficiency of the metalation with an increasing portion of FeTPP molecules, but this conclusion has to be treated with some caution, if one considers the error bars, in particular for the nominal amount of deposited Fe ( $\pm 0.002$  ML per deposition step). Overall, the efficiency of the metalation process is very high. As a statistical process, the impingement of the Fe atoms onto the surface is not directed to the centers of the remaining 2HTPP molecules. Even if one assumes an attractive potential, which guides the impinging atoms towards the complexation sites, it is very likely that a significant fraction of the Fe atoms first hit other regions and undergo some diffusion (probably on the Ag(111) surface), before they complex with a 2HTPP. As a conclusion the process is at least partially surface mediated.

The situation shown in figure 4.3.2 (d) represents the highest achievable percentage of FeTPP in the conducted experiments. Additional evaporation of Fe does not lead to a decrease of the remaining molecules appearing as depressions, instead bright islands with molecules on top form. This is evident from the STM images in figure 4.3.3 (a) and (b), which have been obtained for two different regions of the surface after deposition of  $\sim 0.14$  ML Fe, i.e., 0.10 ML more than necessary to metalate the 2HTPP monolayer. The figures show bright regions (up to 12 nm in width) that are assigned to Fe islands of monoatomic height on the Ag(111) substrate. On top of these regions porphyrins are still resolved in the STM image. The area of the bright regions amount to 11.8 and 7.4% of the surface, which is in good agreement with the expected coverage of 10% ( $=0.10$  ML).

A possible cause for the observation that not all 2HTPP molecules are complexed with Fe could be that this portion of 2HTPP molecules is chemically modified in a way that the metalation does not occur and excess Fe atoms form islands after diffusion on the surface. This could, e.g., be induced by a small fraction of high energetic Fe ions, which are produced by the electron beam evaporator. Alternatively there could be some residual contaminations on the Ag(111) which hinder the surface mediated process. Nevertheless, the data in figure 4.3.2 clearly show that a controlled complexation of at least up to 89% of 2HTPP to FeTPP can be realized. One could imagine that by using

several sources for different metals this in-situ synthesis opens a new route towards the controlled preparation of mixtures of clean metalloporphyrins.

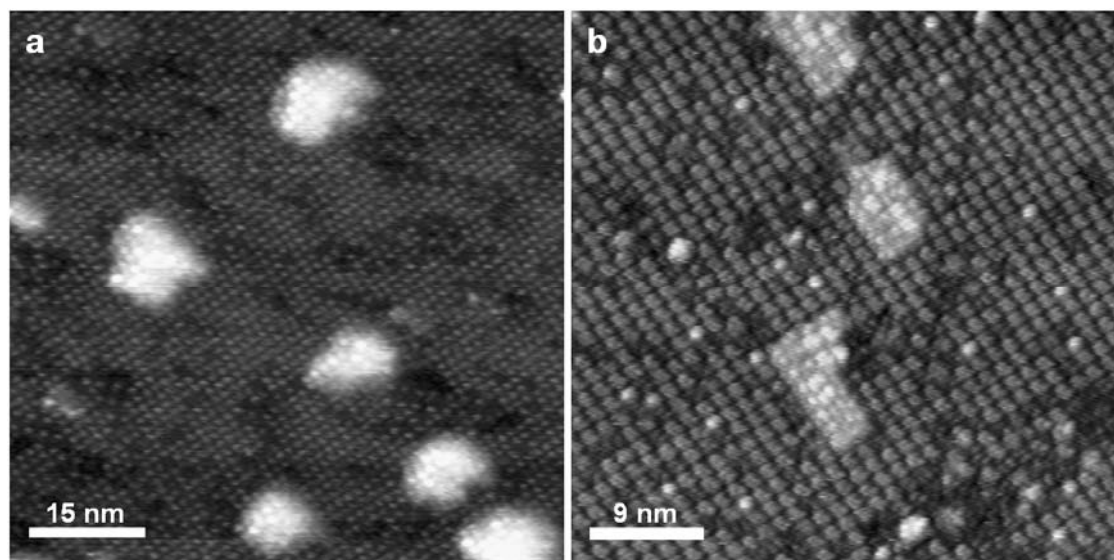


*Figure 4.3.3. Two STM images showing different regions of the surface after the evaporation deposition of ~ 0.14 ML of Fe.*

## **CONCLUSION**

Microscopic evidence of the in-situ complexation of FeTPP was given. It was demonstrated that monolayers of 2HTPP can be metalated with iron atoms in-situ in an ultra clean environment with high efficiency, by deposition using an electron beam evaporator. The number of complexated FeTPP molecules increased with increasing amount of deposited Fe. The FeTPP molecules appeared as protrusions in the STM images, due to an increased tunnelling contribution through the central Fe 3d-orbital system of the molecules and the changed topography. The presented findings not only prove the principle of the direct synthesis of iron porphyrins on a surface, it will also enable future surface science investigations of clean iron porphyrin films under UHV conditions. As iron porphyrins are the central building blocks of important biological molecules, such studies have the potential to give new insights into natural processes like the adsorption, desorption and reaction of oxygen or oxygen containing small

molecules, such as CO or NO, and in particular also the replacement of oxygen by CO in haemoglobin.

### 4.3.2 Coordination of Pre-deposited Iron Atoms by Tetraphenylporphyrin Monolayers

---

As already mentioned, it was previously shown that Zn atoms pre-deposited on Ag(111) can be "picked up" by 2HTPP under the formation of ZnTPP [62]. In order to clarify whether this approach to form metalloporphyrins is also suitable for the preparation of FeTPP, Fe was deposited onto the clean Ag(111) surface to create a reservoir for the metalation of the subsequently deposited 2HTPP. Figure 4.3.4 (a) shows a constant current STM image of the Ag(111) surface covered with a nominal coverage of  $0.020 \pm 0.006$  ML of Fe, deposited at RT. This micrograph reveals that iron forms three-dimensional islands, which decorate the atomic steps on the Ag(111) surface and have a mean diameter of approximately 3.5 nm. It should be noted that the terraces appear unchanged, i.e., free of iron islands. This type of self-assembled structure can be found in a variety of heteroepitaxial systems such as Co on Ag(111) [67], Fe on vicinal Au(111) [68], Co on Cu(111) [69], and Cu on Si(111) [63]. The underlying mechanism is based on a sufficiently high mobility of the adsorbed metal atoms with a diffusion length that exceeds the terrace width [63, 64]. In a general picture, the formation of three-dimensional clusters can be easily understood as a result of the Volmer-Weber growth mode, caused by the substantial lattice mismatch of approximately 15% and hindered diffusion (e.g., due to the Ehrlich-Schwoebel barrier) and/or energetically favorable adsorption sites at the step edges (e.g., [65, 66]). In the case of Fe on Ag(111), an intermixing of Fe with the Ag surface close to the steps is also proposed to contribute to the observed arrangement of the 3D-islands [65].

After vapor-deposition of ca. 0.037 ML of 2HTPP onto the Fe-precovered Ag(111) surface (0.020 ML Fe) at RT, the Fe clusters at the steps persist (figure 4.3.4 (b)). In addition to the clusters, a homogenous adlayer of 2HTPP is observed on the terraces. In

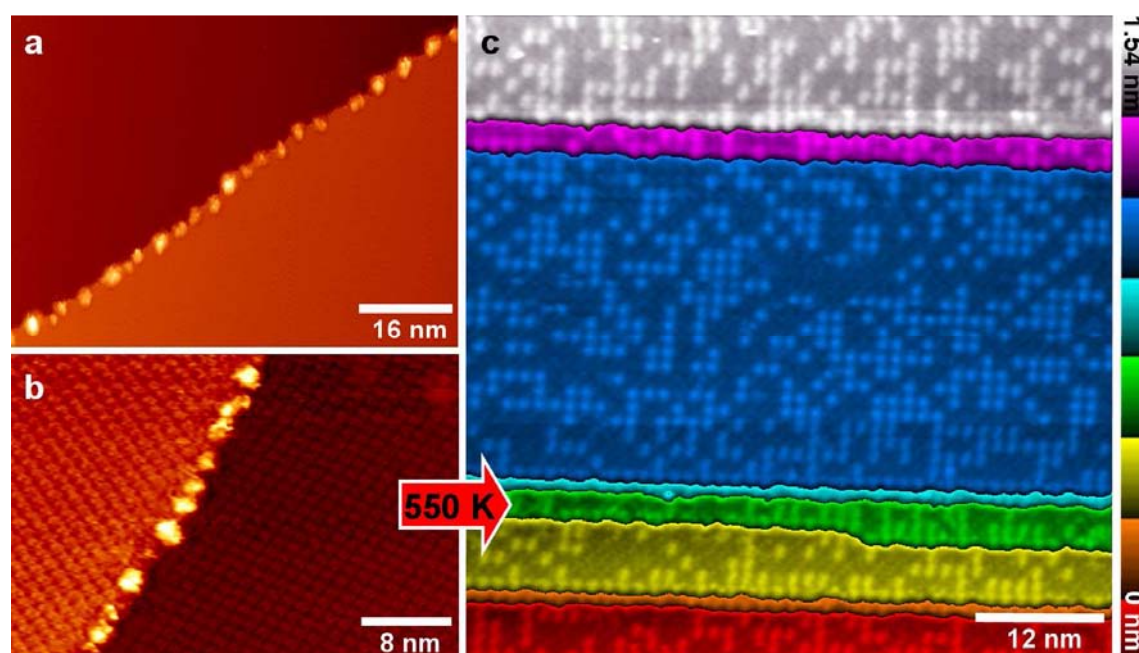


**Figure 4.3.4.** (a) STM image showing the nucleation of Fe on step edges of Ag(111). 0.025 ML of Fe were deposited at RT ( $I = 35$  pA;  $U = -1.2$  V). b) 2HTPP monolayer prepared via vapor-deposition onto the surface depicted in figure 2a ( $I = 24$  pA;  $U = 0.45$  V). The image shows an ordered 2HTPP monolayer at the terraces coexisting with iron clusters at the step edges. c) Situation after heating the surface shown in figure 4.3.4 (b) to 550 K (terraces individually color-coded). The bright spots in c) are again assigned to FeTPP formed by metalation of 2HTPP ( $I = 37$  pA;  $-1.57$  V).

this layer, the molecules show the same square arrangement as was observed on clean Ag(111). Thus, in contrast to the first preparation route (chapter 4.3.1), here a coexistence of Fe clusters on the steps and 2HTPP on the terraces is observed (compare to figure 4.3.4 (b)). The vapor-deposited Fe clusters at the steps were stable for several days at RT, indicating that the metalation reaction is very slow under these conditions.

However, heating to 550 K induces rapid dissolution of the islands and formation of FeTPP (figure 4.3.4 (c)). This temperature was chosen because it is applied for the preparation of 2HTPP monolayers by multilayer desorption (see above) and it is well-established that the 2HTPP molecules remain intact on Ag(111) at this temperature [73]. The STM image in figure 4.3.4 (c), recorded at RT after this heating step, shows again two different types of porphyrin molecules, which are assigned to FeTPP (46%) and

remaining 2HTPP (54%). Moreover, the monoatomic steps are no longer decorated with Fe islands. As was the case for Fe post-adsorption, the coverage of FeTPP agrees well with the amount of deposited Fe also for Fe pre-adsorption, proving that the high efficiency of the metalation reaction is independent of the deposition order.

The STM images with sub-molecular resolution in figure 4.3.5 emphasize the different appearances of 2HTPP and FeTPP. In figure 4.3.5 (a), a homogeneous monolayer of 2HTPP on Ag(111) is depicted. The unit cell has a square symmetry and lattice vectors with a length of  $1.4 \pm 0.05$  nm. The 2HTPP molecules show a characteristic central cavity (regardless of the polarity of the bias voltage), which is assigned to the center of the tetrapyrrolic porphyrin macrocycle. In contrast, the four peripheral phenyl rings appear as weak protrusions. Figure 4.3.5 (b) shows an intermixed layer of FeTPP and 2HTPP, formed by reaction between pre-deposited Fe and 2HTPP at 550 K. The image shows molecules with a central cavity, attributed to 2HTPP, and molecules with two protrusions close to the molecular center, attributed to FeTPP. Very similar images (chapter 4.1 and 4.3.1) have been obtained for the reverse order of deposition, indicating that the appearance of the mixed 2HTPP/FeTPP layer does not depend on the preparation procedure.

In a previous STM study of FeTPP and iron(II)-tetrapyrrolylporphyrin (FeTPyP) on Ag(111), Auwärter et al. also observed a reduced symmetry of the molecules with two weak central protrusions. The rod-like shape [47] was interpreted as a deformation of the porphyrin macrocycle. As exploited in chapter 4.1, for FeTPP on Ag(111), a saddle-shape was assumed [47], possibly induced by steric repulsion between the peripheral H atoms of the tetrapyrrolic macrocycle and the H atoms of the rotated phenyl rings [92, 98]. By alternately rotating the peripheral phenyl substituents, one opposing pair of pyrrole rings is lifted while the other pair is lowered. Therefore, the two protrusions per molecule can be attributed topographically to two opposing pyrrole rings lifted upwards. Indeed, the two bright spots per molecule match the positions of the two opposing pyrrole rings of the tetrapyrrolic macrocycle quite well, as indicated by the superimposed and scaled space-filling models in figure 4.3.5 (b).

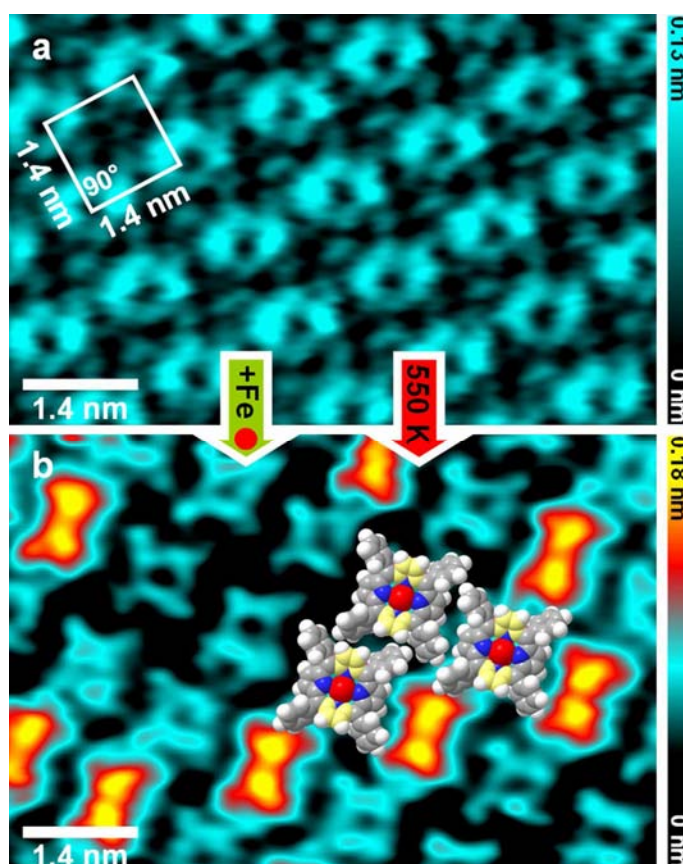


**Figure 4.3.5.** (a) Self-assembled 2HTPP layer on Ag(111) ( $I = 25\text{ pA}$ ;  $U = 0.37\text{ V}$ ). (b) The layer after reaction of pre-deposited Fe with 2HTPP to FeTPP. As indicated by the superimposed structure models, two opposing pyrrol rings per FeTPP molecule (marked yellow) are clearly visible ( $I = 55\text{ pA}$ ;  $U = -0.41\text{ V}$ ).

## CONCLUSION

2HTPP on Ag(111) reacts readily with co-adsorbed iron under formation of Fe(II)TPP. If iron is vapor-deposited onto a 2HTPP monolayer, the reaction proceeds rapidly at RT (chapter 4.3.1). If iron is deposited first, it forms clusters with a mean diameter of 3.5 nm, which decorate the steps on the Ag(111) surface. At RT these Fe clusters do not react with 2HTPP, but the reaction is fast at 550 K. Note that it was demonstrated with XPS, that FeTPP is also formed when iron is vapor-deposited on multilayers of 2HTPP molecules at RT [57].

### 4.3.3 Coordination of Post-deposited Cobalt Atoms by Tetraphenylporphyrin Monolayers

---

The direct metalation of 2HTPP with iron on a Ag (111) surface was demonstrated by STM (chapter 4.3.1 and 4.3.2 [56, 61]). Recent XPS measurements also evidence that cobalt reacts with co-adsorbed 2HTPP on Ag(111) [104]. With this background the goal was now to extend and strengthen these experimental findings and microscopically study the coordination of cobalt atoms with 2HTP [107]. The results were obtained using the same preparation procedure described in chapter 4.3.1.

Figure 4.3.6 (a) shows a high-resolution STM image of a monolayer of 2HTPP. As demonstrated in chapter 4.1, 4.3.1 and 4.3.2, the porphyrin macrocycle is oriented parallel to the surface and the molecules are ordered in a square arrangement with a lattice constant of  $\sim 1.4$  nm. The central porphyrin rings are clearly visible and the centers of the molecules appear as depressions. After the evaporation deposition of cobalt ( $\theta_{\text{Co}} = 0.012 \pm 0.003$ , i.e., one third of the stoichiometric amount required for the complete metalation of the 2HTPP monolayer), the STM image shown in figure 4.3.6 (b) was obtained. About 31% (statistics over larger scan areas) of the molecules now appear as longish protrusions that can be identified as CoTPP, whereas the remainder still exhibit the features associated with 2HTPP. Note that the longish protrusion can be traced back to a deformation of the tetrapyrrolic macrocycle in a saddle-shaped manner as reported above and in previous publications [57, 61] (chapter 4.1, 4.3.2). This again indicates a high efficiency, close to 100%, for the cobalt metalation at the given amount of evaporated cobalt, which is in perfect agreement with the microscopic findings for Fe [56]. These results together with earlier spectroscopic findings by Gottfried et al. [104] provide clear evidence for the cobalt metalation.

Figure 4.3.7 (a)-(d) shows STM micrographs recorded after successively dosing equal portions of  $0.010 \pm 0.003$  ML of Co (calibrated by a quartz microbalance) onto a monolayer of 2HTPP. It is obvious that the number of observed CoTPPs increases as the nominal amount of deposited cobalt is increased. It is noteworthy to mention that for

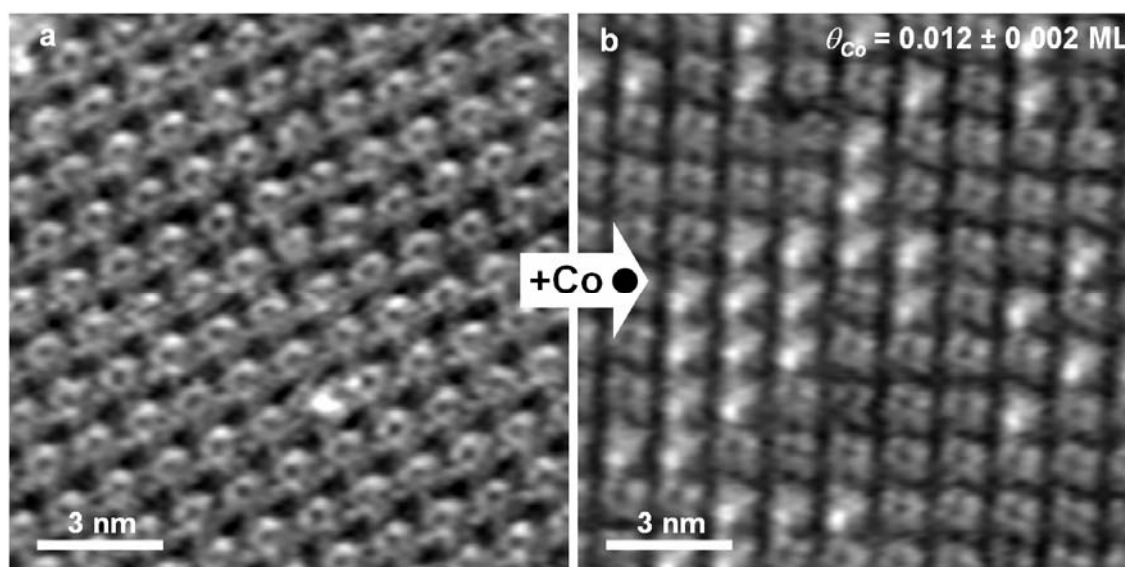


**Figure 4.3.6.** RT constant current STM images of a monolayer of (a) 2HTPP,  $U = -154$  mV,  $I = 29$  pA and (b) after the evaporation deposition of Co,  $\theta_{Co} = 0.012 \pm 0.002$ ,  $U = -213$  mV,  $I = 33$  pA..

the incremental metalation of 2HTPP with Co, the relative amount of formed CoTTPs is similar for different regions on the surface. The corresponding numbers (figure 4.3.7) of free base porphyrins which reacted with Co are: (a) 20 % / 0.010 ML, (b) 43% / 0.020 ML, (c) 57 % / 0.030 ML and (d) 92 % / 0.040. The equally prepared FeTPP layer exhibited a maximum metalation degree of 87% (chapter 4.3.1), whereas 92% of 2HTPP reacted with cobalt. In both metalation experiments it was observed that a certain number of molecules remains unmetalated [56].

An additional deposition of Co, roughly 0.08 ML more than a 2HTPP monolayer can consume (0.12 ML), did not lead to a reaction with the remaining 2HTPPs, but distinctly shaped two-dimensional islands evolved (figure 4.3.8 (a)). It was found that by dosing excess iron ( $\theta_{Fe(excess)} = 0.10$  ML) onto a FeTPP layer (see chapter 4.3.1) bright regions up to 12 nm in width were observed [56]. On top of these regions porphyrins were still resolved in the STM image. The area of the bright regions amounted to roughly 10% of the surface, which was in good agreement with the excess Fe coverage of 10% (= 0.10 ML). Thus it was concluded that these can be assigned to

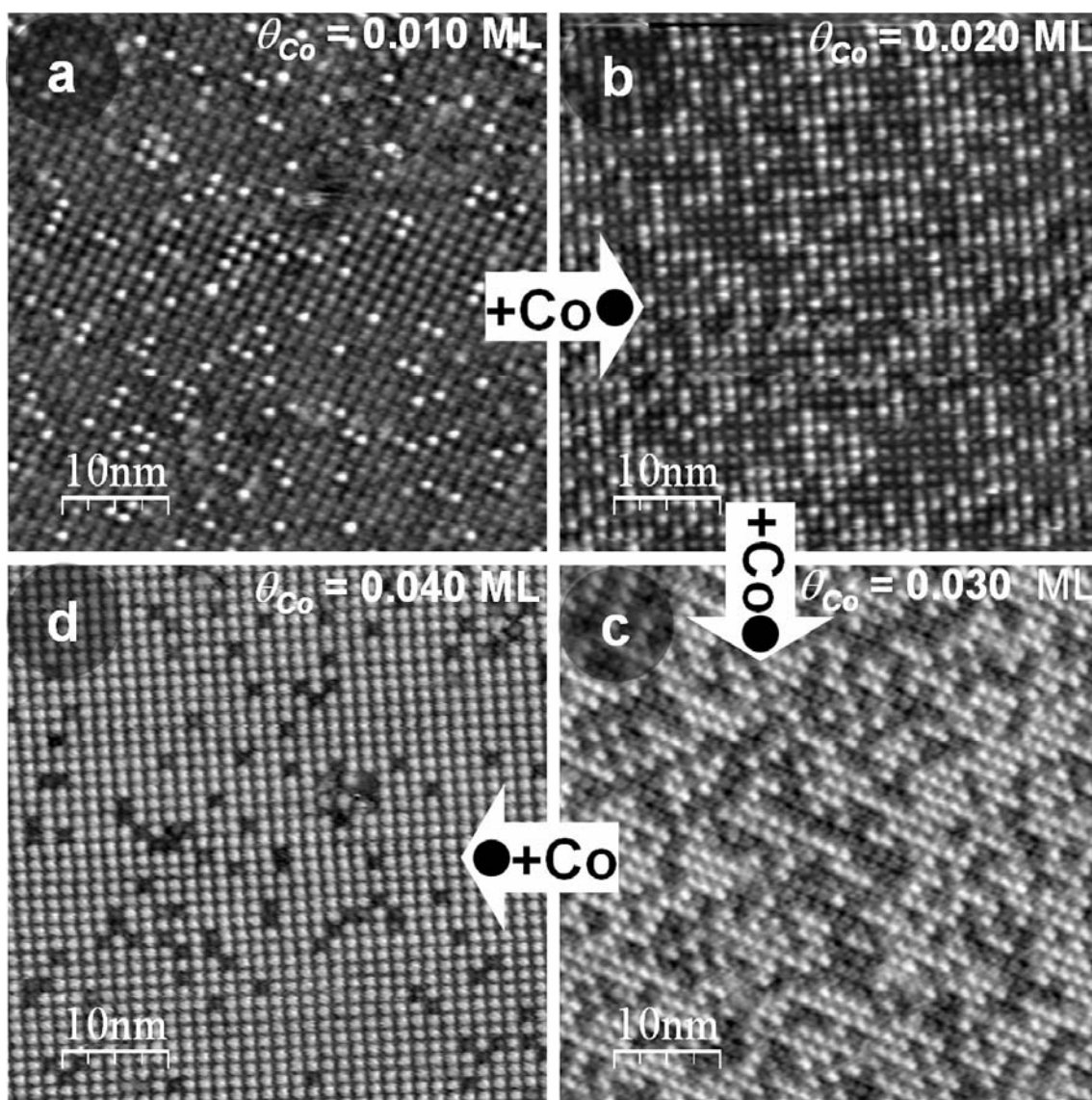


**Figure 4.3.7.** (a–d) Series of STM images after the successive evaporation deposition of equal amounts of Co. (a)  $U = -1.21\text{ V}$ ,  $I = 42\text{ pA}$ ; (b)  $U = -1.25\text{ V}$ ,  $I = 40\text{ pA}$ ; (c)  $U = -1.19\text{ V}$ ,  $I = 48\text{ pA}$ ; (d)  $U = -1.21\text{ V}$ ,  $I = 41\text{ pA}$ .

Fe islands below the FeTPP layer exhibiting monoatomic height on the Ag(111) substrate. As a similar behaviour was observed here for the system CoTPP + Co<sub>excess</sub>, the bright regions shown in the constant current image in figure 4.3.8 (a) are interpreted as Co islands of monoatomic height on Ag(111).

Proceeding the Co deposition to  $\theta_{Co} = 0.20\text{ ML}$ , the size of the formed islands did not further extent above  $\sim 6\text{ nm}$  in one dimension. Additionally, oval-shaped protrusions

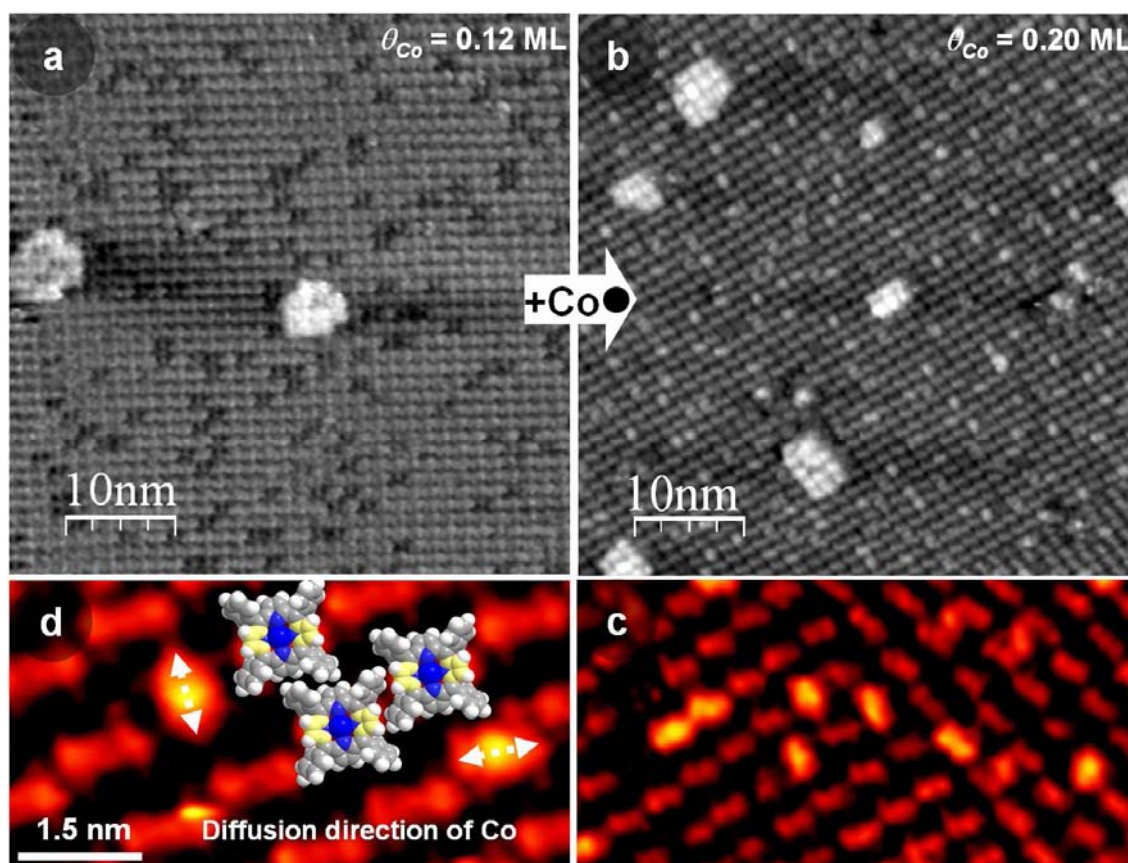


**Figure 4.3.8.** STM image after the evaporation deposition of (a)  $\theta_{Co} \sim 0.12$  ML ( $U = -1.23$  V,  $I = 41$  pA) and (b)  $\theta_{Co} \sim 0.3$  ML ( $U = -1.23$  V,  $I = 41$  pA). (c) High-resolution micrograph extracted from (b), highlighting explicitly oriented features. (d) Corresponding space-filling models were superimposed; the drawn in arrows point out the possible diffusion path below the porphyrins.

with molecular dimension were observed, exhibiting two explicit orientations (figure 4.3.8 (b-d)). In the images in figure 4.3.8 (c) and (d) the reduced symmetry of CoTPP on Ag(111), due to two opposing pyrrol rings which are lifted (chapter 4.1) is clearly visible. Correspondingly scaled space filling models are incorporated in figure 4.3.8 (d). It is striking, that the mentioned protrusions are strictly oriented in the two directions of diametrical opposing pyrrol rings (indicated by white arrows in figure 4.3.8 (d)). Note that these features were also found in the analogue experiment with iron, however due to the lower quality of the micrographs (figure 4.3.3 (b)) rather elevated dots with molecular dimensions were observed. Thus it is highly probable that the formation of

these features underlies the same mechanism both relying on the deposition of excess material, i.e., iron and cobalt. In chapter 4.3.1 it was proposed that the metalation process is at least partially surface mediated [56]. It was discussed [56] (chapter 4.3.1) that the impingement of the Fe atoms onto the surface is a statistical process and not directed towards the centers of the remaining 2HTPP molecules. Further, even if an attractive potential is assumed, which guides the impinging atoms towards the complexation sites, it is very likely that a significant fraction of the Fe atoms first hit other regions and undergo some diffusion (probably on the Ag(111) surface), before they complex with a 2HTPP. Consequently, a diffusion of Co atoms on the Ag(111) surface can also be assumed. Regarding the four phenyl rings per CoTPP, which act also as spacers between the porphyrin macrocycle and the Ag(111) surface (distance  $\sim 0.3$  nm) and obviously as diffusion barriers, two opposing pyrrol rings determine the direction of the available free diffusion path (figure 4.3.8 (d)). Therefore, a possible interpretation is that the elevated dots can be attributed to CoTPP with several cobalt atoms confined below. This occurs preferentially in direction of diametrical opposing pyrrol rings, which present the potential diffusion path. It was demonstrated by Gross et al. [108] that a six-leg single hexa-*t*-butyl-hexaphenylbenzene molecule is able to carry up six copper adatoms on Cu(111), induced by manipulation with the STM tip. This happens such that copper adatoms are firstly trapped between adjacent phenyl rings. The resulting conformational change enables that the Cu adatoms can then be bound under the central moiety. Thus, indeed, the confinement of several cobalt atoms by CoTPP can be assumed.

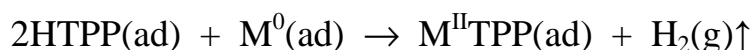
## **CONCLUSION**

It was demonstrated that free base porphyrin monolayers consume stoichiometric amounts of vapor deposited cobalt atoms and react to CoTPP. The formation of two-dimensional islands below the porphyrin layer upon excessively deposited amounts of cobalt, indicate diffusion below the porphyrin layer (also observed in the respective experiments with iron (chapter 4.3.1)). However, it can not be addressed why above a certain dosage of cobalt ( $\theta_{Co} > 0.12$  ML) oval-shaped protrusions appear, whereas the pronounced two-dimensional islands do not grow any further.

## 4.3.4 Discussion of the Metalation Reaction

---

The direct metalation of 2HTPP with iron and cobalt was demonstrated successfully with STM (chapter 4.3.1 - 4.3.3). In that course a theoretical treatment of the metalation process was conducted by Shubina et al. [42]. Note that the microscopic evidence for the complexation of 2HTPP with cobalt (chapter 4.3.3.) contributed to the respective article. The performed density functional theory (DFT) calculations on the metalation of porphyrin molecules with Fe atoms in the gas phase have shown that the reaction proceeds without activation barriers, whereas for other metals, such as Co, Ni, Cu, and Zn, partly substantial barriers were predicted; the respective energy profile for the Co atom insertion into 2H-porphyrin is shown in figure 4.3.9. According to these calculations, the neutral metal atom is first coordinated by the four nitrogen atoms of the intact porphyrin [42]. Subsequently, the two pyrrolic hydrogen atoms migrate to the metal center, where they recombine and desorb as dihydrogen (H<sub>2</sub>). In the course of these H transfer steps, the metal atom is oxidized to the di-cation. The reaction of 2HTPP with different metals, e.g., M = Fe, Co, Zn, can be expressed as:



These gas-phase calculations should be representative for the situation in the multilayer, because it seems reasonable to assume that the interaction of the metal with the neighboring molecules in the multilayer is relatively weak compared to the interaction with the central cavity of the porphyrin to which the metal atom/ion is chemically bound. Indeed the metalation of multilayers was recently demonstrated by XPS [57].

In the case of the metalation of 2HTPP monolayers with pre-adsorbed Fe atoms, however, the situation is different, since the reaction is extremely slow at RT, but rapid at 550 K as demonstrated in chapter 4.3.2 [57]. This indicates the presence of a substantial activation barrier (between ~75 and ~140 kJ/mol), in disagreement with the barrierless reaction path predicted by the gas phase DFT calculations [42]. If the Fe

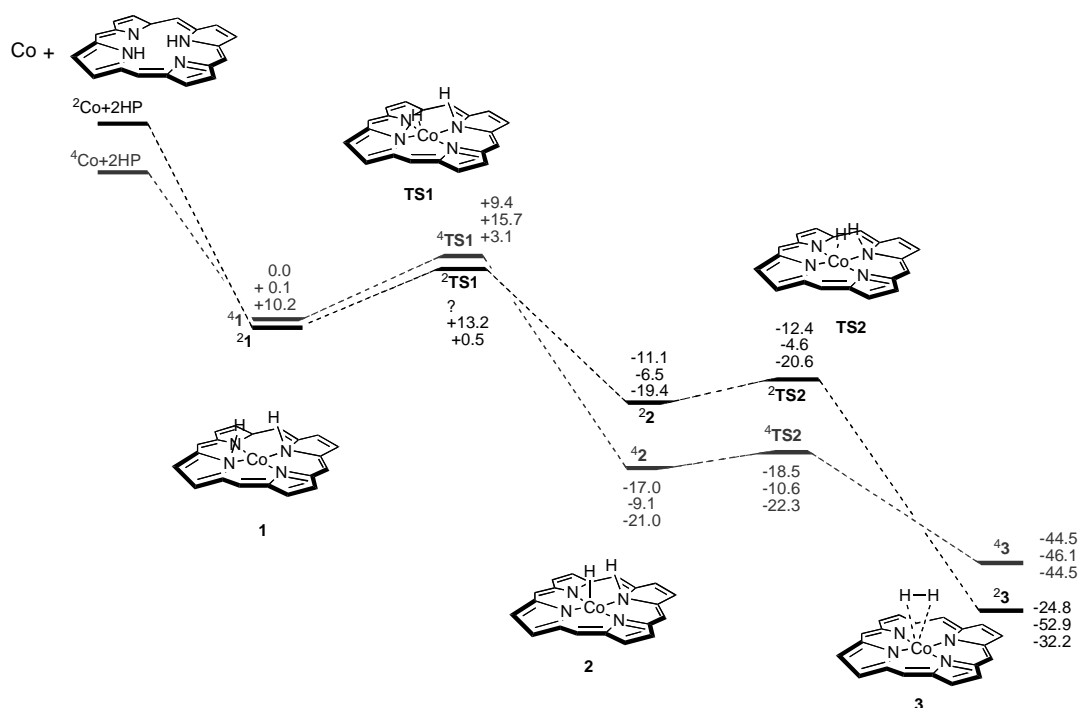


**Figure 4.3.9.** Schematic energy profile for Co atom insertion into 2H-porphyrin, reprinted from the publication of Shubina et al. [42].

atoms are deposited on a 2HTPP monolayer, the reaction is rapid at RT, suggesting that the activation barrier observed in the case of pre-deposited iron is related to the formation of Fe clusters at the step edges. At the steps and in the clusters, the Fe atoms are relatively strongly bound compared to sites at the terraces. In this situation, the rate-limiting factor for the metalation is probably the two-dimensional (2D) phase equilibrium between the Fe clusters and Fe atoms diffusing across the surface, because only the latter can directly react with the porphyrin molecules. The 2D vapor pressure of iron may be too low at RT to observe a reaction on the timescale of several days, but increases exponentially with temperature, resulting in a rapid reaction at 550 K.

The rapid RT reaction in the case of Fe *post*-adsorption indicates that the metalation reaction is fast enough to successfully compete with the diffusion of the Fe atoms to the steps and the formation of island there. In this context, it is important to note that the diffusion may be hindered by the porphyrin layer. In addition, the step sites are already occupied by 2HTPP, which means that the total energy gain resulting from the decoration of the steps with iron atoms or clusters is reduced by the binding energy of

the molecules to the step sites. Both effects facilitate the metalation reaction and disfavor island formation at the steps.

Another factor that may influence the reaction rate and may be responsible for the difference in reactivity for pre- and post-adsorption of Fe atoms is the metalation step itself. Although barrierless in the gas phase, on the surface this step includes cleavage of the bond between the Fe atom and the surface, which makes the occurrence of an activation barrier likely. In the case of Fe post-adsorption, the additional kinetic energy of the Fe atoms (gained by release of the adsorption energy) may help to surmount this activation barrier. This is an alternative explanation for the observation that the reaction proceeds rapidly already at RT. On the other hand, it should be mentioned that the electronic interaction between the surface and the iron atom is not completely suppressed when the latter is coordinated by the porphyrin [73, 109]. Although it has not been possible to quantify the strength of this residual interaction yet, it is likely that it reduces, if attractive, the activation barrier for the coordination of the adsorbed Fe atom.

Similar to the presented results in the work at hand, the reaction of pre-deposited Zn atoms with 2HTPP on Ag(111) was found to be very slow at RT, but rapid at 550 K [110]. However, metalation with Zn also requires elevated temperatures when the metal is post-deposited on the porphyrin monolayer. This is in agreement with the calculated gas phase mechanism, which predicts an activation barrier of  $137 \text{ kJmol}^{-1}$  for the transfer of the first pyrrolic hydrogen atom to the Zn atom; this value is in good agreement with the experimentally determined overall activation energy ( $130 \text{ kJmol}^{-1}$ ) [42]. Thus, the rate of the metalation with Zn may actually be controlled by an intramolecular reaction step, whereas the reaction of pre-deposited Fe with 2HTPP is controlled by a step in which the surface is involved.



## 4.4 Different Aspects of 2H-Tetrakis-ditertbutylphenylporphyrin on Ag(111)

---

Concepts already established (chapter 4.2 and 4.3.1 - 4.3.3), e.g., in-situ metalation of free base porphyrins, were expanded to the free base porphyrin 2H-5,10,15,20-tetrakis-(3,5-di-tert-butyl)-phenylporphyrin (2HTTBPP). The monolayer coverage on Ag(111) was achieved by multilayer desorption (chapter 4.4.1). A herringbone structure was observed and conclusions on the internal conformation were drawn (chapter 4.4.2). The voltage-dependent constant current images visualize different sub-molecular units (chapter 4.4.3). In addition, the principle of the well-established method to generate clean metalloporphyrins on Ag (111) was verified by dosing iron atoms onto a 2HTTBPP layer, resulting in FeTTBPP.

### **INTRODUCTION**

Four ordered monolayer phases of CoTTBPP were found on Ag(111), using two different preparation procedures, as discussed in chapter 4.2 [44]. The orientation and intra-molecular conformation of the individual molecules within these phases was identified, applying two types of intra-molecular deformations; the twist angle  $\Theta$  of the TBP groups and the tilt angle  $\Phi$  out of the tetrapyrrol plane. These deformation types were also proposed by Sekiguchi et al. for 2HTTBPP on Cu(111) [95].

One peculiar finding was the CoTTBPP *herringbone* phase (chapter 4.2), which was solely monitored after heating the sample to 550 K; its formation is interpreted as an activated process. This phase was proven to be very stable due to its interwoven character. Similar structures were observed on several surfaces, e.g., Terui et al. show an STM micrograph of 2HTTBPP on Cu(111) [99], Grill et al. report a structure of CuTTBPP on Cu(111) after the deposition of the porphyrin using a pulse injection technique and subsequent annealing [90]. Regarding the pronounced stability of these specific arrangements, they are candidates for a template for functional devices based

on thin organic layers. After the rigid CoTTBPP *herringbone* structure was observed, in particular by desorption of multilayers at 550K, the goal was now also to study the self-assembly of 2HTTBPP on Ag(111) at RT, applying the same preparation procedure.

In addition, it was aimed to microscopically study the coordination of iron atoms with 2HTTBPP. The direct metalation of free base porphyrins with iron or cobalt on Ag(111) was demonstrated successfully with STM and XPS [47, 56, 57, 61, 104]. However, presently results are limited to the metalation of: (1) 2HTPP with iron and cobalt (chapter 4.3) [47, 56, 57, 104], (2) 2HTPyP with iron [61]. The investigations should now be extended, i.e., the coordination reaction of 2HTTBPP with iron is explored.

## 4.4.1 Monolayer Preparation

---

The preparation of a monolayer of 2HTTBPP on Ag(111) was achieved by desorption of multilayers by heating the sample (see chapter 3.6) [73]. For this purpose, the 2HTTBPP multilayer desorption temperature was verified by TPD measurements (figure 4.4.1), whereat two desorption peaks are identified. The peak at 485 K is attributed to desorption of the multilayer molecules, the one at 630 K to the monolayer molecules. Note that the intensity of the multilayer peak is small as compared to the one of the monolayer signal, because only a small amount of excess multilayer molecules was deposited onto the sample. Nevertheless, it could be deduced from the spectrum that an annealing step up to  $540 \pm 10$  K, the temperature range between the two peaks, should be a good choice for desorbing excess multilayer molecules.

Figure 4.4.2 (a) shows a constant current image of a multilayer of 2HTTBPP after vapor-deposition at RT. The multilayer can be identified by the formation of drop-shaped peninsulas along the axis, which is the scan direction of the tip. Therefore, these features can be ascribed to relatively mobile molecules in the multilayer. It was reported by Comanici et al. [58] that the shape of the observed features can be modified by a change of the scanning direction by 90 degrees.

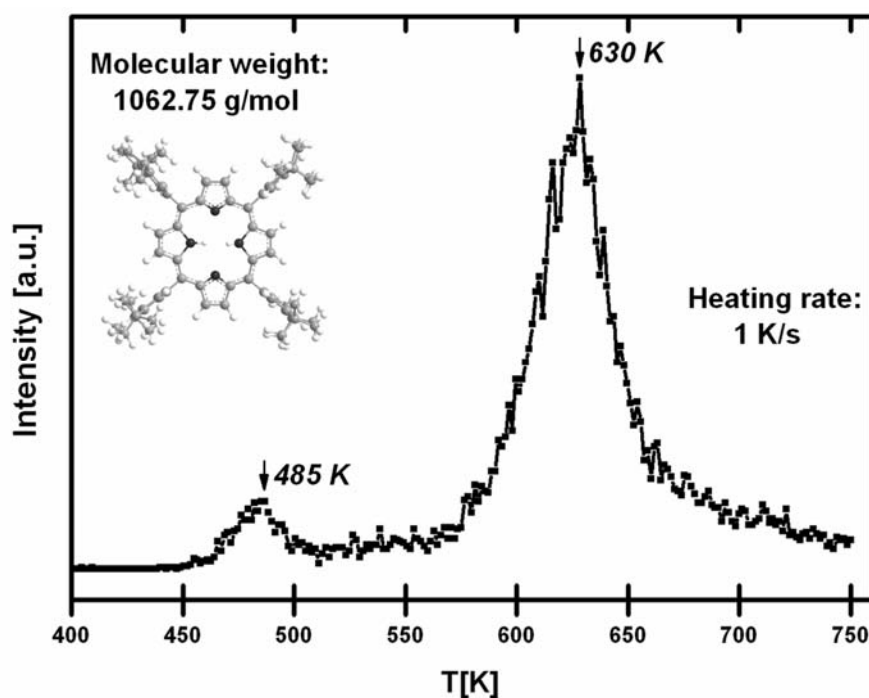


**Figure 4.4.1.** TPD spectrum of 2HTTBPP on Ag(111). The applied heating rate was 1K/s

By doing so, the layer now exhibits horizontal peninsulas (figure 4.4.2 (b)). The slightly distorted shape in vertical direction could be due to the displacement of the molecules induced by the scanning procedure of the image taken immediately before. For the peninsulas, an oblique (but almost hexagonal) arrangement (indicated by the arrows in figure 4.4.2 (b)) with lattice constants (not drawn in the image) of  $a = 2.09 \pm 0.10$  nm,  $b = 1.71 \pm 0.10$  nm and an enclosed angle  $\alpha = 60^\circ \pm 3^\circ$  was observed. It should be noted that the layer could only be imaged by applying a large bias voltage of +2.08 V and a low tunnelling current of 33 pA, i.e., a high tunnelling resistance, which is an indication for the increased resistance in the multilayer regime. After annealing the sample to 550 K for 45 s, the large-scale image ((80 x 80) nm<sup>2</sup>) in figure 4.4.2 (c) was recorded. A long-range ordered and stable arrangement with a quasi-hexagonal symmetry was observed. This is indicated by the Fourier peaks inserted in figure 4.4.2 (d), evidencing the periodicity of the molecular layer. Within the layer, the 2HTTBPP molecules are arranged in an oblique structure with lattice vectors of  $a = 2.09 \pm 0.10$  nm and  $b = 1.67 \pm 0.10$  nm and an enclosed angle  $\alpha = 60^\circ \pm 3^\circ$ . The resemblance with the

multilayer structure indicates that the molecular assembly is mainly governed by lateral interactions.

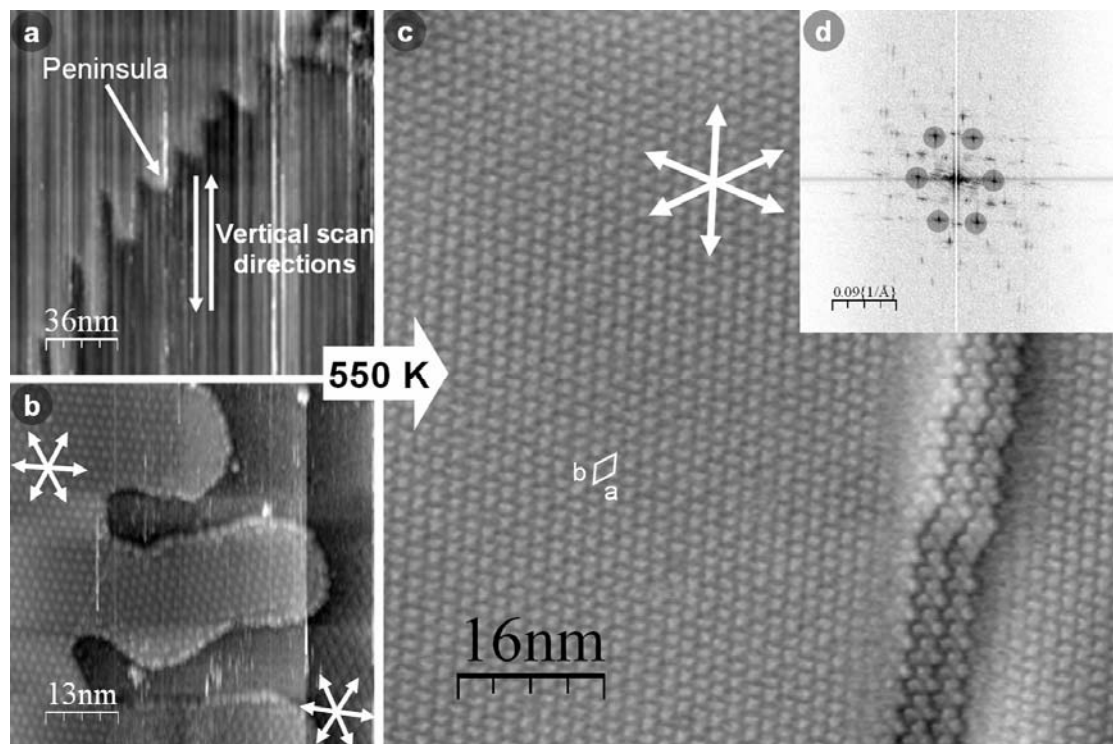


**Figure 4.4.2.** (a) Constant current image of 2HTTBPP in the multilayer regime. Tip-induced peninsulas in vertical direction were observed ( $U = +2.08$  V;  $I = 58$  pA). (b) Micrograph recorded with the tip scanning in horizontal direction, inducing horizontal oriented peninsulas. On top of these, the molecules are arranged oblique ( $U = +2.08$  V;  $I = 33$  pA). (c) Monolayer of 2HTTBPP, which was acquired after heating the multilayer 45 s at 550 K. An oblique structure was observed ( $U = +1.65$  V;  $I = 20$  pA). (d) Sharp 2D-Fourier peaks evidence the periodicity of the structure.

## 4.4.2 Arrangement of 2HTTBPP

---

Figure 4.4.3 (a) shows a constant current image, in which the arrangement and individual appearance of the 2HTTBPP molecules closely resembles that observed for the CoTTBPP *herringbone* phase (figure 4.4.3 (b)) (see drawn in unit cells) [44]. The unit cell of the 2HTTBPP layer is rectangular ( $A = 2.12 \pm 0.10$  nm,  $B = 2.90 \pm 0.10$  nm) and contains two molecules; the central molecule has a different azimuthal orientation (molecules are depicted by rectangles due to their apparent shape). The size appears similar with that of the CoTTBPP *herringbone* phase, shown in figure 4.4.3 (b). However, it is obvious that in the micrographs of 2HTTBPP every second row within the arrangement appears elevated (depicted with “1” in figure 4.4.3 (a)), which is not seen for CoTTBPP. This was found more or less pronounced in several STM images. Probably, different adsorption sites of the molecules in adjacent rows on Ag(111) are responsible for the pronounced height modulation [111].

Figure 4.4.3 (c) and (d) show molecularly resolved and enhanced micrographs of 2HTTBPP (rows are indicated in (c)) and CoTTBPP. In both images, four bright lobes, which are due to the upper tert-butyl groups, constitute the observable intra-molecular features [44]. The rectangular arrangement of the latter and the measured perimeter require a deformation of the molecules to obtain a good fit between space-filling model and the STM images. As porphyrins exhibit a certain flexibility [74, 112], they can be deformed both by the twist angle  $\Theta$ , and the tilt angle  $\Phi$ , as discussed in chapter 4.2 in detail.

The micrograph in figure 4.4.4 (a) emphasizes the 2HTTBPP *herringbone* phase with the corresponding superimposed space filling models. Note that the image was processed by correlation averaging, i.e., repetitive structures in one image can be added such that an average image, exhibiting a low signal to noise ratio can be obtained [113]. Individual molecules were extracted from neighbouring rows and are shown in figure 4.4.4 ((b) and (d)). Interestingly, the shape of 2HTTBPP slightly differs in neighbouring rows, i.e., different aspect ratio and perimeter of the lobes.

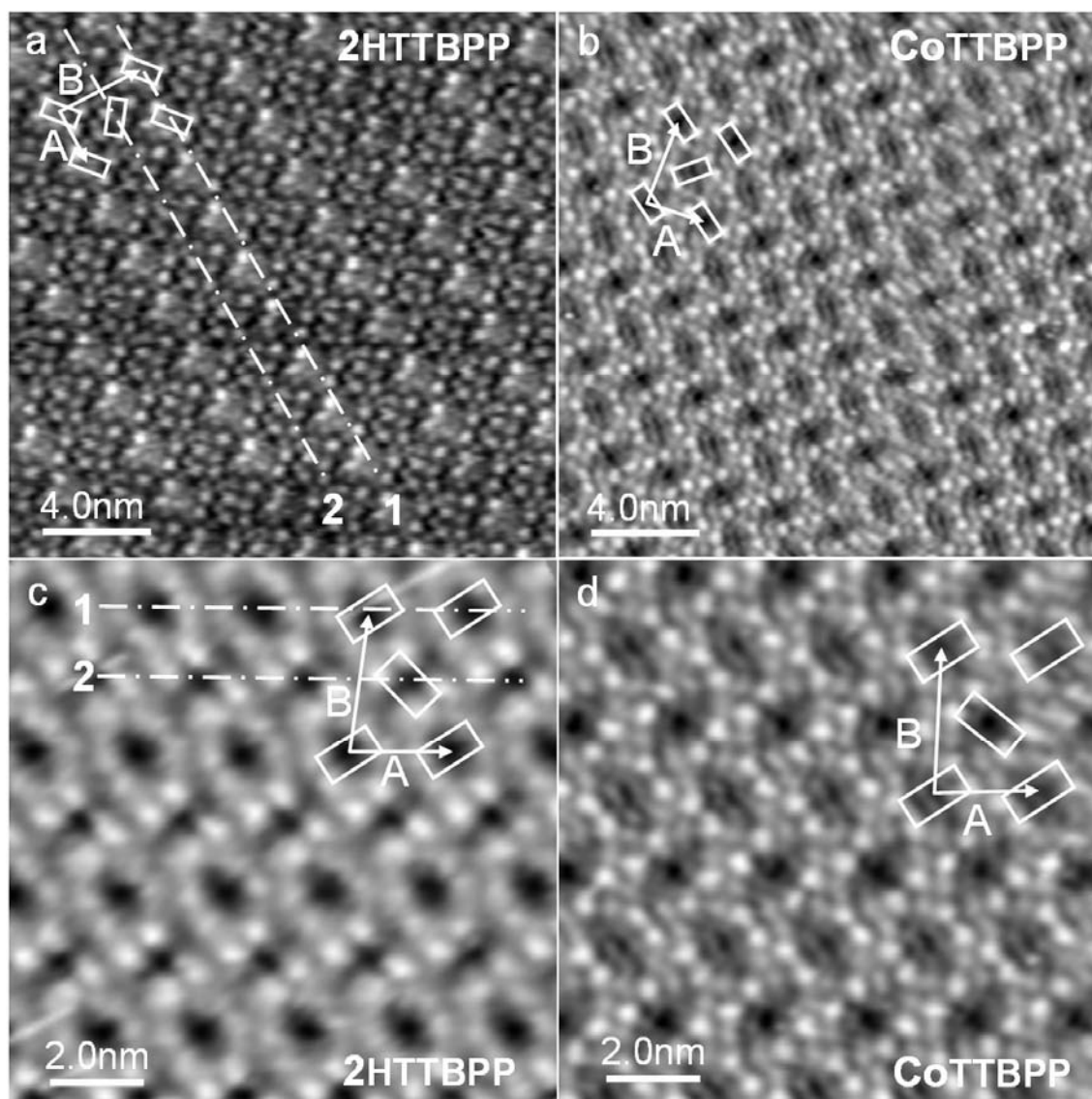


**Figure 4.4.3.** (a) Constant current image of a monolayer of 2HTTBPP ( $U = -967$  mV,  $I = 46$  pA). The unit cell consists of two molecules; the central molecule has a different azimuthal orientation, as indicated by the drawn in rectangles. The dash-dotted lines depict molecular rows 1 and 2, differing by the azimuthal orientation and apparent height. (b) The unit cell consists of two molecules; the central molecule has a different azimuthal orientation, as shown in (a). (c) and (d) Enlarged STM of a monolayer of 2HTTBPP and CoTTBPP.

The dimensions  $a$  and  $b$  are depicted in figure 4.4.4 (c) and (e)). Consequently, the modelling procedure required the generation of two differently deformed molecules.

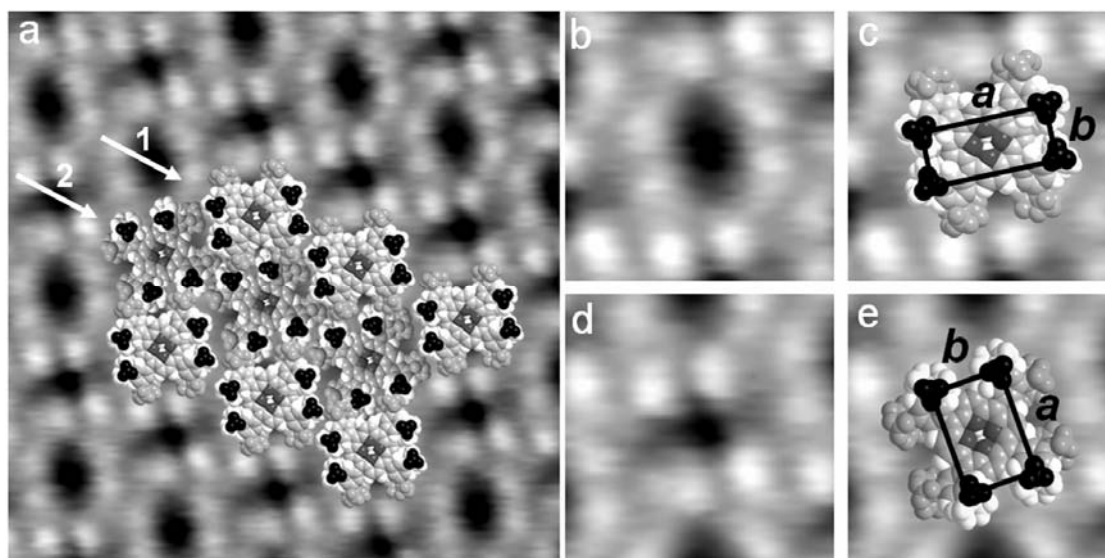


**Figure 4.4.4.** (a) Constant current image showing a monolayer of 2HTTBPP molecules superimposed with corresponding hard-sphere models (+1.12 V and 22 pA). The size of the STM images (b) – (e) is  $(3 \times 3) \text{ nm}^2$ . (b) 2HTTBPP extracted from “row 1”; the four protrusions are attributed to the upper tert-butyl groups. (c) Figure 4.4.5 (b) is superimposed with the corresponding hard-sphere models. (d) and (e) show a single 2HTTBPP molecule extracted from “row 2”.

In the following, conclusions from the respective geometry of the four spots per 2HTTBPP were drawn on the deformation ( $\Theta$ ,  $\Phi$ ). The principle of the modelling process was described in detail in chapter 4.2. The rectangular shape of molecules located in “row 1”, exhibits a perimeter of  $\sim 3.85 \text{ nm}$  ( $a = 1.29 \pm 0.04 \text{ nm}$ ,  $b = 0.65 \pm 0.04 \text{ nm}$ ), indicating a small value for the tilt angle  $\Phi$  (figure 4.4.4 (c)). The high aspect ratio of  $a/b = 2.0$  indicates a low value of  $\Theta$ . The appearance of the individual molecule can be correlated with the space filling model, by twisting the angle of the phenyl rings to  $\Theta = 20^\circ$  and tilting the angle to  $\Phi = 10^\circ$ . Figure 4.4.4 (e) shows the perimeter of the four bright lobes of 2HTTBPP, located in “row 2”, which is  $\sim 3.65 \text{ nm}$  ( $a = 1.15 \pm 0.04 \text{ nm}$ ,  $b = 0.67 \pm 0.04 \text{ nm}$ ), indicating a slightly larger value for the tilt angle  $\Phi$  of  $15^\circ$ . From the aspect ratio of  $a/b = 1.7$ , a value of  $55^\circ$  can be deduced for  $\Theta$ .

Different deformations of 2HTTBPP are reasonable, as this goes along with different absolute heights, which indeed explains the discussed finding. The space-

filling models shown in figure 4.4.5 highlight the proposed deformation of the porphyrins (the respective angles are incorporated). In particular, the side views (figure 4.4.5 (c) and (d)) illustrate that 2HTTBPP located in “row 2” (smaller  $a/b$  and  $2(a+b)$ ) exhibit an increased height (indicated by  $\Delta h$ ). Thus, it can be assumed that the observed height modulations are probably accompanied by different internal conformations of 2HTTBPP in neighbouring rows. Note that in the *herringbone* structure of CoTTBPP, the molecules appear with four spots strictly exhibiting both the same geometry and apparent height. In a previous publication it was shown by density functional methods that for MTPP and MTTBPP ( $M = \text{Co}, \text{Zn}$ ) the chemical nature of the central entity makes a difference in the deformation energies, especially at larger deviations of the twist angle  $\Theta$  out of an energetic minimum ( $55^\circ < \Theta < 90^\circ$ ) [74]. Thus, taking into account the differences of the observed 2HTTBPP and the CoTTBPP layer, the central metal obviously plays a role regarding the respective deformation.

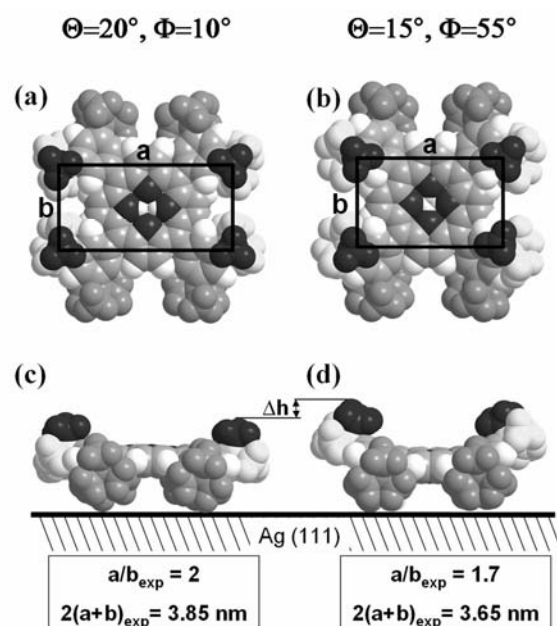


**Figure 4.4.5.** (a) – (d) Space filling models of 2HTTBPP on Ag(111): (a) Top view illustrating the proposed conformation of 2HTTBPP in “row 1”, (b) Conformation of molecules located in “row 2”; (c) Side view on (a), (d) side view on (b); a height difference of the space-filling models with different intra-molecular conformations is clearly visible.

However, the latter interpretation given with respect to the STM images shown so far in this chapter is unsustainable, as also an inverse height modulation was found (figure 4.4.6 (a) and (b)), i.e., 2HTTBPP (larger values of  $a/b$  and  $2(a+b)$ ) formerly observable within the apparently lower molecular rows “1” (depicted with dotted rectangles in figure 4.4.6 (a)), are now observable in the apparently higher rows in figure 4.4.6 (b). Thus, the pure topographic approach (figure 4.4.5) appears to be inconsistent. It is highly probable that the finding can be ascribed to electronic effects, e.g., to a molecule or molecular fragment modifying the STM tip. It was reported that with a clean tip, both CO and oxygen atoms are seen as dark depressions in the STM image. Measuring with a CO-functionalized tip inverts the contrast of the adsorbed CO, the oxygen atoms remain dark [114]. This was traced back to an interference between different tunneling channels [115]. Thus, taking into account a modified tip, locally occurring constructive and/or destructive tunnelling contributions between different tunnelling channels, could explain the observed inverse height modulation; finally, this remains speculative.

## **CONCLUSION**

A stable long-range ordered 2HTTBPP layer with a herringbone-like structure was prepared on Ag(111) by means of multilayer desorption. Adjacent molecular rows appeared with alternating apparent height. In contrast, in the similar CoTTBPP herringbone arrangement all molecules exhibit the same apparent height (chapter 4.2). The finding was interpreted to two types of intra-molecular deformations, which go along with different absolute heights of 2HTTBPP. However, even though the presence of different internal conformations in the layer could explain the observed height modulation of neighbouring molecular rows in the STM images well, the interpretations remain speculative.

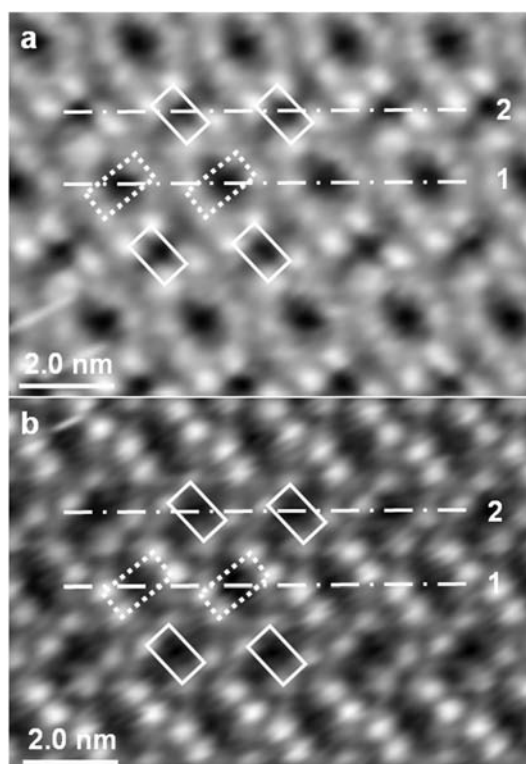


**Figure 4.4.6.** (a) and (b) Inverse height modulation of the depicted 2HTTBPP rows (label 1 and 2). The respective rows contain molecules, which exhibit a specific type of deformation (indicated by rectangles, which are drawn with full or dotted line). Remarkably, the molecules in the apparently elevated rows “2” in (a) appear lowered in (b), even if the corresponding type of deformation of 2HTTBPP is assumed. (a) +1.12 V and 22 pA; (b) + 1.20 V and 23 pA

### 4.4.3 Voltage-Dependent Appearance

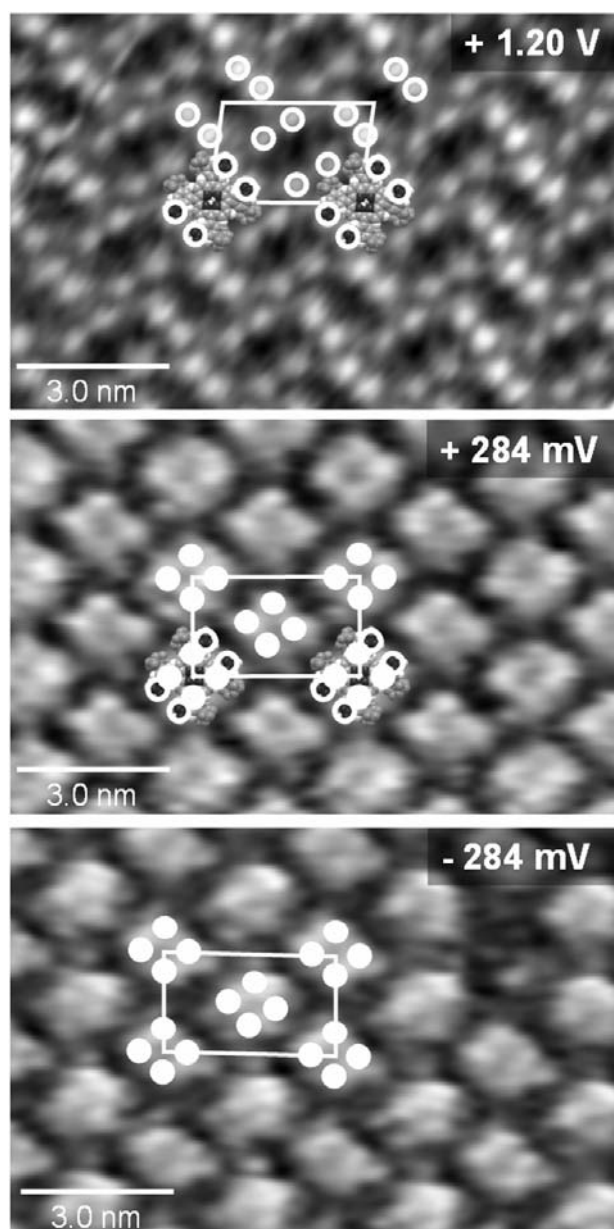
---

Figure 4.4.7 (a) shows a constant current image of the 2HTTBPP herringbone phase acquired at +1.20 V. The individual molecules appear as four spots due to the upper tert-butyl groups (depicted with circles). Note that the image is slightly distorted by thermal drift. The micrograph shown in figure 4.4.7 (b) was recorded at a bias voltage of + 285 mV. Obviously, the individual molecular appearance is different compared to that observed at + 1.20 V. The molecules appear equal also at – 285 mV, which is

evident from the STM images in figure 4.4.7 (b) and (c). The rectangular unit cell is drawn in each STM image, consisting of four corner molecules and a central one (see chapter 4.4.2). At a bias voltage of  $\pm 285$  mV 2HTTBPP internally appear with four spots per molecule in the images (depicted with filled circles in figure 4.4.7 (b) and (c)). However, the molecules exhibit a smaller dimension compared to the four lobes (depicted with circles) in figure 4.4.7 (a). The perimeter of the four bright spots is roughly 2.65 nm ( $a = 0.75 \pm 0.05$  nm,  $b = 0.58 \pm 0.05$  nm), which is significantly smaller than the perimeter of the spots measured in the images acquired at +1.20 V. In the latter case, the four lobes are attributed to the tert-butyl-groups, taking into account the proposed deformation of the porphyrin. Concerning the measured perimeter per molecule inside the micrographs recorded at  $\pm 285$  mV, a correlation between the spots and the tert-butyl-groups can be excluded, as the required out of the plane bending by  $\Phi$  (reduction of perimeter of the upper tert-butyl groups) is beyond the limit of flexibility. Furthermore, reliable deformation angles are already known (chapter 4.4.2) [74]. Taking into account the established deformation angles (chapter 4.4.2), the spots per molecule in the constant current images in figure 4.4.7 (b) and (c) are tentatively correlated with the positions of the phenyl rings.

## **CONCLUSION**

In the STM micrographs, the constant current contour of individual 2HTTBPP changed upon variation of the applied bias voltage. This can be interpreted in terms of molecule-mediated electron transport through respective orbital channels. Probably, at a low bias voltage, i.e.,  $\pm 285$  mV, molecular orbitals at the phenyl rings are addressed. This indicates that HOMO and LUMO contribute very similar to the molecular appearance in STM at the given tunnelling conditions. At a large positive bias voltage of + 1.20 V, orbital mediated tunneling mainly occurs through channels located at the periphery of the molecule.



**Figure 4.4.7.** STM images of 2HTTBPP acquired at different bias voltages. (a). Constant current image recorded at + 1.20 V and 23 pA. Four corner molecules and a central one participate to the unit cell, which is drawn in the images. (b)–(c) Micrographs acquired at  $\pm 284$  mV ( $I = 23$  pA).

## 4.4.4 Direct Metalation of 2HTTBPP with Co-adsorbed Iron

---

Figure 4.4.8 (a) shows a homogenous monolayer of pure 2HTTBPP. A monolayer of 2HTTBPP has a coverage of  $\theta_{Fe} = 0.024$  ML relative to the Ag(111) surface. Thus an amount of  $0.020 \pm 0.005$  ML of Fe, which was now dosed onto the 2HTTBPP layer, equals the theoretical amount for the metalation of 83 % of the molecules inside the monolayer. In fact, the medium-resolution image (figure 4.4.8 (b)) shows that 60% of the molecules appear with an increased apparent height afterwards. This bimodal appearance is typical for mixed layers of metallo- (e.g., Fe, Co) and free base TPPs and TPyPs on Ag(111) at negative bias voltages [42, 56, 60]. The increased apparent height can be ascribed to both orbital mediated tunneling through the Fe(II)  $3d^6$ -orbital system and a changed topography as it has already been reported for other metalloporphyrins [70, 105, 106]. Thus, after metalation with iron, a changed apparent height of the 2HTTBPP within the STM images is expected. The protrusions in figure 4.4.8 (b) can therefore be interpreted as Fe(II)TTBPP molecules formed by coordination of Fe atoms with 2HTTBPPs. The molecules with smaller apparent height are the remaining 2HTTBPPs. The amount of formed FeTTBPP correlates with the amount of deposited iron within the limits of accuracy.

### CONCLUSION

The direct metalation of 2HTPP with iron and cobalt was demonstrated successful (chapter 4.3). One important question was the role of the ligands and the resulting different conformation of the specific porphyrin (compared with 2HTPP) on the metalation reaction. The STM images evidence that the direct metalation of 2HTTBPP with iron on Ag(111) works as well, indicating along with the results for Pc (chapter 4.5) that the metalation is a general behaviour.

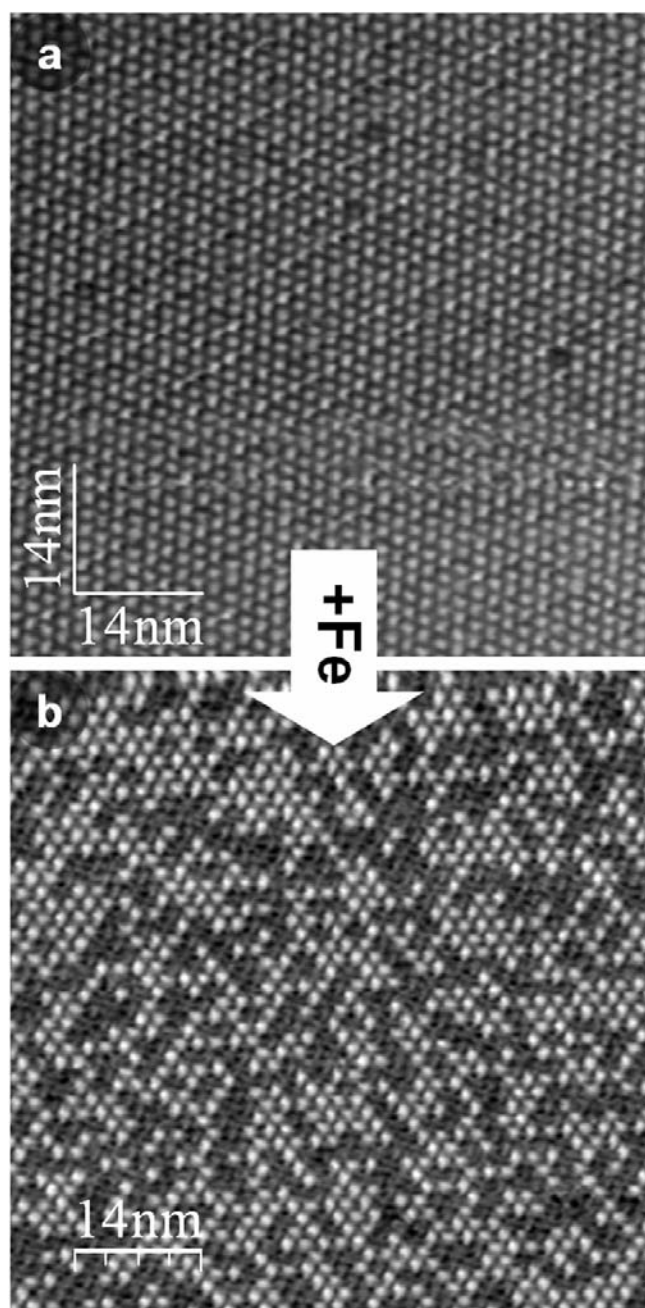


**Figure 4.4.8.** (a) STM image of a monolayer of 2HTTBPP on Ag(111) ( $U = +1.87$  V,  $I = 18$  pA). (b) Mixed monolayer of 2H- and Fe-TTBPP after deposition of 0.02 ML of Fe ( $U = -401$  mV,  $I = 22$  pA). The layer now exhibits a bimodal appearance, showing 60% of protrusions, which can be attributed to FeTTBPP.

## 4.5 Direct Metalation of a Phthalocyanine Monolayer on Ag(111) with co-adsorbed Iron Atoms

---

After the direct metalation of free base porphyrins (2HTPP, 2HTTBPP) with different metal atoms was demonstrated successfully (chapter 4.3, 4.4), analogue experiments were performed with an ordered monolayer of free base phthalocyanine (2HPc) on a silver (111) surface. 2HPc reacts with the stoichiometric amount of co-adsorbed Fe atoms to form iron(II)-phthalocyanine (Fe(II)Pc). The formation of Fe(II)Pc was confirmed by comparison with the directly deposited complex using STM. No side reactions such as the coordination of Fe atoms on the peripheral nitrogen atoms of the phthalocyanine molecules were observed.

### **INTRODUCTION**

It has been demonstrated that adsorbed metalloporphyrins can be synthesized directly on a surface by metalation of the adsorbed porphyrins with vapor-deposited metal atoms, for example Fe, Co, and Zn [42, 47, 56, 76, 104, 116]. Moreover it has been demonstrated (chapter 4.3.2) that the order of deposition is not relevant; the porphyrins also react with metal atoms that have been deposited prior to the adsorption of the porphyrin. This is evident from the reaction between 2HTPP and Zn shown by XPS [62] and 2HTPP and Fe shown by STM [57]. Note that similar reactions have been used for the synthesis of surface-confined metal-organic networks [117-120] and, recently, for the mechanical switching of adsorbed [2]-catenane molecules by complexation with copper atoms [121].

For practical applications, phthalocyanines are more suitable than porphyrins because of their higher stability and lower price. Thus, the question arises whether the direct metalation reaction can also be employed for the in-situ synthesis of metallophthalocyanine monolayers. Naively, one may assume that the reactivity of phthalocyanine towards metal atoms is similar to the reactivity of porphyrins, because

both provide the same coordination environment. However, the phthalocyanine molecule also contains four peripheral iminic nitrogen atoms (figure 4.4.1), which could coordinate co-adsorbed metal atoms and thus give rise to an unwanted side reaction. That such a side reaction is theoretically possible has been demonstrated in a recent study of the interaction of tetrapyrrolylporphyrin (2HTPyP) with Fe on Cu(111). In this study, it was found that the iminic nitrogen atoms of the pyridyl groups strongly attract the co-adsorbed Fe atoms [122]. Phthalocyanine may react in an analogous way, because the peripheral meso-bridging nitrogen atoms should show a similar reactivity as the nitrogen atoms of the pyridyl groups of 2HTPyP.

Another difficulty may arise from the fact that the metal atoms, which are vapor-deposited on the complete monolayer of the ligand molecules, need to diffuse to find a vacant coordination site. In the case of a monolayer of 2HTPP, it was found that Fe and Co atoms are sufficiently mobile on the densely packed 2HTPP monolayer for an almost complete metalation at RT (chapter 4.3). However, the phthalocyanine monolayer may allow less mobility of the metal atoms, because their tetrapyrrole macrocycles are in direct contact to the surface. In contrast, the peripheral phenyl groups of 2HTPP (which are rotated out of the porphyrin plane) act as spacers and create a gap between the porphyrin macrocycle and the surface [73]. It appears likely that the co-adsorbed metal atoms are able to diffuse in this gap with lower activation energy than between a phthalocyanine molecule and the surface. Alternatively, diffusion of the metal atoms on the molecular layer or between the molecules may be possible, but both mechanisms seem energetically unfavorable. In the first case, the bond between the metal atom and the surface must be broken, whereas in the other case the molecules in the densely packed layer must be laterally displaced. For these reasons, metalation of a phthalocyanine monolayer may be slow or require an excess of the metal.

Despite these potential complications, it is demonstrated in this chapter that the metalation of well-ordered monolayers of phthalocyanine on an Ag(111) surface proceeds rapidly at RT and leads to almost complete metalation. In addition, the process appears to be highly selective, i.e., no indications for side reactions were found. The progress of the reaction was monitored by STM.

## RESULTS

Well-ordered monolayers of 2HPc were prepared by vapor-deposition of multilayers onto the Ag(111) substrate held at RT and subsequent annealing, which has been successfully applied for the preparation of well defined monolayers of various metallophthalocyanines [123] and porphyrins [42, 44, 56, 73, 104] (see chapter 3.6). The multilayer desorption temperature for 2HPc was determined analogous to that for 2HTPP (chapter 4.1) and 2HTTBPP (chapter 4.4) by TPD measurements. In the respective spectrum shown in figure 4.5.1, two desorption regions were identified. The peak at 490 K can be attributed to desorption of the multilayer molecules, that one at 705 K to the monolayer molecules. It is noteworthy to mention that the intensity of the multilayer peak is small compared to that one of the monolayer signal. It is highly probable, that only a small amount of excess multilayer molecules was deposited onto the sample. Nevertheless, it was deduced from the spectrum that an annealing step up to  $540 \pm 10$  K, the temperature range between the two peaks, should be adequate for desorbing excess multilayer molecules. Note that also a rather broad peak exhibiting a small intensity was observed at about 550 K. This is possibly due to desorbing molecules from the sample holder. The heating rate of the latter is assumed to be uneven, consequently inducing a broad range peak.

In figure 4.5.2 (a), a high-resolution STM constant current image of the 2HPc monolayer is reproduced. The molecules lie flat on the surface and show symmetric cross-like features. The dark center of each molecule represents the inner cavity, which is surrounded by the four central nitrogen atoms [124, 125]. The unit cell has a square geometry with lattice vectors of  $1.4 \pm 0.05$  nm. This type of arrangement has also been found for monolayers of phthalocyanine and various metallophthalocyanines (CuPc, CoPc, NiPc, FePc, SnPc, PdPc) on Cu(100) [126], Ag(111) [127], Au(111) [128-132], MoS<sub>2</sub> [133], and on graphite (HOPG) [124, 130-133]. The sub-molecular resolution shows the orientation of the molecules relative to the adsorbate lattice, giving an azimuthal angle between one vector of the unit cell and the molecular axis of  $\delta = 60 \pm 3^\circ$  as indicated in figure 4.5.2 (a). By calculating the ratio of substrate and adsorbate unit cell areas, a coverage of  $\theta = 0.037$  ML was determined. This number

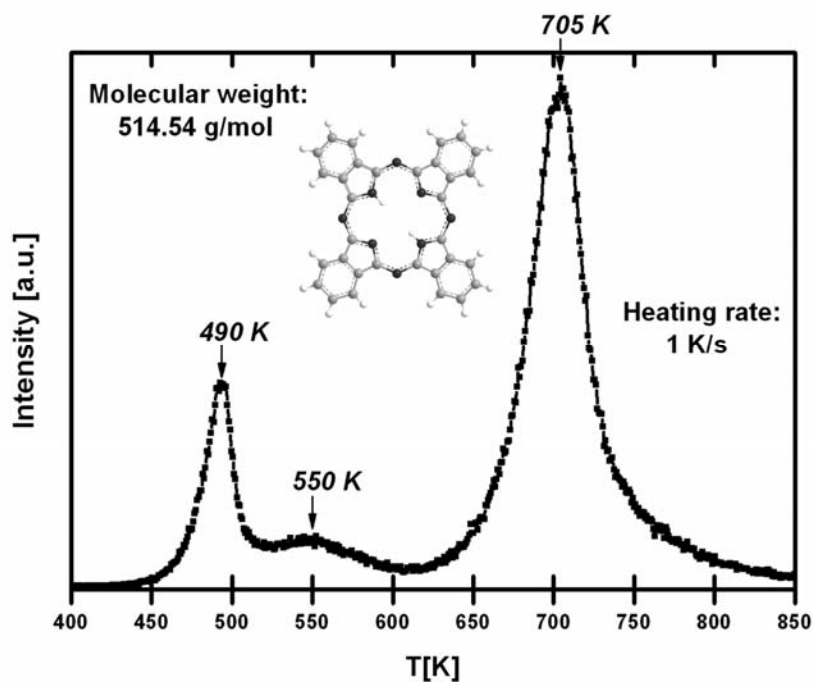


**Figure 4.5.1.** TPD spectrum of 2HPc on Ag(111)

equals the stoichiometric coverage of vapor-deposited Fe atoms necessary for the complete metalation of a 2HPc monolayer.

Figure 4.5.2 (b) shows an STM image of a monolayer of 2HPc after the deposition of iron,  $\theta_{Fe} = 0.012 \pm 0.003$  ML, which is approximately 30% of the stoichiometric amount. Following Fe deposition, some of the molecules appear with a bright central spot, while the other molecules remain unchanged. Figure 4.5.2 (c) shows a profile across one modified and two unmodified molecules, acquired at the position of the green dotted line in figure 4.5.2 (b). It clearly demonstrates an increased apparent height in the former and central cavities in the latter, indicating that the vapor-deposited Fe atoms occupy the central positions of the 2HPc molecules. This result is interpreted as the coordination of the Fe atoms by the phthalocyanine molecules. No Fe atoms can be seen at sites between the 2HPc molecules, which proves that the coordination reaction is fast on the timescale of our experiment (several hours) and that the Fe atoms prefer to bind to the centers of the molecules rather than to the meso-bridging nitrogen atoms at the periphery or to other sites at the Ag surface.

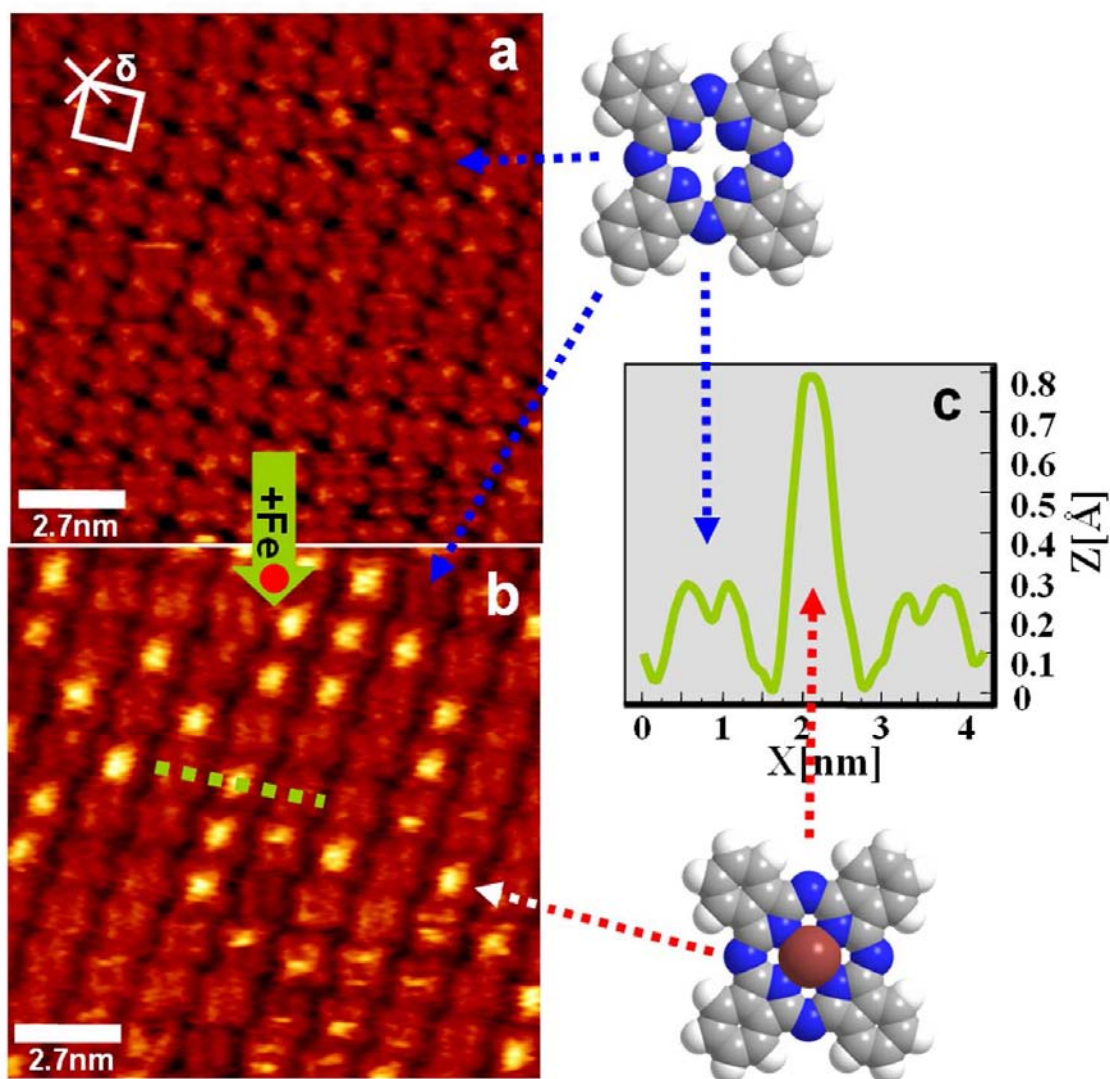


**Figure 4.5.2.** Constant current STM image (a) of a complete monolayer of 2HPc and (b) after the deposition of iron ( $\theta_{Fe} = 0.012$  ML) onto the 2HPc monolayer. In (b) some molecules exhibit a central bright spot, suggesting the formation of FePc. (c) Height profile extracted along the green line in (b). Space-filling models of 2HPc and FePc are shown above and below the height profile, respectively. The arrows indicate the positions of the molecules in the images and the profile. The tunneling parameters of the STM micrographs were: (a) -0.67 V, 39 pA; (b) -1.45 V, 33 pA.

At this point, it is not clear whether this coordination leads to the formation of Fe(II)-phthalocyanine (FePc) through a reaction that includes oxidation of the Fe atom

and the release of the pyrrolic hydrogen atoms as H<sub>2</sub>, or whether the Fe atom is coordinated by a more or less intact 2HPc molecule. The definite proof for the formation of FePc was given by a direct comparison of the STM features of in-situ prepared and directly deposited FePc and by XPS [134]. Meanwhile, this conclusion is also supported by comparison with literature STM data for Fe(II)-phthalocyanine on Au(111) [53, 106] and graphite (HOPG) [124, 125]. In these references, the FePc molecules show a central protrusion, which has been attributed to an orbital mediated tunneling contribution through the Fe(II) d<sup>6</sup> system [53, 106]. However, it is noteworthy to mention that these FePc monolayers were prepared by direct vapor-deposition of FePc, contrary to our approach. FePc is sensitive to oxidation and difficult to obtain as a pure substance. Therefore, the adsorbed FePc that was prepared by in-situ metalation in UHV is most likely of higher purity than that obtained by direct deposition of FePc. This difference may limit the significance of this comparison with literature data.

The long-range order of an extended area of the 2HPc monolayer is displayed in figure 4.5.3 (a). The other STM images (figure 4.5.3 (b)-(d)) were acquired after the successive deposition of equal amounts of Fe ( $\theta_{Fe} = 0.012$  ML in each step) onto this monolayer. Apparently, the number of protrusions (FePc molecules) increases roughly proportional to the amount of deposited Fe. The corresponding numbers of the fraction of protrusions from figure 2 are: (b) 37%, (c) 71%, and (d) 95 %. For comparison, the numbers expected from a stoichiometric reaction are (b) 32%, (c) 65%, and (d) 97%. The small deviations between the experimental and ideal degrees of metalation are within the margins of error (25% of the amount of deposited Fe).

Figure 4.5.3 (a) also shows that the ordered monolayer of 2HPc contains two species with different apparent heights; 83% of the molecules appear brighter and 17% dimmer. We note that the contrast of figure 4.5.3 (a) was enhanced to make the small difference in the apparent heights more obvious. In figures 4.5.3 (b)-(d), an increasing fraction of the molecules appear as protrusions, representing the already described Fe-coordinated phthalocyanine species. As a result of the reduced contrast in comparison to figure 4.5.3 (a), the two different 2HPc species show similar brightness in the latter

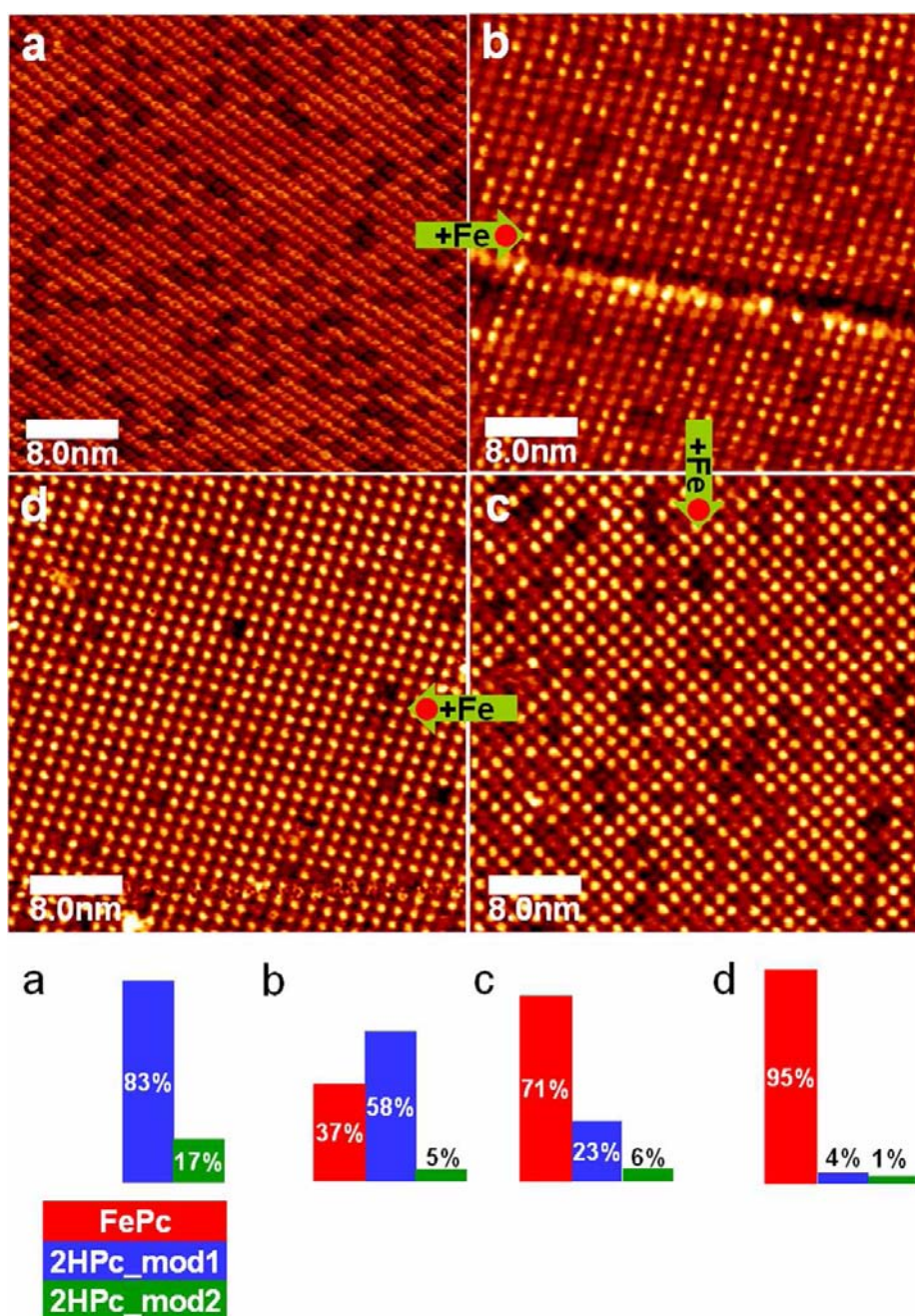


**Figure 4.5.3.** (a) Constant current STM image of a monolayer of 2HPc exhibiting two topographically different 2HPc species. (b)-(d) Clockwise arranged sequence of STM images after the incremental deposition of Fe ( $\theta_{\text{Fe}} = 0.012 \text{ ML}$  in each step). The bar graphs of each figure show the percentages of the two 2HPc species with different apparent heights and of phthalocyanines with coordinated Fe atoms (= FePc). The tunneling parameters of the STM micrographs were: (a) -0.26 V, 22 pA; (b) -1.44 V, 34 pA; (c) -1.42 V, 22 pA; (d) -0.99 V, 0.33 pA.

three images. The ratio of the three different species (two species of 2HPc and FePc) is constant over large areas of the surface, as verified by extended STM images (size:  $50 \times 50 \text{ nm}^2$ ,  $\sim 1300$  molecules) recorded after each deposition step (not shown) (Statistics are indicated in figure 4.5.3). The origin of the two different apparent heights of the 2HPc molecules cannot be adequately addressed at this point. The existence of two different molecular conformations would be a possible explanation, but seems unlikely, considering the planarity of the molecules and the stiffness of the aromatic systems. As another possibility, some of the molecules may have a certain lateral position relative to the substrate atoms, which enables them to weakly coordinate Ag atoms with their central nitrogen atoms. A similar effect has been observed for tetradodecylporphyrin on Au(111) [135].

Furthermore, the images in figure 4.5.3 prove that both 2HPc species have a high affinity to co-adsorbed Fe atoms, although the dimmer molecules are metalated more selectively. This is illustrated by the bar diagrams in figure 4.5.3, which represent the relative fractions of the different species as derived from large images with  $\sim 1300$  molecules. After metalation, the formerly distinguishable 2HPc species are indistinguishable in the STM images.

For a direct comparison of in-situ prepared and directly deposited, commercial FePc, a mixture of 2HPc and FePc was vapor deposited to create a mixed monolayer with 5% FePc (figure 4.5.4 (a)). Subsequent vapor-deposition of Fe atoms ( $\theta_{Fe} = 0.012 \pm 0.003$ ) leads to the formation of additional FePc (figure 4.5.4 (b)), which is indistinguishable from the directly deposited FePc molecules. Figure 4.5.4 (c) shows a larger area of this layer, proving that in-situ and ex-situ prepared FePc lead to identical features in STM.

The observation that all vapor-deposited Fe atoms find a coordination site confirms that the reaction is a surface-mediated process. Clearly, the adsorbed Fe atoms must diffuse across the Ag surface before they are captured by a 2HPc molecule. However, it is debatable whether the Fe atoms diffuse between the molecular layer and the Ag surface, on top of the molecules, or between the 2HPc molecules while the contact to

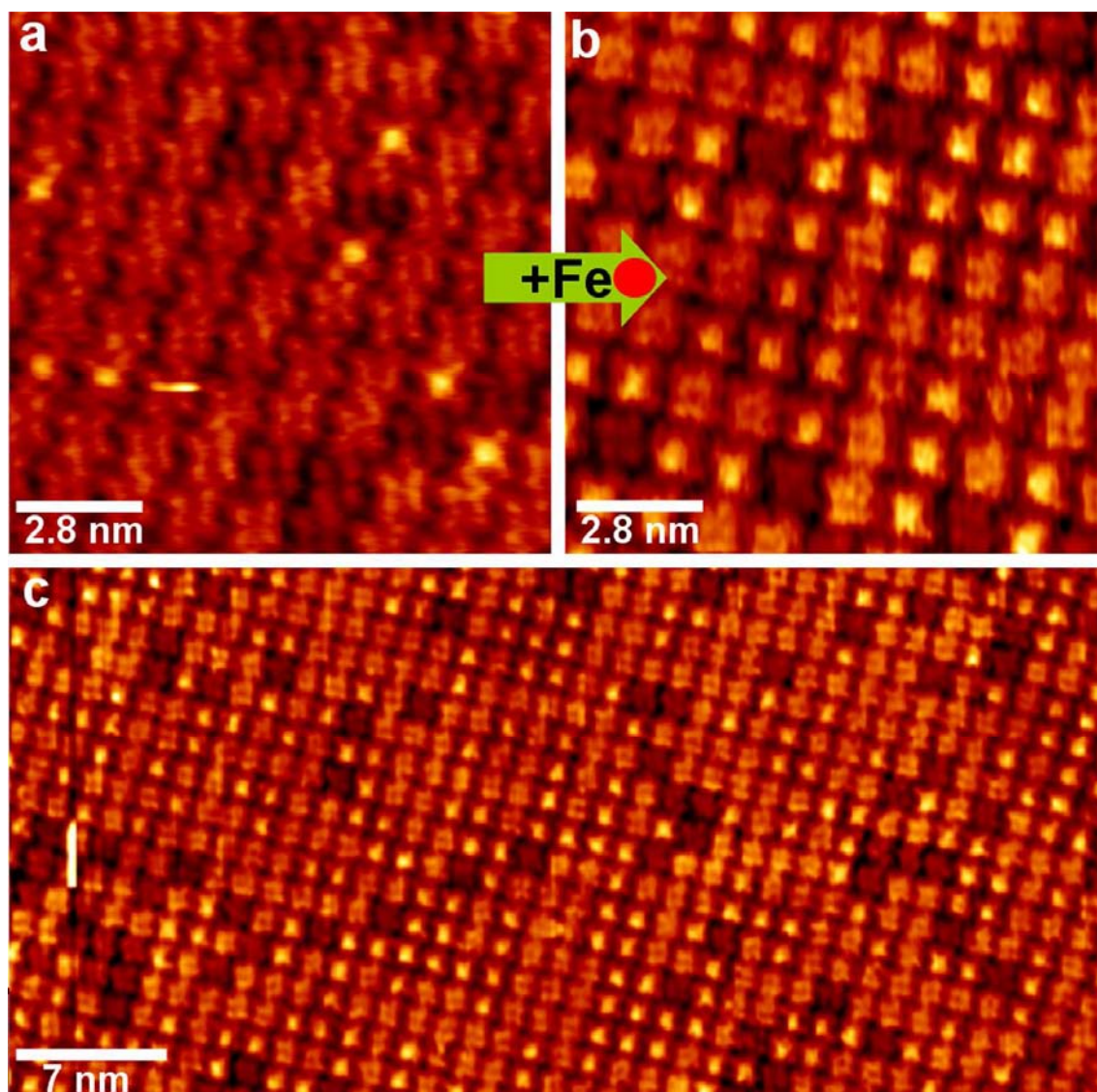


**Figure 4.5.4.** Constant current STM images of (a) a mixed monolayer of 2HPc (95%) and FePc (5%), generated by direct deposition of a 2HPc/FePc mixture; (b) after vapor-deposition of Fe ( $\theta_{Fe} = 0.012 \pm 0.003$  ML) on this mixed monolayer; (c) a larger area of the layer of image 3b. The following tunneling parameters were applied: (a) - 0.88 V, 25 pA; (b) and (c) -1.22 V, 34 pA.

the Ag surface persists. All three processes seem energetically unfavorable, because they imply the cleavage of bonds to the surface or the lateral displacement of molecules.

As mentioned above, 2HPc and 2HTPP have notably different distances between the plane of their tetrapyrrole macrocycles and the underlying surface, because 2HTPP

rests on its four peripheral phenyl substituents, which the planar phthalocyanine lacks. As a result, the distance to the surface of the porphyrin cycle in 2HTPP is larger by approximately 0.3 nm compared to the 2HPc molecule, as has been derived from the van-der-Waals dimensions [73]. For this reason, one may suspect that Fe atoms diffusing within a 2HTPP monolayer have a higher mobility than Fe atoms within a 2HPc monolayer, at least if these atoms diffuse between the Ag surface and the molecular layer. However, if this is the case, it has little influence on the efficiency of the metalation reaction. High degrees of metalation have been found for both molecules, with an even higher value for 2HPc (95% as compared to 89% for 2HTPP [56]).

## **CONCLUSION**

Ordered monolayers of iron(II)-phthalocyanine on an Ag(111) surface were obtained by direct metalation of phthalocyanine monolayers with the stoichiometric amount of vapor-deposited Fe atoms. The reaction proceeds rapidly at RT and leads to a high degree of metalation of the phthalocyanine molecules, i.e., up to 95%. The STM investigations reveal that the Fe atoms are exclusively coordinated by the central nitrogen atoms of the phthalocyanine molecules; no competing coordination on the peripheral meso-bridging nitrogen atoms was observed. In addition, the fact that all deposited Fe atoms up to the stoichiometric amount find a coordination site indicates that the Fe atoms are sufficiently mobile on the surface even in the presence of the densely packed phthalocyanine monolayer. In general, the ultra-high vacuum environment with its very low concentration of contaminants provides excellent conditions for the in-situ preparation of such reactive metal complexes. Therefore, the procedure described here may also be successfully applied for the synthesis of monolayers of M(II)-phthalocyanines with metal ions that are usually not stable in the +2 oxidation state. The presence of the substrate surface may have an additional stabilizing influence on such unusual oxidation states.

## 4.6 Multicomponent Adlayers of Tetraphenylporphyrins on Ag(111)

---

The identification of porphyrins in two- and three-component adlayers is demonstrated in this section. In that course the voltage-dependent appearance of the individual species was exploited. This method is conducted in chapter 4.6.1 for the discrimination of CoTPP and 2HTPP. In this respect also the spectroscopy mode of the STM was applied to interpret the individual appearance in the binary layer. In chapter 4.6.2 it is shown in sub-molecularly resolved STM images that different porphyrins can be chemically identified in a multicomponent adlayer (FeTPP/CoTPP/2HTPP), whereupon in particular CoTPP exhibits a distinct bias-dependent appearance. This study was going along with a successful cooperation with the working group of Andreas Görling (embedded in the framework of the SFB 583), calculating STM images with density functional theory (DFT). In this respect, adsorbate-substrate coupling was demonstrated. In the spectroscopy mode, continuous imaging tunneling spectroscopy (CITS) was performed, also enabling to identify FeTPP/CoTPP/2HTPP in energy-selective maps, showing the local variation of density of states (chapter 4.6.3).

### 4.6.1 Understanding the Contrast Mechanism in STM images of Cobalt Tetraphenylporphyrin on Ag(111)

---

The appearance of TPP in STM images depends strongly on the applied bias voltage. Here the observation and identification of certain features in STM images of CoTPP layers on Ag(111) is reported. It was demonstrated by Comanici et al. that a significant fraction of an ordered monolayer of commercially available CoTPP appears as “pits” at negative bias voltages around  $-1$  V [58, 60]. The obvious possibility that

these pits are missing molecules within the ordered layer could be ruled out by imaging the molecules at reduced bias voltages at which the contrast of the pits fade and at positive bias voltages around +1 V at which the image contrast is inverted. With the investigation of the electronic structure, in particular the density of states close to the Fermi level, of CoTPP and 2HTPP layers by means of UPS and STS, the contrast mechanism could be clarified. The correlation of the bias-dependent contrast with the UPS data enabled to interpret the “pits” as 2HTPP. Additional evidence was provided by imaging layers of different mixtures of 2HTPP and CoTPP and by high-resolution STM imaging of the features in CoTPP.

## **INTRODUCTION**

The investigation of multicomponent porphyrin layers (e.g., NiTPP and CoTPP [105]) and mixed films of phthalocyanines (Pc) and porphyrins (e.g., CoPc and NiTPP [136], CoPc and CoTPP [70]) by means of STM is a topic of special interest with respect to the tailored functionalization of surfaces. Furthermore, an important step towards the engineering of porphyrins was achieved with the direct metalation of the preadsorbed, metal-free ligands with vapor deposited metal atoms (Fe [47, 56], Co [42, 104], Zn [42, 62, 116]) chapter (4.3 – 4.5), which also implicated the exploration of mixed layers of free base porphyrins and metalloporphyrins with STM [42, 47, 56]. In these studies a discrimination and identification of the corresponding molecules was possible on the basis of the appearance of submolecular features [42, 47, 56, 70, 105, 136]. Generally, at negative sample bias free base porphyrins appear as features with a central cavity in high-resolution STM, whereas metalloporphyrins exhibit a central protrusion caused by the central metal ion, as demonstrated in chapter 4.1, 4.3, 4.4. In a binary mixtures of molecules with a central metal ion (different MTPP, MPc and MTPP), CoPc [136] or CoTPP [105] was found to appear particularly bright at negative bias voltages, due to orbital mediated tunneling through the half filled  $d_{z^2}$  orbital of the Co ion. Evidence for a bias-dependent appearance of single iron-tetrapyrrolylporphyrin (FeTPyP) molecules is also found in a study by Auwärter et al. [105], where a contrast inversion of FeTPyP within a layer of 2HTPPy (protrusion at negative bias, depression at positive bias voltage) was reported and correlated with corresponding STS data.

In this chapter the bias-dependent contrast mechanism in a monolayer of CoTPP on Ag(111) is addressed on the basis of medium-resolution STM images. Thereby the local probes STM and STS could be correlated with laterally averaging UPS measurements.

## RESULTS

The bias-dependent appearance of a monolayer of CoTPP on Ag(111) in STM is addressed. The investigations were triggered by the observation that a significant portion of an ordered monolayer, prepared by evaporation of commercially available CoTPP molecules, appears as depressions or “pits” at negative bias voltages around -1 V, as can be seen, e.g., in figure 4.6.1 (a)-(c). In the STM image, the majority of molecules appear as protrusions arranged in a square order with a lattice constant of ~1.4 nm (see chapter 4.1). This type of appearance and arrangement is well known for different MTPP on various substrates [56, 70, 86]. Within this arrangement, a significant number of depressions are clearly visible, which is especially apparent in the 3D plot in figure 4.6.1 (b), as indicated by the white arrows. A statistical analysis over large scan areas resulted in an average amount of 7 – 10 % of “pit” features. Similar observations have occasionally been reported in the literature and were interpreted as missing molecules [71] or impurity molecules [86]. Interestingly, the STM images collected with a bias voltage of -100 mV do not show these “pits”. This is most evident when comparing the images figure 4.6.1 (c) and (d), which show the same region with bias voltages of -1.20 and -100 mV, respectively. Obviously, at -100 mV the pits are not visible anymore, but instead at the former positions of the pits bright features indicating the presence of molecules. Therefore, the identification of the pits as missing molecules can be immediately ruled out.

Since the observed pits are apparently not missing molecules, additional investigations of the electronic structure, in particular of the density of states of Co- and 2H-porphyrin layers were conducted by means of ultraviolet photoelectron spectroscopy (UPS) as previously demonstrated by Comanici et al. [58, 60]. Of particular relevance are the UPS signals near the Fermi level, since this region is accessible with the STM.

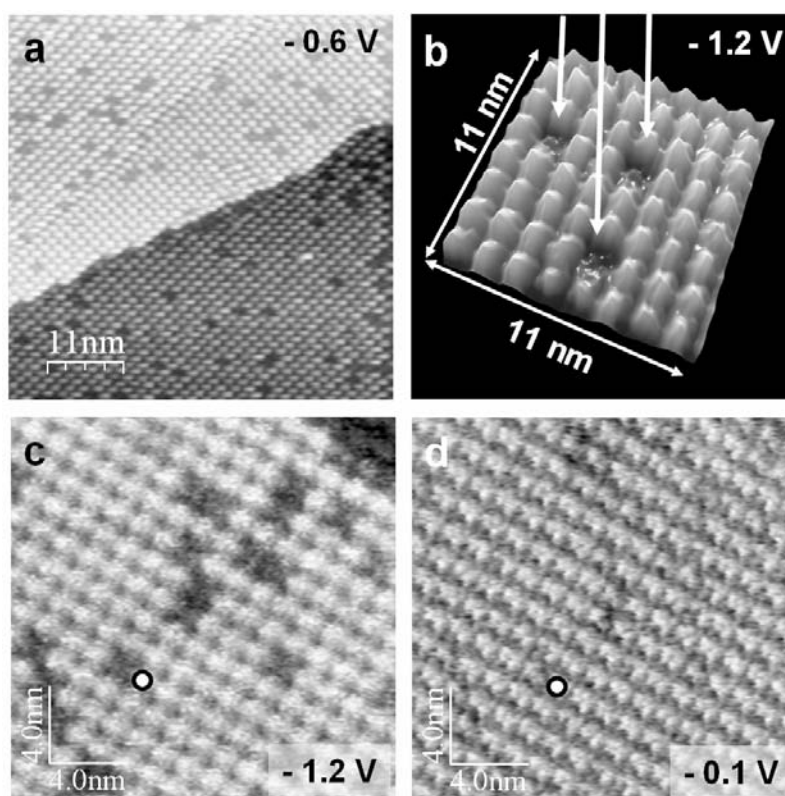


**Figure 4.6.1.** Constant current STM images of a monolayer of CoTPP on Ag (111). All STM micrographs were acquired with a current of  $I_{set} = 0.3$  nA and the indicated bias voltages at RT. In (a-c) the appearance of depressions, denoted as “pits”, is evident for bias voltages of -1.2 and -0.6 V. (a) and (d) are acquired at the identical surface region, but at different bias voltages; in both images the same specific molecule.

Figure 4.6.2 shows a comparison between the STM and the UPS measurements. The UPS spectra for CoTPP and 2HTPP monolayers are shown in the energy range of 0 eV ( $=E_F$ ) to -1.3 eV, e.g., near the Fermi level. The spectrum of 2HTPP is almost featureless in the investigated energy region. For CoTPP, the spectrum is dominated by a peak centered at -0.6 eV below  $E_F$ . As has been discussed in an earlier publication [104], this signal can neither be attributed to the isolated CoTPP molecule (because it is absent for multilayer coverages) nor is it a feature characteristic of the Ag valence band.

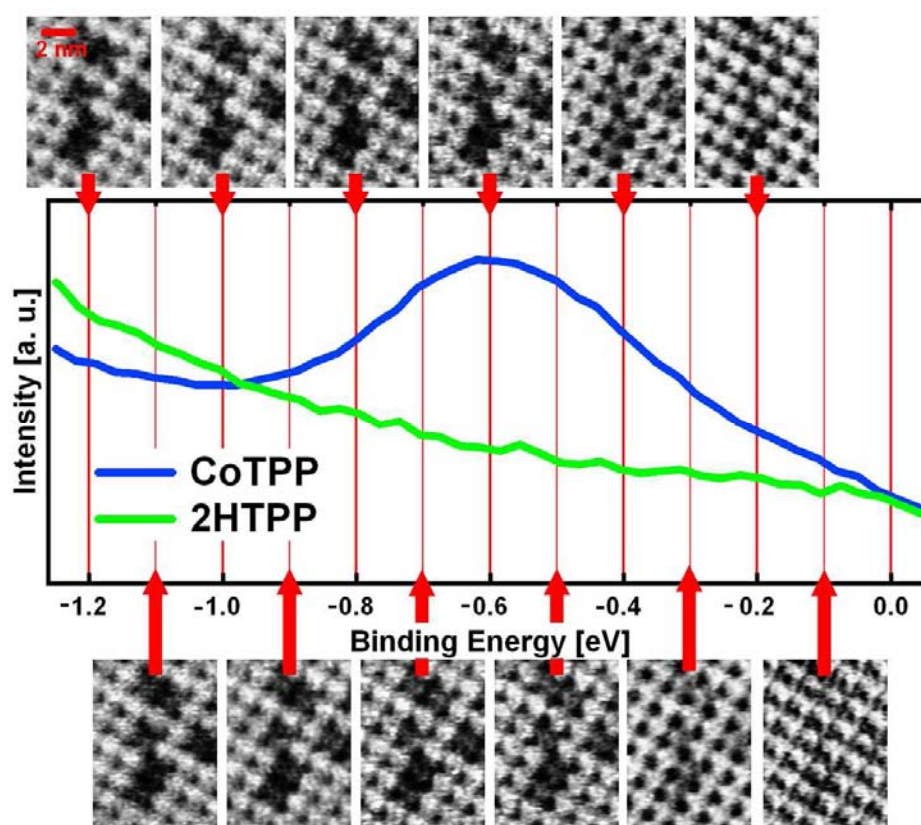


**Figure 4.6.2.** Correlation of UP spectra of homogenous monolayers of 2HTPP (green line) and CoTPP (blue line) with a bias series (-1.2 V to -100 mV in 100 mV steps) of constant current STM images acquired at a current of 0.3 nA. The corresponding bias voltages are marked with the red arrows, referring to the energy scale of the UP spectrum (relative to  $E_F \equiv 0$ ).

Most likely, this signal indicates the formation of a new valence state, which results from the electronic interaction of the Co ion with the Ag surface. This initially unoccupied state is located below the Fermi level and can therefore be filled up with electrons from the Fermi sea. This interpretation, which implies a partial reduction of the Co ion by substrate electrons, is in line with the strong influence of the surface on the energetic positions of the Co 2p core level signals. It is also interesting to note that the signal at -0.6 eV is suppressed when an additional axial ligand such as NO is attached to the Co ion [46].

In figure 4.6.2, it is evident that the pits in the STM images start to disappear at bias voltages around -0.6 eV. This behavior can be understood by considering the UP spectra. Since, for a given bias voltage, all electronic states between the corresponding binding energy and the Fermi level contribute to the tunneling current, the STM signal and thus the contrast can be obtained by integration of all DOS in the UP spectra in this energy region, i.e., on the right hand side of the arrows in figure 2. Consequently, in the STM images with increasing negative bias voltage the contribution of the peak at 0.6 eV due to the Co ion-substrate interactions increases, enhancing the contrast of Co-porphyrins and 2H-porphyrins. On the other hand, at low energies, e.g., at -1 eV, where this peak does not contribute to the integration, the contrast vanishes.

Additional evidence for the interpretation that the pits in (figure 4.6.3 (a)) are indeed 2HTPP molecules is obtained from the high-resolution STM images shown in figure 4.6.3. There the internal structure of the pits (figure 4.6.3 (a)) is resolved as four dim protrusions (figure 4.6.3 (b)), which are assigned to the corresponding phenyl groups of 2HTPP. Figure 4.6.3 (c) shows a “pit” molecule with the superimposed and scaled model of a 2HTPP placed nearby; the left and the right phenyl groups fit perfectly to the corresponding protrusion, whereas the upper and lower protrusions deviate from the position of the remaining phenyl groups, possibly due to tip artifacts and/or a different molecular conformation of the adsorbed TPP molecule compared to the model. However, the most important feature with respect to the topic of this chapter is the central cavity in the STM image in figure 4.6.3 (c) at the center of the molecule, indicating the absence of the central metal ion. This observation is also in line with recent studies on the in-situ metalation of 2HTPP with Fe and Co [42, 47, 56] (chapter 4.1, 4.3), where a similar appearance of 2H-porphyrins was observed.

To further confirm the assignment of the pits to 2H-porphyrins, a mixture of roughly 1:2 of CoTPP to 2HTPP was prepared and thermally evaporated in the same way as the “pure” CoTPP. Figure 4.6.3 (d) shows an STM image of a monolayer of this porphyrin mixture. It is immediately evident that the number of molecules on the surface increased, which appear with a decreased apparent height as compared to the “pure” CoTPP layer (purity of 98%) studied in figure 4.6.3 (a).

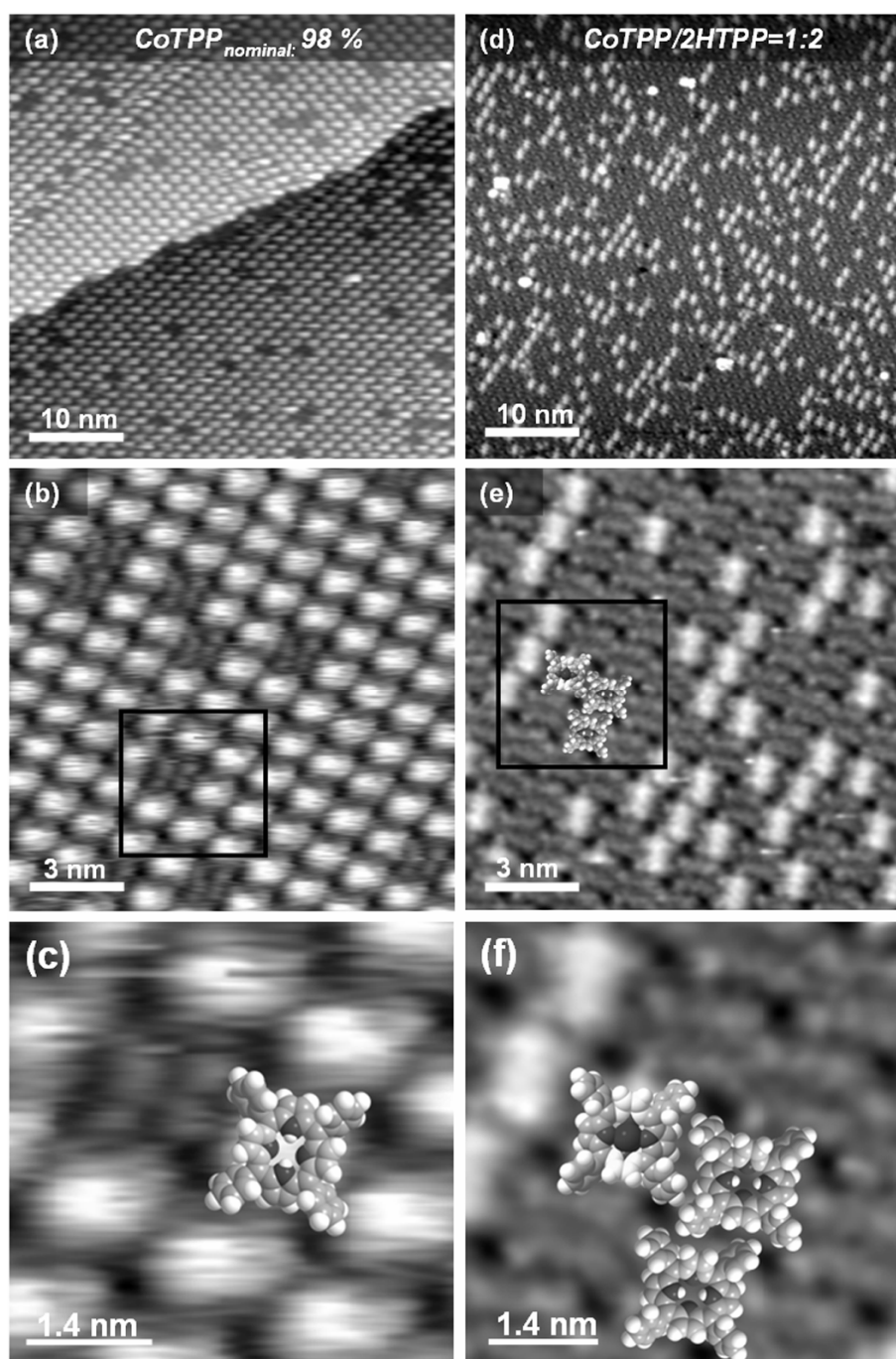


**Figure 4.6.3.** Constant current STM images of a monolayer of CoTPP (a) and (b) and a 1:2 ex-situ mixture of 2HTPP / CoTPP (d) and (e) on Ag (111). Enlarged images (c) and (f) of (b) and (e) respectively. The tunneling parameters are: (a)  $I_{set} = 0.3$  nA,  $U_{bias} = -0.6$  V; (b)-(c)  $I_{set} = 0.3$  nA,  $U_{bias} = -1.0$  V; (d)  $I_{set} = 41$  pA,  $U_{bias} = -1.0$  V; (e)-(f)  $I_{set} = 30$  pA,  $U_{bias} = -1.4$  V

A statistical analysis reveals an increase of the number of pits from 7-10 % in the “pure” CoTPP layer to ~35% in the mixture layer, which serves as strong additional evidence that the pits are indeed due to 2HTPP. Figure 4.6.3 (f) is an enlarged image of figure 4.6.3 (e) superimposed with the corresponding scaled space filling models, which emphasizes that the molecules exhibiting a decreased apparent height, show a central cavity and four protrusions due to the phenyl rings. It is interesting to note that by NMR a concentration of ~10% 2HTPP was determined in the purchased CoTPP powder. This explains the higher concentration in the prepared CoTPP monolayers as compared to value expected from the specified purity of >98%.

So far, the presented data only refers to negative bias voltages, i.e., contributions from the HOMO of the porphyrins to the tunneling contrast. Figures 4.6.4 (a) and (b) are showing two STM images of the same surface area, which were acquired more or less simultaneously with bias voltages of -1 and +1 V, respectively (this was achieved by switching the bias voltage, when switching the scan direction). The STM image obtained with -1 V (figure 4.6.4 (a)) exhibits the appearance described above, with CoTPP as protrusions and 2HTPP as depressions. The same surface area imaged at +1 V (figure 4.6.4 (b)) displays an inverted contrast. This becomes particularly evident by comparing the apparent height along the same line marked in figure 4.6.4 (a) and (b), as plotted in figure 4.6.4 (d). Obviously, the two depressions (pits) at -1 V appear as protrusions at +1 V. The inversion of the contrast can be further visualized in figure 4.6.4 (c), which represents an overlay of the two STM images in figure 4.6.4 (a) and (b), after some data processing. For figure 4.6.4 (a), a threshold operation was applied, such that all points exceeding an apparent height of 0.15 nm (see scale in figure 4.6.4 (d)) are marked red. The resulting image was superimposed onto the contrast-enhanced and green color coded image shown in figure 4.6.4 (b). From figure 4.6.4 (c) it is evident that almost all depressions visible at -1 V coincide with the protrusions found at +1 V, which demonstrates that the contrast of isolated 2HTPP molecules within an ordered array of CoTPP strongly depends on the polarity of the bias voltage. This is because in one case it is the HOMO (negative bias) in the other the LUMO (positive bias) of the molecules, which is imaged in STM. A similar effect was recently also observed by Auwärter et al. [47] for 2H-porphyrins mixed with Fe-porphyrins. There are just a few

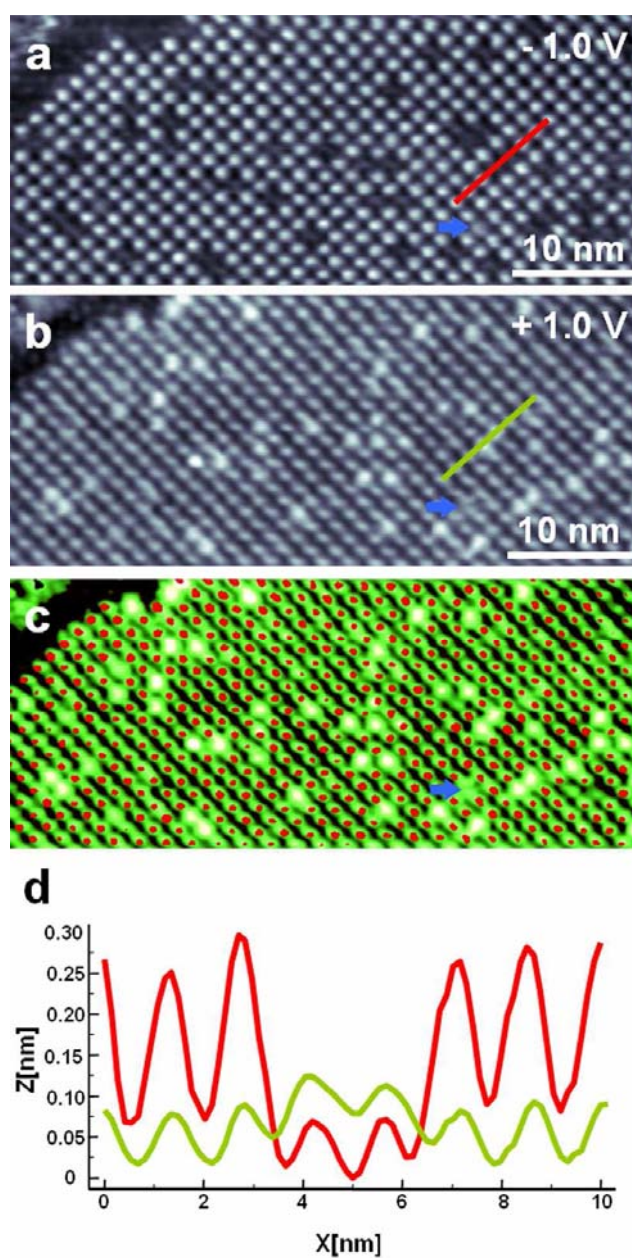


**Figure 4.6.4.** (a) and (b) Constant current STM images (both with  $I_{\text{set}} = 0.27$  nA) of a monolayer CoTPP on Ag (111) at negative bias voltage -1 V (a) and the same surface area at positive bias voltage +1 V (b). The apparent contrast inversion is visualized in (c), which represents an overlay of the processed STM images in (a) and (b) as described in the text. The profiles of the apparent height along the colored lines in (a) and (b) are shown in (d).

lattice sites (indicated with blue arrows) in figure 4.6.4 (a-c), which do not follow the described behavior for CoTPP or 2HTPP. These features can be interpreted as damaged or chemically altered TPP molecules.

To understand the origin of the contrast inversions in the STM images, the electronic structure of the LUMO has to be investigated, which can be done by STS using positive bias voltages. In figure 4.6.5, the corresponding ST spectra of CoTPP (blue) and 2HTPP (red) ranging from -1.5 V to +1.2 V are plotted. In agreement with the UPS data in figure 4.6.2, a dominant peak at -0.6 V is found for CoTPP, while the 2HTPP spectra do not exhibit significant intensity maxima in the negative bias voltage region. At positive bias voltages the 2HTPP spectrum has a dominant peak at +0.6 V, whereas the spectrum for CoTPP exhibits a significantly smaller peak (roughly half in height) slightly below +1 V. Consequently, for a STM image acquired at +1 V the

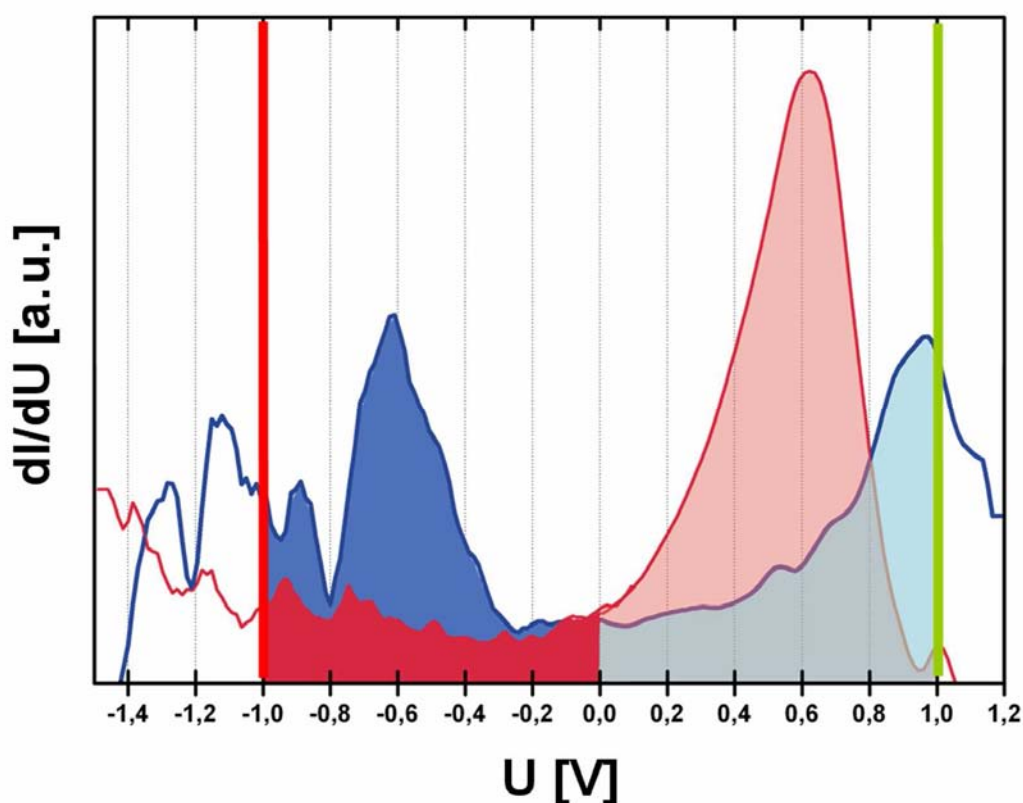


**Figure 4.6.5.** Local ST spectra reflecting the LDOS of CoTPP (blue line) and 2HTPP (red line) are plotted. The ST spectra were extracted from CITS data of a mixed layer of CoTPP and 2HTPP.

integral of the DOS for 2HTPP leads a higher value (shaded in blue) compared to the one of the CoTPP (shaded in red).

## **CONCLUSION**

A consistent picture, on how the bias voltage-dependent appearance of mixed CoTPP/2HTPP layers in STM is related to the corresponding electronic structure was developed. These findings, in addition with high-resolution STM images, prove that the features observed as depressions (pits) within CoTPP layers at bias voltages around -1 V are 2HTPP molecules. The origin of the contrast, i.e., the appearance of CoTPP as protrusion and 2HTPP as depression at negative bias voltages around -1 V can be traced back to an increased DOS around -0.6 V below the Fermi level in the case of CoTPP; this contribution to the DOS is due to the interaction of the central Co ion with the Ag(111) substrate. At positive bias voltages around +1 V the 2HTPP molecules appear brighter than CoTPP, i.e., the contrast is inverted due to a higher density of unoccupied states for the former. If one assumes distinguishable DOS fingerprints for different metalloporphyrins at energies accessible to STM ( $\sim -1.5$  V to  $+1.5$  V), the described contrast mechanism can be exploited to discriminate and identify individual molecules even at medium STM resolution.

### **4.6.2 Fingerprints of different Porphyrins**

---

In this combined experimental and theoretical work it is demonstrated at the example of TPP on Ag(111) how differences in individual adsorbate orbitals and their interaction with the substrate can be exploited to switch the appearance of the adsorbate in STM experiments, such that electronically and chemically very similar large molecules become distinguishable in STM. In particular, an intermixed layer consisting of 2HTPP, CoTPP and FeTPP molecules on Ag(111) was investigated, and it is demonstrated that STM images acquired with different bias voltages constitute fingerprints of the different molecules within the intermixed layer. By means of density-

functional calculations the observed features could be explained in detail and traced back to a direct orbital interaction of the adsorbed molecule with the surface. The findings for TTPs on Ag(111) thus stress the necessity to generally consider the surface in theoretical approaches in order to achieve accurate and reliable STM images.

## **INTRODUCTION**

One route towards the generation of tailor-made supramolecular porphyrin networks is the variation of the side groups of individual molecules [55]. Additionally, the functionality of porphyrinoids can be modified by the choice of the central metal atom, whereat the metal atoms like Zn [62], Co [42, 104] (chapter 4.3.3) and Fe [56], [47, 57, 134] (chapter 4.3.1, 4.3.2, 4.4, 4.5) can be inserted into adsorbed free base porphyrinoids by in-situ metalation in UHV (chapter 4.3, 4.5). Alternative routes are the successive thermal evaporation of different porphyrins [105] or the thermal evaporation of the mixed raw material [59, 60] (chapter 4.6.1). Considering the large variety of possible substituents and/or central metal atoms, it is obvious that molecular arrays, of high structural and chemical complexity can be prepared. In addition, interactions with the surface can be used to change the properties of the adsorbed molecules. As a consequence, the chemical identification of the different molecular species on a surface becomes a challenge.

STM is presently the most important experimental tool to study the inter- and intramolecular structure of molecular assemblies [137]. In many cases, rather simple considerations based on the topography of the molecule are sufficient to interpret the observed apparent heights in the STM images. Such intuitive interpretations work for example for the discrimination of free base and metalloporphyrinoids at certain tunneling conditions [56, 60] typically at bias voltages around -1.0 eV. Two examples can be found in figure 4.6.2.1 (b) and (c), where STM images of different mixtures of 2HTPP and CoTPP on Ag(111) are depicted, with CoTPP appearing as protrusions. However, it should be noted that for CoTPP one observes a contrast inversion by changing the polarity of the bias voltage [60] (chapter 4.6.2), which clearly shows that the simple “topographic approach” is limited.

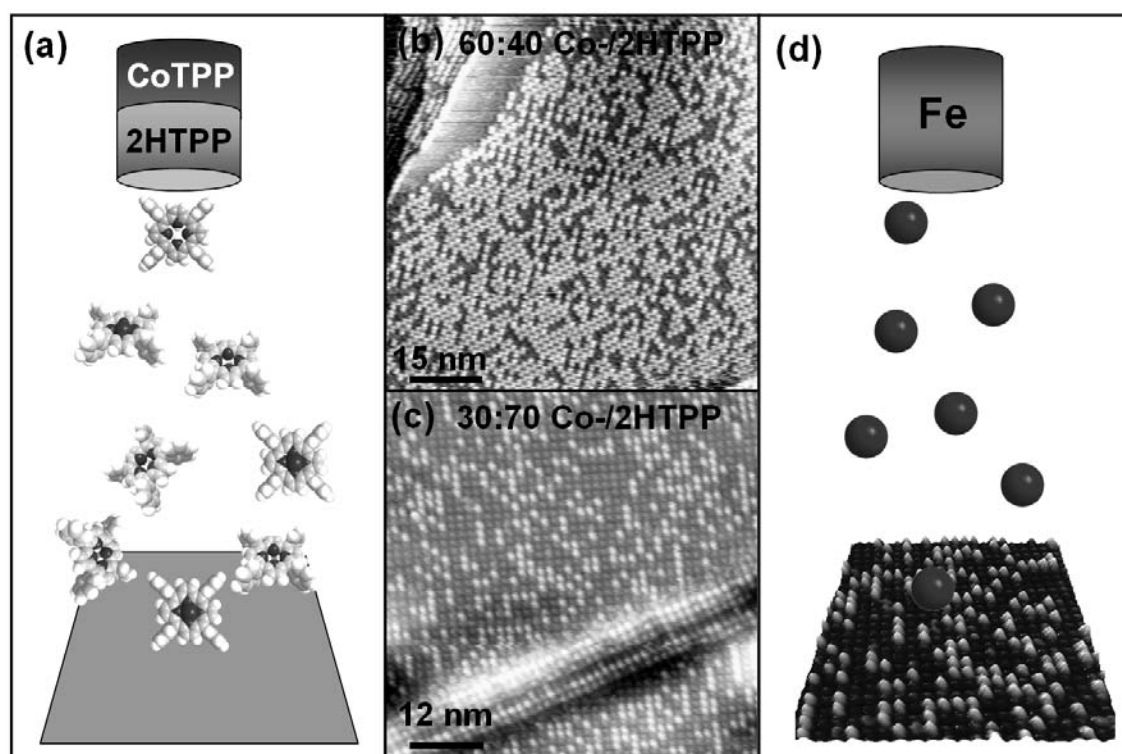


**Figure 4.6.2.1.** Schemes and STM images illustrating the preparation route to generate the intermixed porphyrin layer consisting of the three different species: 2HTPP, CoTPP and FeTPP. (a) Scheme showing the evaporation of a mixture of 2HTPP and CoTPP onto the Ag(111) substrate. (b), (c) Medium-resolution STM images of mixed 2HTPP/CoTPP layers generated from mixtures with different ratios of the two porphyrin species as indicated. Both images were acquired at negative bias voltages around  $-1$  V where the metalloporphyrin (CoTPP) appears as a protrusion. The ratio of the molecules appearing as protrusions is in excellent agreement with the CoTPP portion in the original mixture. (d) Scheme of the in-situ evaporation of Fe onto a mixed 2HTPP/CoTPP layer. Fe will metalate available 2HTPP under the release of  $H_2$  with almost 100% yield. By evaporating a defined amount of Fe the fraction of the resulting FeTPP within the intermixed layer can be controlled. Thus the whole process enables the generation of an intermixed 2HTPP, CoTPP and FeTPP layer with defined ratios of the corresponding species.

It has indeed long been known that STM images in general represent a delicate interplay of electronic and topographic effects, a prominent example being the appearance of graphite in STM [18].

For different metalloporphyrinoids with basically identical topography, the specific electronic structure can be exploited to distinguish them. Scuderio et al. were able to discriminate CoTPP and NiTPP on Au(111) based on an increased apparent height of the CoTPP at a bias voltage of -1 V [105]. They interpreted this observation as due to the half filled  $d_{z^2}$  orbital of the central Co atom ( $3d^7$  electron configuration). However, it is not possible to distinguish, e.g., the very similar porphyrinoids CoPc and FePc in this way, because the FePc is assumed to have a triplet ground state in the tetrapyrrolic environment and thus has a half-filled  $d_z^2$  orbital [106]. In order to distinguish topographically and chemically similar molecules, additional degrees of freedom like changes in the applied bias voltage can be helpful tools. Such a strategy requires, however, a detailed understanding of the contrast mechanism. In this chapter it is demonstrated how differences in individual adsorbate orbitals and their interaction with the substrate can be exploited to switch the appearance of the adsorbate in STM experiments, such that even electronically and chemically very similar molecules become distinguishable.

In order to understand the contrast mechanism of the investigated systems in STM additional information from theory is required in general. While in some cases simple computational approaches such as Extended Hückel Theory calculations can in certain cases be sufficient to reproduce the main features of the STM observations [41, 85, 100, 138], there are also cases where even sophisticated theoretical approaches do not lead to satisfying agreement with the experimental findings [139]. In general, an oversimplification of the problem such as the neglect of the metal surface can present problems, if the surface is an active part of the system. To the best of our knowledge, up to now no state-of-the-art DFT calculations of STM images for large organic molecules, in particular porphyrinoids have been performed, which explicitly take into account molecule-substrate interactions by including a realistic description of the substrate. This is especially remarkable, since the importance of such interactions is indicated in the

literature for metalloporphyrinoids with a singly occupied  $d_{z^2}$  orbital of the metal ion [55, 105, 106, 109].

In this chapter, the characteristic bias-dependent appearance of different metalloporphyrins in mixed layers on Ag(111) in STM images is reported. The investigation of mixed layers allows the comparison of the different appearances in-situ under identical conditions. To understand the experimental observations, especially the role of the substrate, the electronic structures and the STM images of the porphyrins were calculated both in the gas phase and in the adsorbed phase via periodic density-functional calculations in the working group of Andreas Görling. These calculations reproduce the experimental images with high accuracy for all studied porphyrins, and it turns out that the bias-dependence of the STM images can only be explained in terms of the electronic structure of the adsorbed molecules including the surface.

## RESULTS

To allow the in-situ comparison of the different porphyrin derivatives the preparation of intermixed 2H/Co/FeTPP layers with controlled stoichiometry was established. The corresponding preparation route is sketched in figure 4.6.2.1 and described in detail in the figure caption.

Figure 4.6.2.2 (a) shows a constant current STM image acquired on an intermixed layer prepared with a nominal composition of 50% 2HTPP, 30% FeTPP and 20% CoTPP at a moderate negative bias voltage ( $U_{\text{Gap}} = -800$  mV and  $I_{\text{Set}} = 30$  pA). At these tunneling conditions one can distinguish only two different shapes of the molecules, as indicated by the arrows in figure 4.6.2.2 (b). This bimodal appearance is observed over a wide bias voltage range of approximately -400 mV to -1.5 V (larger negative values were not tested). The left molecule in figure 4.6.2.2 (b), which appears with a central depression, can be identified as 2HTPP [42, 56]. The other two exhibit a dumbbell-like shape, as is typically observed for Fe- and Co-porphyrin derivatives at medium negative bias voltages [61, 100, 139]; they are thus assigned accordingly.

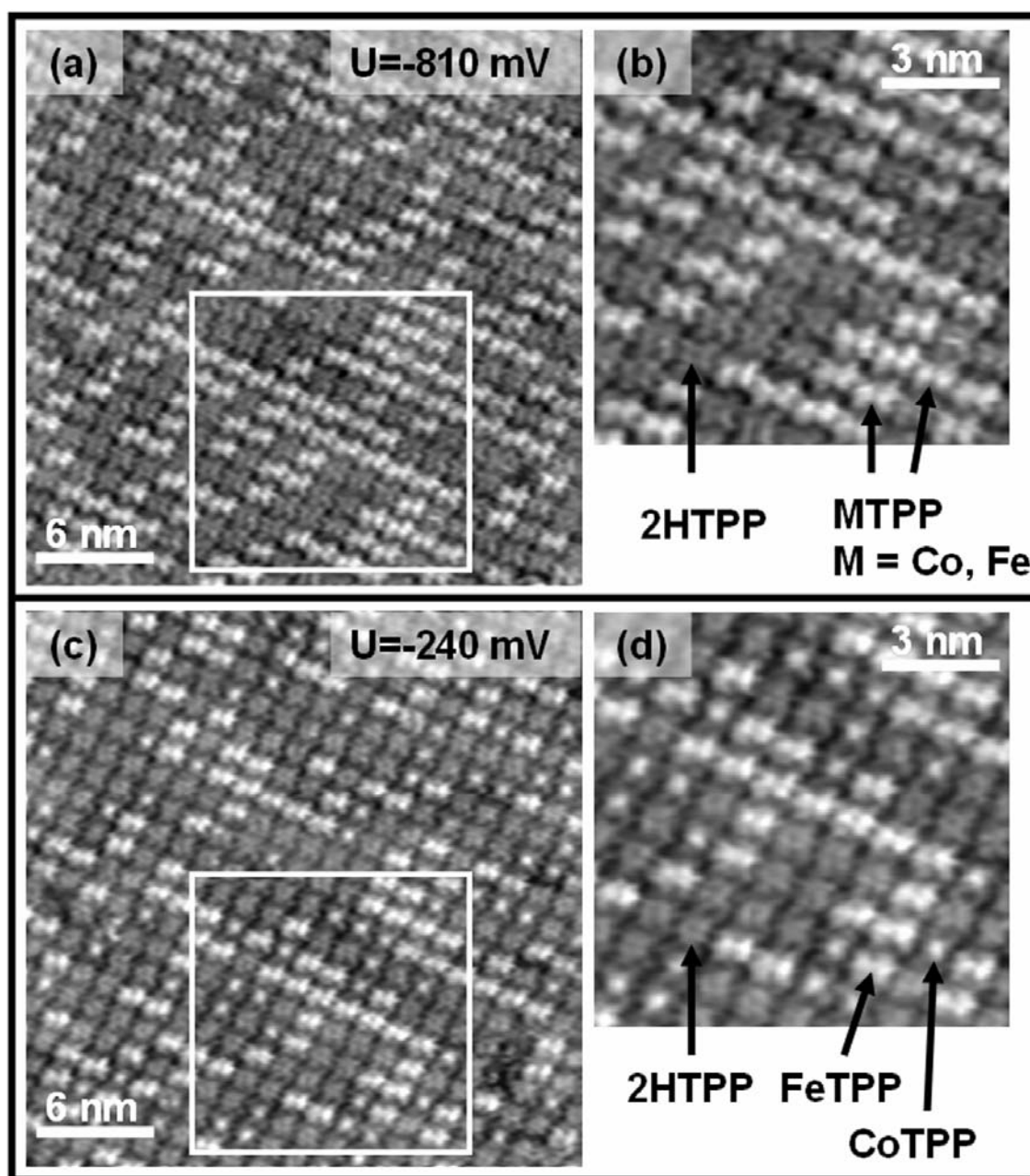


**Figure 4.6.2.2.** STM images of the same surface area of an intermixed 2H-, Co- and FeTPP at different bias voltages. Obviously at the higher bias voltage as shown in (a) and (b) a bimodal appearance of the three porphyrin species is observed ( $U_{\text{Gap}} = -810$  mV and  $I_{\text{Set}} = 30$  pA). The 2HTPP appears with a central depression, whereas the two metalloporphyrin species, namely CoTPP and FeTPP appear both with the typical saddle-shape, which means that they are undistinguishable at the actual tunneling condition. In figure (c) and (d) the same surface areas as in (a) respective (b) are

*imaged at reduced bias voltage ( $U_{\text{Gap}} = -240$  mV and  $I_{\text{Set}} = 35$  pA). It is apparent that at this tunneling condition three different appearances of individual molecules can be observed. Whereas the 2HTPP images remain essentially the same, a fraction of the saddle-shaped molecules now appear with a central protrusion. These molecules can be identified as CoTPP, which means that (in contrast to 2HTPP and FeTPP) CoTPP exhibits a strong bias-dependent appearance in STM. Thus the discrimination of the three species becomes possible at reduced bias voltages.*

This interpretation is corroborated by the fact that the fraction of molecules with the dumbbell-like appearance roughly matches the expected amount of 50% MTPP. As discussed in chapter 4.1, it is well established that upon adsorption, TPP and also other similar molecules exhibit a conformational adaptation: for CoTPP on Ag(111) and CoTPP on Cu(111) [100] a considerable rotation of the phenyl-substituents is concluded. As a consequence, the central porphyrin macrocycle is deformed such that two opposing pyrrole groups are tilted upwards and the other two downwards, which is commonly referred to as a saddle-shape conformation.

A main challenge now is the discrimination CoTPP and FeTPP, since both obviously appear with an oblong (dumbbell) shape (chapter 4.1, 4.3) at the typical tunneling conditions used in figure 4.6.2.2 (a) and (b). As pointed out in the introduction, both metalloporphyrins appear to have a half filled  $d_{z^2}$  orbital, which has been assumed to mediate the tunneling from the tip to the surface [106]. Due to its characteristic out-of-plane “club shape”, the singly occupied  $d_{z^2}$  molecular orbital might be expected to appear in STM as a well defined protrusion centered in the porphyrin macrocycle. However, this is not the case, at least at the tunneling conditions of figure 4.6.2.2 (a) and (b), i.e., in the range from -1.5 to -0.4 eV. Similar conditions have been applied in nearly all STM studies of adsorbed porphyrins in the literature.

At a reduced negative voltage of  $U_{\text{bias}} = -240$  mV, however, an additional third shape is observed in figure 4.6.2.2 (c) and (d), which can be described as the expected central protrusion or bright spot. Comparing the enlarged images in figure 4.6.2.2 (a) and (c) it becomes obvious that a certain fraction of the molecules changed its

appearance from the saddle-shape at  $-810$  mV to the bright spot at  $-240$  mV. These molecules can be identified as CoTPP, since experiments on a pure CoTPP monolayer exhibit exactly the same bias-dependent shape. Counting the molecules over larger scan areas, results in roughly 20% of molecules, which exhibit bright spots and thus match the expected CoTPP content. It should be noted that this bias-dependence was reproduced for several freshly prepared mixed monolayers, with only slight variations in the different shapes (possibly due to an altered tip shape).

The bias-dependent changing appearance of CoTPP (pure CoTPP layer), from a longish protrusion to a bright spot (and vice versa), is highlighted in the STM image in figure 4.6.2.3, where the bias voltage was switched from  $-1$  V to  $-300$  mV at half of the image scan. It was found to occur at roughly  $-400$  mV, again with only slight variations from experiment to experiment (possibly also due to an altered tip).

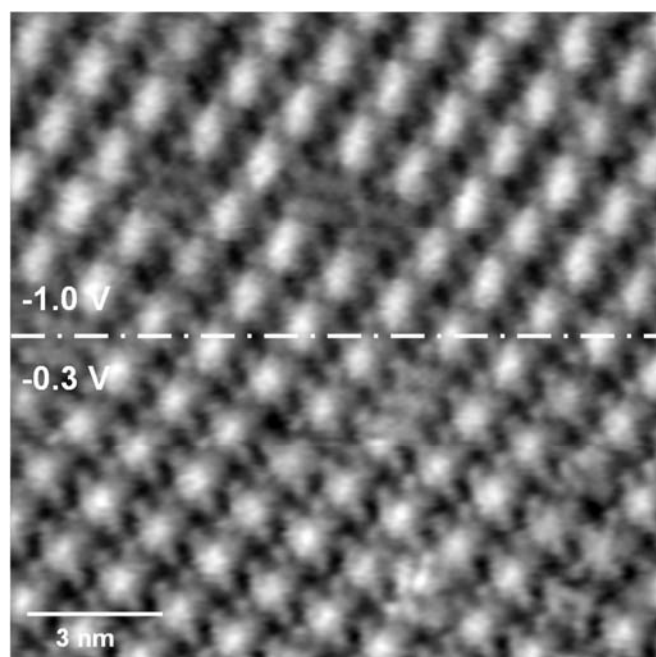


**Figure 4.6.2.3.** STM micrograph demonstrating an altered appearance of CoTPP upon a changing bias voltage from  $-1.0$  V to  $-0.3$  V ( $I = 35$  pA) in one image. In the upper part a longish shape of CoTPP is apparent, whereat in the lower part of the image a central dot presents the main feature.

A possible structural deformation of the CoTPP due to a change in bias around -0.4 V is very unlikely, since (1) the tunneling conditions can be regarded as too “mild” to induce such a change, (2) no dependence of the tunneling current was observed, and (3) FeTPP and 2HTPP do not exhibit such dramatic changes. Therefore, this characteristic bias-dependent shape change is assigned to an electronic effect. Even though CoTPP is quite well investigated by STM, this specific appearance with a centered protrusion was not reported in literature so far. This is especially remarkable since the observed shape intuitively resembles the proposed enhanced tunneling through the half-filled  $d_{z^2}$  orbital.

To obtain a detailed understanding of the experimental findings, STM images of CoTPP, FeTPP and 2HTPP have been simulated via periodic density functional calculations for various bias voltages. These calculations were performed in the working group of Andreas Görling and were recently published as a joint experimental and theoretical study [140]. To corroborate the topographic interpretation given above for each species two different molecular geometries have been considered, with phenyl ring dihedral angles (i.e., angle between the planes of the phenyl group and the porphyrin macrocycle) of  $\Theta = 90^\circ$  and  $\Theta = 60^\circ$ . This is resulting in a planar, and a saddle-shape of the central porphyrin core, respectively (see chapter 4.1). To study the influence of the surface, all calculations were performed in the gas phase (i.e., at an infinite distance from the surface) and on a five-layer Ag(111) slab with a fixed molecule-substrate distance of 0.53 nm (for CoTPP also other distances were considered). A new aspect of this work is the explicit inclusion of the molecule-substrate interaction at this level of theory.

In the following the calculations for CoTPP on Ag(111) will be discussed in detail because the most pronounced bias-dependence was experimentally found for this system.

In figure 4.6.2.4 experimental high-resolution STM images of CoTPP on Ag(111) at low and high bias voltages are compared with corresponding calculated STM images using various settings. A comparison of the images for low bias voltage in figure 4.6.2.4 (upper row) shows that the bright feature in the molecular center is only reproduced in

the calculations if the surface is included, which indicates its important contribution to the observed bias-dependence.

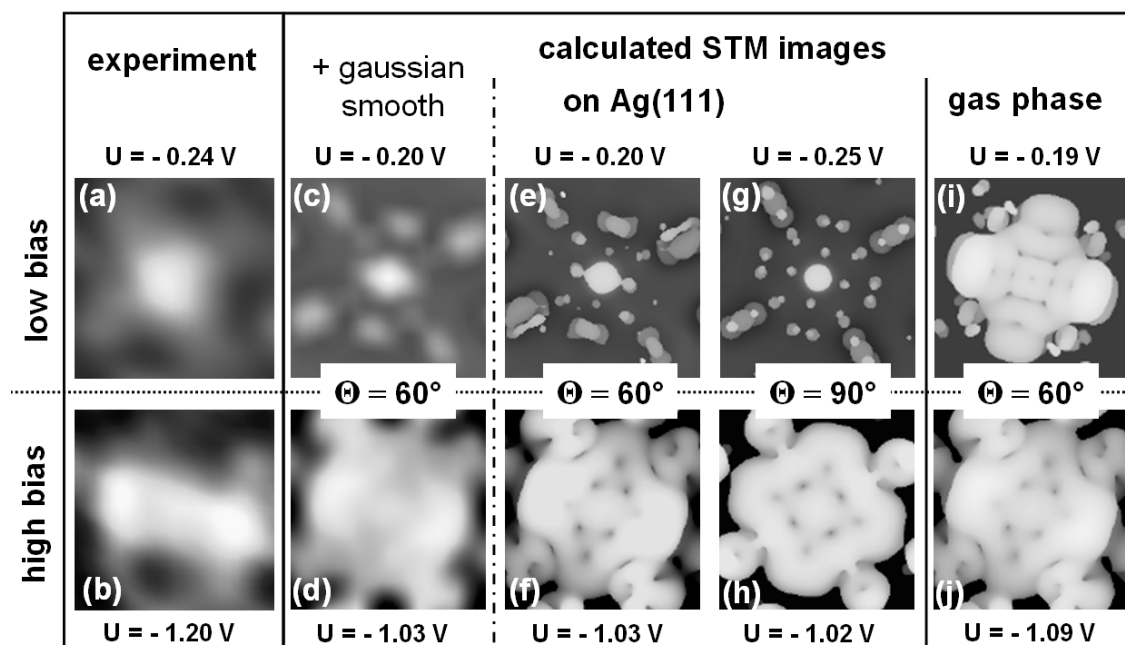


**Figure 4.6.2.4.** Experimental (a, b) and calculated (c-j) STM images of a single CoTPP molecule on Ag(111) at low negative (top row) and high negative bias voltages (bottom row). As indicated in the images the calculations were performed for the porphyrin adsorbed on Ag(111) and for the porphyrin in the gas phase as well as for different intramolecular geometries ( $\Theta = 60^\circ$  and  $\Theta = 90^\circ$ ). The experimental observation of the central protrusion at low bias voltages in (a) could only be reproduced in the simulations in (c), (e) and (g), where the CoTPP is adsorbed on Ag(111), i.e., this characteristic feature could not be reproduced for the gas phase calculations as shown in (i) even though the same molecular geometry has been used. The experimentally observed saddle-shape in the high bias regime in (b) was reproduced assuming  $\Theta = 60^\circ$  in (d), (f) and (j). Thus a good agreement for both bias regimes could only be achieved considering both the molecule surface interaction as well as the dihedral angle  $\Theta = 60^\circ$ . In the calculations an indefinitely sharp tip is assumed, which results in unrealistic details in the calculated STM images. To exemplarily address this problem a gaussian smooth was applied to the images (e) and (d), the results are shown in (c) respective (d).

On the other hand, the STM images for 2HTPP and FeTPP exhibit only minor differences when comparing the calculations with and without including the substrate (not shown); this implies that for those molecules the incorporation of the surface is not essential to achieve reasonable agreement with the experiment.

Second, the geometry of the adsorbed CoTPP molecule is mandatory to reproduce the rod-like shape in the corresponding STM image as can be seen from the data at high bias voltage shown in figure 4.6.2.4 (lower row). The dihedral angle of the phenyl ring of  $60^\circ$  (cf. figure 4.6.2.4 b) goes along with a saddle-type deformation of the porphyrin core with two opposing pyrrole rings bent towards the surface while the other two pyrrole rings are bent away from the surface and hence are closer to the tip of the STM. The rod-shaped appearance of the STM image is thus mainly a consequence of the fact that the two lower pyrrole rings are less "visible" in the STM image for topographic reasons (compare figure 4.6.2.4 (b)). On the other hand, for an undistorted porphyrin core with a dihedral angle of  $90^\circ$  a more or less square-shaped image is obtained from the calculation, because all pyrrole groups have the same distance to the tip. However, such a "square-shaped" STM image is not observed in the experiments. It is therefore concluded that a dihedral angle  $\Theta$  close to  $60^\circ$  or at least with a significant deviation from  $90^\circ$  has to be assumed as the real adsorption geometry. The same appearance is also found for 2HTPP and FeTPP in the present study; similar results were also obtained for CoTPP on Cu(111) and were reproduced by gas phase calculations of the molecular orbitals with extended Hückel theory [100].

Figures 4.6.2.5 (a) and (b) show results from an optimized image preparation process in which the images for the individual molecules were calculated separately, then merged (left: 2HTPP, middle: CoTPP, right: FeTPP) and in the final step a Gaussian smooth was applied. These calculated images are juxtaposed to 3D images (figure 4.6.2.5 (c) and (d)) which were extracted from experimental data. In total, figure 4.6.2.5 shows an almost perfect agreement of the main features of the theoretical and the experimental data drawn as 3D-plots, thus corroborating the accuracy and potential of the present theoretical approach.

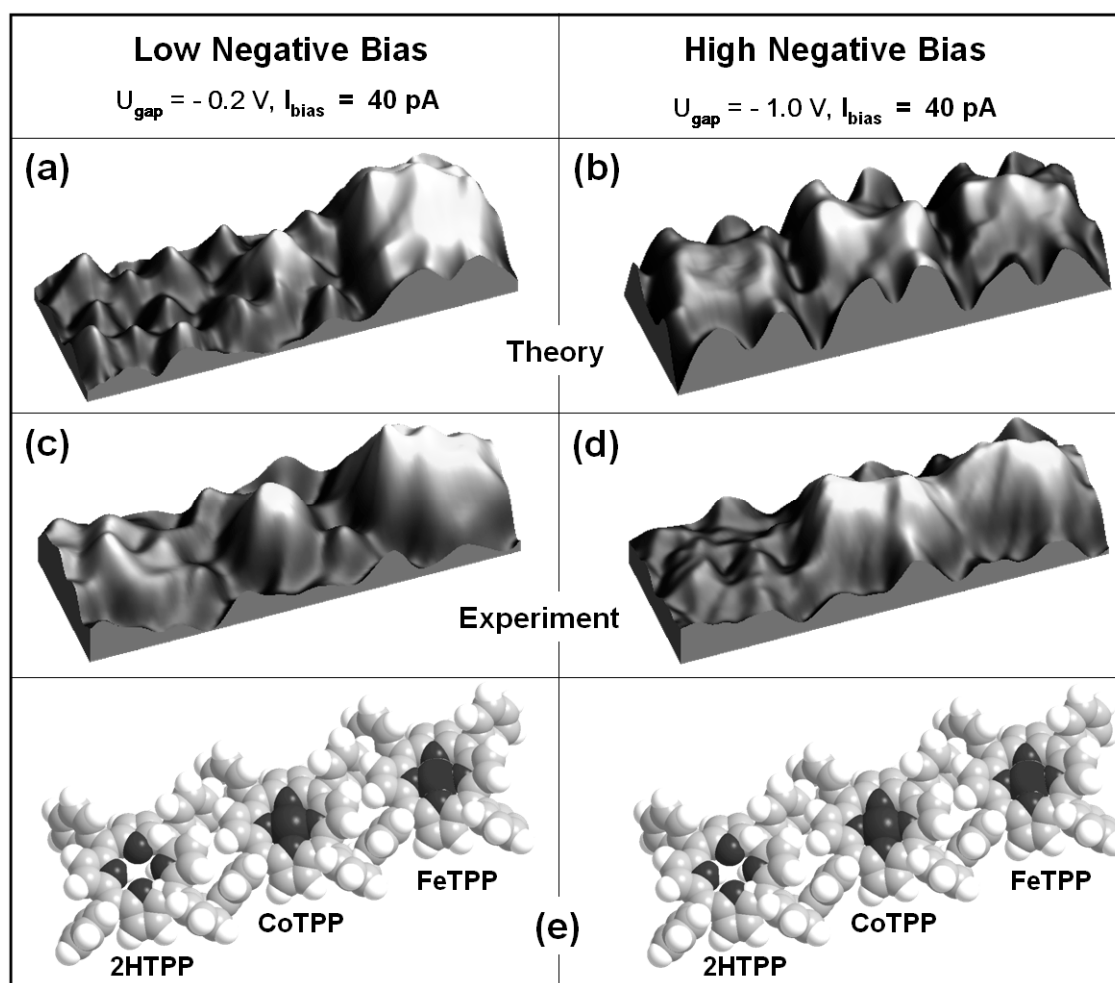


**Figure 4.6.2.5.** Comparison of calculated (a,b) and experimental (c,d) constant current STM images and the corresponding scaled molecular models (e). The calculations were performed individually for the single molecules with the porphyrins adsorbed on Ag(111) and with a phenyl-ring twist angle of  $\Theta = 60^\circ$  (saddle-shape of porphyrin core). The resulting calculated data was then merged in the shown molecule sequence and after that a Gaussian smooth was applied (compare figure 4.6.2.4 (c) and (d)).

Overall, the most striking feature observed experimentally is the pronounced bias-dependence of the STM images of CoTPP. This behavior was reproduced in calculated STM images as evident from figures 4.6.2.4 and 4.6.2.5. Since the molecular conformation of the porphyrin molecules is the same in these simulations, the agreement between theory and experiment proves that the bias-dependent appearance of

CoTPP is solely due to an electronic effect. A detailed analysis in terms of single-particle states (orbitals) is performed in order to explain the general shape of the STM images and the pronounced bias-dependence for CoTPP.

First, the relevant features of the electronic structure of an isolated CoTPP molecule in the gas phase are briefly discussed: The two highest occupied molecular orbitals (HOMOs, labels 115 and 116 in figure 4.6.2.6) are almost degenerate, with large contributions from  $\text{Co}(d_{xz}/d_{yz})$  and  $\pi$ -type orbitals located on the TPP ring. As the  $\text{Co}(d_{z^2})$  orbital is singly occupied in CoTPP two spin channels have to be distinguished. The occupied  $\text{Co}(d_{z^2})$  spin orbital ( $111\alpha$ ) is computed at -1.8 eV, i.e., at a significantly lower energy than the frontier orbitals, while the corresponding unoccupied spin orbital is found to be the lowest unoccupied orbital (LUMO,  $117\beta$ ). In the presence of the surface, the character of the frontier orbitals is changed. The highest occupied orbital (i.e., the new HOMO, label  $941\beta$ , cf. figure 4.6.2.6) is now composed of the  $\text{Co}(d_{z^2})$  orbital and of Ag 5s atomic orbitals from the silver slab (see figure 4.6.2.6). Note that the gap between the corresponding orbitals is reduced. Generally speaking, it thus becomes evident that there is a direct orbital interaction of CoTPP with the substrate as indicated by the new HOMO  $941\beta$  close to the Fermi energy. This goes along with findings by photoelectron spectroscopy (XPS, UPS) that show a strong electronic interaction of CoTPP with the underlying Ag(111) substrate, mediated by the  $d_{z^2}$  orbital [73, 109].

Based on this analysis, the experimental observation of a single bright spot in the STM image of CoTPP at low bias voltage and a rod-like structure at high bias voltage can be explained as follows. At low bias (i.e., below  $\sim 0.3$  eV, according to the calculations, cf. figure 4.6.2.6), the  $\text{Ag}(5s)+\text{Co}(d_{z^2})$  HOMO (label  $941\beta$ ) is the only orbital within the energy window defined by the bias voltage and the Fermi level, which has a significant amplitude on the adsorbed CoTPP molecule and is therefore close enough to the STM tip to contribute to the tunneling current. (Note that the levels of the silver surface below the molecule are not visible in the STM image due to their large separation from the tip.) This orbital therefore dominates the STM image, i.e., it exclusively makes up for the central spot in both the simulated and the experimental

STM image observed a low bias. Side views for different density contour values of this crucial orbital 941 $\beta$  are plotted in figure 4.6.2.7. Here the  $d_{z^2}$ -character of the orbital becomes evident. At higher bias voltages (meaning that lower-energy bands also contribute to the STM image) the CoTPP orbitals (938 $\beta$  and 939 $\beta$  in figure 4.6.2.6) with a large contribution from Co( $d_{xz}/d_{yz}$ ) atomic orbitals and  $\pi$ -type orbitals on the carbon skeleton dominate the simulated STM image.

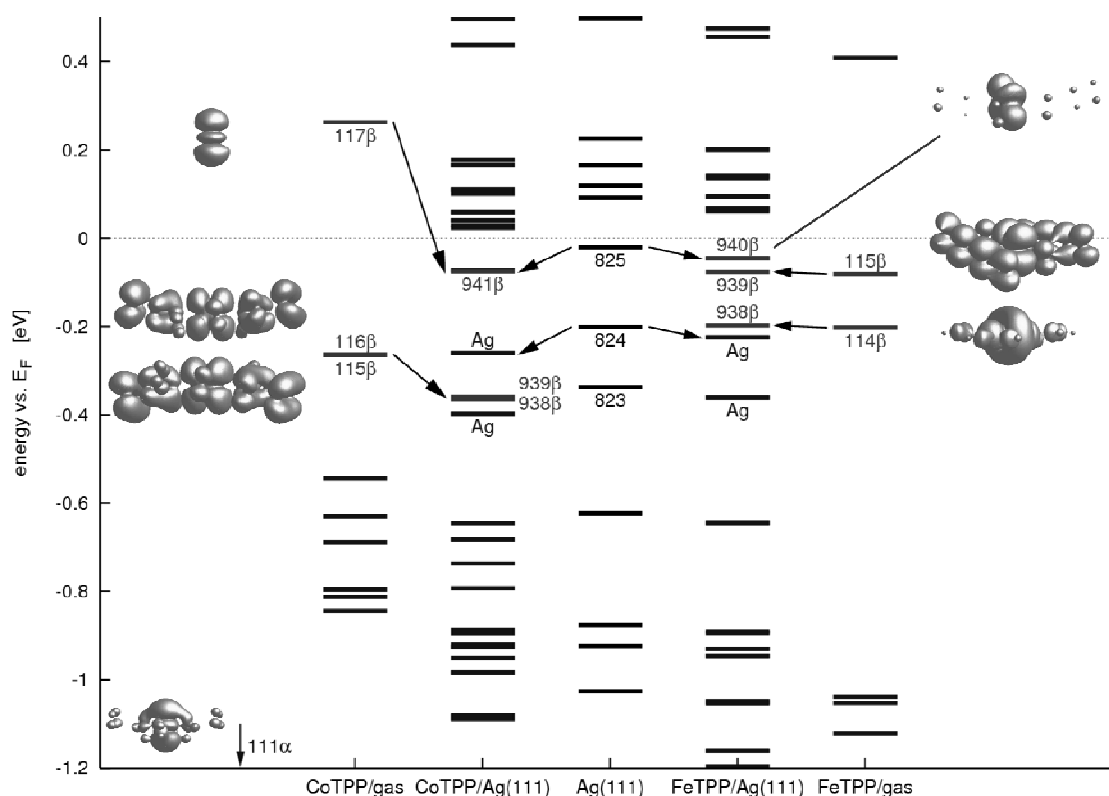


**Figure 4.6.2.6** Density-functional single-particle energy levels of CoTPP (left column), FeTPP (right column), Ag(111) (center, black) and the corresponding adsorbate systems MTPP/Ag(111) (2nd and 4th column). The energy levels have been shifted for each column such that the Fermi energy ( $E_F$ ) is zero; spin label  $\beta$  corresponds to minority spin channel; energy levels of orbitals which significantly contribute to the STM image (cf. figure 4) are color-coded in red; black arrows indicate the contribution of MTPP and Ag(111) orbitals to the corresponding level in the adsorbate system; contour images of salient orbital densities of MTPP have been generated based on a density contour value of  $2.5 \cdot 10^{-3} e/\text{\AA}^3$ .

The shape of these orbitals closely follows the topography of the porphyrin ring, i.e., the saddle-shape for the intramolecular conformation with  $\Theta = 60^\circ$  and two pyrrole rings at opposite sides of the TPP core bent towards the surface and the other two away from it, as discussed above. (Note that assuming a hypothetical, perfect  $D_{2d}$  or  $D_{4h}$  symmetry of the CoTPP molecule, these orbitals descend from the degenerate set of orbitals corresponding to a two-dimensional E irreducible representation.) Hence, the two orbitals with labels 938 $\beta$  and 939 $\beta$ , while being almost degenerate, contribute to the STM image to a different extent due to the saddle-shape of adsorbed CoTPP, i.e., due to topographic effects. This results in the rod-like shape of the submolecularly resolved STM image at high bias voltages, in full agreement with the experimental image (figures 4.6.2.4 and 4.6.2.5) and the appearance of CoTPP and also FeTPP reported in literature so far (at high negative bias voltages).

Note that the central spot is still observed at low bias in STM images of the hypothetical, flat structure ( $D_{4h}$  symmetry,  $\Theta = 90^\circ$ ) of CoTPP, see figure 4.6.2.4 (g) and (h). Again, at high bias the image is dominated by density covering the whole adsorbate molecule. The reason is that in the now flat  $D_{4h}$  symmetric molecule the orbitals corresponding to 938 $\beta$  and 939 $\beta$  from figure 4.6.2.6, which form a degenerate orbital set of E symmetry in the molecules without the surface, no longer are discriminated topographically, and consequently a rod-shaped image is not obtained at any bias voltage. In summary, this means that for CoTPP the STM image is dominated by the details of the electronic structure at low bias voltages, whereas the topography of the adsorbed molecule becomes important at high bias voltages.

In contrast to the situation for CoTPP, the shape of the STM images of 2HTPP and FeTPP shows no pronounced bias-dependence, in neither experiment nor computation. This observation can be rationalized based on their different electronic structures as compared to CoTPP. On the right hand side of figure 4.6.2.6 the orbital energy levels of gas-phase FeTPP and the Ag(111) slab are juxtaposed to the levels of the FeTPP+Ag(111) adsorbate system. Once again, the highest occupied level (label 940 $\beta$ ) is a Ag band with a small admixture of an orbital centered mostly on the Fe center of FeTPP. Only slightly below in energy the HOMO-1 (label 939 $\beta$ ) is computed. It is built

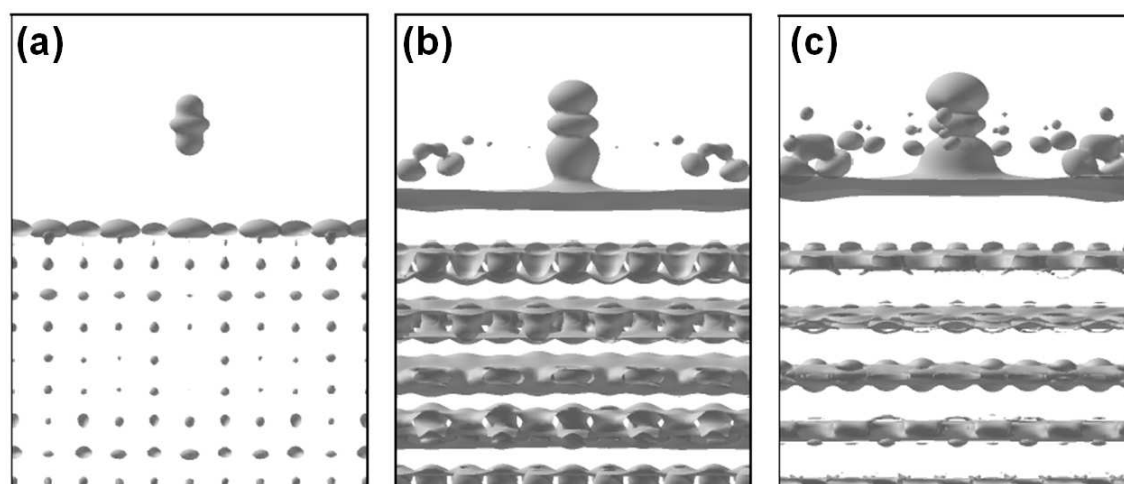


**Figure 4.6.2.7.** Side-view of the orbital density of the highest-occupied orbital (labeled  $941\beta$  in figure 6) in the CoTPP/Ag(111) adsorbate systems at three different density contour values, showing that the  $d_{z^2}$  orbital on the cobalt center of CoTPP has a constructive overlap with the silver 5s band; left:  $17.5 \cdot 10^{-4} e/\text{\AA}^3$ , center:  $1.5 \cdot 10^{-4} e/\text{\AA}^3$ , right:  $0.5 \cdot 10^{-4} e/\text{\AA}^3$ .

from the Fe( $d_{xz}/d_{yz}$ ) orbitals and a  $\pi$ -type orbital located on TPP, very similar to orbitals  $115\beta$  /  $116\beta$  for CoTPP. About 0.1 eV below is another orbital ( $938\beta$ ) with Fe(d) contribution (Note that there is no degeneracy due to the deviation from  $D_{2d}$  symmetry as predicted by the gas-phase geometry optimizations). The important difference between adsorbed CoTPP and FeTPP is that for FeTPP+Ag(111) the  $\pi$ -type orbital ( $939\beta$ ) is very close in energy to the HOMO, so that the STM image is always determined by both orbitals and thus never displays a central protrusion as for CoTPP, not even at low bias. In other words the relevant energy levels in the FeTPP adsorbate system are energetically too close to each other to be resolved experimentally, in contrast to the situation for CoTPP (left part of figure 4.6.2.6).

Finally, for the 2HTPP adsorbate system (energy levels and orbitals not shown), the situation is quite trivial because there is no central metal and therefore no central protrusions are observed in the STM images. Hence, the shape of the STM image is dominated by the  $\pi$ -levels of the porphyrin ring and orbitals on the peripheral phenyl rings.

## CONCLUSION

The main goal of this chapter is to understand the bias-dependence of the appearance of various tetraphenylporphyrins on a Ag(111) surface in STM images. To allow for a direct in-situ comparison of different porphyrins, a preparation route to generate an intermixed layer with a defined composition of 2HTPP, CoTPP and FeTPP molecules on Ag(111) was successfully introduced. In addition, state-of-the-art density-functional slab calculations were performed, which explicitly include the interaction of the porphyrins with the substrate. They provide a consistent interpretation of the bias-dependent STM contrast in terms of the electronic structure of the adsorbate complex. Taking into account the coupling to the substrate is absolutely essential to obtain a good agreement between experimental and simulated STM images and to reproduce their bias-dependent shape for negative bias voltages, from  $-1.5$  to  $-0.1$  V. This is particularly true for low negative bias voltages, where the highest occupied orbitals of the adsorbed porphyrins dominate the STM images. The inclusion of adsorbate-substrate interaction for systems of this size is an important new aspect of the present work, since previous calculations of STM images on similar systems either did not include the substrate at all or were performed at a semi-empirical level [100,139].

The most peculiar observation in the STM images is the pronounced bias-dependence of the appearance of CoTPP: at low negative bias voltages (roughly  $-0.1$  V to  $-0.4$  V), this molecule appears with a central protrusion, which transforms into a dumbbell shape at larger negative bias voltages (below  $-0.4$  V). In contrast, 2HTPP appears with a central depression while FeTPP also features a dumbbell-like shape, but with no pronounced bias-dependence in the investigated bias range. The characteristic appearance of CoTPP featuring a central protrusion at low bias voltage could be tracked down to an orbital predominantly composed of Ag 5s orbitals of the silver slab and the Co( $d_{z^2}$ ) orbital of CoTPP.

CoTPP/Ag(111) can thus be regarded as a prototype example where the STM image is clearly dominated by an electronic effect under certain conditions, i.e., at low negative bias voltages. For 2HTPP and FeTPP in the whole investigated bias range as well as for CoTPP at high negative bias voltages the appearance of the molecules is

found to be mainly determined by topographic effects, i.e., the conformation of the porphyrin molecules. Here a dihedral angle of  $\Theta = 60^\circ$  between the planes of the porphyrin macrocycle and the phenyl substituents, resulting in a saddle-shape deformation of the porphyrin core, led to a good agreement of simulated and experimentally determined STM images, in accordance with the literature.

It is important to note that those STM images which are dominated by topographic effects could probably also be simulated using calculations reported in the literature so far, i.e., without explicitly considering the molecule-substrate interactions. However, the strong bias-dependence found for CoTPP clearly demonstrates the necessity to consider the whole adsorption complex in order to achieve an accurate and complete understanding. This system is one of the few clear-cut cases, where the electronic and the topographic contributions can be unequivocally distinguished. Thus a detailed understanding of the appearance of the large organic molecules in STM could be accomplished, and it is furthermore demonstrated that by a bias-dependent switching of STM images a clear distinction of topographically and electronically similar molecules is possible.

### 4.6.3 Addressing Molecular Orbitals of Cobalt- and Iron-Tetraphenylporphyrins by Continuous Imaging Tunneling Spectroscopy

---

In addition to the acquisition of constant current images of multicomponent adlayers on Ag(111) at RT (chapter 4.6.2), continuous imaging tunneling spectroscopy (CITS) was performed. The method takes advantage of the potential to acquire maps of the local density of states (LDOS). This allows the addressing of molecular orbitals of the porphyrins at selected energies near the Fermi level. By recording such maps, considering the occupied states, it was found that orbital mediated tunneling (OMT) contributes from the central  $Co(d_{z^2})$  atomic orbitals (see chapter 4.6.2) within an energy range from roughly -300 meV to  $E_F$ . The LDOS maps also reveal that below this energy two distinctive spots evolve, which can be traced back to mediated tunneling contribution from  $Co(d_{xz}/d_{yz})$  atomic orbitals (see chapter 4.6.2). LDOS maps of FeTPP strictly show two opposing spots (rod-like shape), which in turn can be attributed to mediated tunneling from a set of orbitals which are energetically too close together to be resolved (see chapter 4.6.2). These peculiar spectro-microscopy findings were also confirmed for a three-component adlayer where the observed electronic fingerprints of the CoTPP and FeTPP could be reproduced.

#### **INTRODUCTION**

Generally, one can state that the acquisition of STM images of porphyrins with sub-molecular resolution is a very challenging task. In medium-resolution micrographs the molecules often appear as homogenous features in the STM image [60] (see chapter 4.6.2). Obviously, it is desirable to gain deeper insight into molecular conformation and/or electronic structure by means of sub-molecular resolved STM micrographs. However, even if high-resolution STM images are available, structural and electronic information can generally not be separated from each other. Thus the interpretation of

the micrographs, in particular considering large molecules on solid surfaces, is difficult [141]. In contrast, STS (see chapter 2.3) can provide direct information of the molecular levels close to the Fermi energy. With the CITS technique current-voltage  $I(V)$  curves are acquired as a function of the lateral position  $(x,y)$  at constant tunnelling resistance. Simultaneously, a constant current image, providing the local variation of the apparent height  $h_{I=const}(x,y)$ , is recorded. The CITS routine results in a four-dimensional data set  $I(x,y,V)$ . From this the  $\partial I(x,y,V)/\partial V$  maps can be calculated, which are proportional to the LDOS [16]. If at a certain voltage OMT occurs,  $\partial I(x,y,V)/\partial V$  locally enlarges, resulting in orbital-specific features in the LDOS maps. The precondition to visualize molecular orbitals is, that the adsorbed molecule exhibits well-separable energy levels [142]. Few publications have dealt with CITS, whereupon the experiments were mostly performed at low temperatures, particularly on metal and semiconductor surfaces [143, 144]. On organic adsorbates  $\partial I/\partial V$  mapping was accomplished by means of lock-in technique, whereby LDOS maps were recorded exclusively for selected peak energies predetermined from STS data. This was demonstrated e.g., for  $C_{60}$  on Ag(100) [145], CoTPP on Cu(111) [100] and a mixed layer of 2H-,Co- and CeTPP on Ag(111) [59]. Alam et al. demonstrated by CITS under ambient conditions, that the metal centers of a cobalt grid-type complex on highly oriented pyrolytic graphite can exclusively be addressed, whereupon the constant current images at RT lack a sub-molecular resolution. Later, this was also demonstrated for different metal ions inside supramolecular assemblies by the same group [146, 147]. In this chapter the goal was to characterize the highest occupied molecular orbitals of 2HTPP, CoTPP and FeTPP within an energy range from -1 eV to  $E_F$ .

## RESULTS

A monolayer of 2HTPP was thermally evaporated on Ag(111). Following the deposition of cobalt atoms, the 2HTPP molecules complexate with the metal, forming CoTPP, as reported in chapter 4.3.3 [104, 107, 148, 149]. Here the experimental focus was set on the electronic structure. In that course a region of  $(128 \times 128) \text{ \AA}^2$  was

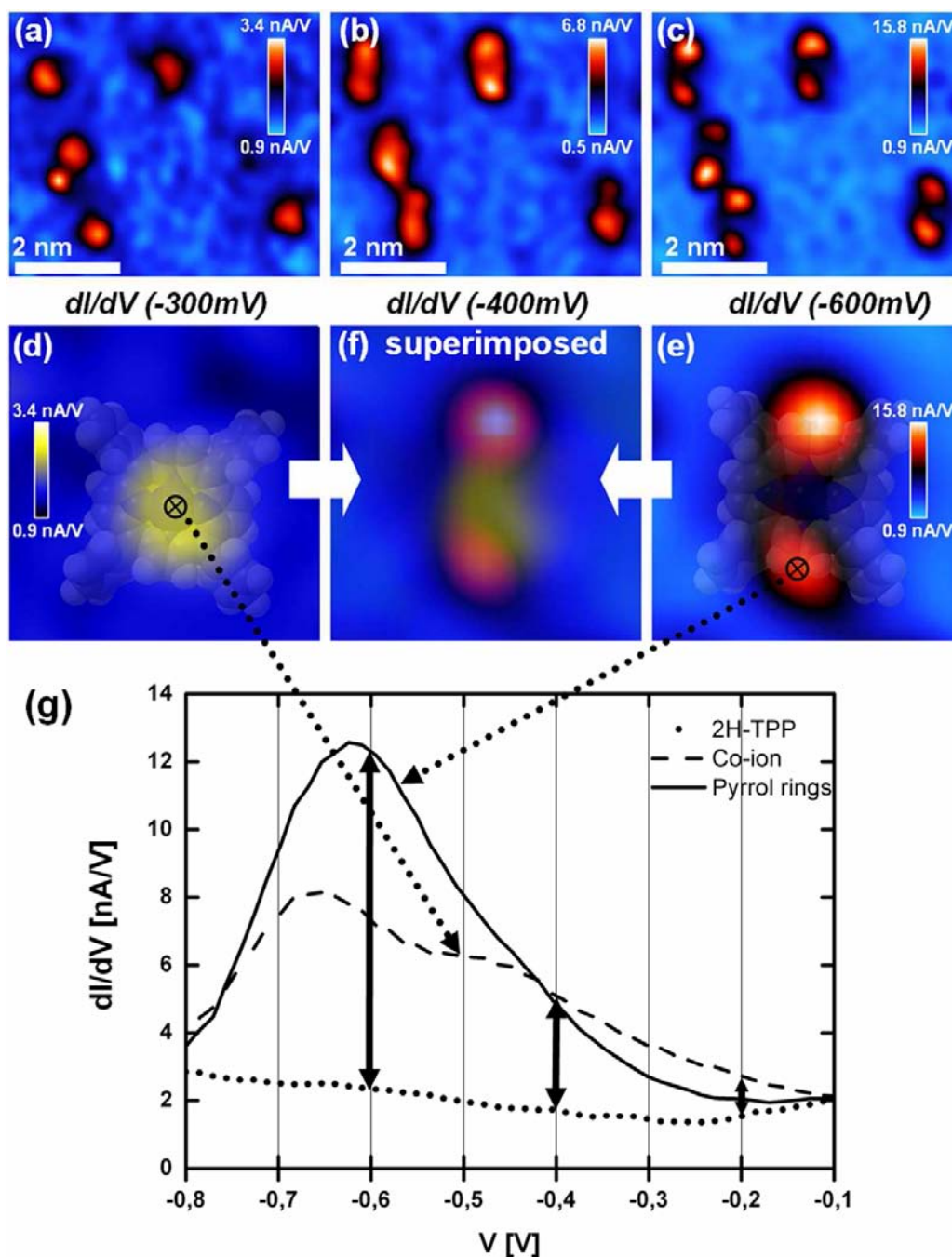


**Figure 4.6.3.1.** (a)-(c) LDOS maps of CoTPP, respectively 300 meV, 400 meV and 600 meV below the Fermi level, which were directly calculated out of experimentally acquired current-voltage curves. (d) and (e) Enlarged LDOS maps with corresponding semitransparent space-filling models. (f) Superimposition of (d) and (e) illustrating the relative location of the energy-disperse features to each other. (g) Local STS curves extracted at distinct positions of the LDOS maps.

Scanned and the feedback loop was interrupted at each pixel, equal to  $1\text{\AA}$ , while respectively one  $I(x, y, V)$  curve was recorded. Note that a constant current image (not shown) was acquired simultaneously at a set point of  $I = 48\text{ nA}$  and  $U = -170\text{ mV}$ , determining the position of the tip above the surface at each pixel, before ramping the voltage.

A  $\partial I(x, y, -300\text{mV})/\partial V$  map of the occupied states  $-300\text{ meV}$  below  $E_F$  is shown in figure 4.6.3.1 (a). Five bright features with an increased LDOS are clearly visible. Since the diameter of CoTPP is roughly  $1.9\text{ nm}$  it is clear that the dots, which have a diameter of roughly  $0.6\text{ nm}$ , can be identified as sub-molecular features. It is noteworthy to mention that the images are distorted by thermal drift due to the relatively long record time of roughly 5 minutes per measurement. The appearance of the dots can be interpreted to OMT from the  $Co(d_{z^2})$  orbital of the central cobalt ion.  $\partial I(x, y, -400\text{mV})/\partial V$  (figure 4.6.3.1 (b)) reveals, that exactly at the position of the bright dots, features with a rod-like shape evolve. Finally in  $\partial I(x, y, -600\text{mV})/\partial V$  (figure 4.6.3.1 (c)) the rod-like shaped objects split into two spots with the center anchored at the position of the dots shown in figure 4.6.3.1 (a). Thus the single dots can be correlated with the position of the central cobalt ion of CoTPP, whereas the two evolving spots with the two opposing pyrrol rings of the tetrapyrrolic macrocycle. The two spots  $600\text{ meV}$  below  $E_F$  can be assigned to mediated tunneling through  $Co(d_{xz}/d_{yz})$  atomic orbitals of CoTPP at the elevated pyrrol rings. The contribution of the electronic  $Co(d_{xz}/d_{yz})$  channel was discussed in chapter 4.6.2 with respect to the interpretation of constant current images [140]. In figures 4.6.3.1 (d) and (e) enlarged images of a single molecule, decorated with corresponding semi-transparent space-filling models are shown. To confirm that the observed dots are located in between the two evolving spots, a superimposed version of these two data sets (different colour coded) is shown in figure 4.6.3.1 (f). The distinct symmetry break in the maps can be explained by the distorted molecular geometry (“saddle-conformation”) (see chapter 4.1) [47, 59, 100]. By selectively performing STS on dissimilar pyrrol rings of the macrocycle for the system CoTPP on Cu(111) [100], it was shown by Weber-Bargioni et al., that the curves appear with different intensity. This also explains the electronic

asymmetry of the porphyrin macrocycle. Furthermore Weber-Bargioni et al. monitored two distinct spots for CoTPP adsorbed on Ag(111) in a  $\partial I(x, y, -600\text{mV})/\partial V$  map acquired by means of lock-in technique. The applied energy was chosen as it corresponds with a resonance peak in STS spectra [59]. The peak 600 meV below the Fermi level was confirmed in a recent study by UPS and STS (chapter 4.6.2) [60].

Particularly interesting in this work is the observation of a single dot per CoTPP in  $\partial I(x, y, -300\text{mV})/\partial V$  (figure 4.6.3.1 (a)), which was not shown in literature so far. Compared with the lock-in technique, one advantage of CITS is that at every pixel of the region of interest, a complete  $\partial I/\partial V$  spectrum is acquired. Thus the probability that OMT-specific features do remain undetected in discretely available LDOS maps ( $\Delta eU = 14\text{ meV}$ ) is low.

Based on the observations shown in figure 4.6.3.1 (a)-(c), local  $\partial I/\partial V$  spectra were extracted both at the position of the central cobalt ion and at that of opposing pyrrol rings (figure 4.6.3.1 (g)), determining the appearance in the LDOS maps. Between  $E_F$  and  $\sim 350\text{ meV}$  below, the LDOS at the central cobalt ion dominates, thus the dots, which are ascribed to as contributions from the  $Co(d_{z^2})$  orbital of the cobalt ion are visible in the LDOS maps. Following the STS data to 400 meV below  $E_F$  the tunnelling is mediated both by the latter effects and contributions from electronic channels from  $Co(d_{xz}/d_{yz})$  atomic orbitals. Below 400 meV contribution from  $Co(d_{xz}/d_{yz})$  atomic orbitals dominate, which is obvious both from the local spectra and the LDOS map.

CITS was also conducted on a mixed monolayer of FeTPP and 2HTPP. A 2HTPP covered Ag(111) surface was exposed to iron atoms, which complexated with 2HTPP forming FeTPP, as also described in chapter 4.3 [47, 56]. The simultaneously recorded constant current image was recorded at  $U = 203\text{ mV}$  and  $I = 46\text{ pA}$  (not shown). The  $\partial I(x, y, -90\text{mV})/\partial V$  map is shown in figure 4.6.3.2 (a), filtering the occupied states 90 meV below  $E_F$ . In contrast to CoTPP, even very close to the Fermi level, a rod-like shaped electronic signature, corresponding to the distorted molecular geometry, is

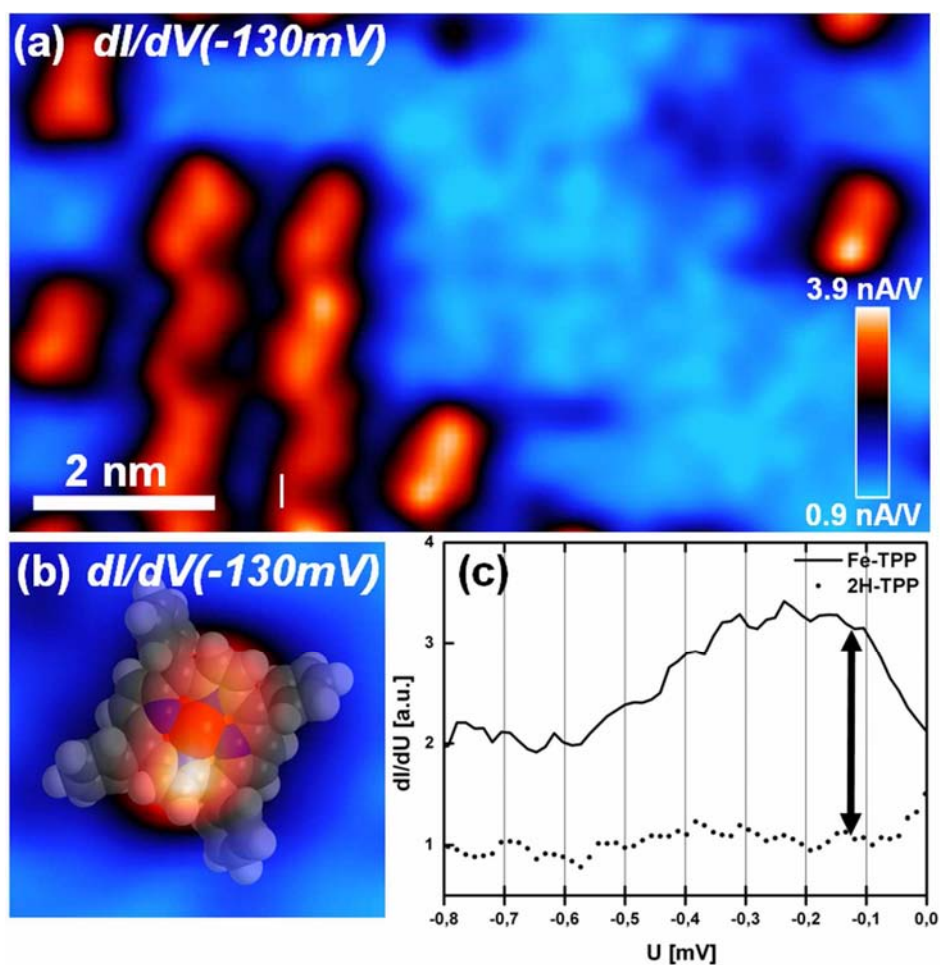


**Figure 4.6.3.2.** (a) LDOS map of FeTPP 130 meV below the Fermi level, which was calculated out of experimentally acquired current-voltage curves. (b) Enlarged LDOS map superimposed with a semitransparent space-filling mode. (c) Local ST curves extracted from FeTPP and 2HTPP.

observed. The latter continuously appears inside an energy range to roughly 400 meV below  $E_F$ . Note that no dot due to selective OMT over the central metal ion was found for FeTPP. The evolving rod-like shaped protrusion can be attributed to a set of orbitals built from  $Fe(d_{xz}/d_{yz})$  orbitals and TPP  $\pi$  orbitals. These orbitals are energetically too close to be resolved by STS at RT, as reported in chapter 4.6.2. The corresponding STS spectrum is displayed in figure 4.6.3.2 (c). A broad peak can be seen, which increases in close proximity to the Fermi level and decays at roughly 500 meV below  $E_F$ .

To further verify these spectro-microscopic findings, a three-component adlayer was prepared. The corresponding layer was prepared by thermal sublimation of a mixture of 2HTPP and CoTPP (1:3) on Ag(111) followed by dosing a small portion of iron which complexates with available 2HTPP (see chapter 4.6.2). figure 4.6.3.3 (a) shows a constant current image ( $U = 202$  mV and  $I = 36$  pA) of the three component adlayer of FeTPP, CoTPP and 2HTPP, which was simultaneously recorded with the CITS routine. The square arrangement is highlighted by the drawn in unit cell. Figure 4.6.3.3 (b) is a blow up of the micrograph shown in (a) and figure 4.6.3.3 (c) represents the corresponding LDOS map  $\partial I(x, y, -150\text{mV})/\partial V$ . Three different species are distinguishable in the constant current image and are marked by numbers. Roughly one third of the molecules exhibit an increased apparent height (label 1), one third shows a weak central protrusion (label 2) and the remaining appear relatively featureless (label 3). In the LDOS map three different molecular species can be clearly identified on the basis of the results shown before. In the LDOS maps in figure 4.6.3.1 (a) and 4.6.3.2 (b) it was found, that around 200 meV below  $E_F$  the CoTPP and FeTPP reveal individual electronic fingerprints, e.g., a central dot for CoTPP and a rod-like shape, respectively two spots, for FeTPP. For 2HTPP no peculiar electronic feature could be monitored in the experiments. Thus FeTPP (label 1) and CoTPP (label 2) can clearly be identified inside the  $\partial I(x, y, -150\text{mV})/\partial V$  map, whereas the discrimination inside the constant current image acquired at a bias of 202 mV is not as pronounced.

In figure 4.6.3.3 (d) and (e) enlarged images of the same region but at different energies are depicted. In  $\partial I(x, y, -200\text{mV})/\partial V$  FeTPP (label 1), CoTPP (label 2) and 2HTPP (label 3) are depicted. In  $\partial I(x, y, -800\text{mV})/\partial V$  (figure 4.6.3.3 (e)) the electronic structure priory visible for FeTPP (label 1) faded. This is reasonable, as the value of the  $\partial I(V)/\partial V$  curve (figure 4.6.3.2 (c)) is strongly decreased below 500 meV. As expected CoTPP (label 2) now appears with two spots (figure 4.6.3.3 (e)). In figure 4.6.3.3 (f)  $\partial I(x, y, -200\text{mV})/\partial V$  and  $\partial I(x, y, -800\text{mV})/\partial V$  were differently colour coded and superimposed to show the relative location of the observed CoTPP dot (figure 4.6.3.3 (d)) with respect to the two CoTPP spots (figure 4.6.3.3 (e)). The dot is anchored in between the two spots and can be correlated with contributions from molecular orbitals,

as demonstrated before with respect to the two-component layer. 2HTPP (label 3) shows no pronounced electronic signature within the multicomponent layer. In particular, the individual electronic fingerprints of Fe- and CoTPP could be reproduced even inside a multicomponent adlayer.

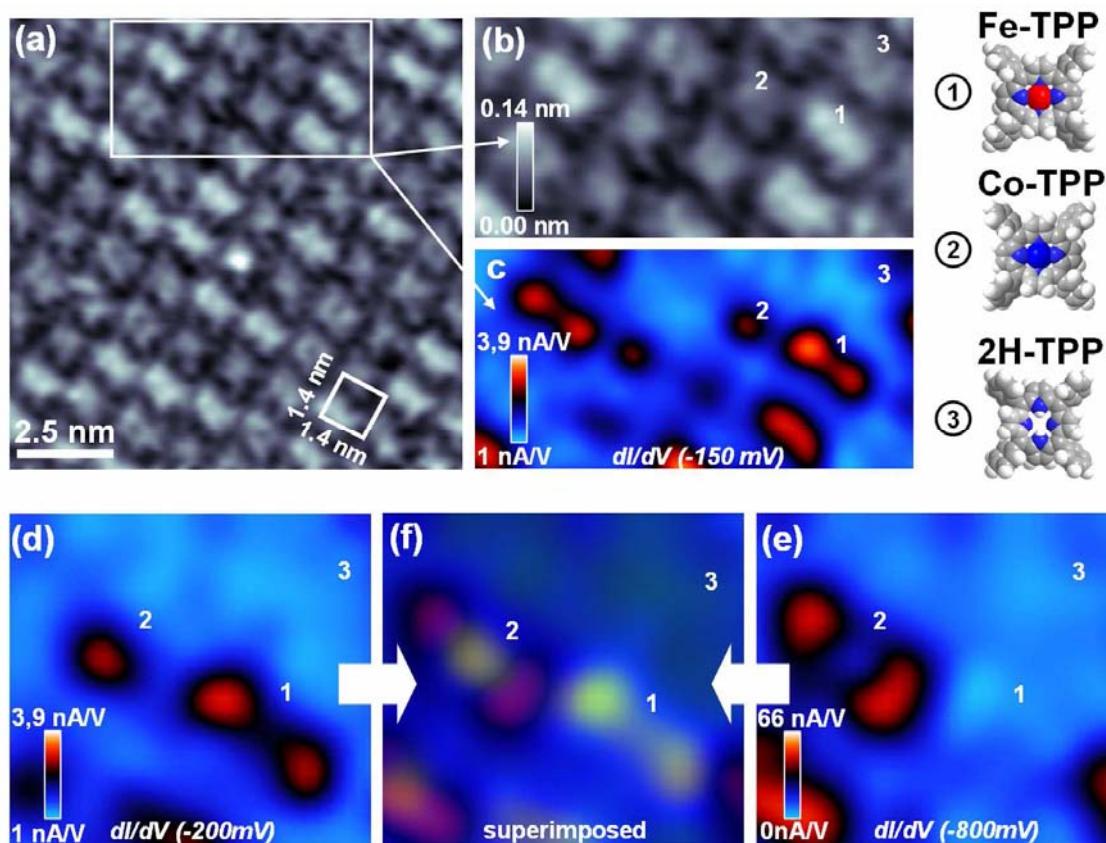


**Figure 4.6.3.3.** (a) Constant current image recorded at  $U=202$  mV and  $I=36$  pA. (b) Enlarged version of (a) with the individual molecules marked by numbers and space-filling models nearby. (c) Corresponding LDOS map of the same area 150 meV below the Fermi level. (d) and (e) Enlarged LDOS maps respectively 200 meV and 800 meV below  $E_F$ . (f) Superimposed version of (d) and (e) illustrating the relative position of the energy-dispersive features.

## CONCLUSION

The CITS technique allowed to extract electronic information of 2HTPP, CoTPP and FeTPP adsorbed on Ag(111), whereupon molecular orbitals could be visualized, displaying individual electronic fingerprints. The procedure was performed on mixed layers of 2HTPP/CoTPP and 2HTPP/FeTPP as well. Furthermore, the reproduction of the results in a multicomponent adlayer containing 2HTPP/CoTPP/FeTPP was successful. In particular, for CoTPP energy-dependent contributions both through the  $Co(d_{z^2})$  orbital ( $\sim -300$  meV to  $E_F$ ) and  $Co(d_{xz}/d_{yz})$  atomic orbitals ( $< -400$  meV) were separately visualized. For FeTPP continuously ( $< E_F$ ) an anisotropic electronic signature could be observed, corresponding to mediated tunneling through the  $Fe(d_{xz}/d_{yz})$  atomic orbitals and an orbital located mostly on the Fe center. These energy levels are too close to be resolved by STS at RT.



## 4.7 Modification of the Growth of Iron on Ag(111) by Predeposited Organic Monolayers

---

The modification of the growth behavior of iron on Ag(111) by preadsorbed monolayers of 2HPc and 2HTPP with STM, upon Fe deposition in UHV at RT was studied. The growth of iron on clean Ag (111) follows the scheme expected from reports of similar systems: For low coverages (up to  $\sim 0.3$  ML) an almost exclusive agglomeration of iron clusters at step edges occurs, with continue to grow in a dendritic fashion at higher coverages. Upon deposition onto Ag(111) precovered with monolayers of 2HTPP and 2HPc, at coverages up to 0.037 ML no growth of Fe islands but complete metalation, i.e., incorporation of the Fe atoms in the macrocycle of the preadsorbed molecules is found (see chapter 4.3 and 4.5). For higher amounts of deposited Fe ( $0.037 \text{ ML} < \theta_{Fe} < 0.30 \text{ ML}$ ), the formation of Fe islands is observed, which occurs differently for 2HPc and 2HTPP. While on 2HTPP two-dimensional islands are formed underneath a FeTPP monolayer, for 2HPc the behavior is dominated by the formation of small 3D-islands on the FePc monolayer. At  $\theta_{Fe} = 2.0 \text{ ML}$ , both systems exhibit small three dimensional Fe islands. These results are discussed considering different aspects like the molecular conformation of FeTPP and FePc on Ag(111) and the diffusion properties of Fe on the clean and modified substrate.

### INTRODUCTION

The heteroepitaxial growth of thin films on metal substrates is of fundamental interest for different branches in natural sciences and technology. The initial stages of this process (i.e., at low coverages of the deposited materials) have been subject of intense investigations due to their role as a determining factor for the morphology of the films to be grown and, at least equally important, as a method to generate low-dimensional structures. Since the physical and chemical properties of self-assembled structures depend on their size and shape, considerable efforts has been made to explore the processes underlying their formation, in order to be able to tune the growth with the

final goal to generate tailored nanostructures. One prominent target in this regard is the engineering of magnetic nanostructures for high density data storage devices. Here, a number of different model systems with ferromagnetic metals (Co, Fe, Ni) as the deposited material on, e.g., noble metal single crystal surfaces were investigated by STM in UHV. In basically all of these systems the agglomeration of 3D clusters was observed. In a simplified picture, this growth behavior is triggered by a sufficient lattice mismatch between the substrate and the deposited material. As a consequence, the nucleation of small 3D clusters with the intrinsic lattice constant of the material is energetically more favorable than layer by layer growth, which would induce high strain. The clusters mainly nucleate on defect sites, dislocations or other sites, where the deposited material has a reduced mobility. The actual shape and distribution of the clusters can be influenced by, e.g., the substrate temperature [66, 67, 150], a buffer layer [151-154] and/or a more or less well defined patterns of nucleation sites [67, 150, 155, 156]. Examples for such patterns can be found in the nucleation of Ni islands [156] and Co clusters [67] at lattice dislocations of the Au(111) “herringbone” reconstruction or in the generation of a periodic array of Fe islands on a strain-relief pattern on a Pt(111) surface precovered with a Cu bilayer [155].

In this chapter, the growth of Fe on a Ag(111) is explored and how this growth is influenced by a monolayer of 2HTPP or a monolayer of 2HPc. Both molecules self-assemble on Ag(111) in a square order with a lattice constant of ~1.4 nm and therefore constitute a predefined pattern, which could presumably influence the diffusive properties of the deposited material; the coverage of a saturated monolayer corresponds to 0.037 ML (see chapter 3.7).

## 4.7.1 Growth of Fe on Ag(111)

---

In a first step the growth of Fe on the clean Ag(111) surface was studied. Therefore, a successive deposition of Fe with intermittent microscopic investigations was conducted; the corresponding STM micrographs are shown in figure 4.7.1. Starting with the three lowest coverages of  $\theta_{Fe} = 0.05, 0.25$  and  $0.50$  ML, the corresponding figures 4.7.1 (a), (b) and (c) reveal that the formerly clean atomic silver steps are now decorated with three-dimensional Fe islands. These islands exhibit an apparent height between  $0.4 - 0.8$  nm and a diameter of  $\sim 3.5$  nm. In this coverage range formation of islands on terraces is rare. The formation of metal clusters at steps was observed before for several other heteroepitaxial systems (e.g., Co on Ag(111) [67], Fe on vicinal Au(111) [68], Co on Cu(111) [69], and Cu on Si(111) [63]) and is exemplary for the Volmer-Weber growth mode. This formation of three-dimensional Fe clusters can be interpreted as due to the substantial lattice mismatch of  $\sim 15\%$  with the Ag surface. Considering the fact that the Fe atoms statistically impinge on the surface, but agglomerate at the step edges, one has to conclude that their diffusion length exceeds the terrace width at the given sample temperature, i.e., RT [63, 64]. The preferential nucleation positions are then caused by energetically favorable adsorption sites at the step edges and/or hindered diffusion (e.g., due to the Ehrlich-Schwoebel barrier [65, 66]). In the case of Fe on Ag(111), an intermixing of Fe with the Ag surface close to the steps is also likely to contribute to the observed arrangement of the 3D-islands [65].

Upon successively increasing the amount of Fe, from  $\theta_{Fe} = 0.5$  ML to  $10.3$  ML, an increasing number of three dimensional islands with steadily increasing size is found on the terraces, (figure 4.7.1 (d)-(i)). The scattered islands on the terraces for  $\theta_{Fe} = 0.50$  ML exhibit an apparent height of up to  $0.8$  nm, which closely resembles the maximum height observed for the clusters on the steps. Interestingly, Morgenstern et al. studied the growth of Co on Ag(111) also up to a coverage of  $\theta_{Co} = 0.50$  ML and found that the height of these Co islands also amounts to a maximum apparent height of  $0.80$  nm, which they identified with 4 layers of Co [67]. Co as the neighboring element to Fe

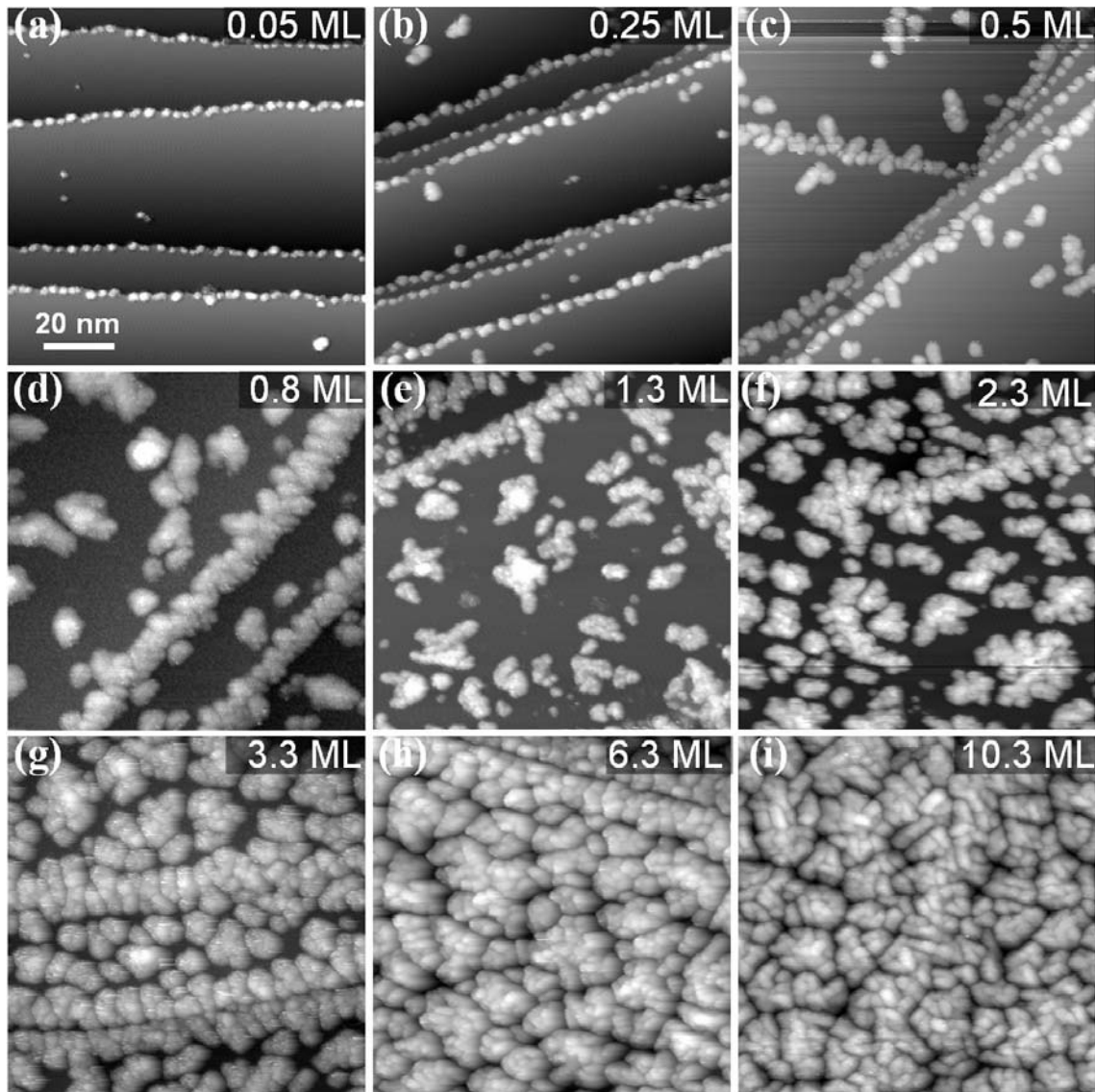


**Figure 4.7.1.** STM images acquired after successive deposition of iron onto Ag(111). The coverage  $\theta_{Fe}$  is indicated in the corresponding STM images. The size/scale of all shown micrographs is identical ( $100 \times 100$ ) nm<sup>2</sup>. The corresponding tunnelling parameters are: (a)  $I = 166$  pA,  $U = -930$  mV (b)  $I = 50$  pA,  $U = -263$  mV (c)  $I = 100$  pA,  $U = -287$  mV (d)  $I = 50$  pA,  $U = -212$  mV (e)  $I = 58$  pA,  $U = -289$  mV (f)  $I = 61$  pA,  $U = -305$  mV (g)  $I = 44$  pA,  $U = -199$  mV (h)  $I = 68$  pA,  $U = -302$  mV (i)  $I = 68$  pA,  $U = -313$  mV.

in the periodic table has very similar properties, e.g., the lattice constant is almost the same.

From this fact and the observation that the apparent heights of Fe islands and the height differences within the clusters in the present STM investigation were predominantly multiples of 0.2 nm, we conclude that the height of a single Fe layer amounts to  $\sim 0.2$  nm; consequently the local number of Fe layers can be estimated by dividing the apparent height by 0.2 nm.

The STM images shown in figure 4.7.1 (d)-(g) were recorded for iron coverages,  $\theta_{Fe}$ , ranging from 0.80 to 3.30 ML. The height of the clusters on the steps did not increase significantly, but the clusters grew laterally mainly perpendicular to the steps, from sizes of  $\sim 3.5$  nm for small coverages (figure 4.7.1 (b)) to about 20 nm for  $\theta_{Fe} = 3.30$  ML (figure 4.7.1 (g)). The lateral dimensions of the islands on the terraces also increased up to a diameter of 14 to 18 nm (figure 4.7.1 (g)), resulting in the decrease of “free space” in between the clusters. In this course, it is also observed that the maximum apparent height  $h(\theta_{Fe})$  of the iron clusters increased:  $h(0.5 \text{ ML}) \approx 1.0$  nm,  $h(1.30 \text{ ML}) \approx 1.4$  nm,  $h(3.30 \text{ ML}) \approx 1.6$  nm. It is noteworthy to mention that the highest values were mostly observed on the terraces. The Fe clusters on the steps show branches mainly perpendicular to the steps, whereas the islands on the terraces appear randomly branched, which was also observed in previous studies on fcc(111) surfaces [66, 157-159]. It is well-known that at RT a dendritic growth is not feasible [157] and fractal islands exhibiting the mentioned shape might evolve. This can be understood as a result of the energetic difference between the atom-atom bond energy within the islands and the strain energy due to the lattice mismatch [150]. The strain energy for Fe on Ag is relatively high due to the large lattice mismatch of approximately 15%, as mentioned above. The branching of the iron islands is induced by the compressive strain within the islands. Upon branching, the islands increase in perimeter, whereby strain can efficiently be released. At even higher Fe coverages of 6.30 and 10.3 ML (see figure 4.7.1(h) and (i), respectively), the Ag(111) surface is completely covered with Fe islands, i.e., there is no free space to allow for further lateral strain release. As a consequence the Fe clusters can just grow in height, which leads to apparent islands heights of up to 2 nm.

## 4.7.2 Growth of Fe on Ag(111) precovered with different tetrapyrrolic monolayers

---

The molecules to be studied as modifiers for the Fe growth are depicted as hard sphere models in figure 4.7.2 (a)-(d). The top view of a free base phthalocyanine (2HPc) molecule is shown in figure 4.7.2 (a), with the central “pocket” terminated by two hydrogen atoms clearly visible. This is also the general theme for the 2HTPP (not shown here). Upon evaporation of Fe onto a monolayer of 2HPc or 2HTPP in UHV, with the sample held at RT, one metal atom can be complexed in the central pocket under the release of the two hydrogens as H<sub>2</sub> [42]. This type of surface-mediated metalation reaction seems to be of general nature, since it has been reported to work similarly with very high yield for a variety of metals (e.g., Zn [62, 116], Co [42, 104] and Fe [56, 57, 61, 85, 134]) and different tetrapyrrolic molecules (e.g., 2HTPP [42, 56, 57, 62, 104, 116], 2HTPyP [47], 2HPc [134] and 2HTMPyP [85]). A model of FeTPP, i.e., 2HTPP metalated with Fe, is shown in figure 4.7.2 (b) in top view and (d) in side view. In figure 4.7.2 (e) and (f) high-resolution STM images of monolayers of in-situ metalated FePc and FeTPP are depicted, respectively. The metalation of the molecules is evidenced by their characteristic appearance [56, 57, 134] (note that the free base molecules 2HPc or 2HTPP appear with central depressions at similar tunneling conditions). The metalation reaction occurs with a yield close to 100%, i.e., the reaction is completed at a coverage of  $\theta_{Fe} = 0.037$  ML, which is the stoichiometric amount needed to coordinate each of the latter with one iron atom (chapter 4.3 and 4.5).

The FePc molecules are lying flat on the surface, exhibiting a square unit cell with a lattice constant of  $1.40 \pm 0.05$  nm (scaled molecule models are superimposed in figure 4.7.2 (e)). Each of the molecules appears with a central dot, due to a simple topographic effect and an enhanced tunneling contribution through the 3d<sup>6</sup> orbital system of the central Fe<sup>2+</sup> ion [134]. FeTPPs also form a square unit cell with the identical lattice constant (scaled molecule models are superimposed in figure 4.7.2 (f)). In contrast to the individual FePc molecule, FeTPP appears with reduced symmetry.

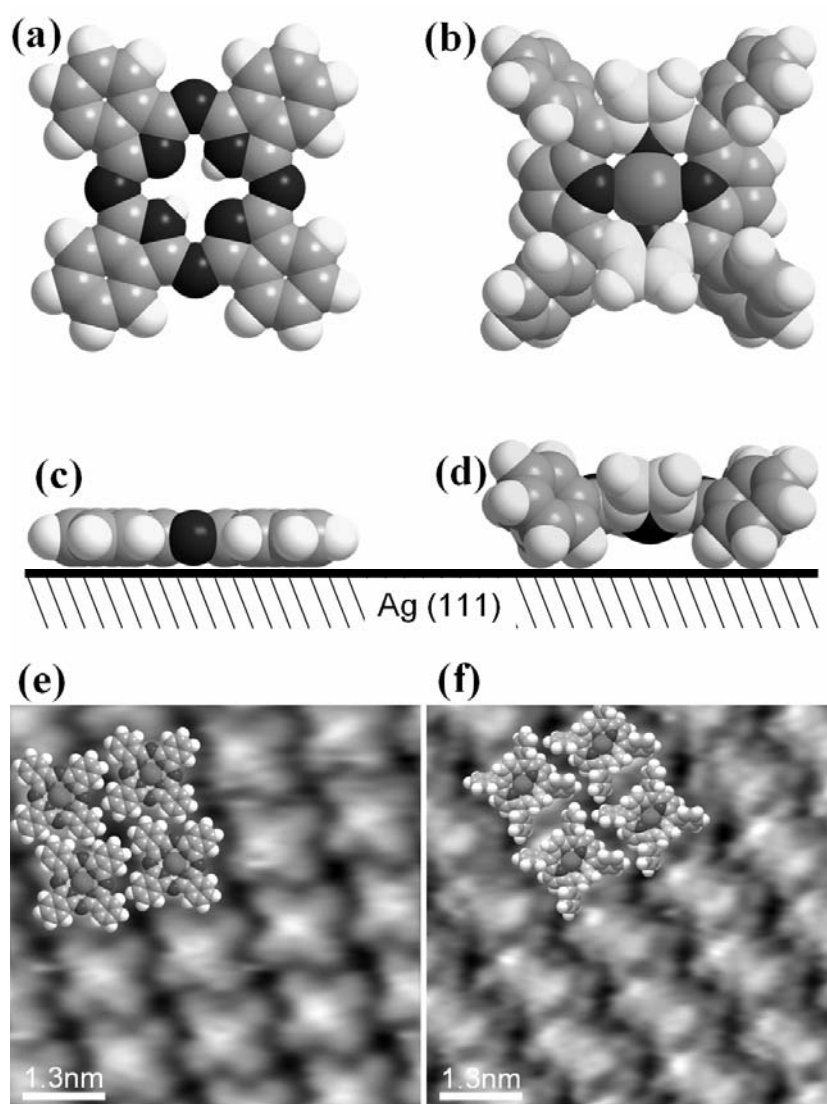


**Figure 4.7.2.** (a-d) space filling models of flat lying 2HPc and FeTPP on Ag(111): (a) top view of 2HPc, (b) top view of FeTPP, (c) side view of 2HPc(d) side view of FeTPP; for the latter, the terminal phenyl rings determine that the porphyrin macrocycle is lifted off from the surface. (e) STM image ( $I = 32 \text{ pA}$ ,  $U = -1.49 \text{ V}$ ) showing a square arrangement of FePc molecules on Ag(111). The central dot per molecule can be attributed to the iron ion. Corresponding space filling models in the image illustrate the arrangement. (f) STM image ( $I = 61 \text{ pA}$ ,  $U = -10 \text{ mV}$ ) showing a square arrangement of FeTPP molecules on Ag(111). Each of the molecules exhibits three dots, which correspond with the position of two opposing pyrrol rings and the central iron ion, emphasized by the superimposed models.

Auwärter et al. reported the same observation in a previous STM study, both for FeTPP and FeTPyP on Ag(111) [47]. This rod-like shape can be attributed to a conformational adaptation of the porphyrin, resulting in a “saddle” shape of the macrocycle (two pyrrols are lifted up; two are lowered as indicated in figure 4.7.2 (b)). This deformation is induced by the repulsion between the terminal H atoms of the tetrapyrrolic macrocycle and the phenyl rings, in combination with a rotation of the latter by roughly  $60^\circ$  out of the porphyrin plane [97, 98] (see chapter 4.1). With the described intramolecular conformation of FeTPP a gap in between the central tetrapyrrolic macrocycle and the substrate of roughly 0.15 - 0.20 nm is established. In contrast, phthalocyanines consist of a porphyrin macrocycle with benzene rings directly connected to the four tetrapyrrole rings, resulting in a flat conformation.

The picture of the metalation process established so far consists of mainly three steps: (1) the statistical impinging of iron atoms onto the surface, (2) the diffusion of the iron atom to the corresponding tetrapyrrolic pocket and (3) the complexation reaction with the release of  $H_2$ . One might suspect that due to the overall flat conformation of 2HPc a sufficient mobility/diffusion to the complexation sites might not be given, whereas in the case of 2HTPP the metal atoms might be free to move in the gap between the plane of the macrocycle and the surface. However, the experimental findings evidence similar metalation yields for both 2HPc and 2HTPP, suggesting a sufficient mobility of Fe on or under the molecules in both cases [56, 134].

The consequence of the above discussion is that no nucleation of Fe islands could be observed up to  $\theta_{Fe} = 0.037$  ML due to the fact that the growth of Fe on the corresponding Ag(111)/2HTPP and Ag(111)/2HPc surfaces is changed simply by the fact that all metal atoms are obviously “consumed” by the organic monolayer in the described surface mediated metalation reaction. The more interesting range starts with the amount of deposited Fe surpassing  $\theta_{Fe} = 0.037$  ML, since excess Fe is then available on the substrate. In figure 4.7.3, STM data for  $\theta_{Fe} = 0.30$  ML on Ag(111)/2HTPP (upper row) and  $\theta_{Fe} = 0.20$  ML on Ag(111)/2HPc (bottom row) are shown. Figure 4.7.3 (a) demonstrates that the square ordering of the FeTPP monolayer is still intact but extended areas appear brighter, i.e., exhibit an increased apparent height. Also, on these

islands individual FeTPP molecules are still resolved and the square order is conserved (see blow-up in figure 4.7.3 (b)). With the increase of the apparent height of these areas being roughly 0.2 nm these features can be associated with the formation of flat Fe layers (presumably 1 layer) underneath the FeTPP molecules. This obvious suppression of the three dimensional growth mode could be simply due to a confinement of Fe under the porphyrin macrocycles, which act as a boundary for the vertical growth. Following this interpretation, we conclude that the excess Fe diffuses more or less freely, presumably under the porphyrins, and forms the observed 2D islands with FeTPPs seemingly “floating” on top.

Following the deposition of a  $\theta_{Fe} = 0.20$  ML onto a FePc monolayer, as shown in figure 4.7.3 (c), we find a different behavior: One can easily distinguish three types of islands. By far the minority species is a flat extended 2D island, similar to the one described above for FeTPP; an example can be seen in the lower left corner of figure 3 (c). It is 4.7.3 evident that the original square order of the FePc molecules on top and in the vicinity of the island is distorted. The other two types of islands are more frequently found; a blow-up is depicted in figure 4.7.3 (d). These islands are either centered around a “four-fold hollow” site of the square FePc lattice, confined by a square area formed by four  $(1.4 \text{ nm})^2$ , or centered around an “on top” site of the square FePc lattice, confined by a square area of five  $(1.96 \text{ nm})^2$  molecules (indicated by the dotted squares in figure 4.7.3 (d)). The “fourfold hollow” islands exhibit with roughly 0.2 nm a smaller apparent height than the “on top” islands with  $\sim 0.4$  nm. Since the increased apparent height can be associated with more agglomerated Fe material it might be suspected that the first type discussed above is a precursor of the latter island type. Obviously, the lateral extensions of both types are significantly smaller than those of the flat 2D islands, which exhibit side length of up to ten times of the FePc lattice constant. Furthermore, the density of the smaller islands is higher; the “on top” type with the larger average apparent height of roughly 0.4 nm has a more three dimensional character, as compared to the hollow type ( $\sim 0.2$  nm).

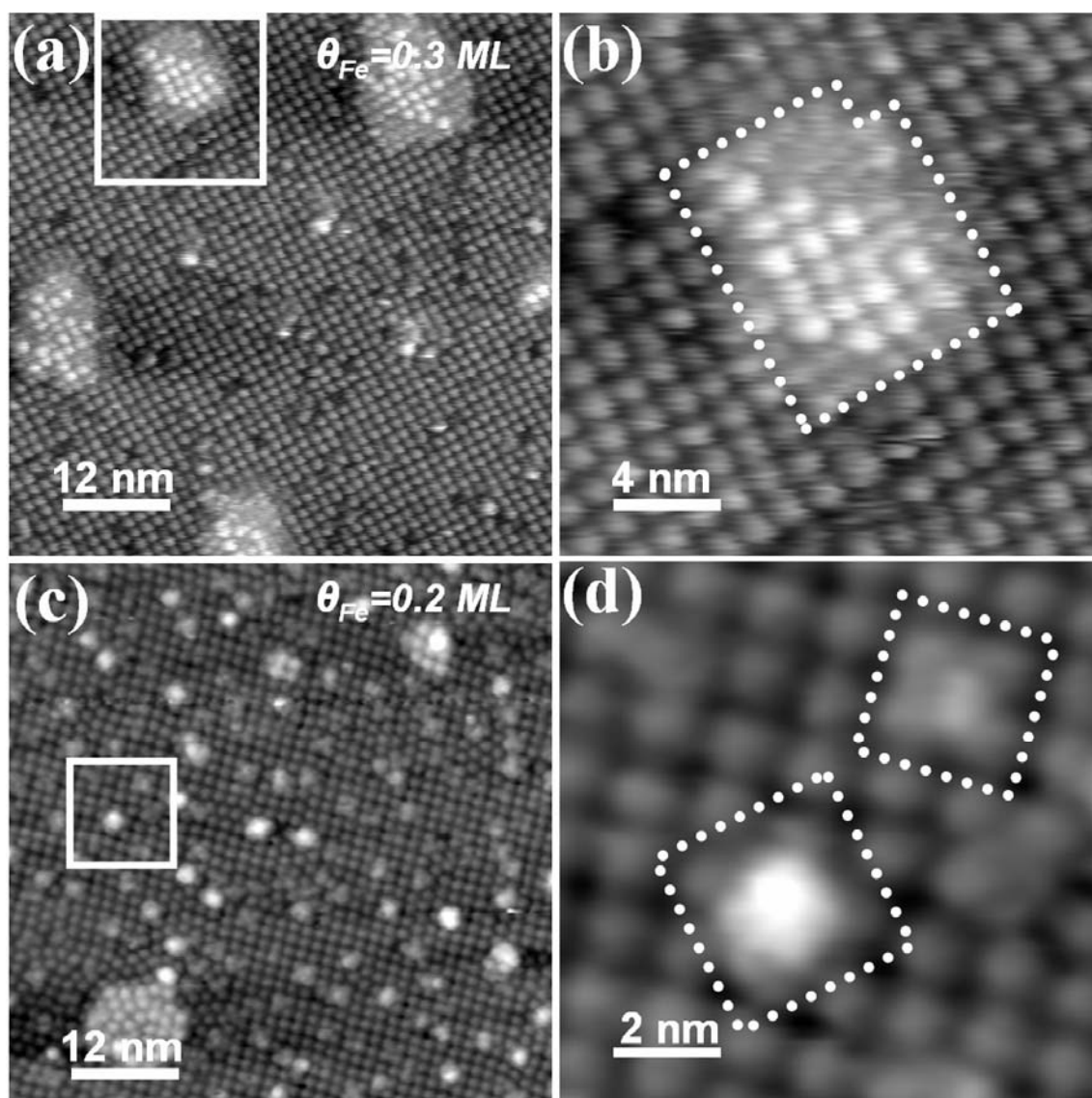


**Figure 4.7.3.** STM images obtained (a) after deposition of  $\theta_{Fe} = 0.3$  ML onto a monolayer of 2HTPP ( $I = 34$  pA,  $U = -197$  mV) and (b) the corresponding blow-up of the area marked with a white square in (a) highlighting the two dimensional iron islands. The small bright spots ( $\sim 1$  nm diameter) correspond to a complete monolayer of FeTPP due to metalation of 2HTPP with Fe. (c) STM image obtained after after deposition of  $\theta_{Fe} = 0.2$  ML onto a monolayer of 2HPc ( $I = 23$  pA,  $U = -1.88$  V) and (d) the corresponding blow-up of the area marked with white square in (c) highlighting two different types of Fe islands. The small bright spots ( $\sim 1$  nm diameter) correspond to a complete monolayer of FePc due to metalation of 2HPc with Fe.

At this point it should be noted that no preferential growth of Fe clusters on the step edges was observed for Fe deposition onto the tetrapyrrolic monolayers, whereas for Fe on the clean Ag(111) surface iron islands almost exclusively agglomerated at the steps for comparable coverages, i.e., up to  $\sim 0.5$  ML (see figure 4.7.1 (a)-(c)).

Thus both molecular monolayers act as diffusion traps for iron atoms. As discussed above, it seems plausible, that the free diffusion length of the impinging iron atoms is smaller for the FePc layer than for the FeTPP layer, due to the comparably larger distance between the surface and the porphyrin macrocycle. A reduced mobility of the deposited material can also be realized by a reduced sample temperature, which is known to yield smaller clusters with higher densities as compared to the situation at higher temperatures [3]. Relating to the systems investigated here, the higher mobility of Fe for Ag(111)/FeTPP (mimicking an increased sample temperature) would lead to the formation of larger islands with reduced density, which is in line with the observations so far. Another simple argument, also based on the gap in between FeTPP and the substrate, could be that the corresponding cavity can act as a nucleation space, where the Fe atoms can agglomerate. Such a “free space” under the FePc is obviously not available, therefore the Fe clusters have to nucleate in the rather small gaps between the Pc molecules or possibly attach to a central Fe atom of the latter, leading to the growth of rather small islands with a higher density. Furthermore, in the case of phthalocyanine the additional nitrogen atoms at the meso-position between two pyrrol rings could play an important role as energetically favorable “trapping” sites for the Fe atoms. One of these three effects or a mixture of them could account for the observed differences, namely the preferential assembly of predominantly rather small three-dimensional iron clusters with a high density for FePc and larger flat iron islands below the FeTPP layer.

In figure 4.7.4 STM micrographs are depicted, which document the development of the Fe growth upon further increase of the Fe coverage, namely (a)  $\theta_{Fe} = 0.80$  ML on 2HTPP and (b)  $\theta_{Fe} = 0.60$  ML on 2HPc. In figure 4.7.4 (a) the area and number of the flat islands has increased, with their apparent height remaining unchanged.

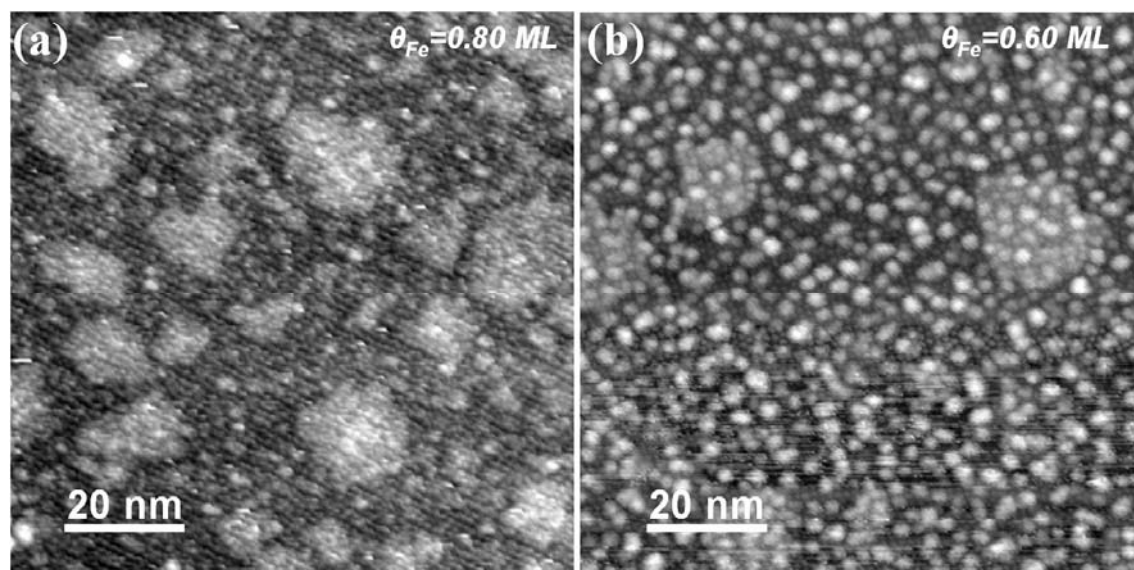


**Figure 4.7.4.** STM images obtained after deposition of (a)  $\theta_{Fe} = 0.8 \text{ ML}$  onto a 2HTPP monolayer ( $I = 36 \text{ pA}$ ,  $U = -1.21 \text{ V}$ ), (b)  $\theta_{Fe} = 0.6 \text{ ML}$  onto a 2HPc monolayer ( $I = 41 \text{ nA}$ ,  $U = -1.50 \text{ V}$ ).

Also, the square molecular order of FeTPP seems to persist. In addition, an increased number of small clusters with an apparent height of  $\sim 0.4 \text{ nm}$  can be observed. The surface initially precovered with 2HPc (figure 4.7.4 (b)) exhibits an increased density of small islands (roughly by a factor of two as compared to figure 4.7.3 (c)), whereas the larger flat islands seemed to grow only laterally. Even though individual FePc molecules are still visible in between the islands, the original square order appears to be mostly distorted. Therefore, the identification of the described “hollow”-type and “on top”-type islands by their lattice sites is not possible anymore. However, in contrast to the situation for the lower Fe coverage most of the islands appear now with a minimum apparent height of  $0.4 \text{ nm}$  and an increased maximum height of up to  $0.8 \text{ nm}$ ; the “hollow”-type islands associated with an apparent height of  $0.2 \text{ nm}$  are significantly reduced in number. This could indicate that they are energetically less stable or more likely that they are indeed a precursor for the “on top” type clusters as speculated above. Apart from that, the growth of the observed structures can be similarly explained as for the lower coverages discussed above.

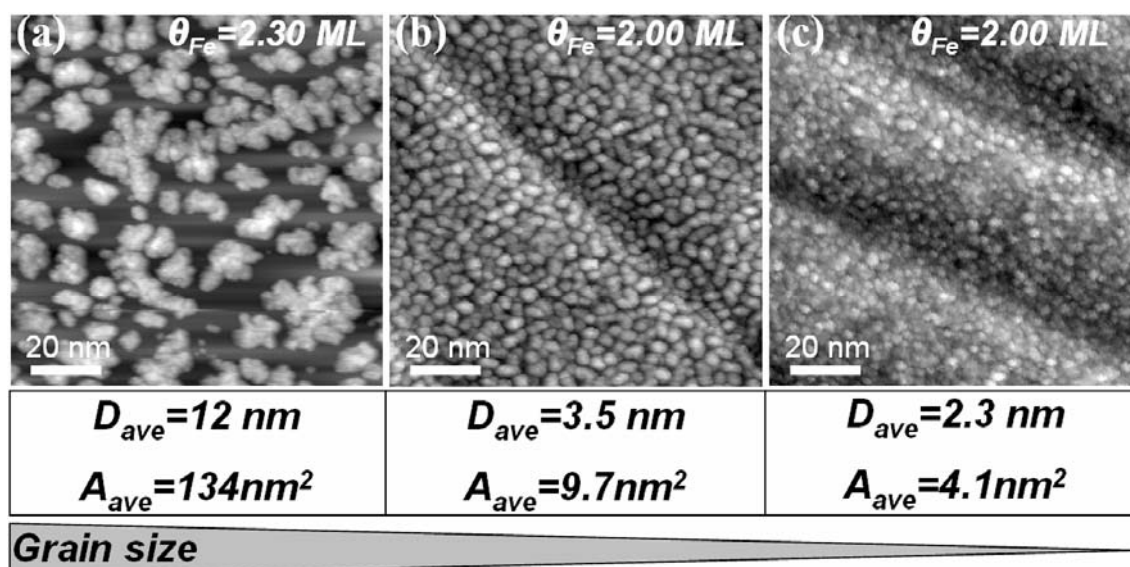


**Figure 4.7.5.** STM images obtained after deposition of roughly 2 ML of iron onto (a) Ag(111) ( $I = 61 \text{ pA}$ ,  $U = -305 \text{ mV}$ ), (b) 2HPc on Ag(111) ( $I = 32 \text{ pA}$ ,  $U = -1.20 \text{ V}$ ) and (c) 2HTPP on Ag(111) ( $I = 47 \text{ pA}$ ,  $U = -1.10 \text{ V}$ ).

The STM images in figure 4.7.5 show the surfaces after evaporating  $\sim 2 \text{ ML}$  Fe onto: (a) Ag(111), (b) FeTPP/Ag(111), (c) FePc/Ag(111). It is apparent that all of these surfaces are covered with iron clusters, exhibiting significantly different grain sizes.

A grain size analysis was conducted in which only clearly separable clusters were included. The micrographs in figure 4.7.5 reveal that the three dimensional islands grown on Ag(111) exhibit larger grain sizes than that grown on the preadsorbed molecular layers. The corresponding average cluster areas/diameters were calculated to be  $134 \text{ nm}^2/12 \text{ nm}$  on Ag(111),  $9.7 \text{ nm}^2/3.5 \text{ nm}$  on Ag(111)/Pc, and  $4.1 \text{ nm}^2/2.3 \text{ nm}$  on Ag(111)/TPP. It is remarkable that the Fe island area on clean Ag(111) is an order of magnitude larger than the ones for the surface precovered with the tetrapyrrolic species. Here again the presumably reduced mobility of the Fe species of the latter surfaces can account for this observation. In addition, it is important that the size of the Fe clusters grown on the molecular monolayers is very small with a narrow distribution and that for both systems almost no coalescence of the islands occurs. It is quite surprising that the clusters on Ag(111)/TPP are smaller after the predominant growth of large flat islands at lower Fe coverages.

Following the arguments concerning the gap in between the molecular layer and the substrate given above, one might have to distinguish between the growth before and after the corresponding cavity is “filled up” with Fe and possibly a complete Fe monolayer is formed underneath the FeTPP monolayer. After completion, the same considerations given for the growth of the three dimensional island on Ag(111)/Pc account, i.e., the size or the shape of the interspace between the molecules might determine the final size of the Fe clusters. One might speculate on the basis of the STM images shown in figure 4.7.2 (e) and (f) that the depressions (dark areas) at the position where four molecules meet are slightly larger for FePc than for FeTPP. These areas are presumably associated with uncovered the Ag(111) and hence might serve as nucleation centers for the Fe island growth. This would be in line with the observed nucleation of the “four-fold hollow”-type islands and the interpretation that these islands serve as precursors for the Fe clusters with 3D-character.

## **CONCLUSION**

The investigations demonstrate that the growth of Fe on a Ag(111) surface can be strongly modified by monolayers of large organic molecules. For the clean Ag(111) surface, at low Fe coverages an almost exclusive growth of three dimensional islands along the step edges was observed. While increasing the amount of Fe first the additional agglomeration of Fe clusters on the terraces and then a lateral and vertical growth of the existing branched structures occurs. The underlying mechanism was discussed in terms of diffusion and strain-induced effects, in agreement with similar heteroepitaxial systems reported in literature. If the surface is modified by a preadsorbed layer of 2HPc or 2HTPP, dramatic changes in the growth behavior occur. For low coverages up to  $\theta_{Fe} = 0.037$  ML no growth of iron islands occurs, but the Fe atoms are completely consumed by the free base tetrapyrrols in a metalation reaction resulting in FePc or FeTPP monolayers. At higher coverages ( $0.037 \text{ ML} < \theta_{Fe} < \sim 0.3 \text{ ML}$ ) differences are found for the two preadsorbed molecules: For Fe deposition on 2HTPP, the predominant growth of few extended flat Fe island underneath a FeTPP monolayer is found, whereas on 2HPc the growth of a large number of small 3D Fe clusters on the FePc monolayer dominates the growth. A key aspect for the

interpretation of these observations was to consider of the gap in between the central macrocycle of the FeTPP molecules and the Ag substrate in terms of diffusion and available space for the island formation. Another factor which might contribute is the additional nitrogen atoms of the FePc, which might act as “traps” for Fe. Upon increasing the Fe coverage to ~2 ML for both 2HPc and 2HTPP the growth of small 3D Fe islands (average diameters: 3.5 nm for Ag(111)/Pc, 2.3 nm for Ag(111)/TPP) was observed. In regard to possible applications it should be pointed out that in the observed size range quantum confinement effects are expected. Even though some interpretations are of speculative character, it can be concluded that the modification of the heteroepitaxial growth of a metal on a substrate with a sufficient lattice mismatch appears to be a promising approach towards the bottom up large scale fabrication of tailored nanostructures.



## 4.8 Geometric and Electronic Aspects of CoTPP upon Dosage of NO

---

The interaction of well-ordered monolayers of CoTPP on Ag(111) with NO was studied with in-situ STM. Upon NO exposure the initially square ordered CoTPP monolayer reorganizes showing a wealth of highly ordered NO+CoTPP coadsorbate phases with increasing size of the unit cell, attributed to attractive lateral dipole-dipole interactions between the two species (chapter 4.8.1). The STM images in combination with XP spectra confirm the coadsorption of NO [160].

The changing appearance of a fraction of CoTPP in high-resolution STM images upon dosage of NO is interpreted to the formation of NO-CoTPP (chapter 4.8.2). This specific interpretation can be given, as corresponding UPS experiments by Flechtner et al. [109] demonstrate a suppression of the electronic interaction between the central cobalt ion of the porphyrin and the silver surface. This is coherent with switched off orbital mediated tunnelling in the STM experiment, which indeed can explain the modified appearance of a fraction of molecules in the STM images.

### **INTRODUCTION**

The influence of small co-adsorbed molecules, such as carbon oxide (CO) or nitrogen oxide (NO), on the arrangement of large organic molecules has not been addressed up to now, despite the fact that their unintended or intended co-adsorption can lead to new ordered surface phases for smaller organic adsorbates, e.g., for benzene on Rh(111) [161] or Ni(111) [162]. The mutual stabilization of benzene and CO was employed in 1988 for imaging individual adsorbed benzene molecules for the first time in real space with STM [163].

Furthermore, the interaction of small molecules such as NO, O<sub>2</sub> or CO with metalloporphyrin monolayers has been studied in the past under the aspect of the coordination to the central metal ion, a process that is of great interest due to the

corresponding functionalities in biological systems. Generally, metalloporphyrin provide two potential axial coordination sites. If the macrocycle is adsorbed parallel to the surface, one of two axial coordination sites is occupied by the surface, while the second remains as potential coordination site. It was reported in an STM study by Williams et al. about the reversible attachment of an axial ligand to an adsorbed porphyrin, i.e., the coordination of the nitrogen base DABCO (1,4-diazabicyclooctane) to the metal center of ZnTTBPP molecules on Ag(100) [87]. Furthermore, it was shown by Flechtner et al. with XPS that  $\text{NH}_3$  coordinates to ZnTPP on Ag(111) below 130 K [116]. Axial coordination was also employed for the realization of a surface anchored, porphyrin based molecular pinwheel. Its rotor consists of a ZnTTBPP molecule, which is pinned to the surface by 4-methoxypyridine. It was proposed that this ligand binds to the Zn ion through the pyridine N atom, while it is bound to the Ag(100) surface through the  $-\text{OCH}_3$  group. On this molecular support, the porphyrin can spin, resulting in a circular symmetry as observed by STM [164].

In chapter 4.8.1 a novel aspect of the interaction of NO with adsorbed CoTPP, i.e., the massive lateral rearrangement of an initially square ordered CoTPP layer upon large exposures of NO is reported. The rearrangement was followed continuously at RT by STM under UHV conditions. Evidence is presented that this rearrangement process is induced by the coadsorption of NO [160].

Encouragement for studying the interaction of NO with monolayers of CoTPP with STM was promoted by the work of Flechtner et al. It was demonstrated in a XPS/UPS study that NO can be reversibly attached to CoTPP adsorbed on Ag(111) under UHV conditions [109]. The observed changes of the valence states near the Fermi energy upon dosage of NO should also be accessible with STM.

In chapter 4.8.2 the results with respect to the influence of the axial ligand on the appearance in STM micrographs at RT are shown.

## 4.8.1 In-situ Observation of the Rearrangement of CoTPP on Ag(111)

---

Figure 4.8.1 shows a series of STM images acquired at RT during exposure of an ordered CoTPP submonolayer ( $\theta_{\text{abs}} \sim 0.3$ ) on Ag(111) to NO gas. In the medium resolution STM images the individual CoTPP molecules appear as protrusions [60]. Figure 4.8.1 (a) was acquired at an NO dosage of 576 L ( $\sim 2$  h @  $1 \times 10^{-7}$  mbar). Up to this exposure, no significant changes in the arrangement of the CoTPP layer were observed. The square unit cell of CoTPP on Ag(111) with a lattice constant of  $\sim 1.4$  nm is in agreement with previous studies of TTP on various substrates [55].

In figure 4.8.1 (b), which was acquired at 606 L (i.e., 30 L after figure 4.8.1 (a)), the molecular order changed in the vicinity of the step edge and the dark rectangular area vanished and is now “filled” with molecules. The boundary of the altered lateral arrangement is marked by the two arrows. After further exposure to NO, this boundary propagates away from the step edge as indicated in figure 4.8.1 (c) and 4.8.1 (d). This proceeds until two domains with a slightly distorted hexagonal molecular arrangement are observed in figure 4.8.1 (e). At even higher NO doses, the hexagonal structure continues to rearrange and finally transforms into the oblique structure without domain boundaries as shown in figure 4.8.1 (f). Analysis of the data reveals an increase of the unit cell area with increasing NO dosage, from initially  $1.91 \text{ nm}^2$  to  $2.74 \text{ nm}^2$ . At this point it should be noted that the axial coordination of NO to the central metal ion of CoTPP was reported to occur already at much lower NO doses at 140 K [109]. This can also be observed in STM at RT (chapter 4.8.2), but the NO molecules are easily removed upon scanning the sample at the given tunneling parameters, leaving the molecular arrangement unchanged. In conclusion, NO, coordinated to the cobalt center does not account for the observed rearrangement effects.

The most plausible explanation for the structural changes and the increasing size of the unit cell is the co-adsorption of NO directly on the Ag substrate.

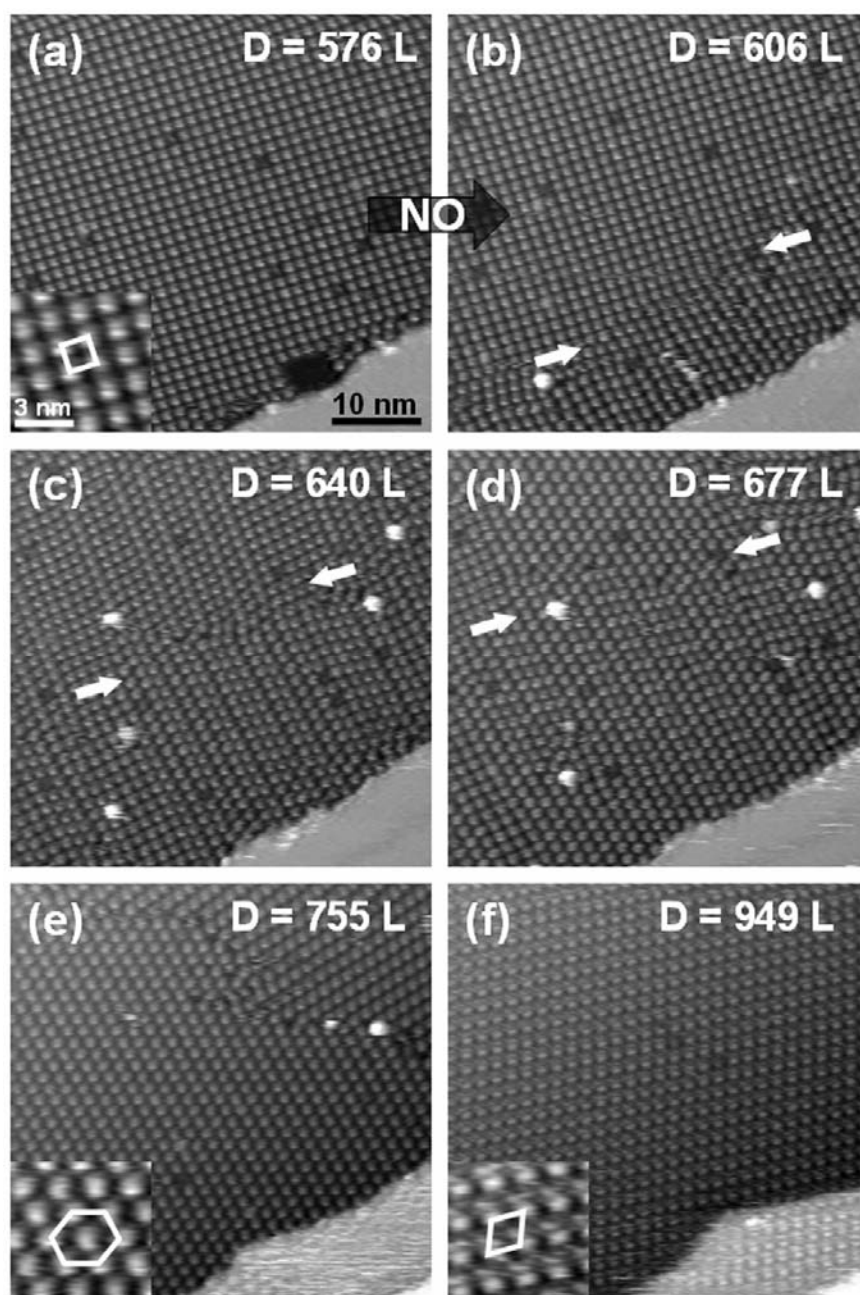


**Figure 4.8.1.** STM image series of a CoTPP layer on Ag(111) during exposure to NO at RT. The corresponding NO dosages are inserted in the micrographs. The rearrangement with increasing NO dose starting from the undisturbed square order in a) to an almost hexagonal arrangement in e) to an oblique structure in f) is obvious and clearly develops towards larger unit cells. The unit cell areas as extracted from the experimental data are: a)  $1.91 \text{ nm}^2$  and f)  $2.74 \text{ nm}^2$ . All images have a size of  $(47 \times 47) \text{ nm}^2$  and were acquired at  $U_{\text{BIAS}} = -0.23 \text{ V}$  and  $I_{\text{SET}} = 300 \text{ pA}$ .

In this picture, the unit cell area increases as a result of the accumulation of coadsorbed NO, i.e., due to steric reasons. Note that there is a pronounced induction period corresponding to more than 500 L without changes in the initial square order, followed by massive and fast propagating rearrangements (figure 4.8.1 (b)-(f)). This highly nonlinear process is interpreted to be due to the slow formation of a nucleus for the hexagonal phase.

To gain information on the azimuthal orientation and the intramolecular conformation within the CoTPP+NO layers, additional experiments were performed, where images with sub-molecular resolution could be acquired. Figure 4.8.2 is organized such that the size of the unit cell increases again continuously from (a) to (m), now from 1.91 nm<sup>2</sup> to 3.16 nm<sup>2</sup>. In column one the unit cell vectors, the density of molecules per unit area and the NO dose is given. The STM images in the second column have a size of (20 x 20) nm<sup>2</sup> that in the third and fourth (7.5 x 7.5) nm<sup>2</sup>. Corresponding space filling models were superimposed in the fourth column.

Figure 4.8.2 (a)-(c) shows the STM image of the undisturbed CoTPP square arrangement, prior to NO exposure. A rod-like feature dominates the appearance of an individual molecule and reflects the “saddle-shape” deformation of the adsorbed porphyrin macrocycle [100], as shown in chapter 4.1. The analysis shows that not only the long-range order changes upon NO dosage but also the azimuthal orientation of the individual molecules, represented by their anisotropy axes. In figure 4.8.2 (d)-(f), the orientation of every second row is changed. The arrangement is nominated to as *hex I* phase. The reorganisation implies rotary motions of CoTPP. In figure 4.8.2 (g)-(i), an STM image acquired at RT after an exposure of 2368 L NO at RT is depicted (phase: *straight square*). Now all molecules are arranged in a rectangular lattice with the anisotropy axes aligned along one of the unit cell vectors. Figure 4.8.2 (j)-(l) shows constant current images recorded after additional dosage of 940 L (phase: *hex II*). The azimuthal orientation of the individual molecules closely resembles that observed for the *straight square* phase, however the molecular rows aligned along one of the unit cell vectors are shifted by half of the latter, forming the phase *hex II*.

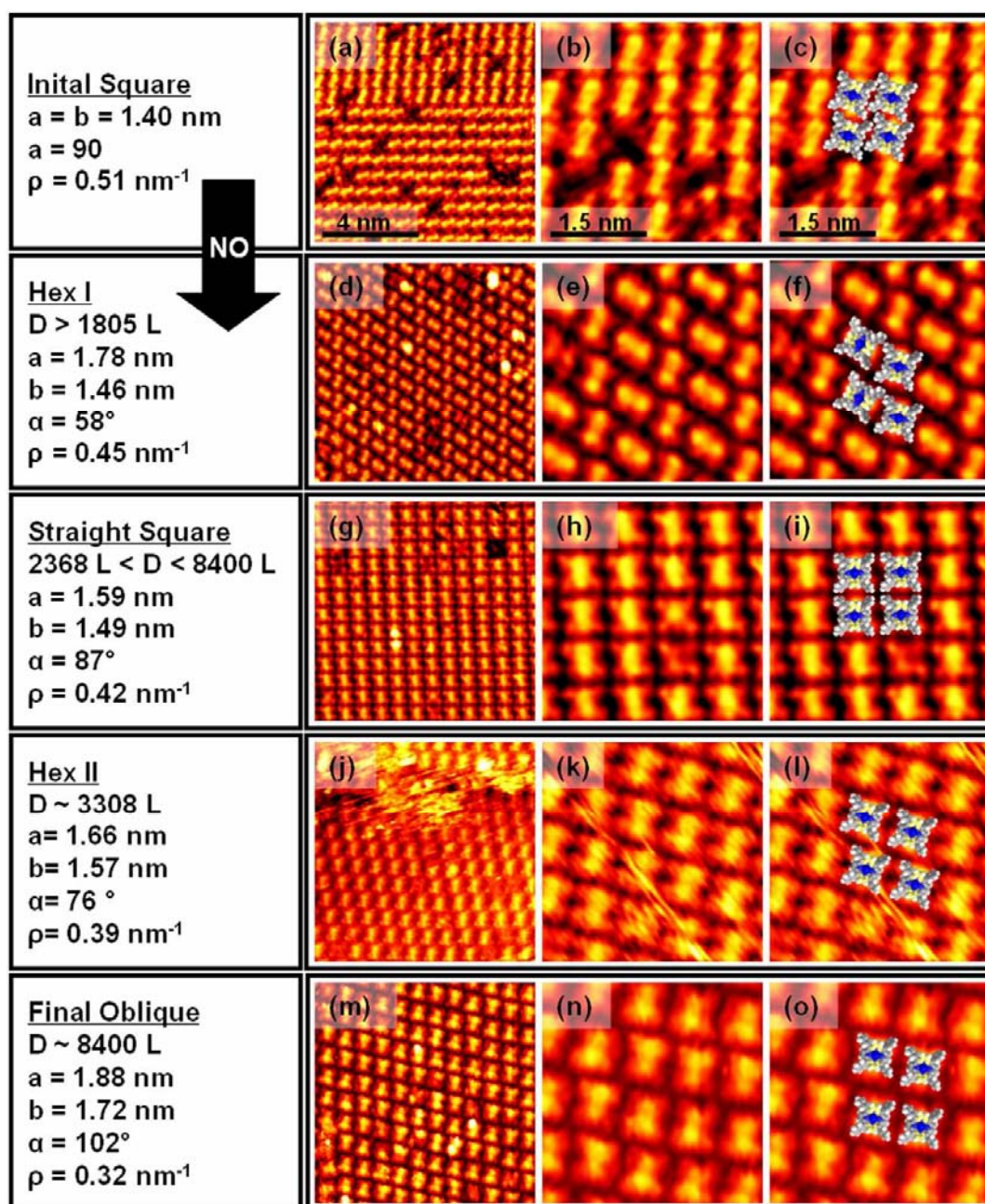


**Figure 4.8.2.** (a)-(o) STM images of ordered phases of CoTPP on Ag(111) before (a)-(c) and after (d)-(o) NO exposure. The corresponding values for NO exposure, the lattice vectors and angle and the density of the molecules per unit area are inserted in column one. The respective area of the unit cell and the tunnelling parameters are as follows: a)  $U = -1.18 \text{ V}$ ,  $I = 58 \text{ pA}$  /  $A = 1.96 \text{ nm}^2$ ; d)  $U = -1.9 \text{ V}$ ,  $I = 45 \text{ pA}$  /  $A = 2.22 \text{ nm}^2$ ; g)  $U = -1.90 \text{ V}$ ,  $I = 45 \text{ pA}$  /  $A = 2.38 \text{ nm}^2$ ; j)  $U = -1.90 \text{ V}$ ,  $I = 48 \text{ pA}$  /  $A = 2.56 \text{ nm}^2$ . m)  $U = -0.94 \text{ V}$ ,  $I = 70 \text{ pA}$  /  $A = 3.13 \text{ nm}^2$ .

Figure 4.8.2 (m)-(o) shows another structure obtained for a NO dose of 8400 L, with again a different and expanded unit cell (phase: final oblique). Inspection of the different images reveals that, despite the change in the lateral arrangement, the appearance and, thus, the intramolecular conformation of individual molecules in the different superstructures remain the same; this is obvious for the zoom images shown in figure 4.8.2 in column two ((b)-(n)).

In some cases the rearrangement was reversible upon heating to ~500 K. Even though the experimental conditions (e.g., CoTPP precoverage) were not directly comparable, within one experimental run always an expansion of the unit cell with increasing NO dosage was observed. It should be noted that while the basic findings presented so far were reproduced several times, some aspects such as the reversibility or the CoTPP coverage dependence still need further investigation.

Note that in a recent publication evidence for the coadsorption of NO is given by means of low temperature (LT) STM data (not shown) [160]. The high-resolution LT-STM image was provided from the scientific working group of J.V. Barth et al.. The micrograph shows a low temperature STM image of CoTPP after exposure to 5000 L NO at RT. Upon close inspection of the micrograph, protrusions between the CoTPP molecules are resolved. These protrusions are associated with coadsorbed NO.

Complementary spectroscopic information was acquired to verify this conclusion. Figure 4.8.3 (extracted from the PhD thesis of Ken Flechtner [165]) shows an N 1s XP spectrum of a CoTPP monolayer after exposure to 6500 L NO at RT. Four components are identified, which are assigned to nitrogen atoms in the porphyrin macrocycle (purple), the NO molecule coordinated to Co in CoTPP (blue), the NO molecularly adsorbed on Ag(111) (red) and an unidentified species (green), in agreement with previous XPS studies of adsorbed NO/CoTPP complexes [109] and literature N 1s binding energies for NO on metal surfaces [166]. From the fact that the areas under the red (NO on Ag) and the purple peak (N in porphyrin) are very similar, one can conclude that roughly four NO molecules are coadsorbed per porphyrin. Assigning the green peak to coadsorbed NO in a different local environment, this number would increase to approximately five NO molecules per CoTPP. The value corresponds well with the five

protrusions per porphyrin, as observed in the low temperature STM image [160]. Therefore it can be concluded that these protrusions are indeed due to individual NO molecules, evidencing the coadsorption of NO as the source of the observed rearrangement processes.

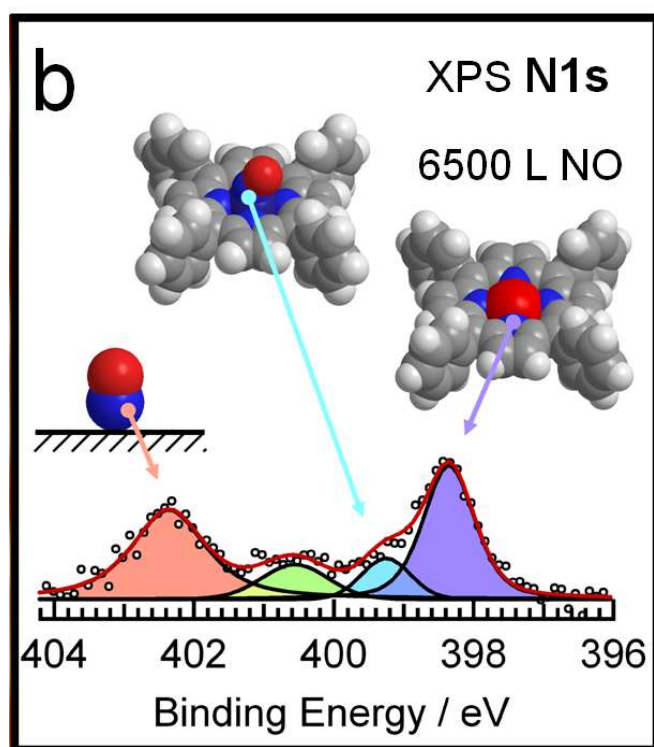


**Figure 4.8.3.** XP spectra of the N1s region of a CoTPP layer on Ag(111) after exposure to 5000 L NO. The corresponding fitted peaks are identified with different nitrogen species as indicated. (The XPS data are extracted from [165]).

## CONCLUSION

Considering the experimental evidence discussed above, the following conclusions concerning the NO induced rearrangement of ordered CoTPP layers on Ag(111) are drawn. The formation of well ordered CoTPP+NO layers indicates that these coadsorbed structures are energetically favourable under the given experimental conditions. Upon NO coadsorption, the unit cell of the CoTPP layer increases,

indicating an increasing number of NO molecules per unit cell (note the filling of the hole in figure 4.8.1 (a) and the increasing appearance of molecules on the terrace in the lower right corner in figure 4.8.1 (f)). On the other hand, the interaction of NO with the bare Ag(111) surface is very weak and no adsorption occurs on Ag(111) at RT and comparable or higher NO doses [32, 33]. Nevertheless, when coadsorbed with CoTPP, NO is bound on the surface so strongly (stable up to ~450 K) that the energy cost of rearranging the CoTPP is overcompensated. This effect is attributed to significant attractive lateral dipole-dipole interactions of the electropositive CoTPP (which lowers the work function [73]) and the electronegative NO (which typically increases the work function, e.g., [33]). These interactions favour and stabilize the mixing of the coadsorbates. The formation of a variety of mixed benzene+CO and benzene+NO layers on various metal substrates is well known in the literature and has been interpreted along the same lines [161, 162], strengthening our interpretation.

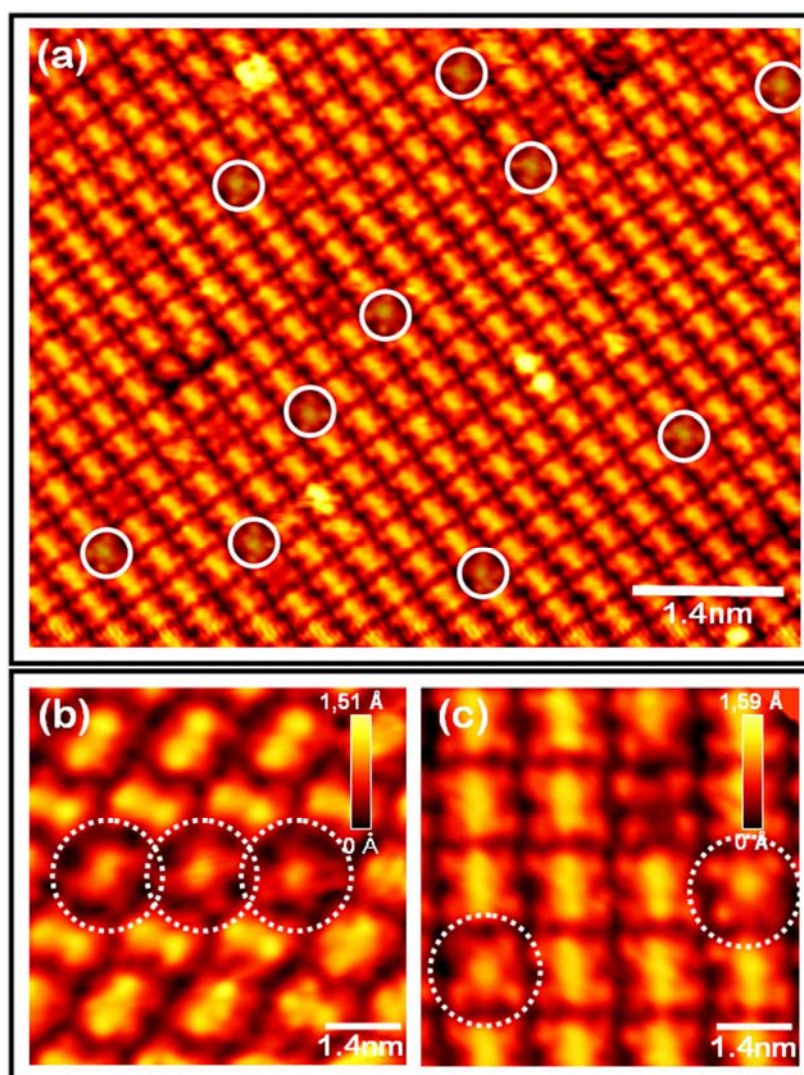
Regarding the richness of the observed structures in the presented system and the presumably general nature of the described process one might envision the coadsorption of small molecules as an excellent tool to control the ordering, the intermolecular distances and the molecule-substrate interactions of large functional molecules with high accuracy. In addition, similar effects have to be expected and considered quite generally in the production of functional layers from large organic molecules under ambient conditions or after exposure to small electronegative molecules.

## 4.8.2 Modification of the Appearance of CoTPP upon Formation of NO-CoTPP

---

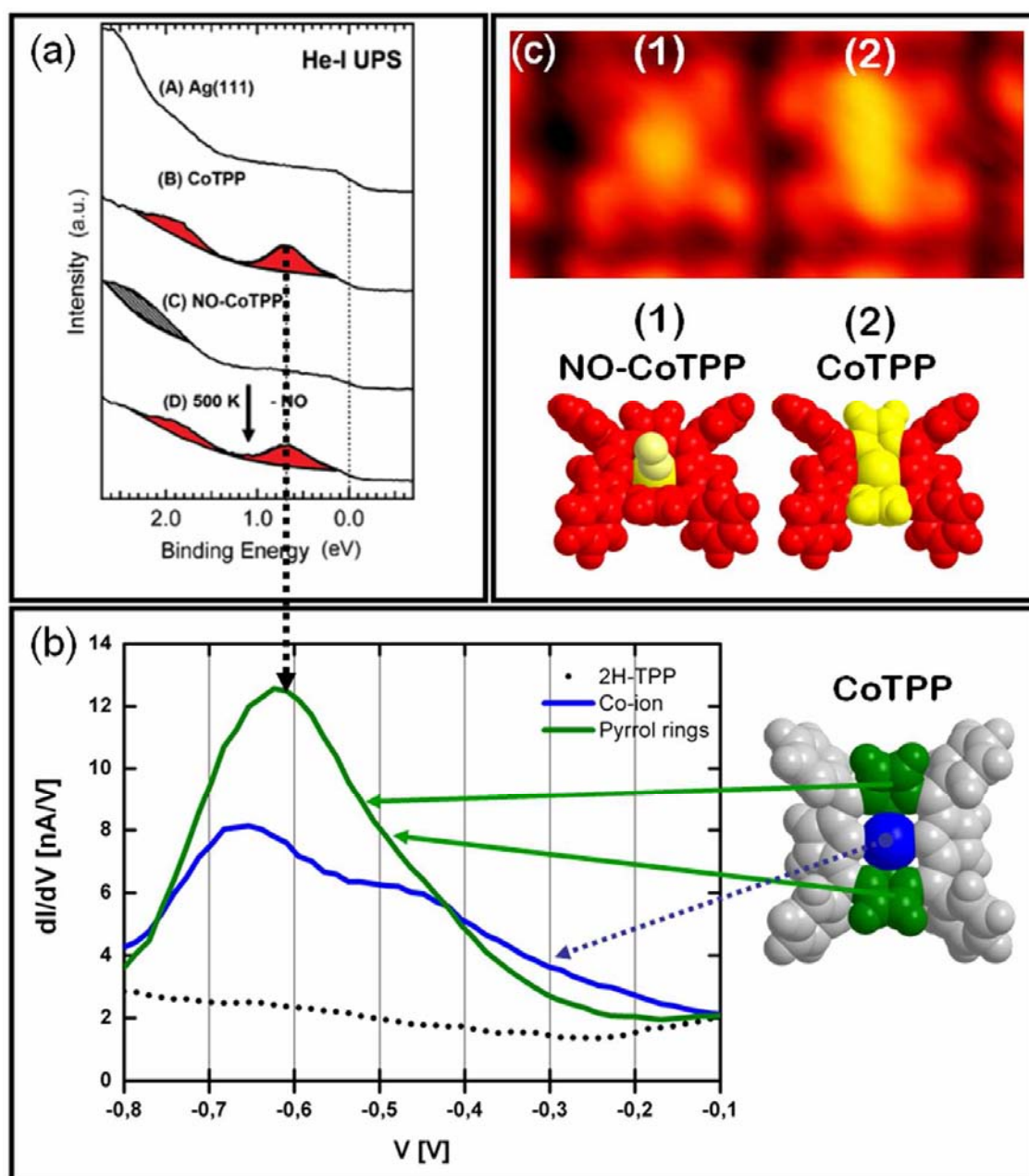
In figure 4.8.4 (a) a well-ordered monolayer, arranged in the formation referred to as *straight square* is shown ( $D_{\text{NO}} \sim 2400 \text{ L}$ ) (see chapter 4.8.1). As established, CoTPP appears with a longish protrusion at large negative bias voltages ( $U = -1.90 \text{ V}$ ) [57, 100] (chapter 4.1). The terminal phenyl groups of CoTPP are apparent with medium height. The described appearance is present for the majority of the molecules, however roughly 3% of the molecules do not exhibit that shape (marked with circles). This was solely obtained during, or after dosing experiments ( $D_{\text{NO}} > 500\text{L}$ ). Enlarged STM images highlight the pronounced porphyrins both within the *hex I* phase (figure 4.8.4 (b)) and the *straight square* phase (figure 4.8.4 (c)). A central dot due to the central cobalt ion and dimmer features due to the tetrapyrrolic macrocycle and the phenyl groups are observable. Interestingly, the appearance resembles the STM images of CoTPP acquired at low negative bias voltages ( $U \sim -200 \text{ mV}$ ) (chapter 4.6.2); however, the data in Figure 4.8.4 (with NO doses) were recorded at a bias voltage of  $-1.90 \text{ V}$ . As such molecules could only be observed when dosing NO, it can be assumed that they are chemically modified in that course. A possible explanation is the formation of (nitrosyl)-(tetraphenylporphyrinato)-cobalt(II) (NO-CoTPP) by attachment of an NO ligand to cobalt.

Figure 4.8.5 (a) was reprinted from the publication of Flechtner et al. [109]. It shows UP spectra, which were recorded both after dosage of NO onto a monolayer of CoTPP at 140 K and after subsequent heating up to 500 K. Prior to dosage, the signal at roughly 0.6 eV in figure 4.8.5 (a) (indicated in (B)) was observed and attributed to an electronic interaction of the coordinated Co ion with the Ag surface [116]. It was proposed that the half-filled Co(II)  $3d_{22}$ -orbital interacts with states of the silver surface resulting in new levels below the Fermi energy, which are accessible for electrons from the Fermi sea. This interpretation was found to be consistent with the observation of a



**Figure 4.8.4.** (a) Constant current image of the straight square phase ( $U = -1.90$  V,  $I = 45$  pA). A fraction of molecules appears modified (marked with circles). (b) Micrograph of the hex I phase exhibiting three molecules which appear modified ( $U = -1.9$  V,  $I = 45$  pA) (c) Enhanced image of (a).

peak shift of the Co  $2p_{3/2}$  XPS signal towards lower binding energies in the monolayer regime compared with that in multilayers. Thus a transfer of electron density from the Ag surface to the Co ion was assumed. The discussed peak 600 meV below the Fermi energy was confirmed by Comanici et al. by means of UPS and STS [60] (see chapter 4.6.1).



**Figure 4.8.5.** (a) He-I UP spectra ( $h\nu = 21.22$  eV) of (A) clean Ag(111) surface, (B) CoTPP monolayer, (C) NO-CoTPP monolayer, and (D) after heating the NO-CoTPP monolayer to 500 K for removal of the NO ligand [109]. (b) Local ST spectra recorded at opposing pyrrol rings and the central cobalt. (c) Enlarged STM image of CoTPP (label 2), including a modified version of the porphyrin (label 1), which is probably induced by attachment of NO ( $U = -1.9$  V,  $I_T = 45$  pA).

The UP spectrum after dosage of NO in Figure 4.8.5 (a) (indicated with (C)) shows that the pronounced peak at 0.6 eV is suppressed upon attachment of an axial NO ligand to CoTPP. It was suggested that the NO ligand weakens the interaction between the Co ion and the Ag surface, due to the so-called trans-effect [109]. This is interpreted as a competition of the ligands in trans-position concerning the same metal d orbitals, resulting in a weakened bond to the Ag surface. Thereby the interaction between the Co  $3d_{z^2}$  orbital and the Ag surface is “replaced” by the stronger interaction between the Co  $3d_{z^2}$  orbital and the  $\pi^*$  orbital of NO. The interaction leads to a larger energetic separation between occupied and unoccupied states, with the result that the latter is now located above  $E_F$ . Therefore, it cannot be occupied with electrons from the Fermi sea and the electron transfer from the surface to the Co ion is suppressed. It was required to heat the sample to 500 K to observe the reappearance of the peak at 0.6 eV (figure 4.8.5 (a) (indicated with (D))). Thus, the process is reversible [109].

In addition to the space averaging UP spectroscopy, complementary local measurements of the density of valence states have been performed with STS. The averaged ST data exhibits a peak at 0.6 eV as shown in chapter 4.6.1, which is in good agreement with the UP spectrum. Note that all shown ST spectra were recorded with the CITS technique described in chapter 4.6.3. Thus it is possible to selectively extract LDOS curves at certain positions, i.e., the central cobalt atom (blue curve in figure 4.8.5 (b)) and the opposing pyrrol rings of CoTPP (green curve). Note that the latter mainly determine the discussed peak. The characteristics of the curves can be ascribed to mediated tunnelling through the respective molecular orbitals, i.e., a channel of the Co( $d_{z^2}$ ) orbital and channels through both Co( $d_{xz} / d_{yz}$ ) and TPP  $\pi$  orbitals, as discussed in chapter 4.6.2 and 4.6.3 [140].

Taking into account the suppressed UPS peak upon NO dosage [109], it can be expected that the corresponding peak in the complementary ST spectra should also disappear (note that tunnelling spectroscopy was not performed after NO dosage). This is attributed to the fact that orbital mediated tunnelling does not occur, since the corresponding electronic states have shifted in energy. Thinking in terms of a constant current contour (figure 4.8.5 (c)), the integral of the LDOS is decreased, resulting in a

reduced tip height at these positions: (1) opposing elevated pyrrol rings, (2) metal center.

Indeed the appearance of the molecules in figure 4.8.5 (c) can be interpreted in this way. The molecule depicted with “1” shows a central dot and differs significantly from the anisotropic shape of CoTPP (“2”). A transformation of “2” to “1” can be attained with a reduction of the apparent height at elevated pyrrol rings, coinciding with switched off orbital mediated tunnelling upon attachment of an axial NO ligand. The similar apparent height at the center of the molecules can be interpreted to as a competition between two effects: (1) increased apparent height of NO-CoTPP by the attached ligand; (2) decreased apparent height through suppressed orbital mediated tunneling. Thus, the observed appearance of the molecule (label 1) indicates the formation of NO-CoTPP. The inserted space-filling models (figure 4.8.5 (c)) emphasize the discussed situation.

As aforementioned, it was demonstrated by Flechtner et al. with UPS that the NO-CoTPP complex is stable at RT [109]. The observed depletion of NOs directly coordinated to CoTPP is attributed to a tip-induced desorption of NO in an earlier stage of the STM experiment, i.e., before sub-molecularly resolved images were recorded.

## **CONCLUSION**

The modified appearance of a fraction of molecules in STM upon dosing NO, i.e., a central dot instead of a longish protrusion, at large negative bias voltages, was interpreted by means of complementary spectroscopy methods, i.e., UPS and STS. From a detailed analysis it appears very likely that the modification can be attributed to the formation of NO-CoTPP at RT.

## 4.9 Self-Assembly and Voltage-dependent Appearance of Octaethylporphyrins

---

In this chapter, the self-assembly of intermixed layers of octaethylporphyrins, namely 2HOEP and CoOEP, on Ag(111) was studied with STM at RT. The monolayer coverage was achieved with the thermal desorption of excessively deposited multilayer molecules, as discussed in chapter 3.6. The different porphyrins in the intermixed monolayer could clearly be identified in STM micrographs with submolecular resolution, indicating a flat, undistorted conformation of the tetrapyrrole. A voltage-dependent contrast of CoOEP and 2HOEP was observed and is discussed.

### **INTRODUCTION**

Numerous porphyrin-based supramolecular architectures on flat surfaces have been reported in literature, with the porphyrinoids terminated with different ligands [76]. Only few investigations of monolayers of octaethylporphyrins have been reported so far, e.g., nickel OEP on Au(111) [167], cobalt and vanadyl OEP on HOPG [168] and nickel OEP on HOPG [169]. Top and side views of space filling models of 2HOEP are shown in figure 4.9.1 (a) and (b). The specific internal conformation, with the tetrapyrrolic macrocycle lying flat on a surface, was proposed by Scudiero et al. for the system nickel OEP adsorbed on Au(111) [167].

Thin layers of TPPs were frequently studied on Ag(111) [56, 57, 61] (and chapters 4.1 – 4.3, 4.6 – 4.8), where the tetrapyrrolic macrocycle is not in direct contact with the surface; the distance to the surface is roughly estimated to be ~ 0.3 nm (figure 4.9.1 (c) and (d)) and results from the overall conformation of the TPP molecules, as discussed in chapter 4.1. Thus it is particularly interesting to study layers of OEPs on Ag(111) at RT via STM, with their macrocycle (and the metal) being expected to be significantly closer to the surface.

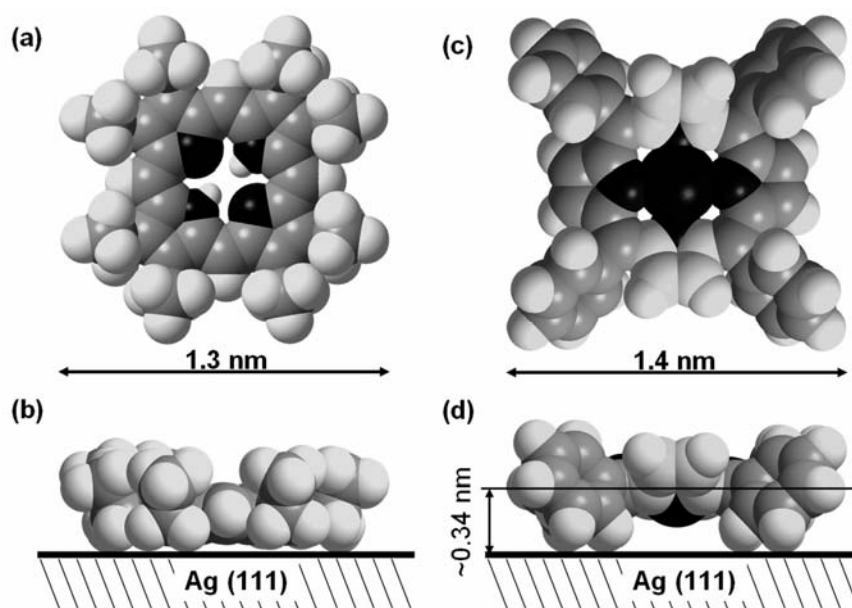


**Figure 4.9.1.** (a) Top and (b) side view on space filling models of 2HOEP on Ag(111). The upwardly directed conformation of the ethyl groups was chosen based on high-resolution STM images from literature [167]. (c) Top and (d) side view on a MTPP model, emphasizing the distance of the porphyrin macrocycle to the surface.

## RESULTS

As described in chapter 3.6 the vapor-deposition of multilayers at RT, followed by the desorption of excess multilayer porphyrins by heating the sample, was applied to prepare a monolayer coverage on Ag(111). Prior to TPD, an intermixed multilayer of 2HOEP and CoOEP with a nominal ratio of 2:1 was deposited on the sample. TPD spectra were acquired simultaneously for both CoOEP and 2HOEP (figure 4.9.2). Two desorption peaks can be identified in each of the spectra, roughly with the maxima at the same temperature. The peak at 432 K is attributed to desorption of the multilayer molecules, the one at 625 K to the monolayer molecules. The multilayer peak of the 2HOEP spectrum shows an exponential increase at roughly 400 K and a rapid decrease above 432 K. This specific shape indicates zeroth order desorption, which is typical for desorption of multilayers.

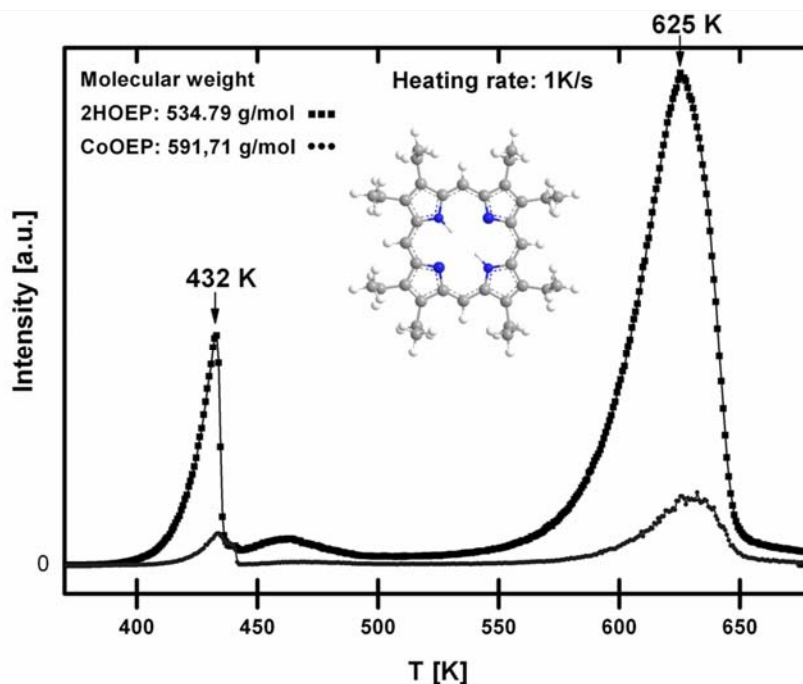


**Figure 4.9.2.** Simultaneously acquired TPD spectra of 2HOEP and CoOEP on Ag(111). The applied heating rate was 1K/s.

It is noteworthy to mention, that the intensity of the multilayer peak is small both for CoOEP and 2HOEP, compared to the monolayer signal. This indicates that a small amount of excess multilayer molecules were deposited onto the sample ( $\theta_{\text{abs}} \sim 1.3$ ). The relatively broad peak at  $\sim 460$  K is attributed to desorption from the sample holder. From the spectra, a multilayer desorption temperature of 500 K, which is well below the monolayer desorption peak, was deduced.

Following the preparation of a monolayer, the medium-resolution image in figure 4.9.3 (a) was recorded, showing a long-range ordered intermixed monolayer, with hexagonal close packing. In the constant current image 34 % of the molecules appear as bright dots, i.e., with an increased apparent height. The STM image resembles previously reported STM images of mixed monolayers of CoTPP/2HTPP and FeTPP/2HTPP [42, 56, 60]. It is assumed that the molecules with the increased apparent height in figure 4.9.3 (a) can be attributed to CoOEP, i.e., contain a central Co ion. The appearance of CoOEP in STM at a given tunneling resistance can be attributed to both a

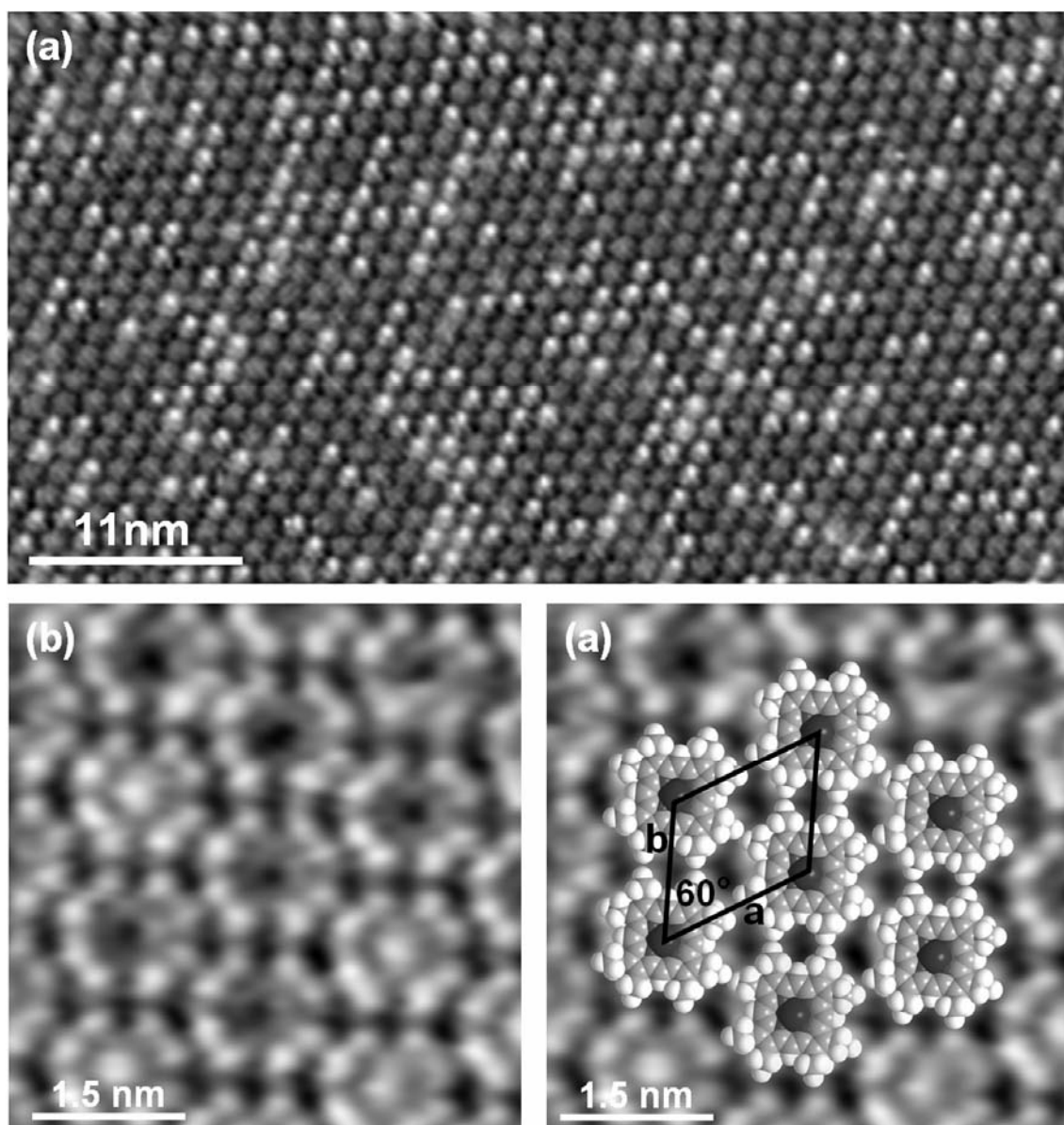


**Figure 4.9.3.** (a) Long-range ordered intermixed 2HOEP/CoOEP monolayer with a nominal amount of 2:1 ( $U = -1.17$  V,  $I = 31$  pA). (b) High-resolution constant current image ( $U = -200$  mV,  $I = 37$  pA) (c) The micrograph in figure (b) was superimposed with corresponding space filling models. The unit cell is drawn in, exhibiting lattice vectors of  $a = 1.55 \pm 0.10$ ;  $b = 1.55 \pm 0.10$ ;  $\alpha = 60^\circ \pm 3^\circ$ .

topographic effect and orbital mediated tunneling through the Co(II)  $3d^6$  system [56, 106]: Thus the molecules with smaller apparent height are identified as 2HTPP. The observed ratio of CoOEP/2HOEP correlates well with the nominal ratio (1:2) in the ex-

situ mixture. It is noteworthy to mention that the contrast in the CoOEP/2HOEP array tends to fade for bias voltages close to the Fermi energy, i.e.,  $> -200$  mV (not shown here) [170]. Considering the interpretation for the discrimination of CoTPP, given in chapter 4.6.1, this finding consequently indicates an electronic state of the CoOEP/Ag(111) adsorbate complex between  $-1.17$  eV and  $-0.2$  eV, which was indeed evidenced by UPS at  $-0.6$  eV by Bai et al. [170].

In figure 4.9.3 (b), a molecularly resolved STM image of an intermixed 2HOEP/CoOEP monolayer is depicted. The individual molecules appear either with a central depression (2HOEP) or with an elevated center (CoOEP), surrounded by eight protrusions. Note that in close proximity to the respective center, the porphyrin macrocycle is visible with intermediate height. The intermixed 2HOEP/CoOEP monolayer exhibits an oblique (but almost hexagonal) arrangement with lattice constants of  $a = 1.55 \pm 0.10$  nm,  $b = 1.45 \pm 0.10$  nm and an enclosed angle  $\alpha = 60^\circ \pm 3^\circ$  (figure 4.9.3 (c)). To achieve a good fit of the scaled space filling models with the image in figure 4.9.3 (c), it was necessary to apply the internal conformation to the model, which was proposed in figure 4.9.1, i.e., with the side groups pointing away from the surface. Thus, the eight ethyl groups of the model can be correlated with the eight peripheral protrusions per molecule, which are clearly observable in the micrograph. As these protrusions appear with a similar apparent height it can be assumed that all ethyl groups point upward. It is therefore reasonable that the tetrapyrrolic macrocycle lies flat on the surface.

A series of STM images (figure 4.9.4) emphasizes the voltage-dependent appearance of the 2HOEP/CoOEP array. While at low bias voltages,  $-400$  mV  $< U < -200$  mV, the 2HOEP/CoOEP array appears as shown above in figure 4.9.4 (a) and (b), below  $\sim -500$  mV the substituents of CoOEP appear elevated as compared to the ones of 2HOEP ((figure 4.9.4 (c) and (d)). This goes along with an increased apparent height of the central metal.

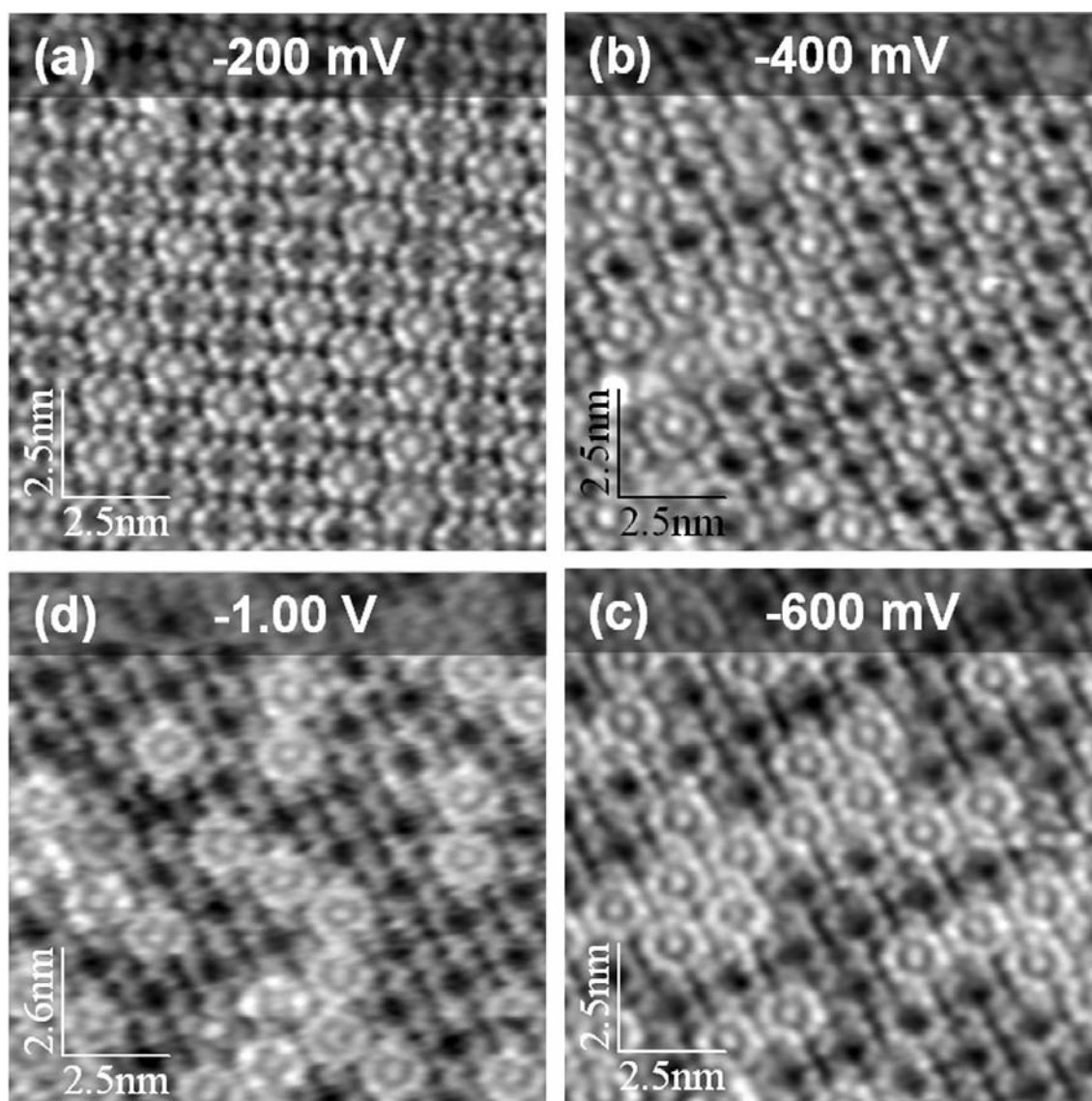


**Figure 4.9.4.** Series of STM images of a 2HOEP/CoOEP layer acquired at different bias voltages; (a)  $U = -200$  mV ( $I = 37$  pA), (b)  $U = -400$  mV ( $I = 39$  pA), (c)  $U = -600$  mV ( $I = 36$  pA) and (d)  $U = -1.00$  V ( $I = 34$  pA).

Enlarged STM images, acquired at bias voltages of -200 mV and -1.00 V are shown in figure 4.9.5 (a) and (b). The height profiles in figure 4.9.5 (c) and (d) were extracted from respectively two ethyl groups of CoOEP and 2HOEP (see dotted lines). Four peaks due to the side groups are visible in each profile. In figure 4.9.5 (c) a similar height of the peaks can be found, whereat in figure 4.9.5 (d) two apparently higher and two lower peaks are observed, highlighting the pronounced voltage-dependence. As the

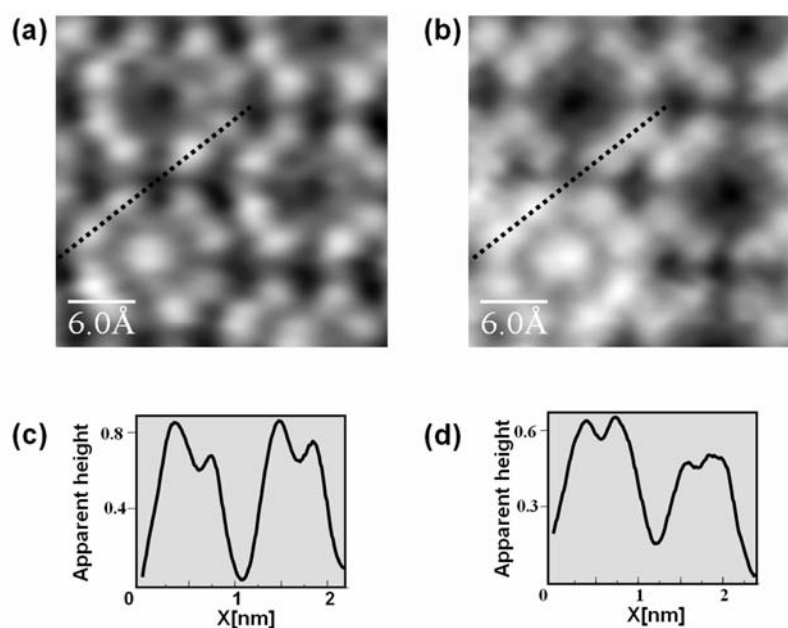


**Figure 4.9.5.** (a) and (b) Enlarged STM image of an intermixed 2HOEP/CoOEP layer acquired at -200 mV and -1.00 V respectively. (c) and (d) Extracted height profiles over the side groups of CoOEP and 2HOEP at the indicated positions ((a)  $I=37$  pA, (b)  $I=34$  pA).

substituents attached to the porphyrin are assumed to be oriented upward and obviously possess the same conformation and topography for both CoOEP and 2HOEP, the observation can be traced back to electronic effects. Mediated tunnelling through the Co(II)  $3d^6$ -orbital system might explain the increasing apparent height of the cobalt ion with increasing negative bias voltages; however, a simple interpretation for the increasing height of the side groups of CoOEP can not be given in the framework of the work at hand.

Note that the symmetric appearance of the porphyrins persists at least over a bias voltage range from -1.2 V to -0.1 V, i.e., there is no indication for a reduced symmetry due to a saddle-shape deformation, as found for the conformationally adapted CoTPP and discussed in detail in chapter 4.6.2. Consequently, it can be concluded that the OEP molecules, in particular also CoOEP, adsorb on Ag(111) such that the porphyrin macrocycle remains in a flat, undistorted conformation.

**CONCLUSION**

A long-range ordered intermixed 2HOEP/CoOEP monolayer was prepared on Ag(111) by means of desorption of excess multilayers (see chapter 3.6). The porphyrins were identified in high-resolution STM images: CoOEP appears with a bright central dot due to the central metal ion, 2HOEP with a central cavity. Furthermore, eight peripheral protrusions per molecule were observed in the micrographs and could be correlated with the terminal groups of the porphyrin. This specific appearance, which was observed over a large bias voltage range, indicates that the porphyrin macrocycle adsorbs flat and undistorted. The voltage-dependent appearance is attributed to mediated tunneling through the Co(II)  $3d^6$ -orbital system.

## 5 Summary and Outlook

---

Different tetrapyrrole complexes adsorbed on Ag(111) were studied in detail by STM at RT. These investigations resulted in a detailed understanding of their *supramolecular ordering and intramolecular conformation*, their *electronic interaction with the surface* and their *reactivity towards atoms and molecules*.

### **MOLECULAR ORDERING AND INTRAMOLECULAR CONFORMATION**

A central aspect of the work at hand is the self-assembly of TPP, TTBPP, OEP and Pc with and/or without a central metal (Co, Fe) on Ag(111). For all investigated systems, supramolecular ordering was observed and the corresponding contributions of molecule/substrate and molecule/molecule interactions as well as the intramolecular conformations could be determined.

In particular, all investigated TPP species assembled in a square order with a lattice constant of 1.4 nm. Even though a certain registry to the substrate was observed for sub-monolayer coverages, the driving force for the square assembly was identified as attractive T-type interactions between the phenyl rings of neighbouring molecules, independent of the nature of the central metal or its absence. In addition *local organisational chirality* was observed, i.e., the square assembly occurred in two enantiomeric forms in the primitive unit cell. Interestingly, all observed domain boundaries separated enantiomeric arrays, thus indicating a reduced long-range order due to the observed *local organisational chirality*. Individual TPP molecules appear with a “dumbbell shape” in STM, which is attributed to a saddle-shape distortion of the porphyrin macrocycle upon adsorption on Ag(111).

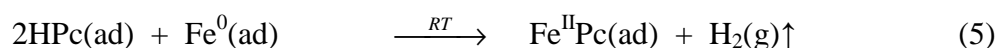
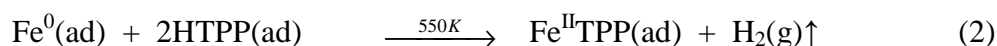
In contrast to the unique square arrangement of TPP, four different phases were found for CoTTBPP on Ag(111). From sub-molecularly resolved STM images, the orientation and internal conformation of the individual molecules within the different phases could be deduced. In particular, the extremely stable *herringbone* phase was

solely observed after heating the sample; indicating the formation in an activated process. Modeling of the different molecular arrangements, considering the internal conformation as well as the long range order, enabled to understand the intermolecular interactions and the different stabilities of the observed phases. Interestingly, in contrast to the intuitive expectation, it was found that the comparably bulky ligands of CoTTBPP do not result in a considerably larger distance of the macrocycle to the surface than found for CoTPP with simple phenyl ligands.

Pure and mixed monolayers of 2HOEP and CoOEP were shown to assemble hexagonally close-packed on Ag(111), indicating weak lateral interactions. Sub-molecularly resolved STM images indicate that the porphyrin ring is not distorted and thus adsorbs planar on Ag(111), with the eight ethyl groups pointing away from the surface.

### **COORDINATION OF METAL ATOMS BY FREE BASE PORPHYRINOIDS**

Microscopic evidence for the direct metalation of free base porphyrinoids with different metals, i.e., cobalt or iron, was given. The central cavity of free base porphyrinoids can be resolved in high-resolution STM micrographs. Upon defined dosage of the respective metal, a corresponding fraction of molecules appears with a modified appearance, which is attributed to the formation of metalloporphyrinoids. This novel type of surface reaction could be evidenced with STM for the following reaction schemes:



Generally, the in-situ metalation of self-assembled porphyrin arrays on Ag(111) under UHV condition enables the generation of ultra-clean metalloporphyrins.

## **ELECTRONIC PROPERTIES OF PORPHYRINS**

One particular interesting observation was the voltage-dependent appearance of CoTPP on Ag(111): the molecule appears with a central protrusion at low negative bias voltages ( $\sim -0.1$  to  $-0.4$  V) and anisotropic at elevated negative bias voltages ( $< -0.4$  V). In contrast, FeTPP generally appear anisotropic, independent of the applied bias voltages ( $\sim -0.1$  V to  $-1.5$  V). All observed shapes of the different molecules could be reproduced by simulated STM images [140], calculated by the working group of Prof. Dr. Andreas Görling (SFB 583). The appearance of 2HTPP and FeTPP is dominated by the topography of the molecule, i.e., by the saddle-shaped distortion and the central cavity or the central Fe atom. For the reproduction of the shape of CoTPP it was necessary to consider the molecule-substrate interaction in the calculations. The appearance the CoTPP with a central protrusion could be tracked down to an orbital composed of silver 5s atomic states with an admixture of Co( $d_{z^2}$ ) states; this is exclusively an electronic effect, demonstrating that adsorbate-substrate coupling could be monitored with STM. At a higher negative bias voltage the appearance of CoTPP is very similar to that of FeTPP. This is attributed to the contribution of orbitals basically resembling the topography of the CoTPP. With *continuous imaging tunneling spectroscopy* (CITS), a spectro-microscopic technique, the corresponding orbitals could be visualized in LDOS maps. Thus electronic and topographic contributions, determining the appearance of the molecules in STM images, were separated and a detailed understanding of the appearance in constant current images was accomplished.

## **INTERACTION WITH SMALL MOLECULES**

Upon dosage of NO onto an ordered sub-monolayer of CoTPP an expansive rearrangement of the CoTPP layer was observed in-situ with STM. This effect was attributed to the formation of mixed CoTPP + NO layers, indicating that these coadsorbed structures are energetically favourable. The expansion of the CoTPP layer upon NO coadsorption indicates an increasing number of NO molecules per unit cell. This effect was attributed to significant attractive lateral dipole-dipole interactions of the electropositive CoTPP and the electronegative NO.

Upon NO exposure, a fraction of molecules showed a modified appearance in the constant current images. A consistent interpretation could be given with complementary spectroscopic methods, i.e., UPS [109] and STS. It was reported by Flechtner et al. that the competition of the ligands (NO and Ag(111)) in trans-position with respect to the same metal d orbitals results in a weakened bond to the Ag surface [109]. In that course electron tunneling through the Co (II)  $3d^6$ -orbital system is suppressed, thus explaining the pronounced modification of the appearance. Therefore the formation of a NO-CoTPP complex at RT can be assumed.

## **OUTLOOK**

Large organic molecules on surfaces are promising candidates for the generation of functional devices. The findings discussed in the work at hand contain valuable information to engineer such devices, e.g., the extremely rigid herringbone structure of CoTTBPP is suggested to serve as template for the aggregation of more complex hierarchical structures. However the experiments reported here are restricted to the substrate Ag(111). For a better understanding of the role of the applied type of metal surface and the adsorbed tetrapyrrols, and in order to engineer its properties, the investigations should be expanded to other substrate materials and to pre-structured substrates. First explorative results on a Cu(111) surface with nickel islands indicate a local functionalization of the investigated 2HOEP molecules on the Ni islands. Therefore, a future challenge should be the investigation of tetrapyrrols on nanostructured surfaces with the goal to extract strategies for the local functionalization of the surface based on different adsorbate/substrate interactions of the adsorbed molecules with the corresponding substrate regions.

## 6 Zusammenfassung und Ausblick

---

Im Rahmen der vorliegenden Arbeit wurden verschiedene Tetrapyrrolkomplexe auf Ag(111) adsorbiert und mittels STM bei Raumtemperatur untersucht. Daraus ergab sich ein detailliertes Verständnis der *supramolekularen Anordnung, der intramolekularen Konformation, der elektronischen Wechselwirkung mit der Oberfläche* und der *Reaktivität mit Atomen und Molekülen*.

### **MOLEKÜLANORDNUNG UND INTRAMOLEKULARE KONFORMATION**

Ein zentraler Aspekt dieser Arbeit war die Selbst-Aggregation von TPP, TTBPP, OEP und Pc mit und/oder ohne zentralem Metallatom (Co, Fe) auf Ag(111). Die supramolekulare Anordnung aller untersuchten Systeme konnte aufgezeigt werden und sowohl auf entsprechende Wechselwirkungen zwischen Molekül/Substrat bzw. Molekül/Molekül, als auch auf die intramolekulare Konformation, zurückgeführt werden.

Alle untersuchten TPPs aggregierten quadratisch mit einer Gitterkonstante von 1.4 nm. Obwohl im Submonolagenbereich eine Registrierung zum Substrat nachgewiesen werden konnte, wurde die Triebkraft der Aggregation als eine attraktive „T-typ“ Wechselwirkung zwischen den Phenylringen benachbarter Moleküle identifiziert. Dies konnte unabhängig von der Natur des zentralen Metalls, oder dessen Abwesenheit, bestätigt werden. Des Weiteren wurde die quadratische Anordnung in zwei enantiomeren Formen der primitiven Einheitszelle vorgefunden. Sämtliche beobachteten Domänengrenzen wurden von Enantiomeren begleitet. Folglich limitiert die *lokale organisatorische Chiralität* die weit reichende Ordnung. Individuelle TPPs erscheinen „hantelförmig“ auf den STM Bildern. Hierfür ist die sattelförmige Verzerrung der Porphyrinringe adsorbierter Moleküle verantwortlich.

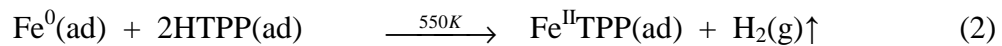
Im Gegensatz zur einheitlichen quadratischen Anordnung der TPPs, wurden vier unterschiedliche CoTTBPP Phasen auf Ag(111) aufgedeckt. Auf den hochaufgelösten

STM Bildern konnte sowohl die Orientierung, als auch die interne Konformation der Moleküle, innerhalb der entsprechenden Phasen, ausgemacht werden. Die ausgesprochen stabile *herringbone* Phase konnte lediglich nach dem Heizen der Probe beobachtet werden. Daraus kann gefolgert werden, dass diese Formation im Zuge eines aktivierten Prozesses entstanden ist. Die Modellierung der unterschiedlichen molekularen Anordnungen, implizit der internen Konformation und weit reichenden Ordnung, ermöglichte die Aufklärung der intermolekularen Wechselwirkungen und dementsprechend die Deutung der unterschiedlichen Stabilitäten dieser Phasen. Somit konnte auch gezeigt werden, dass die vergleichsweise voluminösen Liganden des CoTTBPP, nicht unbedingt mit einem größeren Abstand des Porphyrinrings zur Oberfläche, als dem für CoTPP, einhergehen.

Reine und gemischte Monolagen von 2HOEP und CoOEP aggregierten hexagonal dicht gepackt auf Ag(111), welches auf schwache laterale Wechselwirkungen schließen lässt. STM Bilder mit sub-molekularer Auflösung zeigen, dass der Porphyrinring keine Verzerrung aufweist und somit planar adsorbiert, dabei sind die acht Ethylgruppen der Oberfläche abgewandt ausgerichtet.

### **KOORDINIERUNG VON METALLATOMEN DURCH 2H-PORPHYRINOIDE**

Der mikroskopische Nachweis für die direkte Metallierung von 2H-Porphyrinoiden mit verschiedenen Metallen, z.B. Kobalt oder Eisen, konnte erbracht werden. Die zentrale Kavität der 2H-Porphyrinoide ist auf den hochaufgelösten STM Bildern zu erkennen. Nach der Dosierung einer definierten Menge des jeweiligen Metalls, erscheint eine entsprechende Molekülfraktion verändert. Der Grund hierfür ist die Ausbildung von Metall-Porphyrinoiden. Dieser neuartige Typ der Oberflächenreaktion konnte mittels STM für die folgenden Reaktionen nachgewiesen werden:



Im Allgemeinen ermöglicht die in-situ Metallierung der selbst-aggregierten Porphyrinoide auf Ag(111) die Erzeugung von ultra-reinen Metallporphyrinen unter UHV-Bedingungen.

### **ELEKTRONISCHE EIGENSCHAFTEN DER PORPHYRINE**

Das spannungsabhängige Erscheinungsbild von CoTPP auf Ag(111) stellt sich wie folgt dar: die Moleküle erscheinen mit einer zentralen Erhebung bei niedrigen negativen Spannungswerten ( $\sim -0.1$  to  $-0.4$  V) und anisotrop bei einer entsprechend höheren negativen Spannungen ( $< -0.4$  V). Im Gegensatz dazu, erscheint FeTPP generell anisotrop, unabhängig davon, welche negativen Spannungen angelegt werden ( $\sim -0.1$  V to  $-1.5$  V). Alle erhaltenen Erscheinungsbilder der verschiedenen Porphyrine wurden in der Arbeitsgruppe von Prof. Dr. Andreas Görling (SFB 583) mittels simulierter STM Bilder reproduziert. Die Erscheinung von 2HTPP und FeTPP ist durch die Topographie des jeweiligen Moleküls dominiert, d.h. durch die sattelförmige Verzerrung und die zentrale Kavität oder durch das zentrale Fe Atom. Um das CoTPP Erscheinungsbild zu reproduzieren, war es nötig, die Molekül-Substrat Wechselwirkung mit einzubeziehen. Die zentrale Erhebung des CoTPP konnte somit auf ein Orbital herunter gebrochen werden, welches aus Silber 5s-Zuständen und einer Beimischung von  $\text{Co}(d_{z^2})$  Zuständen zusammengesetzt ist; dies zeigt einen ausschließlich elektronischen Effekt. Somit ist klar, dass hierbei Adsorbat-Substrat Wechselwirkung mittels STM beobachtet wurde. Bei höheren negativen Tunnel-spannungen erscheinen CoTPP und FeTPP sehr ähnlich. Dies kann man durch den Beitrag von Orbitalen erklären, welche der Topographie des CoTPP folgen. Mittels spektromikroskopischer Technik, *continuous imaging tunneling spectroscopy* (CITS), konnten die entsprechenden Orbitale in LDOS Bildern visualisiert

werden. Somit konnten die elektronischen und topographischen Informationsgehalte der STM Bilder separiert und ein detailliertes Verständnis der STM Aufnahmen erreicht werden.

### **WECHSELWIRKUNG MIT KLEINEN MOLEKÜLEN**

Nach der Dosierung von NO auf eine geordnete Sub-Monolage von CoTPP, wurde in-situ eine Umordnung der CoTPP Lage beobachtet. Dieser Effekt konnte der Formierung einer gemischten CoTPP + NO Lage zugeschrieben werden, woraus man folgern kann, dass derart koadsorbierte Strukturen energetisch günstiger sind. Die Expansion der CoTPP Lagen nach der Dosierung von NO, lässt auf eine Zunahme der Anzahl von NO Molekülen per Einheitszelle schließen. Dies kann auf die attraktiven, lateralen Dipol-Dipol Wechselwirkungen zwischen dem elektropositiven CoTPP und dem elektronegativen NO zurückgeführt werden. Nach entsprechender NO-Dosierung, wies ein Teil der Moleküle ein verändertes Erscheinungsbild im STM auf. Dies konnte mittels komplementärer Methoden, UPS [109] und STS, konsistent interpretiert werden. Flechtner u.a. berichtete bereits, dass die Liganden (NO und Ag(111)) in *trans*-Stellung um dasselbe d-Metallorbital konkurrieren, was wiederum zu einer Abschwächung der Bindung zur Silberoberfläche führt [109]. In diesem Zuge wird der Tunnelbeitrag der Elektronen über das Co(II)  $3d^6$ -Orbital System unterdrückt, wodurch die beschriebene Veränderung des Erscheinungsbildes erklärt werden kann. Somit kann die Bildung eines NO-CoTPP Komplexes angenommen werden.

### **AUSBLICK**

Große organische Moleküle auf Oberflächen sind viel versprechende Kandidaten zur Erzeugung funktioneller Baugruppen auf kleinstem Maßstab. Die in dieser Arbeit diskutierten Ergebnisse können einen wichtigen Beitrag zur Erzeugung derartiger Einheiten darstellen, z.B. die bemerkenswert robuste CoTTBPP *herringbone* Struktur wird als Templat zur Aggregation von komplexeren hierarchischen Strukturen vorgeschlagen. Die dargestellten Ergebnisse sind nun auf Ag(111) beschränkt. Um ein besseres Verständnis bezüglich der Rolle des verwendeten Metallsubstrats und des

adsorbierten Tetrapyrrols zu bekommen, sollen die Untersuchungen auf weitere und im Besonderen, auf vorstrukturierte Substrate erweitert werden. Dies soll erlauben, Systeme mit maßgeschneiderten Eigenschaften zu entwickeln. Erste Untersuchungen, an einer mit Nickelinseln präparierten Cu(111) Oberfläche, deuten auf eine lokale Funktionalisierung der verwendeten 2HOEP Moleküle auf den Inseln hin. Dem entsprechend stellen Untersuchungen von Tetrapyrrolen auf nanostrukturierten Oberflächen eine zukünftige Herausforderung dar. Das Ziel hierbei ist die Findung von Strategien zur lokalen Funktionalisierung, basierend auf der unterschiedlichen Adsorbat/Substrat Wechselwirkung des adsorbierten Moleküls mit den entsprechenden Substratbereichen.



## List of Abbreviations

CITS	Continuous Imaging Tunneling Spectroscopy
DFT	Density Functional Theory
DOS	Density of States
HOMO	Highest Occupied Molecular Orbital
HOPG	Highly Oriented Pyrolytic Graphite
LEED	Low Energy Electron Diffraction
LUMO	Lowest Unoccupied Molecular Orbital
MTPP	Metallotetraphenylporphyrin
OEP	Octaethylporphyrin
OMT	Orbital Mediated Tunneling
Pc	Phthalocyanine
QMS	Quadrupole Mass Spectrometry
STM	Scanning Tunneling Microscopy
STS	Scanning Tunneling Spectroscopy
TPD	Thermal Programmed Desorption
TPP	Tetraphenylporphyrin
TPyP	Tetrapyridylporphyrin
TTBPP	Tetrakisdi-tert-butylphenylporphyrin
RT	Room Temperature
UHV	Ultra High Vacuum
UPS	Ultraviolet Photoelectron Spectroscopy
XPS	X-ray Photoelectron Spectroscopy



# Figure Caption

<b>Figure 3.1.1.</b> Scheme of the UHV system.....	22
<b>Figure 3.2.1.</b> (a) and (b) STM scan head. (c) Sample holder. The drawings are re-printed from RHK's User Guide [29].....	24
<b>Figure 3.2.2.</b> Scan head touched down on the sample holder. The drawing is reprinted from RHK's User Guide [29]. .....	25
<b>Figure 3.4.1.</b> (a) Face centered cubic (fcc) lattice of the silver crystal with the drawn in (111) plane. (b) Top view on the (111) plane [31].....	28
<b>Figure 3.4.2.</b> (a) STM image of the pure Ag(111) surface with atomic resolution ( $U = -38$ mV, $I = 1.22$ nA). The unit cell and the preferential directions are drawn in. (b) Corresponding LEED pattern of the clean Ag(111) surface.....	29
<b>Figure 3.5.1.</b> (a-d) Top view on space filling models of the applied porphyrinoids, as expected in the gas phase. (e-f) Side view, illustrating how the individual substituents could determine the distance of the porphyrin macrocycle to the Ag(111) surface in this naive model. (g) and (h) anticipate the conformation on a flat surface. ....	32
<b>Figure 3.6.1.</b> QMS spectrum of 2HTPP .....	34
<b>Figure 3.7.1.</b> Calibration of the metal flux of (a) cobalt and (b) iron. The flux monitor of the evaporator was adjusted to $I_{\text{flux}} = 5$ nA. To calibrate the metal flux, the thickness was measured as a function of time by a microbalance. ....	36
<b>Figure 4.1.1.</b> Sequence of STM images of CoTPP on Ag(111) acquired upon incremental increase of the coverage $\theta_{\text{abs}}$ . (a) The Ag(111) steps are decorated with CoTPP at a low coverage ( $U = -1.25$ V, $I = 15$ pA). (b) Two-dimensional islands evolve at medium coverage ( $U = -1.20$ V, $I = 255$ pA). (c) Monolayer of CoTPP ( $U = -1.21$ V, $I = 41$ pA). (d) STM image of the multilayer regime ( $U = 5.13$ V, $I = 25$ pA). ....	41
<b>Figure 4.1.2.</b> TPD spectrum of 2HTPP on Ag(111).....	43
<b>Figure 4.1.3.</b> Side view on the potential adsorption of CoTPP in the multilayer regime. The molecules in the 1 <sup>st</sup> layer are lying with the porphyrin macrocycle parallel to the surface $\delta_n = 0$ . The compression of the multilayer is explained by a gradual change of the tilt angle $0^\circ < \delta_n < 90^\circ$ within one domain, limiting the size of the domains. The observed domain boundaries can be traced back to a reverse gradual change of the tilt angle $\pm \delta_n$ . ....	44

**Figure 4.1.3.** Space-filling models showing top and side view on TPP adsorbed on Ag(111). The incorporated sign “+” addresses elevated positions on the model, “-“ depressed. STM images nearby highlight the anisotropic appearance of individual  $x$ -TPP ( $x=Fe, Co, 2H$ ). The latter observation is less pronounced for 2HTPP ( $U_{FeTPP} = -1.25$  V,  $I_{FeTPP} = 15$  pA) ( $U_{CoTPP} = -1.18$  V,  $I_{CoTPP} = 58$  pA), ( $U_{2HTPP} = -7$  mV,  $I_{2HTPP} = 54$  pA)..... 45

**Figure 4.1.4.** Potential arrangements of TPP on Ag(111). (a) A rotation of the molecular axis out of the unit cell by  $15^\circ$  results in a parallel alignment of adjacent phenyl legs, i.e.,  $\pi$ - $\pi$  stacking. (b) A rotation by  $30^\circ$  results in a perpendicular motif of neighbouring phenyl rings, i.e., T-stacking. The space-filling models applied in (c) and (d) exhibit the internal conformation of TPP on Ag(111) as determined by STM (see figure 4.1.3) and show the corresponding arrangements with respect to (a) and (b). Obviously the arrangement of the aggregate in (c) is highly unfavourable because of a large steric hindrance..... 48

**Figure 4.1.5.** (a) STM image of a mixed monolayer of FeTPP/2HTPP ( $U = -100$  mV,  $I = 46$  pA). (b) Enlarged image of (a), which is superimposed with corresponding space-filling models. The proximate substituents show a “T”-shaped arrangement (c) Mixed layer of CoTPP/2HTPP exhibiting the same arrangement as the layer in (a) ( $U = -1.35$  V,  $I = 35$  pA). The T-shaped motif is again apparent and illustrated by the included molecular axis. (d) 2HTPP monolayer showing the analogue arrangement as the layers in (a) and (c) ( $U = +454$  mV,  $I = 25$  pA)..... 50

**Figure 4.1.6.** (a) Constant current image of a monolayer of FeTPP/2HTPP emphasizing the chiral domain I and II ( $U = -7$  mV,  $I = 11$  pA). The domains differ by the sense of rotation. (b) Enlarged image of the superimposed and scaled space-filling models, which underline the surface chirality. Note that at the domain boundary the unit cells are shifted by half of the length of a lattice vector. (c)-(e) STM image of layers of 2HTPP and CoTPP confirming 2D-chirality ( $U_{2HTPP} = 461$  mV,  $I_{FeTPP} = 24$  pA) ( $U_{CoTPP} = -1.18$  V,  $I_{CoTPP} = 58$  pA), ( $U_{CoTPP} = 1.82$  V,  $I_{CoTPP} = 23$  pA)..... 52

**Figure 4.1.7.** (a) Constant current image of a sub-monolayer of FeTPP/2HTPP. The domains are rotated by multiples of  $60^\circ$ . Internally, each of the domains exhibits 2D-chirality ( $U = -213$  mV,  $I = 37$  pA). (b) The individual unit cells of the domains are shown enlarged and the corresponding molecular axis of FeTPP are depicted. The drawn in dumb-bells highlight the anisotropy axis per molecule. The high-symmetry directions of the Ag(111) surface are marked by arrows. In each of the drawn in unit cells strictly one of the two molecular axis points towards one high-symmetry direction of Ag(111)..... 53

**Figure 4.1.8.** (a) and (b) Space-filling models placed on a Ag(111) model surface. The changing registration of respectively one of the two molecular axis per molecule in chiral domains towards one of the main axis of Ag(111) is highlighted. The lateral stabilization of the square arrangement is driven by two T-type”-structures at each phenyl ring..... 55

**Figure 4.2.1.** Top view (a) and side view (b) of CoTTBPP, with the phenyl group oriented perpendicular to the plane of the porphyrin macrocycle (twist angle  $\Theta = 90^\circ$ ). In (c) a possible molecular deformation is shown, with the TB-phenyl substituent rotated out of the porphyrin macrocycle plane ( $\Theta < 90^\circ$ ). Thereby,

the quadratic arrangement of the upper TB groups (indicated in yellow) changes to a rectangle. In (d) the TB-phenyl ligands are tilted towards the porphyrin macrocycle (tilt angle  $\Phi$ ). Thereby the distance between the upper TB groups (yellow) is reduced.....59

**Figure 4.2.2.** STM constant current images of a self-assembled CoTTBPP film on Ag(111), with a coverage slightly below one monolayer. Three phases with different long range order and different molecular conformations are clearly distinguishable, as indicated by the capital letters A, B, and C. For each phase several domains are observed; (a) and (b) show different regions of the same sample. According to their structure, the different molecular phases are indicated as hex A (A), hex B (B), and square (C). The arrows in the upper left corner of (a) indicate the three azimuthal orientations of different domains of phase hex A (A), which are rotated to each other by  $120^\circ$ . .....61

**Figure 4.2.3.** (a) Typical STM image of CoTTBPP in the multilayer regime. The stripy features are tip induced. (b)-(d) STM images of a monolayer of CoTTBPP, acquired after a thermal treatment (45 s at 550 K) of the multilayer. Mainly two situations are found: The minority observation is a mixture of the square and the hex B phase, shown in (b). Most of the investigated areas exhibited the herringbone phase, shown in (c) as large area image and (d) as a high-resolution image. ....62

**Figure 4.2.5.** Overview of STM images of the four phases with and without the corresponding molecular models superimposed: (a-d) square phase, (e-h) hex A phase, (i-l) hex B phase and (m-p) herringbone phase. The size of the STM images is  $(10 \times 10) \text{ nm}^2$  for the first two columns and  $3 \times 3 \text{ nm}$  for the remaining. The molecular models are scaled to fit and placed by hand in the STM images. ....66

**Figure 4.2.7.** (a) Constant current image of a monolayer of CoTTBPP, recorded at a negative bias voltage ( $U = -803 \text{ mV}$ ,  $I = 44 \text{ pA}$ ). (b) CoTTBPP layer, acquired at a positive bias voltage ( $U = +1.17 \text{ mV}$ ,  $I = 36 \text{ pA}$ ). (c) Zoom on a single molecule extracted from figure (a), whereupon a centered oval-shaped protrusion, probably due to both the central cobalt ion and two opposing pyrrol rings, is visible. (d) Enlarged image of a single molecule acquired at positive polarity, extracted from (b). The peripheral upper tert-butyl-groups appear elevated; the central cobalt ion is not visible. ....75

**Figure 4.3.1.** (a) STM image of a monolayer of 2HTPP on Ag(111). b) STM image of a monolayer of 2HTPP on Ag(111) after evaporation of 0.03 ML Fe. c) Height profile extracted along the line in figure 4.3.1(b). Above the profile a filled space model of 2HTPP and below a model of FeTPP is shown. The arrows indicate the positions of the molecules in the images and the profile. ....80

**Figure 4.3.2.** (a)-(d) Series of STM images after the successive evaporation deposition of equal amounts of Fe.....81

**Figure 4.3.3.** Two STM images showing different regions of the surface after the evaporation deposition of  $\sim 0.14 \text{ ML}$  of Fe. ....83

**Figure 4.3.4.** (a) STM image showing the nucleation of Fe on step edges of Ag(111). 0.025 ML of Fe were deposited at RT ( $I = 35 \text{ pA}$ ;  $U = -1.2 \text{ V}$ ). b) 2HTPP monolayer prepared via vapor-deposition onto

the surface depicted in figure 2a ( $I = 24$  pA;  $U = 0.45$  V). The image shows an ordered 2HTPP monolayer at the terraces coexisting with iron clusters at the step edges. c) Situation after heating the surface shown in figure 4.3.4 (b) to 550 K (terraces individually color-coded). The bright spots in c) are again assigned to FeTPP formed by metalation of 2HTPP ( $I = 37$  pA;  $-1.57$  V). ..... 85

**Figure 4.3.5.** (a) Self-assembled 2HTPP layer on Ag(111) ( $I = 25$  pA;  $U = 0.37$  V). (b) The layer after reaction of pre-deposited Fe with 2HTPP to FeTPP. As indicated by the superimposed structure models, two opposing pyrrol rings per FeTPP molecule (marked yellow) are clearly visible ( $I = 55$  pA;  $U = -0.41$  V). ..... 87

**Figure 4.3.6.** RT constant current STM images of a monolayer of (a) 2HTPP,  $U = -154$  mV,  $I = 29$  pA and (b) after the evaporation deposition of Co,  $\theta_{Co} = 0.012 \pm 0.002$ ,  $U = -213$  mV,  $I = 33$  pA. .... 89

**Figure 4.3.9.** Schematic energy profile for Co atom insertion into 2H-porphyrin, reprinted from the publication of Shubina et al. [42]. ..... 94

**Figure 4.4.1.** TPD spectrum of 2HTTBPP on Ag(111). The applied heating rate was 1K/s ..... 99

**Figure 4.4.2.** (a) Constant current image of 2HTTBPP in the multilayer regime. Tip- induced peninsulas in vertical direction were observed ( $U = 2.08$  V;  $I = 58$  pA). (b) Micrograph recorded with the tip scanning in horizontal direction, inducing horizontal oriented peninsulas. On top of these, the molecules are arranged oblique ( $U = 2.08$  V;  $I = 33$  pA). (c) Monolayer of 2HTTBPP, which was acquired after heating the multilayer 45 s at 550 K. An oblique structure was observed ( $U = 1.65$  V;  $I = 20$  pA). (d) Sharp 2D-Fourier peaks evidence the periodicity of the structure. .... 100

**Figure 4.4.3.** (a) Constant current image of a monolayer of 2HTTBPP ( $U = -967$  mV,  $I = 46$  pA). The unit cell consists of two molecules; the central molecule has a different azimuthal orientation, as indicated by the drawn in rectangles. The dash-dotted lines depict molecular rows 1 and 2, differing by the azimuthal orientation and apparent height. (b) The unit cell consists of two molecules; the central molecule has a different azimuthal orientation, as shown in (a). (c) and (d) Enlarged STM of a monolayer of 2HTTBPP and CoTTBPP. .... 102

**Figure 4.4.4.** (a) Constant current image showing a monolayer of 2HTTBPP molecules superimposed with corresponding hard-sphere models ( $+1.12$  V and 22 pA). The size of the STM images (b) – (e) is  $(3 \times 3)$  nm<sup>2</sup>. (b) 2HTTBPP extracted from “row 1”; the four protrusions are attributed to the upper tert-butyl groups. (c) Figure 4.4.5 (b) is superimposed with the corresponding hard-sphere models. (d) and (e) show a single 2HTTBPP molecule extracted from “row 2”. .... 103

**Figure 4.4.5.** (a) – (d) Space filling models of 2HTTBPP on Ag(111): (a) Top view illustrating the proposed conformation of 2HTTBPP in “row 1”, (b) Conformation of molecules located in “row 2”; (c) Side view on (a), (d) side view on (b); a height difference of the space filling models with different intra-molecular conformations is clearly visible. .... 104

**Figure 4.4.6.** (a) and (b) Inverse height modulation of the depicted 2HTTBPP rows (label 1 and 2). The respective rows contain molecules, which exhibit a specific type of deformation (indicated by rectangles, which are drawn with full or dotted line). Remarkably, the apparently elevated rows “2” in (a) appear lowered in (b), even if a corresponding type of deformation of 2HTTBPP is assumed. ((a) +1.12 V and 22 pA; (b) + 1.20 V and 23 pA). .....106

**Figure 4.4.7.** STM images of 2HTTBPP acquired at different bias voltages. (a). Constant current image recorded at + 1.20 V and 23 pA. Four corner molecules and a central one participate to the unit cell, which is drawn in the images. (b)–(c) Micrographs acquired at  $\pm 284$  mV ( $I = 23$  pA). .....108

**Figure 4.4.8.** (a) STM image of a monolayer of 2HTTBPP on Ag(111) ( $U = +1.87$  V,  $I = 18$  pA). (b) Mixed monolayer of 2H- and Fe-TTBPP after deposition of 0.02 ML of Fe ( $U = -401$  mV,  $I = 22$  pA). The layer now exhibits a bimodal appearance, showing 60% of protrusions, which can be attributed to FeTTBPP. ....110

**Figure 4.5.1.** TPD spectrum of 2HPc on Ag(111). .....114

**Figure 4.5.2.** Constant current STM image (a) of a complete monolayer of 2HPc and (b) after the deposition of iron ( $\theta_{Fe} = 0.012$  ML) onto the 2HPc monolayer. In (b) some molecules exhibit a central bright spot, suggesting the formation of FePc. (c) Height profile extracted along the green line in (b). Space-filling models of 2HPc and FePc are shown above and below the height profile, respectively. The arrows indicate the positions of the molecules in the images and the profile. The tunneling parameters of the STM micrographs were: (a) -0.67 V, 39 pA; (b) -1.45 V, 33 pA. ....115

**Figure 4.5.3.** (a) Constant current STM image of a monolayer of 2HPc exhibiting two topographically different 2HPc species. (b)–(d) Clockwise arranged sequence of STM images after the incremental deposition of Fe ( $\theta_{Fe} = 0.012$  ML in each step). The bar graphs of each figure show the percentages of the two 2HPc species with different apparent heights and of phthalocyanines with coordinated Fe atoms (= FePc). The tunneling parameters of the STM micrographs were: (a) -0.26 V, 22 pA; (b) -1.44 V, 34 pA; (c) -1.42 V, 22 pA; (d) -0.99 V, 0.33 pA. ....117

**Figure 4.5.4.** Constant current STM images of (a) a mixed monolayer of 2HPc (95%) and FePc (5%), generated by direct deposition of a 2HPc/FePc mixture; (b) after vapor-deposition of Fe ( $\theta_{Fe} = 0.012 \pm 0.003$  ML) on this mixed monolayer; (c) a larger area of the layer of image 3b. The following tunneling parameters were applied: (a) -0.88 V, 25 pA; (b) and (c) -1.22 V, 34 pA. ....119

**Figure 4.6.1.** Constant current STM images of a monolayer of CoTPP on Ag (111). All STM micrographs were acquired with a current of  $I_{set} = 0.3$  nA and the indicated bias voltages at RT. In (a-c) the appearance of depressions, denoted as “pits”, is evident for bias voltages of -1.2 and -0.6 V. (a) and (d) are acquired at the identical surface region, but at different bias voltages; in both images the same specific molecule. ....124

**Figure 4.6.2.** Correlation of UP spectra of homogenous monolayers of 2HTPP (green line) and CoTPP (blue line) with a bias series (-1.2 V to -100 mV in 100 mV steps) of constant current STM images acquired at a current of 0.3 nA. The corresponding bias voltages are marked with the red arrows, referring to the energy scale of the UP spectrum (relative to  $E_F \equiv 0$ ). ..... 125

**Figure 4.6.3.** Constant current STM images of a monolayer of CoTPP (a) and (b) and a 1:2 ex-situ mixture of 2HTPP / CoTPP (d) and (e) on Ag (111). Enlarged images (c) and (f) of (b) and (e) respectively. The tunneling parameters are: (a)  $I_{set} = 0.3$  nA,  $U_{bias} = -0.6$  V; (b)-(c)  $I_{set} = 0.3$  nA,  $U_{bias} = -1.0$  V; (d)  $I_{set} = 41$  pA,  $U_{bias} = -1.0$  V; (e)-(f)  $I_{set} = 30$  pA,  $U_{bias} = -1.4$  V ..... 127

**Figure 4.6.4.** (a) and (b) Constant current STM images (both with  $I_{set} = 0.27$  nA) of a monolayer CoTPP on Ag (111) at negative bias voltage -1 V (a) and the same surface area at positive bias voltage +1 V (b). The apparent contrast inversion is visualized in (c), which represents an overlay of the processed STM images in (a) and (b) as described in the text. The profiles of the apparent height along the colored lines in (a) and (b) are shown in (d). ..... 129

**Figure 4.6.5.** Local ST spectra reflecting the LDOS of CoTPP (blue line) and 2HTPP (red line) are plotted. The ST spectra were extracted from CITS data of a mixed layer of CoTPP and 2HTPP. .... 130

**Figure 4.6.2.1.** Schemes and STM images illustrating the preparation route to generate the intermixed porphyrin layer consisting of the three different species: 2HTPP, CoTPP and FeTPP. (a) Scheme showing the evaporation of a mixture of 2HTPP and CoTPP onto the Ag(111) substrate. (b), (c) Medium-resolution STM images of mixed 2HTPP/CoTPP layers generated from mixtures with different ratios of the two porphyrin species as indicated. Both images were acquired at negative bias voltages around -1 V where the metalloporphyrin (CoTPP) appears as a protrusion. The ratio of the molecules appearing as protrusions is in excellent agreement with the CoTPP portion in the original mixture. (d) Scheme of the in-situ evaporation of Fe onto a mixed 2HTPP/CoTPP layer. Fe will metalate available 2HTPP under the release of  $H_2$  with almost 100% yield. By evaporating a defined amount of Fe the fraction of the resulting FeTPP within the intermixed layer can be controlled. Thus the whole process enables the generation of an intermixed 2HTPP, CoTPP and FeTPP layer with defined ratios of the corresponding species. .... 133

**Figure 4.6.2.2.** STM images of the same surface area of an intermixed 2H-, Co- and FeTPP at different bias voltages. Obviously at the higher bias voltage as shown in (a) and (b) a bimodal appearance of the three porphyrin species is observed ( $U_{Gap} = -810$  mV and  $I_{set} = 30$  pA). The 2HTPP appears with a central depression, whereas the two metalloporphyrin species, namely CoTPP and FeTPP appear both with the typical saddle-shape, which means that they are undistinguishable at the actual tunneling condition. In figure (c) and (d) the same surface areas as in (a) respective (b) are imaged at reduced bias voltage ( $U_{Gap} = -240$  mV and  $I_{set} = 35$  pA). It is apparent that at this tunneling condition three different appearances of individual molecules can be observed. Whereas the 2HTPP images remain essentially the same, a fraction of the saddle-shaped molecules now appear with a central protrusion. These molecules can be identified as CoTPP, which means that (in contrast to 2HTPP and FeTPP) CoTPP exhibits a

strong bias-dependent appearance in STM. Thus the discrimination of the three species becomes possible at reduced bias voltages. ....136

**Figure 4.6.2.3.** STM micrograph demonstrating an altered appearance of CoTPP upon a changing bias voltage from -1.0 V to -0.3 V ( $I=35$  pA) in one image. In the upper part a longish shape of CoTPP is apparent, whereat in the lower part of the image a central dot presents the main feature. ....138

**Figure 4.6.2.4.** Experimental (a, b) and calculated (c-j) STM images of a single CoTPP molecule on Ag(111) at low negative (top row) and high negative bias voltages (bottom row). As indicated in the images the calculations were performed for the porphyrin adsorbed on Ag(111) and for the porphyrin in the gas phase as well as for different intramolecular geometries ( $\Theta = 60^\circ$  and  $\Theta = 90^\circ$ ). The experimental observation of the central protrusion at low bias voltages in (a) could only be reproduced in the simulations in (c), (e) and (g), where the CoTPP is adsorbed on Ag(111), i.e., this characteristic feature could not be reproduced for the gas phase calculations as shown in (i) even though the same molecular geometry has been used. The experimentally observed saddle-shape in the high bias regime in (b) was reproduced assuming  $\Theta = 60^\circ$  in (d), (f) and (j). Thus a good agreement for both bias regimes could only be achieved considering both the molecule surface interaction as well as the dihedral angle  $\Theta = 60^\circ$ . In the calculations an indefinitely sharp tip is assumed, which results in unrealistic details in the calculated STM images. To exemplary address this problem a gaussian smooth was applied to the images (e) and (d), the results are shown in (c) respective (d). ....140

**Figure 4.6.2.5.** Comparison of calculated (a,b) and experimental (c,d) constant current STM images and the corresponding scaled molecular models (e). The calculations were performed individually for the single molecules with the porphyrins adsorbed on Ag(111) and with a phenyl-ring twist angle of  $\Theta = 60^\circ$  (saddle-shape of porphyrin core). The resulting calculated data was then merged in the shown molecule sequence and after that a Gaussian smooth was applied (compare figure 4.6.2.4 (c) and (d)). ....142

**Figure 4.6.2.6** Density-functional single-particle energy levels of CoTPP (left column), FeTPP (right column), Ag(111) (center, black) and the corresponding adsorbate systems MTPP/Ag(111) (2nd and 4th column). The energy levels have been shifted for each column such that the Fermi energy ( $E_F$ ) is zero; spin label  $\beta$  corresponds to minority spin channel; energy levels of orbitals which significantly contribute to the STM image (cf. figure 4) are color-coded in red; black arrows indicate the contribution of MTPP and Ag(111) orbitals to the corresponding level in the adsorbate system; contour images of salient orbital densities of MTPP have been generated based on a density contour value of  $2.5 \cdot 10^{-3} e/\text{\AA}^3$ . ....144

**Figure 4.6.2.7.** Side-view of the orbital density of the highest-occupied orbital (labeled  $941\beta$  in figure 6) in the CoTPP/Ag(111) adsorbate systems at three different density contour values, showing that the  $d_{z^2}$  orbital on the cobalt center of CoTPP has a constructive overlap with the silver 5s band; left:  $17.5 \cdot 10^{-4} e/\text{\AA}^3$ , center:  $1.5 \cdot 10^{-4} e/\text{\AA}^3$ , right:  $0.5 \cdot 10^{-4} e/\text{\AA}^3$ . ....146

**Figure 4.6.3.1.** (a)-(c) LDOS maps of CoTPP, respectively 300 meV, 400 meV and 600 meV below the Fermi level, which were directly calculated out of experimentally acquired current-voltage curves. (d)

and (e) Enlarged LDOS maps with corresponding semitransparent space-filling models. (f) Superimposition of (d) and (e) illustrating the relative location of the energy-disperse features to each other. (f) Local STS curves extracted at distinct positions of the LDOS maps. .... 151

**Figure 4.6.3.2.** (a) LDOS map of FeTPP 130 meV below the Fermi level, which was calculated out of experimentally acquired current-voltage curves. (b) Enlarged LDOS map superimposed with a semitransparent space-filling mode. (c) Local ST curves extracted from FeTPP and 2HTPP. .... 154

**Figure 4.6.3.3.** (a) Constant current image recorded at  $U=202$  mV and  $I= 36$  pA. (b) Enlarged version of (a) with the individual molecules marked by numbers and space-filling models nearby. (c) Corresponding LDOS map of the same area 150 meV below the Fermi level. (d) and (e) Enlarged LDOS maps respectively 200 meV and 800 meV below  $E_F$ . (f) Superimposed version of (d) and (e) illustrating the relative position of the energy-dispersive features. .... 156

**Figure 4.7.1.** STM images acquired after successive deposition of iron onto Ag(111). The coverage  $\theta_{Fe}$  is indicated in the corresponding STM images. The size/scale of all shown micrographs is identical ( $100 \times 100$ ) nm<sup>2</sup>. The corresponding tunnelling parameters are: (a)  $I = 166$  pA,  $U = -930$  mV (b)  $I = 50$  pA,  $U = -263$  mV (c)  $I = 100$  pA,  $U = -287$  mV (d)  $I = 50$  pA,  $U = -212$  mV (e)  $I = 58$  pA,  $U = -289$  mV (f)  $I = 61$  pA,  $U = -305$  mV (g)  $I = 44$  pA,  $U = -199$  mV (h)  $I = 68$  pA,  $U = -302$  mV (i)  $I = 68$  pA,  $U = -313$  mV. .... 162

**Figure 4.7.2.** (a-d) space filling models of flat lying 2HPc and FeTPP on Ag(111): (a) top view of 2HPc, (b) top view of FeTPP, (c) side view of 2HPc (d) side view of FeTPP; for the latter, the terminal phenyl rings determine that the porphyrin macrocycle is lifted off from the surface. (e) STM image ( $I = 32$  pA,  $U = -1.49$  V) showing a square arrangement of FePc molecules on Ag(111). The central dot per molecule can be attributed to the iron ion. Corresponding space filling models in the image illustrate the arrangement. (f) STM image ( $I = 61$  pA,  $U = -10$  mV) showing a square arrangement of FeTPP molecules on Ag(111). Each of the molecules exhibits three dots, which correspond with the position of two opposing pyrrol rings and the central iron ion, emphasized by the superimposed models. .... 165

**Figure 4.7.3.** STM images obtained (a) after deposition of  $\theta_{Fe} = 0.3$  ML onto a monolayer of 2HTPP ( $I = 34$  pA,  $U = -197$  mV) and (b) the corresponding blow-up of the area marked with a white square in (a) highlighting the two dimensional iron islands. The small bright spots ( $\sim 1$  nm diameter) correspond to a complete monolayer of FeTPP due to metalation of 2HTPP with Fe. (c) STM image obtained after after deposition of  $\theta_{Fe} = 0.2$  ML onto a monolayer of 2HPc ( $I = 23$  pA,  $U = -1.88$  V) and (d) the corresponding blow-up of the area marked with white square in (c) highlighting two different types of Fe islands. The small bright spots ( $\sim 1$  nm diameter) correspond to a complete monolayer of FePc due to metalation of 2HPc with Fe. .... 168

**Figure 4.7.4.** STM images obtained after deposition of (a)  $\theta_{Fe} = 0.8$  ML onto a 2HTPP monolayer ( $I = 36$  pA,  $U = -1.21$  V), (b)  $\theta_{Fe} = 0.6$  ML onto a 2HPc monolayer ( $I = 41$  nA,  $U = -1.50$  V). .... 170

**Figure 4.7.5.** STM images obtained after deposition of roughly 2 ML of iron onto (a) Ag(111) ( $I = 61$  pA,  $U = -305$  mV), (b) 2HPc on Ag(111) ( $I = 32$  pA,  $U = -1.20$  V) and (c) 2HTPP on Ag(111) ( $I = 47$  pA,  $U = -1.10$  V). .....171

**Figure 4.8.1.** STM image series of a CoTPP layer on Ag(111) during exposure to NO at RT. The corresponding NO dosages are inserted in the micrographs. The rearrangement with increasing NO dose starting from the undisturbed square order in a) to an almost hexagonal arrangement in e) to an oblique structure in f) is obvious and clearly develops towards larger unit cells. The unit cell areas as extracted from the experimental data are: a)  $1.91$  nm<sup>2</sup> and f)  $2.74$  nm<sup>2</sup>. All images have a size of  $(47 \times 47)$  nm<sup>2</sup> and were acquired at  $U_{BIAS} = -0.23$  V and  $I_{SET} = 300$  pA. ....178

**Figure 4.8.2.** (a)-(o) STM images of ordered phases of CoTPP on Ag(111) before (a)-(c) and after (d)-(o) NO exposure. The corresponding values for NO exposure, the lattice vectors and angle and the density of the molecules per unit area are inserted in column one. The respective area of the unit cell and the tunnelling parameters are as follows: a)  $U = -1.18$  V,  $I = 58$  pA /  $A = 1.96$  nm<sup>2</sup>; d)  $U = -1.9$  V,  $I = 45$  pA /  $A = 2.22$  nm<sup>2</sup>; g)  $U = -1.90$  V,  $I = 45$  pA /  $A = 2.38$  nm<sup>2</sup>; j)  $U = -1.90$  V,  $I = 48$  pA /  $A = 2.56$  nm<sup>2</sup>. m)  $U = -0.94$  V,  $I = 70$  pA /  $A = 3.13$  nm<sup>2</sup>. ....180

**Figure 4.8.3.** XP spectra of the N1s region of a CoTPP layer on Ag(111) after exposure to 5000 L NO. The corresponding fitted peaks are identified with different nitrogen species as indicated. (The XPS data are extracted from [165]). .....182

**Figure 4.8.4.** (a) Constant current image of the straight square phase ( $U = -1.90$  V,  $I = 45$  pA). A fraction of molecules appears modified (marked with circles). (b) Micrograph of the hex I phase exhibiting three molecules which appear modified ( $U = -1.9$  V,  $I = 45$  pA) (c) Enhanced image of (a). 185

**Figure 4.8.5.** (a) He-I UP spectra ( $h\nu = 21.22$  eV) of (A) clean Ag(111) surface, (B) CoTPP monolayer, (C) NO-CoTPP monolayer, and (D) after heating the NO-CoTPP monolayer to 500 K for removal of the NO ligand [109]. (b) Enlarged STM image of CoTPP (right), including a modified version of the porphyrin (left), which is probably induced by attachment of NO ( $U = -1.9$  V,  $I_T = 45$  pA). (c) Local ST spectra recorded at opposing pyrrol rings and the central cobalt. ....186

**Figure 4.9.1.** (a) Top and (b) side view on space filling models of 2HOEP on Ag(111). The upwardly directed conformation of the ethyl groups was chosen based on high-resolution STM images from literature [167]. (c) Top and (d) side view on a MTPP model, emphasizing the distance of the porphyrin macrocycle to the surface. ....190

**Figure 4.9.2.** Simultaneously acquired TPD spectra of 2HOEP and CoOEP on Ag(111). The applied heating rate was 1K/s. ....191

**Figure 4.9.3.** (a) Long-range ordered intermixed 2HOEP/CoOEP monolayer with a nominal amount of 2:1 ( $U = -1.17$  V,  $I = 31$  pA). (b) High-resolution constant current image ( $U = -200$  mV,  $I = 37$  pA)

(c) The micrograph in figure (b) was superimposed with corresponding space filling models. The unit cell is drawn in, exhibiting lattice vectors of  $a = 1.55 \pm 0.10$ ;  $b = 1.55 \pm 0.10$ ;  $\alpha = 60^\circ \pm 3^\circ$ ..... 192

**Figure 4.9.4.** Series of STM images of a 2HOEP/CoOEP layer acquired at different bias voltages; (a)  $U = -200$  mV ( $I = 37$  pA), (b)  $U = -400$  mV ( $I = 39$  pA), (c)  $U = -600$  mV ( $I = 36$  pA) and (d)  $U = -1.00$  V ( $I = 34$  pA)..... 194

**Figure 4.9.5.** (a) and (b) Enlarged STM image of an intermixed 2HOEP/CoOEP layer acquired at -200 mV and -1.00 V respectively. (c) and (d) Extracted height profiles over the side groups of CoOEP and 2HOEP at the indicated positions ((a)  $I=37$  pA, (b)  $I=34$  pA). ..... 195

## References

- [1] J. V. Barth, G. Costantini, K. Kern, *Nature* 437 (2005) 671.
- [2] K. M. Kadish, *The Porphyrin Handbook, Vol. 13*, San Diego (2003).
- [3] B. Kräutler, Ostermann, S., *The Porphyrin Handbook, Vol. 11*, San Diego (2003).
- [4] D. Mansuy, P. Battioni, *The Porphyrin Handbook, Vol. 4*, Academic Press, San Diego (2000).
- [5] J. Bardeen, *Phys. Rev. Lett.* 6 (1961) 57 LP
- [6] A. D. Gottlieb, Wesoloski, L., *Nanotechnology* 17 (2006) R57.
- [7] J. Tersoff, D. R. Hamann, *Phys. Rev. Lett.* 50 (1983) 1998 LP
- [8] A. Selloni, P. Carnevali, E. Tosatti, C. D. Chen, *Phys. Rev. B* 31 (1985) 2602 LP
- [9] N. D. Lang, *Phys. Rev. B* 34 (1986) 5947 LP
- [10] G. Binnig, H. Rohrer, C. Gerber, E. Weibel, *Phys. Rev. Lett.* 49 (1982) 57 LP
- [11] V. Simic-Milosevic, M. Heyde, N. Nilius, T. Köhlig, H.-P. Rust, M. Sterrer, T. Risse, H.-J. Freund, L. Giordano, G. Pacchioni, *J. Am. Chem. Soc.* 130 (2008) 7814.
- [12] L. Ramoino, M. von Arx, S. Schintke, A. Baratoff, H.-J. Güntherodt, T. A. Jung, *Chem. Phys. Lett.* 417 (2006) 22.
- [13] P. K. Hansma, J. Tersoff, *J. Appl. Phys.* 61 (1987) R1.
- [14] C. B. Duke, *Tunneling in Solids*, Academic, New York (1969).
- [15] J. Tersoff, D. R. Hamann, *Phys. Rev. B* 31 (1985) 805 LP
- [16] C. Wagner, R. Franke, T. Fritz, *Phys. Rev. B* 75 (2007) 235432.
- [17] C. J. Chen, *Phys. Rev. Lett.* 65 (1990) 448 LP
- [18] D. Tománek, S. G. Louie, *Phys. Rev. B* 37 (1988) 8327 LP
- [19] I. S. Tilinin, M. K. Rose, J. C. Dunphy, M. Salmeron, M. A. Van Hove, *Surf. Sci.* 418 (1998) 511.
- [20] B. Koslowski, C. Dietrich, A. Tschetschetkin, P. Ziemann, *Phys. Rev. B* 75 (2007) 035421.
- [21] J. A. Stroscio, R. M. Feenstra, A. P. Fein, *Phys. Rev. Lett.* 57 (1986) 2579 LP
- [22] V. A. Ukraintsev, *Phys. Rev. B* 53 (1996) 11176 LP
- [23] J. K. Spong, H. A. Mizes, L. J. LaComb Jr, M. M. Dovek, J. E. Frommer, J. S. Foster, *Nature* 338 (1989) 137.
- [24] G. V. Nazin, S. W. Wu, W. Ho, *Proc. Natl. Acad. Sci. U. S. A.* 102 (2005) 8832.

- [25] W. Mizutani, M. Shigeno, K. Kajimura, M. Ono, *Ultramicroscopy* 42-44 (1992) 236.
- [26] A. M. de Jong, J. W. Niemantsverdriet, *Surf. Sci.* 233 (1990) 355.
- [27] P. A. Redhead, *Vacuum* 12 (1962) 203.
- [28] E. Habenschaden, J. Küppers, *Surf. Sci.* 138 (1984) L147.
- [29] I. RHK Technologies, *UHV 300 User's Guide*, Rochester Hills, Michigan USA
- [30] J. M. MacLeod, Master Thesis, Queen's University Kingston (2001).
- [31] S. Griessl, Dissertation, Ludwig-Maximilian-Universität München (2004).
- [32] D. Zemlyanov, R. Schlögl, *Surf. Sci.* 470 (2000) L20.
- [33] A. F. Carley, P. R. Davies, M. W. Roberts, A. K. Santra, K. K. Thomas, *Surf. Sci.* 406 (1998) L587.
- [34] L.-g. Liu, W. A. Bassett, *J. Appl. Phys.* 44 (1973) 1475.
- [35] R. G. Musket, W. McLean, C. A. Colmenares, D. M. Makowiecki, W. J. Siekhaus, *Appl. Surf. Sci.* 10 (1982) 143.
- [36] N. Quaas, M. Wenderoth, R. G. Ulbrich, *Surf. Sci.* 550 (2004) 57.
- [37] M. Eßer, K. Morgenstern, G. Rosenfeld, G. Comsa, *Surf. Sci.* 402-404 (1998) 341.
- [38] T. Lukasczyk, K. Flechtner, L. R. Merte, N. Jux, F. Maier, J. M. Gottfried, H. P. Steinrück, *J. Phys. Chem. C* 111 (2007) 3090.
- [39] T. A. Jung, R. R. Schlittler, J. K. Gimzewski, *Nature* 386 (1997) 696.
- [40] A. Alkauskas, L. Ramoino, S. Schintke, M. von Arx, A. Baratoff, H.-J. Güntherodt, T. A. Jung, *J. Phys. Chem. B* 109 (2005) 23558.
- [41] W. Auwärter, F. Klappenberger, A. Weber-Bargioni, A. Schiffrin, T. Strunskus, C. Woll, Y. Pennec, A. Riemann, J. V. Barth, *J. Am. Chem. Soc.* 129 (2007) 11279.
- [42] T. E. Shubina, H. Marbach, K. Flechtner, A. Kretschmann, N. Jux, F. Buchner, H. P. Steinrück, T. Clark, J. M. Gottfried, *J. Am. Chem. Soc.* 129 (2007) 9476.
- [43] S. Berner, M. de Wild, L. Ramoino, S. Ivan, A. Baratoff, H. J. Guntherodt, H. Suzuki, D. Schlettwein, T. A. Jung, *Phys. Rev. B* 68 (2003)
- [44] F. Buchner, K. Comanici, N. Jux, H.-P. Steinrück, H. Marbach, *J. Phys. Chem. C* 111 (2007) 13531.
- [45] F. Armijo, M. C. Goya, Y. Gimeno, M. C. Arevalo, M. J. Aguirre, A. H. Creus, *Electrochem. Commun.* 8 (2006) 779.
- [46] W. Auwärter, F. Klappenberger, A. Weber-Bargioni, A. Schiffrin, T. Strunskus, C. Woll, Y. Pennec, A. Riemann, J. V. Barth, *J. Am. Chem. Soc.* 129 (2007) 11279.
- [47] W. Auwärter, A. Weber-Bargioni, S. Brink, A. Riemann, A. Schiffrin, M. Ruben, J. V. Barth, *Chemphyschem* 8 (2007) 250.

- [48] V. Arima, E. Fabiano, R. I. R. Blyth, F. Delia Sala, F. Matino, J. Thompson, R. Cingolani, R. Rinaldi, *J. Am. Chem. Soc.* **126** (2004) 16951.
- [49] F. Nishiyama, T. Yokoyama, T. Kamikado, S. Yokoyama, S. Mashiko, *Appl. Phys. Lett.* **88** (2006)
- [50] M. Takada, H. Tada, *Chem. Phys. Lett.* **392** (2004) 265.
- [51] D. Barlow, L. Scudiero, K. W. Hipps, *Ultramicroscopy* **97** (2003) 47.
- [52] Z. H. Cheng, L. Gao, Z. T. Deng, Q. Liu, N. Jiang, X. Lin, X. B. He, S. X. Du, H. J. Gao, *J. Phys. Chem. C* **111** (2007) 2656.
- [53] Z. H. Cheng, L. Gao, Z. T. Deng, N. Jiang, Q. Liu, D. X. Shi, S. X. Du, H. M. Guo, H.-J. Gao, *J. Phys. Chem. C* **111** (2007) 9240.
- [54] H. Huang, W. Chen, A. T. S. Wee, *J. Phys. Chem. C* **112** (2008) 14913.
- [55] J. M. a. M. Gottfried, H., *Z. Phys. Chem.* **223** (2009) 53.
- [56] F. Buchner, V. Schwald, K. Comanici, H.-P. Steinrück, H. Marbach, *ChemPhysChem* **8** (2007) 241.
- [57] F. Buchner, K. Flechtner, Y. Bai, E. Zillner, I. Kellner, H.-P. Steinrück, H. Marbach, J. M. Gottfried, *J. Phys. Chem. C* **112** (2008) 15458.
- [58] K. Comanici, *PhD* (2007)
- [59] A. Weber-Bargioni, J. Reichert, A. P. Seitsonen, W. Auwärter, A. Schiffrin, J. V. Barth, *J. Phys. Chem. C* **112** (2008) 3453.
- [60] K. Comanici, F. Buchner, K. Flechtner, T. Lukasczyk, J. M. Gottfried, H.-P. Steinrück, H. Marbach, *Langmuir* **24** (2008) 1897.
- [61] W. Auwärter, A. Weber-Bargioni, S. Brink, A. Riemann, A. Schiffrin, M. Ruben, J. V. Barth, *ChemPhysChem* **8** (2007) 250.
- [62] A. Kretschmann, M. M. Walz, K. Flechtner, H. P. Steinrück, J. M. Gottfried, *Chem. Commun.* (2007) 568.
- [63] A. V. Zotov, D. V. Gruznev, O. A. Utas, V. G. Kotlyar, A. A. Saranin, *Surf. Sci.* **602** (2008) 391.
- [64] A. Kirakosian, J.-L. Lin, D. Y. Petrovykh, J. N. Crain, F. J. Himpsel, *J. Appl. Phys.* **90** (2001) 3286.
- [65] J. J. de Miguel, R. Miranda, *J. Phys.-Condes. Matter* **14** (2002) R1063.
- [66] F. Besenbacher, *Rep. Prog. Phys* **59** (1996) 1737.
- [67] K. Morgenstern, J. Kibsgaard, J. V. Lauritsen, E. Laegsgaard, F. Besenbacher, *Surf. Sci.* **601** (2007) 1967.
- [68] S. Shiraki, H. Fujisawa, M. Nantoh, M. Kawai, *Appl. Surf. Sci.* **237** (2004) 284.
- [69] J. E. Prieto, J. de la Figuera, R. Miranda, *Phys. Rev. B* **62** (2000) 2126 LP
- [70] D. E. Barlow, L. Scudiero, K. W. Hipps, *Langmuir* **20** (2004) 4413.
- [71] S. Yoshimoto, A. Tada, K. Suto, R. Narita, K. Itaya, *Langmuir* **19** (2003) 672.

- [72] H. Yanagi, H. Mukai, K. Ikuta, T. Shibutani, T. Kamikado, S. Yokoyama, S. Mashiko, *Nano Letters* 2 (2002) 601.
- [73] T. Lukasczyk, K. Flechtner, L. R. Merte, N. Jux, F. Maier, J. M. Gottfried, H.-P. Steinrück, *J. Phys. Chem. C* 111 (2007) 3090.
- [74] T. Wölfle, A. Gorling, W. Hieringer, *PhysChemChemPhys* 10 (2008) 5739.
- [75] F. Klappenberger, M. E. Canas-Ventura, S. Clair, S. Pons, U. Schlickum, Z. R. Qu, H. Brune, K. Kern, T. Strunskus, C. Woll, A. Comisso, A. De Vita, M. Ruben, J. V. Barth, *ChemPhysChem* 8 (2007) 1782.
- [76] W. Auwärter, A. Weber-Bargioni, A. Riemann, A. Schiffrin, O. Groning, R. Fasel, J. V. Barth, *J. Chem. Phys.* 124 (2006) 194708.
- [77] W. Hieringer, Woelfle, T., Warnick, K-G., Görling, A., unpublished
- [78] E. G. Cox, D. W. J. Cruickshank, J. A. S. Smith, *P. Roy. Soc. A-Math. Phys.* 247 (1958) 1.
- [79] R. K. C. Emmanuel A. Meyer, François Diederich, *Angew. Chem. Int. Edit.* 42 (2003) 1210.
- [80] S. Burley, G. Petsko, *Science* 229 (1985) 23.
- [81] R. Laatikainen, J. Ratilainen, R. Sebastian, H. Santa, *J. Am. Chem. Soc.* 117 (2002) 11006.
- [82] S. M. Barlow, R. Raval, *Surf. Sci. Rep.* 50 (2003) 201.
- [83] Manfred Parschau, Daniele Passerone, Karl-Heinz Rieder, Hans J. Hug, Karl-Heinz Ernst, *Angew. Chem. Int. Edit.* 48 (2009) 4065.
- [84] R. Fasel, M. Parschau, K.-H. Ernst, *439* (2006) 449.
- [85] D. Ecija, M. Trelka, C. Urban, P. d. Mendoza, E. Mateo-Marti, C. Rogero, J. A. Martin-Gago, A. M. Echavarren, R. Otero, J. M. Gallego, R. Miranda, *J. Phys. Chem. C* (2008)
- [86] L. Scudiero, D. E. Barlow, U. Mazur, K. W. Hipps, *J. Am. Chem. Soc.* 123 (2001) 4073.
- [87] F. J. Williams, O. P. H. Vaughan, K. J. Knox, N. Bampos, R. M. Lambert, *Chem. Commun.* (2004) 1688.
- [88] T. Terui, S. Yokoyama, H. Suzuki, S. Mashiko, M. Sakurai, T. Moriwaki, *Thin Solid Films* 499 (2006) 157.
- [89] T. Yokoyama, S. Yokoyama, T. Kamikado, S. Mashiko, *J. Chem. Phys.* 115 (2001) 3814.
- [90] L. Grill, I. Stass, K. H. Rieder, F. Moresco, *Surf. Sci.* 600 (2006) L143.
- [91] T. Kamikado, T. Sekiguchi, S. Yokoyama, Y. Wakayama, S. Mashiko, *Thin Solid Films* 499 (2006) 329.
- [92] F. Moresco, G. Meyer, K. H. Rieder, H. Ping, H. Tang, C. Joachim, *Surf. Sci.* 499 (2002) 94.

- [93] C. Loppacher, M. Guggisberg, O. Pfeiffer, E. Meyer, M. Bammerlin, R. Luthi, R. Schlittler, J. K. Gimzewski, H. Tang, C. Joachim, *Phys. Rev. Lett.* **90** (2003)
- [94] G. W. Gribble, E. R. Olson, J. H. Brown, C. H. Bushweller, *J. Org. Chem.* **58** (1993) 1631.
- [95] T. Sekiguchi, Y. Wakayama, S. Yokoyama, T. Kamikado, S. Mashiko, *Thin Solid Films* **464-65** (2004) 393.
- [96] T. Terui, T. Sekiguchi, Y. Wakayama, T. Kamikado, S. Mashiko, *Thin Solid Films* **464-65** (2004) 384.
- [97] F. Moresco, G. Meyer, K.-H. Rieder, J. Ping, H. Tang, C. Joachim, *Surf. Sci.* **499** (2002) 94.
- [98] Y. Okuno, T. Kamikado, S. Yokoyama, S. Mashiko, *J. Mol. Struct. - THEOCHEM* **594** (2002) 55.
- [99] T. Terui, T. Kamikado, Y. Okuno, H. Suzuki, S. Mashiko, *Curr. Appl. Phys.* **4** (2004) 148.
- [100] A. Weber-Bargioni, W. Auwärter, F. Klappenberger, J. Reichert, S. Lefrancois, T. Strunskus, C. Woll, A. Schiffrin, Y. Pennec, J. V. Barth, *ChemPhysChem* **9** (2008) 89.
- [101] Shunichi Fukuzumi, *Journal of Porphyrins and Phthalocyanines* **4** (2000) 398.
- [102] E. Baciocchi, O. Lanzalunga, A. Lapi, L. Manduchi, *J. Am. Chem. Soc.* **120** (1998) 5783.
- [103] D. Wohrle, *Journal of Porphyrins and Phthalocyanines* **4** (2000) 418.
- [104] J. M. Gottfried, K. Flechtner, A. Kretschmann, T. Lukasczyk, H.-P. Steinrück, *J. Am. Chem. Soc.* **128** (2006) 5644.
- [105] L. Scudiero, D. E. Barlow, K. W. Hipps, *J. Phys. Chem. B* **104** (2000) 11899.
- [106] X. Lu, K. W. Hipps, *J. Phys. Chem. B* **101** (1997) 5391.
- [107] T. E. Shubina, H. Marbach, K. Flechtner, A. Kretschmann, N. Jux, F. Buchner, H.-P. Steinrück, T. Clark, J. M. Gottfried, *J. Am. Chem. Soc.* **129** (2007) 9476.
- [108] L. Gross, K.-H. Rieder, F. Moresco, S. M. Stojkovic, A. Gourdon, C. Joachim, *Nat. Mater.* **4** (2005) 892.
- [109] K. Flechtner, A. Kretschmann, H.-P. Steinrück, J. M. Gottfried, *J. Am. Chem. Soc.* **129** (2007) 12110.
- [110] K. Flechtner, A. Kretschmann, L. R. Bradshaw, M.-M. Walz, H.-P. Steinrück, J. M. Gottfried, *J. Phys. Chem. C* (2007)
- [111] R. Gutzler, H. Walch, G. Eder, S. Kloft, W. M. Heckl, M. Lackinger, *Chem. Commun.* (2009) 4456.
- [112] M. O. Senge, *Chem. Commun.* (2006) 243.
- [113] *SPIP*, 3.3.9.0, Image Metrology A/S, DK-2970 Hørsholm, Lyngsø Alle 3A, Denmark

- [114] L. Bartels, G. Meyer, K.-H. Rieder, *Appl. Phys. Lett.* **71** (1997) 213.
- [115] T. J. Neal, S. J. Kang, C. E. Schulz, W. R. Scheidt, *Inorg. Chem.* **38** (1999) 4294.
- [116] K. Flechtner, A. Kretschmann, L. R. Bradshaw, M. M. Walz, H. P. Steinrück, J. M. Gottfried, *J. Phys. Chem. C* **111** (2007) 5821.
- [117] N. Lin, A. Dmitriev, J. Weckesser, J. V. Barth, K. Kern, *Angew. Chem. Int. Edit.* **41** (2002) 4779.
- [118] A. Dmitriev, H. Spillmann, N. Lin, J. V. Barth, K. Kern, *Angew. Chem. Int. Edit.* **42** (2003) 2670.
- [119] S. Clair, S. Pons, S. Fabris, S. Baroni, H. Brune, K. Kern, J. V. Barth, *J. Phys. Chem. B* **110** (2006) 5627.
- [120] S. Stepanow, N. Lin, D. Payer, U. Schlickum, F. Klappenberger, G. Zoppellaro, M. Ruben, H. Brune, J. V. Barth, K. Kern, *Angew. Chem. Int. Edit.* **46** (2007) 710.
- [121] D. Payer, S. Rauschenbach, N. Malinowski, M. Konuma, C. Virojanadara, U. Starke, C. Dietrich-Buchecker, J.-P. Collin, J.-P. Sauvage, N. Lin, K. Kern, *J. Am. Chem. Soc.* **129** (2007) 15662.
- [122] W. Auwärter, F. Klappenberger, A. Weber-Bargioni, A. Schiffrin, T. Strunskus, C. Wöll, Y. Pennec, A. Riemann, J. V. Barth, *J. Am. Chem. Soc.* **129** (2007) 11279.
- [123] C. Stadler, S. Hansen, F. Pollinger, C. Kumpf, E. Umbach, T.-L. Lee, J. Zegenhagen, *Phys. Rev. B* **74** (2006) 035404.
- [124] K. Nilson, J. Ahlund, B. Brena, E. Gothelid, J. Schiessling, N. Martensson, C. Puglia, *J. Chem. Phys.* **127** (2007) 114702.
- [125] J. Ahlund, J. Schnadt, K. Nilson, E. Gothelid, J. Schiessling, F. Besenbacher, N. Martensson, C. Puglia, *Surf. Sci.* **601** (2007) 3661.
- [126] P. H. Lippel, R. J. Wilson, M. D. Miller, C. Wöll, S. Chiang, *Phys. Rev. Lett.* **62** (1989) 171.
- [127] J.-Y. Grand, T. Kunstmann, D. Hoffmann, A. Haas, M. Dietsche, J. Seifritz, R. Moller, *Surf. Sci.* **366** (1996) 403.
- [128] X. Q. Lu, L. M. Zhang, M. R. Li, X. Q. Wang, Y. Zhang, X. H. Liu, G. F. Zuo, *ChemPhysChem* **7** (2006) 854.
- [129] X. Lu, K. W. Hipps, X. D. Wang, U. Mazur, *J. Am. Chem. Soc.* **118** (1996) 7197.
- [130] K. Walzer, M. Hietschold, *Surf. Sci.* **471** (2001) 1.
- [131] T. G. Gopakumar, M. Lackinger, M. Hietschold, *Jpn. J. Appl. Phys.* **45** (2006) 2268.
- [132] T. G. Gopakumar, M. Lackinger, M. Hackert, F. Muller, M. Hietschold, *J. Phys. Chem. B* **108** (2004) 7839.

- [133] C. Ludwig, R. Strohmaier, J. Petersen, B. Gompf, W. Eisenmenger, *J. Vac. Sci. Technol. B* 12 (1994) 1963.
- [134] Y. Bai, F. Buchner, M. T. Wendahl, I. Kellner, A. Bayer, H.-P. Steinrück, H. Marbach, J. M. Gottfried, *J. Phys. Chem. C* 112 (2008) 6087.
- [135] N. Katsonis, J. Vicario, T. Kudernac, J. Visser, M. M. Pollard, B. L. Feringa, *J. Am. Chem. Soc.* 128 (2006) 15537.
- [136] L. Scudiero, K. W. Hipps, D. E. Barlow, *J. Phys. Chem. B* 107 (2003) 2903.
- [137] J. K. Gimzewski, C. Joachim, *Science* 283 (1999) 1683.
- [138] M. Lackinger, T. Muller, T. G. Gopakumar, F. Muller, M. Hietschold, G. W. Flynn, *J. Phys. Chem. B* 108 (2004) 2279.
- [139] L. A. Zotti, G. Teobaldi, W. A. Hofer, W. Auwärter, A. Weber-Bargioni, J. V. Barth, *Surf. Sci.* 601 (2007) 2409.
- [140] F. Buchner, K.-G. Warnick, T. Wölfle, A. Görling, H.-P. Steinrück, W. Hieringer, H. Marbach, *J. Phys. Chem. C* 113 (2009) 16450.
- [141] O. Paz, I. Brihuega, J. M. Gomez-Rodriguez, J. M. Soler, *Phys. Rev. Lett.* 94 (2005) 056103.
- [142] M. S. Alam, S. Stromsdorfer, V. Dremov, P. Müller, J. Kortus, M. Ruben, J. M. Lehn, *Angew. Chem., Int. Edit.* 44 (2005) 7896.
- [143] H. S. Yoon, J. E. Lee, S. J. Park, I.-W. Lyo, M.-H. Kang, *Phys. Rev. B* 72 (2005) 155443.
- [144] A. Schiffrin, J. Reichert, W. Auwärter, G. Jahnz, Y. Penneç, A. Weber-Bargioni, V. S. Stepanyuk, L. Niebergall, P. Bruno, J. V. Barth, *Physical Review B* 78 (2008) 035424.
- [145] X. Lu, M. Grobis, K. H. Khoo, S. G. Louie, M. F. Crommie, *Phys. Rev. Lett.* 90 (2003) 096802.
- [146] M. Ruben, J.-M. Lehn, P. Muller, *Chem. Soc. Rev.* 35 (2006) 1056.
- [147] S. K. Dey, T. S. M. Abedin, L. N. Dawe, S. S. Tandon, J. L. Collins, L. K. Thompson, A. V. Postnikov, M. S. Alam, P. Muller, *Inorg. Chem.* 46 (2007) 7767.
- [148] P. G. Gassman, A. Ghosh, J. Almlöf, *J. Am. Chem. Soc.* 114 (1992) 9990.
- [149] J. Otsuki, S. Kawaguchi, T. Yamakawa, M. Asakawa, K. Miyake, *Langmuir* 22 (2006) 5708.
- [150] H. Brune, *Surf. Sci. Rep.* 31 (1998) 125.
- [151] J. H. Weaver, G. D. Waddill, *Science* 251 (1991) 1444.
- [152] C. Haley, J. H. Weaver, *Surf. Sci.* 518 (2002) 243.
- [153] J. Zhang, D. Repetto, V. Sessi, J. Honolka, A. Enders, K. Kern, *Eur. Phys. J. D* 45 (2007) 515.

- [154] R. Skomski, J. Zhang, V. Sessi, J. Honolka, K. Kern, A. Enders, Proceedings of the 52nd Annual Conference on Magnetism and Magnetic Materials, 103, 07D519.
- [155] H. Brune, M. Giovannini, K. Bromann, K. Kern, *Nature* 394 (1998) 451.
- [156] D. D. Chambliss, R. J. Wilson, S. Chiang, *Phys. Rev. Lett.* 66 (1991) 1721 LP
- [157] H. Brune, G. S. Bales, J. Jacobsen, C. Boragno, K. Kern, *Phys. Rev. B* 60 (1999) 5991 LP
- [158] B. Müller, L. Nedelmann, B. Fischer, H. Brune, J. V. Barth, K. Kern, *Phys. Rev. Lett.* 80 (1998) 2642 LP
- [159] R. Q. Hwang, J. Schröder, C. Günther, R. J. Behm, *Phys. Rev. Lett.* 67 (1991) 3279 LP
- [160] F. Buchner, K. Seufert, W. Auwärter, D. Heim, J. V. Barth, K. Flechtner, J. M. Gottfried, H.-P. Steinrück, H. Marbach, *ACS Nano* 3 (2009) 1789.
- [161] C. M. Mate, G. A. Somorjai, *Surf. Sci.* 160 (1985) 542.
- [162] P. Zebisch, W. Huber, H.-P. Steinrück, *Surf. Sci.* 258 (1991) 1.
- [163] H. Ohtani, R. J. Wilson, S. Chiang, C. M. Mate, *Phys. Rev. Lett.* 60 (1988) 2398 LP
- [164] O. P. H. Vaughan, M. Turner, F. J. Williams, A. Hille, J. K. M. Sanders, R. M. Lambert, *J. Am. Chem. Soc.* 128 (2006) 9578.
- [165] K. Flechtner, Dissertation, Friedrich-Alexander-Universität Erlangen-Nürnberg (2007).
- [166] A. Pashutski, M. Folman, *Surf. Sci.* 216 (1989) 395.
- [167] L. Scudiero, D. E. Barlow, K. W. Hipps, *J. Phys. Chem. B* 106 (2002) 996.
- [168] Y. Miyake, H. Tanaka, T. Ogawa, *Colloid Surface A* 313-314 (2008) 230.
- [169] A. Ogunrinde, K. W. Hipps, L. Scudiero, *Langmuir* 22 (2006) 5697.
- [170] Y. Bai, Buchner, F., Kellner, I., Schmid, M., Vollnhals, F., Steinrück, H.-P., Marbach, H. and Gottfried J.M., *New J. Phys. in press* (2009)

## List of Publications

- 1 F. Buchner, V. Schwald, K. Comanici, H.-P. Steinrück, H. Marbach, *ChemPhysChem* 8 (2007) 241.
- 2 T. E. Shubina, H. Marbach, K. Flechtner, A. Kretschmann, N. Jux, F. Buchner, H.-P. Steinrück, T. Clark, J. M. Gottfried, *J. Am. Chem. Soc.* 129 (2007) 9476.
- 3 F. Buchner, K. Comanici, N. Jux, H.-P. Steinrück, H. Marbach, *J. Phys. Chem. C* 111 (2007) 13531.
- 4 K. Comanici, F. Buchner, K. Flechtner, T. Lukasczyk, J. M. Gottfried, H.-P. Steinrück, H. Marbach, *Langmuir* 24 (2008) 1897.
- 5 Y. Bai, F. Buchner, M. T. Wendahl, I. Kellner, A. Bayer, H.-P. Steinrück, H. Marbach, J. M. Gottfried, *J. Phys. Chem. C* 112 (2008) 6087.
- 6 F. Buchner, K. Flechtner, Y. Bai, E. Zillner, I. Kellner, H.-P. Steinrück, H. Marbach, J. M. Gottfried, *J. Phys. Chem. C* 112 (2008) 15458.
- 7 F. Buchner, *Z. Phys. Chem.* 223 (2009) 131.
- 8 F. Buchner, K. Seufert, W. Auwärter, D. Heim, J. V. Barth, K. Flechtner, J. M. Gottfried, H.-P. Steinrück, H. Marbach, *ACS Nano* 3 (2009) 1789.
- 9 F. Buchner, K.-G. Warnick, T. Wölfle, A. Görling, H.-P. Steinrück, W. Hieringer, H. Marbach, *J. Phys. Chem. C* 113 (2009) 16450.
- 10 Y. Bai, Buchner, F., Kellner, I., Schmid, M., Vollnhals, F., Steinrück, H.-P., Marbach, H. and Gottfried J.M., *New J. Phys.*, in press (2009)
- 11 F. Buchner et al., *Ordering Aspects of TPPs*, in preparation (2009)
- 12 F. Buchner et al., *Addressing Molecular Orbitals of TPPs with CITS*, in preparation (2009)



# Appendix

Figure	STM file	Figure	STM file	Figure	STM file
4.1.1 (a)	80114042	4.4.2 (b)	70712016	4.7.1 (g)	71016009
4.1.1 (b)	60313040	4.4.2 (c)	7071267	4.7.1 (h)	71016027
4.1.1 (c)	70314040	4.4.3	70806007	4.7.1 (i)	71016040
4.1.1 (d)	80507028.	4.4.4	70806007	4.7.2 (e)	71114030
4.1.4	70426074.	4.4.6 (a)	70717042	4.7.2 (f)	70423055
4.1.4	80123011	4.4.6 (b)	7071633	4.7.3 (a), (b)	71212070
4.1.4	70423056	4.4.6 (c)	7071632	4.7.3 (c), (d)	71001036
4.1.6 (a)	70426074	4.4.7 (a)	7071267	4.7.4 (a)	71212092
4.1.6 (b)	70426074	4.4.7 (b)	70718057	4.7.4 (b)	71002020
4.1.6 (c)	80131027	4.5.2 (a)	70905044	4.7.5 (a)	71015006
4.1.6 (d)	71204058	4.5.2 (b)	70926017	4.7.5 (b)	71002054
4.1.7 (a)	70423056	4.5.3 (a)	70924043	4.7.5 (c)	71217018
4.1.7 (c)	71204047	4.5.3 (b)	70926020	4.8.1 (a)	60427059
4.1.7 (d)	80123011	4.5.3 (c)	70926048	4.8.1 (b)	60427062
4.1.7 (e)	80602008	4.5.3 (d)	70927029	4.8.1 (c)	60427066
4.1.8	70425007	4.5.4 (a)	71219024	4.8.1 (d)	60427070
4.2.2 (a)	51117100	4.5.4 (b)	71219050	4.8.1 (e)	60427076
4.2.2 (b)	51118016	4.5.4 (c)	71219052	4.8.1 (f)	60427085
4.2.3 (a)	60620001	4.6.1 (a)	60112052	4.8.2 (a) - (c)	80123010
4.2.3 (b)	60629002	4.6.1 (b)	05613015	4.8.2 (d) - (f)	80611081
4.2.3 (c)	60629003	4.6.1 (c)	05613015	4.8.2 (g) - (i)	80521063
4.2.3 (d)	60622021	4.6.1 (d)	05613027	4.8.2 (j)	80521081
4.2.5 (a) - (d)	51118016	4.6.2	05613015-27	4.8.2 (k) - (l)	80521062
4.2.5 (e) - (h)	51118015	4.6.3 (a)	60112052	4.8.2 (m) - (o)	80613200
4.2.5 (i) - (l)	60627073	4.6.3 (b)	60303026	4.8.4 (a), (c)	80521063
4.2.5 (m) - (p)	60622021	4.6.3 (c)	60303026	4.8.4 (b)	80611080
4.2.7 (a), (c)	60622032	4.6.3 (d)	80131003	4.8.5 (b)	80521063
4.2.7 (b), (d)	60622021	4.6.3 (e)	80131020	4.9.3 (a)	81006001
4.3.1 (a)	60801046	4.6.3 (f)	80131020	4.9.3 (b), (c)	81002031
4.3.1 (b)	60717053	4.6.4 (a)	60117033	4.9.4 (a)	81002031
4.3.2 (a)	60821069	4.6.4 (b)	60117034	4.9.4 (b)	81009005
4.3.2 (b)	60823020	4.6.5	70222113	4.9.4 (c)	81009003
4.3.2 (c)	60823034	4.6.2.1 (b)	60310011	4.9.4 (d)	81009002
4.3.2 (d)	60824038	4.6.2.1 (c)	61019013	4.9.5 (a)	81002031
4.3.3 (a)	60718005	4.6.2.2 (a), (b)	61102060	4.9.5 (b)	81002040
4.3.3 (b)	60719003	4.6.2.2 (c), (d)	61102062		
4.3.4 (a)	71204024	4.6.2.3	80122012		
4.3.4 (b)	71204060	4.6.2.4 (a)	61102062		
4.3.4 (c)	71206007	4.6.2.4 (b)	80123010		
4.3.5 (a)	71204048	4.6.2.5 (c)	80202023		
4.3.5 (b)	70517023	4.6.2.5 (d)	80202041		
4.3.6 (a)	61221015	4.6.3.1	70222113		
4.3.6 (a)	61221043	4.6.3.2	71206015		
4.3.7 (a)	70307007	4.6.3.3	80202016		
4.3.7 (b)	70307030	4.7.1 (a)	71009039		
4.3.7 (c)	70312036	4.7.1 (b)	71011020		
4.3.7 (d)	70314040	4.7.1 (c)	71011030		
4.3.8 (a)	70314005	4.7.1 (d)	71012024		
4.3.8 (b) - (d)	70314071	4.7.1 (e)	71012039		
4.4.2 (a)	70712009	4.7.1 (f)	71015006		

Nomenclature of STM files according to yymmddxxx (yy: year, mm: month, dd: day, xxx number)



## Danksagung

An dieser Stelle möchte ich mich bei all denen Bedanken, die mich im Laufe der vergangenen Jahre mit Rat und Tat unterstützt haben. Besonderer Dank gilt Herrn Prof. Dr. Hans-Peter Steinrück für die freundliche Aufnahme in seine Arbeitsgruppe und das entgegengebrachte Vertrauen. Herzlichen Dank an Dr. Hubertus Marbach für die stets sehr gute und fruchtbare Zusammenarbeit. Des Weiteren möchte ich folgenden Personen danken: Ina Kellner für die ausgezeichnete Zusammenarbeit im Labor; Carmen Comanici für die freundliche Einführung in die Vorgehensweise mit der UHV Apparatur, Hans-Peter Bäumler für die hervorragende Abdeckung aller elektronischen Fragestellungen, allen Mitarbeitern der Werkstatt für die perfekte Umsetzung der konstruktiven Wünsche, Andreas Bayer und Thomas Lukasczyk für ihre Hilfestellungen, zahlreiche Diskussionen und auch das Korrektur lesen, meinen Kollegen im Labor im Rahmen ihrer jeweiligen Abschlussarbeiten: Veronika Schwald, Christina Drahten, Florian Vollnhals, Elisabeth Zillner, Michael Röckert und Stefanie Gläbel, Berndt Kreß für sein Wirken in Sachen Labortechnik, Uwe Sauer für alle rechner-technischen Hilfestellungen; Dr. Michael Gottfried, Yun Bai und Ken Flechtner für die spektroskopischen Messungen, die Diskussionen und gemeinsamen schriftlichen Ausführungen, den Kollegen aus der theoretischen Chemie: Prof. Dr. Andreas Görling, Dr. Wolfgang Hieringer, Thorsten Wölfle und Karl-Georg Warnick für die fruchtbare Zusammenarbeit. Insgesamt möchte ich den Mitgliedern des Arbeitskreises für die allseits vorhandene Hilfsbereitschaft und dem sehr angenehmen Arbeitsklima danken.



# Lebenslauf

## ANGABEN ZUR PERSON

**Name** Buchner, Florian

**Geburtsort** Burghausen

**Nationalität** deutsch

## HOCHSCHULBILDUNG UND

## BERUF

**Seit 09/2005** **Wissenschaftlicher Mitarbeiter am Lehrstuhl für Physikalische Chemie an der Friedrich-Alexander-Universität Erlangen-Nürnberg**  
PhD: Untersuchung der Anordnung, der elektronischen Eigenschaften und der Reaktivität von Porphyrinen auf Ag(111) mittels STM

**03/2004-03/2005** **Master Thesis an der Ludwig-Maximilian-Universität München:** STM/STS Untersuchungen wasserstoffverbrückter Netzwerke and der flüssig-Festkörper Grenzfläche

**10/02-03/2005** **Masterstudiengang: Mikro- und Nanotechnik an der Fachhochschule München**

**09/2000-03/2003** **Dipl.-Ing. in Produktion und Service bei TuiLaser, Germering**

**01/2000-07/2000** **Diplomarbeit im Laserforschungslabor der Ludwig-Maximilian-Universität München:** Optisches System zur Visualisierung funktionaler Areale des Cortex

**10/1995-09/2000** **Diplomstudiengang: Feinwerk- und Mikrotechnik an der Fachhochschule München**

## WEHRDIENST

**07/1994- 07/1995** Wehrdienstleistender bei der Gebirgsjägerbrigade 23, Bad Reichenhall

## SCHULBILDUNG

**09/1981** Einschulung in die Grundschule, Burghausen

**07/1994** Erlangung der Fachhochschulreife an der Fachoberschule, Altötting